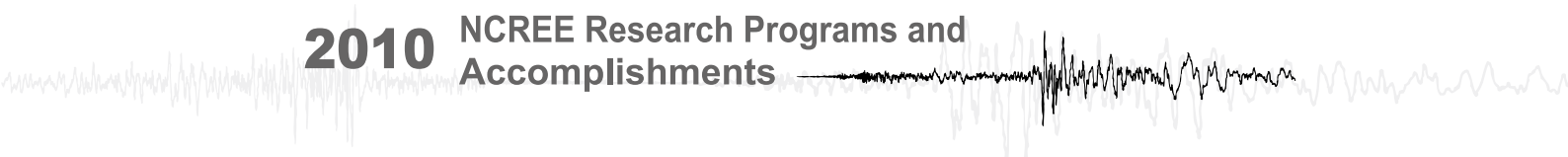


2010

NCREE Research Programs and Accomplishments



National Center for Research on Earthquake Engineering



2010 NCREE Research Programs and
Accomplishments

Foreword

The “2010 Report on Research Progress and Accomplishments” is the eleventh issue of its kind. With this publication, some important ongoing research projects conducted at the National Center for Research on Earthquake Engineering (NCREE), Taiwan are highlighted. This year, 41 selected articles are contained in this report covering a broad spectrum of research efforts made in the year 2010. Seven major categories are encompassed as follows:

- Research on performance-based seismic design methods, seismic performance assessment, and retrofit techniques
- Research on disaster reaction, risk evaluation, and management
- Development of advanced experimental technologies, numerical simulation software, and imagery measurement capability
- Integrated platform for multi-disciplinary research on bridge health monitoring
- Development and implementation of earthquake early warning system
- Display platform of high-resolution digital earth geographic information

It is our sincere hope that the vivacious research efforts at NCREE could be evaluated and recognized by the earthquake engineering community through the continuous publication of such progress reports. We look forward that this information will create opportunities for exchange of research findings as well as make contributions to the national coordination and international collaboration in the field of earthquake engineering.

The full version of each research included in the progress report can be requested from the corresponding authors. The electronic version (in PDF format) of the report can be also downloaded from NCREE’ s official web site (<http://www.ncee.org>).

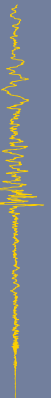
Kuo-Chun Chang, Director
June 1, 2011



Contents

- 1 Preliminary Improvement on the Performance-Based Seismic Design of Buildings in Taiwan (IV)**
Tsung-Jen Teng, Juin-Fu Chai, Wen-I Liao, Wen-Yu Jean, Yuan-Tao Weng, Shyh-Bin Chiou, Fan-Ru Lin, and Te-Kuang Chow
- 5 Scaling of Earthquake Ground Motion Records for Bi-directional Response-History Analyses**
Yuan-Tao Weng, Jui-Liang Lin and Keh-Chyuan Tsai
- 9 Study on Design Earthquakes for Kinmen, Matsu and Penhu Areas**
Yu-Wen Chang, Wen-Yu Jean, Shyh-bin Chiou
- 13 Application and Improvement of the Coefficient Method of Displacement**
Yuan-Tao Weng, Shyh-Jiann Hwang
- 17 Seismic Evaluation Method of Geometrically Eccentric Reinforced Concrete Structure with Torsional Plastic Hinge**
Lap-Loi Chung, Lai-Yun Wu, Chi-Hsiang Sun, Kuan-Hua Lien, Yao-Sheng Yang, Zen-Hao Chen, Guo-Luen Huang, Yeong-Kae Yeh, Te-Kuang Chow
- 21 Experimental and Numerical Study on Dynamic Collapse of Reinforced Concrete Frames**
Chiun-lin Wu, Shyh-Jiann Hwang, Yuan-Sen Yang and Kenneth Elwood
- 25 Axial Loading Capacity of Retrofitted Full-scale Rectangular RC Columns**
Min-Lang Lin, Ying-Han Wu, Chih-Tsung Lin and Pei-Ching Chen
- 29 Inelastic Response Spectra for Two-Way Asymmetric-Plan Structures under Bi-Directional Ground Excitations**
Jui-Liang Lin, Keh-Chyuan Tsai and Wen-Chia Yang
- 33 Study on the Earthquake Damage Evaluation for RC Framed Buildings and on the School Building Damage Database**
Yi-Hsuan Tu, Lai-Cheng Ao and Wen-Yu Jean
- 37 Verification of Detailed Seismic Evaluation Method Using 921 Seismic Damage Records of School Buildings**
Yeong-Kae Yeh, Fu-Pei Hsiao and Li-Ming Tseng
- 41 Seismic Upgrading Strategy for Near-Fault School Buildings**
Fu-Pei Hsiao, Hui-Hsien Lo, Wen-Yu Chien and Shyh-Jiann Hwang
- 45 Pushover Analysis of Irregular Bridges**
Hsiao-Hui Hung, Chang-Wei Huang and Hao-Jen Liao
- 49 Bridge Load Testing in the Malingkeng Qidu Road Section of Freeway No.3 near Xizhi, Keelung**
Zheng-Kuan Lee
- 53 Seismic Behavior of Scoured Bridges (I)**
Kuo-Chun Chang, Shiou-Chun Wang, Kuang-Yen Liu, Tzou-Shin Ueng, Chia-Han Chen and Cheng-Hsing Chen
- 57 A Study on the Simplified Seismic Evaluation and Preliminary Design Method for Critical Equipment**
Juin-Fu Chai and Fan-Ru Lin

- 61 **Development of Raw Data Storage Module on a Structural Health Monitoring Prototype**
Ming-Yi Shen, Tzu-Kang Lin and Kuo-Chun Chang
- 65 **Analytical and Experimental Studies on Seismic Behavior of Mid-Story Isolated Buildings (II)**
Shiang-Jung Wang, Kuo-Chun Chang, Jenn-Shin Hwang, Jia-Yi Hsiao and Ying-Chen Hung
- 69 **Evaluation of the Maximum Sliding Displacements of Unanchored Equipment under Seismic Excitations**
Keng-Chang Kuo, Hung-Wei Chiang, Pei-Yang Lin and Fan-Ru Lin
- 73 **Experimental Study on Seismic Performance of Equipment with Vibration Isolation Devices (II)**
Jenn-Shin Hwang, Fan-Ru Lin and Min-Fu Chen
- 77 **Seismic Behaviors of High Strength RC Columns under High Axial Loads**
Ker-Chun Lin, Shyh-Jiann Hwang and Fong-Chan Chang
- 81 **Optimal Design Formulae for Nonlinear Friction Pendulum Tuned Mass Dampers**
Lap-Loi Chung, Lai-Yun Wu, Mei-Chun Lin, Kuan-Hua Lien, Hsu-Hui Huang and Yong-An Lai
- 85 **Optimal Design of Bidirectional Friction Pendulum Tuned Mass Damper with Varying Curvature**
L.L. Chung, L.Y. Wu, T.H. Lin, M.C. Lin, P.S. Kao and K.H. Lien
- 89 **Study on Eccentric Rolling Isolation System with Additional Friction Damping**
Cho-Yen Yang, Cheng-Hsin Hsieh, Lap-Loi Chung, Lai-Yun Wu and Hung-Ming Chen
- 93 **Decentralized Control using Smart Control Device**
Shieh-Kung Huang, Kung-Chun Lu and Chin-Hsiung Loh
- 97 **Verification of Predicted Structural Response by Scenario-based Technique**
Bing-Yun Wu and Tzu-Kang Lin
- 101 **On-line Structural Damage Localization and Quantification Using Wireless Sensors**
Ting-Yu Hsu, Shieh-Kung Huang, Kung-Chung Lu, Chin-Hsiung Loh
- 105 **Theoretical and Experimental Study on the Dynamic Characteristic of Stayed Cable**
Shieh-Kung Huang, Pei-Yang Lin and Chin-Hsiung Loh
- 109 **Shaking Table Tests on Model Pile in Liquefiable Ground**
Tzou-Shin Ueng, Chia-Han Chen, Cheng-Hsing Chen and Chang-Liang Lin
- 113 **Development of Damage Evaluation Techniques for Structural Foundation (II)**
Yung-Yen Ko, Wei-Kuang Chang and Chia-Han Chen
- 117 **Lateral Loading-Unloading Behavior of an Aluminum Model Pile in Saturated Sand**
Jiunn-Shyang Chiou, Wei-Lun Tai, Chia-Han Chen and Cheng-Hsing Chen
- 121 **Earthquake Source Parameters and Micro-tremor Site Characteristics Study-Geochemical Monitoring**
Vivek Walia, Shih-Jung Lin, Tsanyao Frank Yang and Kuo-Liang Wen



- 125 **Characteristics of Near-Surface S-wave Velocity**
Chun-Hsiang Kuo, Kuo-Liang Wen, Hung-Hao Hsieh and Che-Min Lin
- 129 **Earthquake Source Parameters and Micro-tremor Site Characteristics (Micro-Earthquake Monitoring)**
Che-Min Lin, Tao-Ming Chang, Hung-Hao Hsieh, Kuo-Liang Wen, and Chun-Hsiang Kuo
- 133 **Assessment of Damage and Serviceability of Water Systems Following Earthquakes**
Gee-Yu Liu and Hsiang-Yuan Hung
- 137 **Engineering Geological Database for TSMIP**
Kuo-Liang Wen, Hung-Hao Hsieh and Chun-Hsiang Kuo
- 141 **An Image-based Measurement Method for Plane Strain and Crack Observations**
Yuan-Sen Yang, Chang-Wei Huang, Chiun-lin Wu
- 145 **Numerical Simulation Studies of Buried Pipes**
Ren-Zuo Wang, Bing-Chang Lin, Steve (C.H.) Huang, Xin-Han You and You-Hao Wang
- 149 **Design of Experiment and Numerical Analyses of Impacts on Concrete**
Ren-Zuo Wang, Keh-Chyuan Tsai, Bin-Chang Lin and Fan-Jun Xie
- 153 **Numerical Simulation on the Effect of Bound Slip in Reinforced Concrete Structures**
Ren-Zuo Wang, Chung-Yue Wang and Jen-Hui Liu
- 157 **A Neural Network-Based Approach for On-site Earthquake Early Warning System**
Chu-Chieh Jay Lin and Ze-Ping Shen
- 161 **Application of Seismic Hazard Mitigation on 3D-GIS/3D-VR Platform**
Chin-Hsun Yeh, Chu-Chieh Jay Lin and Chih-Hsin Chen

Preliminary Improvement on the Performance-Based Seismic Design of Buildings in Taiwan (IV)

Tsung-Jen Teng¹, Juin-Fu Chai², Wen-I Liao³, Wen-Yu Jean⁴,

Yuan-Tao Weng⁵, Shyh-Bin Chiou⁶, Fan-Ru Lin⁷, and Te-Kuang Chow⁸

鄧崇任¹、柴駿甫²、廖文義³、簡文郁⁴、翁元滔⁵、邱世彬⁶、林凡茹⁷、周德光⁸

Abstract

The objective of this study is to link efficiently the current classical force-based design code to a future version of performance-based design guideline. For this purpose, a transition design framework has been proposed to combine the concepts of seismic use group and seismic design category, which are both recommended by FEMA450 and IBC2006. Moreover, the provisions and the associated commentaries were developed, and it can be expected to serve as an intermediate version of the performance-based design code.

Keywords: intermediate version of performance-based design, performance objective, deformation requirement, performance evaluation, acceptance criteria

Introduction

The seismic performance of a building depends on both its strength and deformation capacities. The main objective of the traditional seismic design code is only to achieve the strength requirement based on a predefined deformation capacity. In order to link smoothly the current classical force-based design code to a future version of performance-based design code, a design framework was proposed to incorporate the current sophisticated force-based design methodology with the concepts of seismic use group and seismic design category which are recommended by FEMA 450 and IBC 2006. Based on the design framework, the provisions and commentaries were developed, and it can be expected to serve as an intermediate version of performance-based design guideline.

The strategy to develop the intermediate version of performance-based design guideline is to arrange the

performance related provisions in specific chapters: (1) the design performance objectives are specified in Chapter 1: General Provision, (2) the seismic demands are specified in Chapter 2: Ground Motions, (3) the deformation requirement (deflection and drift limits) is specified in Chapter 3: Structural Design Criteria, and (4) the procedures to determine the story drift is specified in Chapter 4: Structural Analysis.

Digested Provisions

The deformation requirement (deflection and drift limits) is specified in Chapter 3: Structural Design Criteria, and the key provision is specified as follows:

¹ Research Fellow, National Center for Research on Earthquake Engineering, tjteng@ncree.org.tw.

² Research Fellow, National Center for Research on Earthquake Engineering, chai@ncree.org.tw.

³ Associated Professor, Department of Civil Engineering, National Taipei University of Technology, wiliao@ntut.edu.tw.

⁴ Research Fellow, National Center for Research on Earthquake Engineering, wychien@ncree.org.tw.

⁵ Associated Research Fellow, National Center for Research on Earthquake Engineering, ytweng@ncree.org.tw.

⁶ Assistant Research Fellow, National Center for Research on Earthquake Engineering, sbchiou@ncree.org.tw.

⁷ Assistant Research Fellow, National Center for Research on Earthquake Engineering, frlin@ncree.org.tw.

⁸ Assistant Technology Fellow, National Center for Research on Earthquake Engineering, tkchow@ncree.org.tw.

3.5.2 Deflection and drift limits.

The design story drift, Δ , shall not exceed the allowable story drift, Δ_a , as obtained from Table 3-4 for any story. For structures with significant torsional deflections, the maximum drift shall include torsional effects.

The procedures to determine the story drift is specified in Chapter 4: Structural Analysis, and the key provision about the nonlinear static analysis (push over analysis) is specified as follows:

4.5.5 Target displacement

The target displacement of the control point, δ_T , shall be determined using Equation (4-22) as follows:

$$\delta_T = C_0 C_1 S_{aD} \left(\frac{T_e}{2\pi} \right)^2 g \quad (4-22)$$

where the spectral acceleration, S_{aD} , and the effective fundamental period, T_e , are determined from either Secs. 2.4 or 2.5, g is the acceleration of gravity, and the coefficients C_0 and C_1 are determined as follows.

$$C_0 = \frac{\sum_{i=1}^n W_i \phi_i}{\sum_{i=1}^n W_i \phi_i^2} \quad (4-23)$$

where

W_i = the portion of the seismic weight, W , at Level i ,
 ϕ_i = the amplitude of the shape vector at Level i .

Where the effective fundamental period of the structure in the direction under consideration, T_e , is greater than T_0^D , the coefficient C_1 shall be taken as 1.0. Otherwise, the value of the coefficient C_1 shall be calculated using Eq. (4-24) as follows:

$$C_1 = \frac{1}{R_d} \left[1 + \frac{(R_d - 1) T_0^D}{T_e} \right] \quad (4-24)$$

where R_d is given by Eq. (4-25) as follows:

$$R_d = \frac{S_{aD}}{V_y / W} \quad (4-25)$$

where T_0^D is defined in Sec. 2.4 or 2.5, and V_y is defined in Sec. 4.5.3.

4.5.6 Story drift

The design story drift, Δ , taken as the value obtained for each story at the step at which the target displacement is reached shall not exceed the drift limit specified in Sec. 3.5 multiplied by $0.85 \times 1.4 \alpha_y F_u / C_d$.

Design Example

The building model selected for design is a 6-story RC frame structure. The analyzed model of the building structure is shown in Fig. 1. The lateral force resisting system for the building is the special moment resisting frame with 5 bays and 2 bays in X-dir and Y-dir, respectively. The story height for all stories is 3.0 m. The seismic effective weight of the building is 1260 t. The building is assumed to be located in the Taichung city and belong to the seismic group I, and site 1 (hard site) condition is adopted herein for the seismic design. In this example, the linear static procedure is used firstly for the determination of the structural member size and required reinforcements. Then the nonlinear static procedure and nonlinear dynamic procedure are utilized for the check of the required performances of the designed structure.



Fig. 1 Analyzed model of the designed structure

From the table of the report of this research, the short-period spectral acceleration ($T=0.3$ s) S_{DS} and one-second spectral acceleration ($T=1.0$ s) S_{D1} of Taichung city are $0.7g$ and $0.45g$, respectively. Then the characteristic period T_0^D (corner period of the response spectrum) is 0.73 sec. The site class of the example is assumed as site 1 (hard site), and hence, the site amplification factors F_a for the short period response and factor F_v for the long period response are equal to 1.0. The fundamental period T_e of the designed structure is 0.61 s. It is smaller than the characteristic period; therefore the corresponding design spectral acceleration S_{aD} of this structure is $0.7g$. Design lateral force for the linear static procedure is calculated as

$$V_{dx} = \frac{S_{aD} I}{1.4 \alpha_y F_u} W = \frac{0.7 \times 1.0}{1.4 \times 1.5 \times 3.53} \times 1260 = 118.9 \text{ t}$$

and the USD method is applied for the design of the reinforcements of the beam-column members.

After the preliminary design procedure, the moment capacity and plastic rotation angle of beams

and columns should be determined firstly for the performance check procedure. The yield moment and corresponding plastic rotation angle are determined by the regulation of FEMA 356. The structural seismic performance level is check by the nonlinear pushover analysis. The lateral load distribution, selection of control node, modeling parameters and numerical acceptance criteria for nonlinear pushover analysis are following the regulation of this research. The target displacement δ_T of the push over analysis is

$$\delta_T = C_0 C_1 S_{ad} \left(\frac{T_c}{2\pi} \right)^2 g = 28.3cm$$

where C_0 is the modification factor to relate the spectral displacements of multiple degree of freedom system to displacements of single degree of freedom system. The factor C_1 is to relate expected maximum inelastic displacements to displacements calculated for linear elastic response. Figure 2 shows the capacity of the designed structure, and the associated yield strength V_y (=310 t) and yield displacement δ_y (=18 cm) are also shown in the figure.

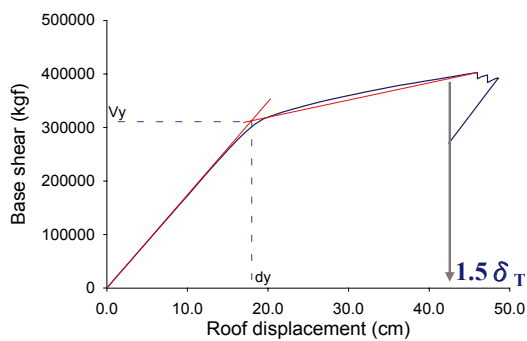


Fig. 2 Capacity curve of the designed structure

There are three seismic performance criteria for the seismic demand of 475 years return period shall be checked are:

1. The base shear shall be increased as the roof displacement increased for the roof displacement less than $1.5\delta_T$ (=42.4cm) at the capacity curve. From Fig. 2, we know that the base shear of the capacity of the analyzed structure decreased starting at point of displacement about 46 cm. Therefore, the capacity curve satisfies the required performance criteria.
2. Story drifts of all stories shall be less than $0.85 \times 1.4 \alpha_y F_u \Delta_d / C_d = 6.6cm$ (2.2% story drift) at the state of roof displacement equal to target displacement. Table 1 shows the story drifts of the designed structure at the roof displacement corresponding to the target displacement δ_T . No drift of any story exceed the required criteria 2.2%, then the performance of story drift is satisfied.
3. Displacement demands of all members shall be less than 2/3 maximum allowable displacement demand at the state of roof displacement equal to target displacement. In this example, the maximum plastic hinge rotation angles for beam and column are 0.025 rad and 0.02 rad, respectively. The performance criteria Life Safety for members is setting as the 2/3 maximum rotation angle of the members, then we can judge the seismic performance level by the plastic distribution figure. Figure 3 shows the plastic distribution of beams and columns at the roof displacement corresponding to the target displacement δ_T . From this figure we know that the demands of all members are less than the regulated demand.

Table 1. Story drifts at target displacement

Story	drift
RF	0.005890
6F	0.011568
5F	0.017707
4F	0.021381
3F	0.021297
2F	0.012625

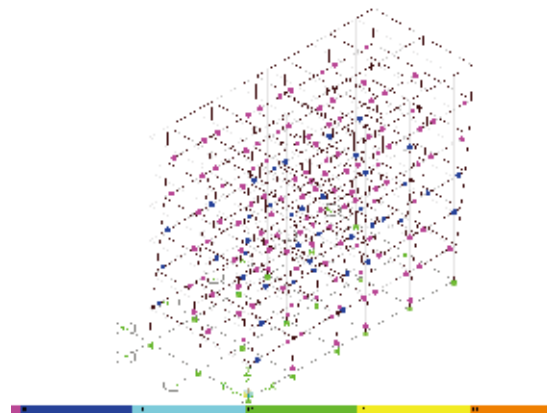


Fig. 3 Plastic hinge distribution at target displacement

The stick model with Takeda hysteretic model is adopted in this study for simulating the dynamic behavior of the designed structure. Each story of the building is modeled by a horizontal nonlinear spring with lumped point mass. The force displacement relation of each degree of freedom of the stick model is obtained from the story shear and story drift of the structure by push over analysis. Figure 4 shows the relation of story shear and story drift by push over analysis. The earthquake record at station TCU052 is used as the base for obtaining the spectral compatible time history. According to the regulation of the report of this research project, the original seismogram TCU052 is adjusted in the frequency domain to the simulated seismogram having the

spectral compatibility characteristic. Figure 5 shows the recorded seismogram, simulated seismogram and corresponding response spectrum of record at TCU052. The simulated time history is scaled to $PGA=0.4S_{DS}=0.28g$ (475 years return period) as the input ground motion for the nonlinear dynamic analysis. The corresponding seismic performance criteria for nonlinear dynamic procedure is the story drift shall less than 6.6 cm at $PGA=0.28g$. Figure 6 shows the Time histories of story drift of each story to simulated input ground motion with $PGA=0.28g$. The maximum story drift occurs at story 3F and have the value about 6.4 cm. It is less than the limited story drift 6.6 cm.

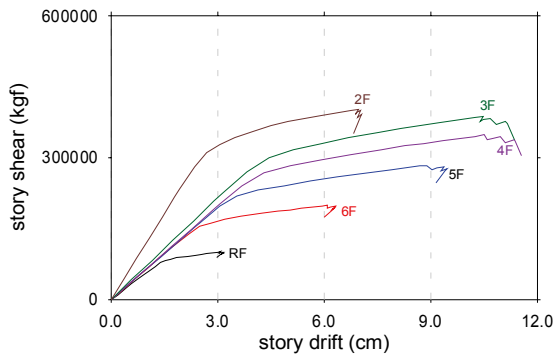


Fig. 4 Relation of story shear and story drift by push over analysis.

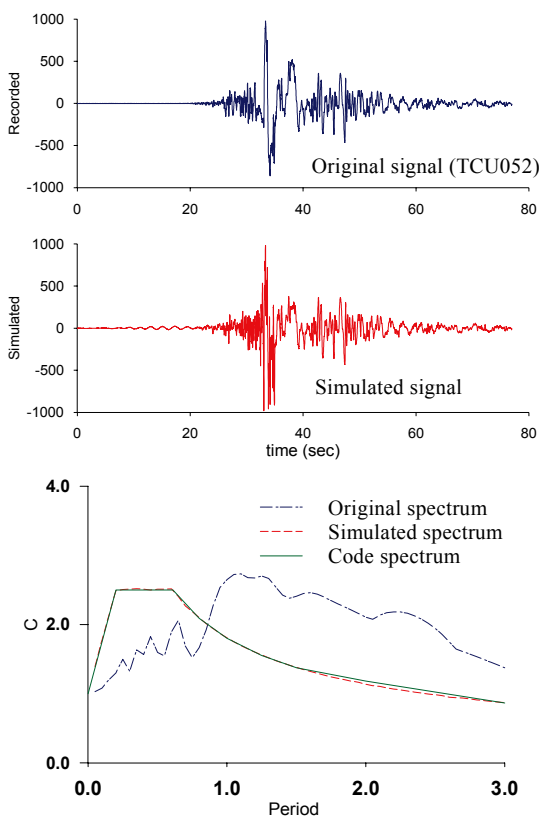


Fig. 5 Recorded seismogram, simulated history and corresponding normalized response spectrum.

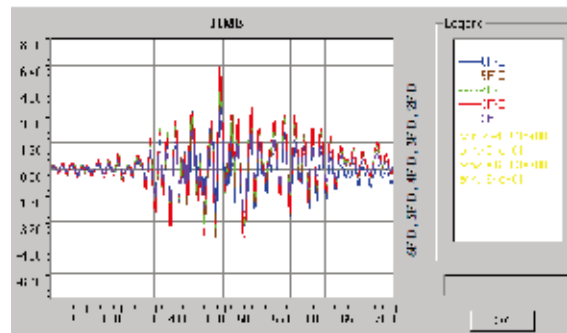


Fig. 6 Time histories of story drift.

Conclusions

In order to incorporate the proposed performance matrix into the current seismic design code, the design framework and the contents of the current seismic design code has been reorganized for the additional provisions on the analysis procedures to evaluate the maximum story drift and the acceptance criteria. The intermediate version has the merit of, for example, when a structural engineer designs a building in accordance with the requirements on the various Seismic Use Group, he can determine and make sure if the building can achieve the specified design objectives. This implies that he needs not to perform the performance evaluation procedure that may be much cumbersome. In this situation, it makes no difference with the classical one. Also, this intermediate version provides an option beyond the current seismic code, as it is designed for specific performance, rather than simply achieving code compliance. It is expected that the intermediate version as proposed in this study can link smoothly the current classical force-based design code to the future version of performance-based design guideline.

References

- FEMA-450 (2003), Building Seismic Safety Council. Recommended provisions for seismic regulations for new buildings and other structures Part1: Provisions, Washington DC, Building Seismic Safety Council, National Institute of Building Sciences.
- Teng, T.-J., J.-F. Chai, W.-I Liao, Y.-T. Weng, W.-Y. Jean, S.-B. Chiou, F.-R. Lin, and T.-K. Chow (2010), Preliminary Improvement for Performance-based Design for Buildings in Taiwan (III), NCREE Report, NCREE-10-013 (in Chinese).

Scaling of Earthquake Ground Motion Records for Bi-Directional Response-History Analyses

Yuan-Tao Weng¹, Jui-Liang Lin¹ and Keh-Chyuan Tsai²

翁元滔¹、林瑞良²、蔡克銓³

Abstract

Most building structures are 3D in nature and stiffness or mass asymmetries in conjunction with directivity of the earthquake signal with respect to the principal axes of the structure can result in very complex 3-dimensional responses that make the dynamic behavior largely unpredictable. It appears that there was no one ground motion scaling method properly incorporating the higher-mode effects ever developed for the bi-directional RHA of building structures. In this study, a multi-mode scaling (MMS) procedures incorporating the higher-mode effects for 3-D frames' bi-directional RHA is developed. This study is to evaluate the effectiveness of the proposed MMS in reducing the scatter in estimated peak seismic demands for the 3-D building structures. The MMS analysis results are compared with those obtained from using other ground motion scaling methods.

Keywords: ground motion scaling, bi-directional response-history analysis, design spectra

Introduction

As non-linear dynamic analysis is becoming a more frequently used procedure for the seismic assessment of structures, it is increasingly important to develop a ground motion scaling method that effectively reduces the scatter in the seismic demand estimates. When earthquake records are used for dynamic response analyses (especially in the non-linear range), many efforts should be made to find ground motions having appropriate values in both time and frequency domains. Recent researches have demonstrated that for a particular seismic design approach, certain ground motion scaling methods can introduce large scatter in the estimated seismic demand (Shome and Cornell 1998; Kurama and Farrow 2003). According to the similarity in the procedures for selecting and scaling ground motions, the PEER Ground Motions Selection and Modification (GMSM) Program has identified and categorized a lot of ground motion selecting and scaling methods developed by several researchers and practitioners (Haselton 2009). Commonly, the historical earthquake records are scaled to fit a target spectral acceleration

S_a associated with a given period T or a range of periods. Selecting adequately T and the reference level for $S_a(T)$ are two important aspects of the seismic assessment.

Current codified procedures for response-history analysis (RHA) of buildings subjected to uni-axial earthquake ground accelerations often involve scaling ground motions to match a target spectrum. For response-history analysis of buildings subjected to the bi-directional earthquake load effects, it is recommended to scale the amplitude of the pairs of ground accelerations using one single scaling factor (ASCE 2006). After applying the scale factor, the square root of the sum of the squares (SRSS) of the associated 5% damped spectral ordinates at each period point is not less than 0.9 of 1.3 times the corresponding ordinate of the 5% damped target spectrum for periods from $0.2T_1$ to $1.5T_1$, where T_1 is the first mode period of the structure. In addition, within the aforementioned period range the average of these SRSS values must be no less than the average of the target response spectrum. In practical application, fulfilling this condition in such a wide range of

¹ Researcher, National Center for Research on Earthquake Engineering, ytweng@ncree.narl.org.tw

² Researcher, National Center for Research on Earthquake Engineering, jllin@ncree.narl.org.tw

³ Professor, National Taiwan University, kctsai@ncree.narl.org.tw

periods was proved inappropriate (Haselton 2009, Weng et al. 2010).

Shome et al. (1998) proposed a ground-motion scaling method for a suite of ground accelerations to compute the median response of nonlinear structures that involved scaling ground motions to a selected spectral acceleration at the linear-elastic fundamental period of the building ($S_a(T_1)$) being analyzed. This method is termed $S_a(T_1)$ scaling method herein. The $S_a(T_1)$ method implicitly assumed that the structural response, and the spectral values of the periods other than T_1 are of minor importance. This should be true when the response of the structure is elastic and is controlled by the first mode of vibration. When building's high mode effects are pronounced, this method may not be suitable (Kurama and Farrow 2003; Weng et al. 2010). Nevertheless, these common GSM methods often consider the effects of each period of interest are equal. If a ground acceleration record is scaled without properly incorporating the design spectral accelerations at the significant periods of a building, it could seriously overestimate or underestimate the seismic demand as defined in the target response spectrum. The resulting seismic demand may be biased (Baker 2007, Weng et al. 2010), leading to a design with unknown margins of safety. In addition, the number of tall buildings built or planned in seismic regions has substantially increased in recent years. The seismic inter-story drift response at high floors in a tall building can be much more influenced by higher modes. In order to take the high mode effects into account, a multi-mode ground motion scaling (MMS) method has been proposed and verified (Weng et al. 2009 and 2010). It should also be noted that the majority of the researches on ground motion scaling methods have been for the RHA of planar frames. However, most building structures are 3D in nature and stiffness or mass asymmetries in conjunction with directivity of the earthquake signal with respect to the principal axes of the structure can result in very complex 3-dimensional responses that make the dynamic behavior largely unpredictable (Thanoon et al. 2004). It appears that there was no one ground motion scaling method properly incorporating the higher-mode effects ever developed for the bi-directional RHA of building structures.

In this study, the first objective is to introduce the development of a multi-mode scaling (MMS) procedures incorporating the higher-mode effects for 3-D frames' bi-directional RHA. The second objective of this study is to evaluate the effectiveness of the proposed MMS in reducing the scatter in estimated peak seismic demands for the 3-D building structures. The MMS analysis results are compared with those obtained from using other ground motion scaling methods.

Bi-directional Multi-Mode Ground Motion Scaling Procedures

● Bi-directional Response Spectral Analysis

The response spectral analysis (RSA) to 3D buildings under bi-directional seismic ground motions is stated as follows:

The equation of motion for a typical 3D N -story building under bi-directional seismic ground motions with each floor represented as a rigid diaphragm with three DOFs is

$$\begin{aligned} \mathbf{M}\ddot{\mathbf{u}} + \mathbf{C}\dot{\mathbf{u}} + \mathbf{K}\mathbf{u} &= \mathbf{p}_{\text{eff}}(\mathbf{t}) = -\mathbf{M}\mathbf{t}_X\ddot{u}_{gX}(\mathbf{t}) - \mathbf{M}\mathbf{t}_Y\ddot{u}_{gY}(\mathbf{t}) \\ &= -\sum_{n=1}^{3N} s_{Xn}\ddot{u}_{gX}(\mathbf{t}) - \sum_{n=1}^{3N} s_{Yn}\ddot{u}_{gY}(\mathbf{t}) = -\sum_{n=1}^{3N} \Gamma_{Xn}\mathbf{M}\phi_n\ddot{u}_{gX}(\mathbf{t}) - \sum_{n=1}^{3N} \Gamma_{Yn}\mathbf{M}\phi_n\ddot{u}_{gY}(\mathbf{t}) \\ &= -\sum_{n=1}^{3N} (\Gamma_{Xn}\ddot{u}_{gX} + \Gamma_{Yn}\ddot{u}_{gY})\mathbf{M}\phi_n \end{aligned} \quad (1)$$

The displacement vector \mathbf{u} , mode shape ϕ_n , mass matrix \mathbf{M} and stiffness matrix \mathbf{K} are

$$\begin{aligned} \mathbf{u} &= \begin{bmatrix} \mathbf{u}_X \\ \mathbf{u}_Y \\ \mathbf{u}_\theta \end{bmatrix}_{3N \times 1}, \quad \phi_n = \begin{bmatrix} \phi_{Xn} \\ \phi_{Yn} \\ \phi_{\theta n} \end{bmatrix}_{3N \times 1}, \quad \mathbf{M} = \begin{bmatrix} \mathbf{m}_X & 0 & 0 \\ 0 & \mathbf{m}_Y & 0 \\ 0 & 0 & \mathbf{I}_0 \end{bmatrix}_{3N \times 3N} \\ \mathbf{K} &= \begin{bmatrix} \mathbf{k}_{XX} & \mathbf{k}_{XY} & \mathbf{k}_{X\theta} \\ \mathbf{k}_{YX} & \mathbf{m}_Y & \mathbf{k}_{Y\theta} \\ \mathbf{k}_{\theta X} & \mathbf{k}_{\theta Y} & \mathbf{I}_0 \end{bmatrix}_{3N \times 3N} \end{aligned} \quad (2)$$

The influence vector \mathbf{t}_X and \mathbf{t}_Y are equal to $\mathbf{t}_X = [1^T \ 0^T \ 0^T]^T$ and $\mathbf{t}_Y = [0^T \ 1^T \ 0^T]^T$, respectively, where 1 and 0 are $N \times 1$ column vectors with all elements equal to one and zero, respectively. The \mathbf{m}_X , \mathbf{m}_Y and \mathbf{I}_0 are the $N \times N$ X-directional mass matrix, Y-directional mass matrix and the mass moment of inertia matrix, respectively.

In an elastic state, the displacement vector, \mathbf{u} , can be assembled by the modal coordinate, $\mathbf{Y}(\mathbf{t})$, as follows :

$$\mathbf{u}(\mathbf{t}) = [\phi]_{3N \times 3N} \{\mathbf{Y}(\mathbf{t})\}_{3N \times 1} \quad (3)$$

The Γ_{Xn} and Γ_{Yn} are the n^{th} modal participating factor in the X- and Y-direction, respectively, equal to

$$\Gamma_{Xn} = \frac{\{\phi\}_n^T \mathbf{M} \mathbf{t}_X}{\{\phi\}_n^T \mathbf{M} \{\phi\}_n} = \frac{\mathbf{L}_{Xn}}{\mathbf{M}_n}, \quad \Gamma_{Yn} = \frac{\{\phi\}_n^T \mathbf{M} \mathbf{t}_Y}{\{\phi\}_n^T \mathbf{M} \{\phi\}_n} = \frac{\mathbf{L}_{Yn}}{\mathbf{M}_n} \quad (4)$$

Since Γ_{Xn} and Γ_{Yn} are usually unequal to each other, they cannot be eliminated from both sides of Equation (1) by using accustomed definition, Equation (1) can be decomposed into $3N$ equations, each equation representing an SDOF modal equation of motion, as follows :

$$\begin{aligned} & \{\phi\}_n^T M \{\dot{Y}(t)\} + \{\phi\}_n^T C \{\dot{Y}(t)\} + \{\phi\}_n^T K \{\dot{Y}(t)\} \\ & = p_{eff}(t) = -\{\phi\}_n^T M \mathbf{L}_X \ddot{u}_{gX}(t) - \{\phi\}_n^T M \mathbf{L}_Y \ddot{u}_{gY}(t) \\ & \bar{M}_n \ddot{Y}_n(t) + \bar{C}_n \dot{Y}_n(t) + \bar{K}_n Y_n(t) = -L_{Xn} \ddot{u}_{gX}(t) - L_{Yn} \ddot{u}_{gY}(t) \\ & n = 1 \sim 3N \end{aligned} \quad (5)$$

where $\bar{M}_n = \{\phi\}_n^T M \{\phi\}_n$, $\mathbf{L}_{Xn} = \{\phi\}_n^T M \mathbf{L}_X$, $\mathbf{L}_{Yn} = \{\phi\}_n^T M \mathbf{L}_Y$. Using Duhamel's integral to solve Equation (5), as follows:

$$\begin{aligned} Y_n(t) &= \frac{L_{Xn}}{M_n \omega_n} \int_0^t \ddot{u}_{gX}(\tau) e^{-\xi \omega_n(t-\tau)} \sin \omega_d(t-\tau) d\tau + \frac{L_{Yn}}{M_n \omega_n} \int_0^t \ddot{u}_{gY}(\tau) e^{-\xi \omega_n(t-\tau)} \sin \omega_d(t-\tau) d\tau \\ &= \frac{L_{Xn}}{M_n \omega_n} S_{Y_{Xn}} + \frac{L_{Yn}}{M_n \omega_n} S_{Y_{Yn}} = \mathbf{F}_{Xn} S_{DXn} + \mathbf{F}_{Yn} S_{DYn} \end{aligned} \quad (6)$$

The n^{th} modal equivalent seismic force can be expressed as follows:

$$\begin{aligned} \{f_s(t)\}_n &= K \{\phi\}_n Y_n(t) = \omega_n^2 M \{\phi\}_n Y_n(t) = \omega_n^2 M \{\phi\}_n (\mathbf{F}_{Xn} S_{DXn} + \mathbf{F}_{Yn} S_{DYn}) \\ &= \mathbf{F}_{Xn} S_{aXn} M \{\phi\}_n + \mathbf{F}_{Yn} S_{aYn} M \{\phi\}_n \end{aligned} \quad (7)$$

The the n^{th} modal elastic base shear in the X- and Y-direction, respectively, equal to

$$\begin{aligned} V_{nX} &= \mathbf{L}_X^T \{f_s(t)\}_n = \mathbf{F}_{Xn} S_{aXn} \mathbf{L}_X^T M \{\phi\}_n + \mathbf{F}_{Yn} S_{aYn} \mathbf{L}_X^T M \{\phi\}_n = \frac{L_{Xn}^2}{M_n} S_{aXn} + \frac{L_{Xn} L_{Yn}}{M_n} S_{aYn} \\ V_{nY} &= \mathbf{L}_Y^T \{f_s(t)\}_n = \mathbf{F}_{Xn} S_{aXn} \mathbf{L}_Y^T M \{\phi\}_n + \mathbf{F}_{Yn} S_{aYn} \mathbf{L}_Y^T M \{\phi\}_n = \frac{L_{Xn} L_{Yn}}{M_n} S_{aXn} + \frac{L_{Yn}^2}{M_n} S_{aYn} \end{aligned} \quad (8)$$

The n^{th} modal elastic roof displacement in the X- and Y-direction, respectively, equal to

$$\begin{aligned} u_{roof,nX} &= \phi_{nX,roof} (\mathbf{F}_{Xn} S_{DXn} + \mathbf{F}_{Yn} S_{DYn}) \\ &= \phi_{nX,roof} \frac{1}{\omega_n^2} (\mathbf{F}_{Xn} S_{aXn} + \mathbf{F}_{Yn} S_{aYn}) \end{aligned} \quad (9a)$$

$$\begin{aligned} u_{roof,nY} &= \phi_{nY,roof} (\mathbf{F}_{Xn} S_{DXn} + \mathbf{F}_{Yn} S_{DYn}) \\ &= \phi_{nY,roof} \frac{1}{\omega_n^2} (\mathbf{F}_{Xn} S_{aXn} + \mathbf{F}_{Yn} S_{aYn}) \end{aligned} \quad (9b)$$

In the above equation, $\phi_{nX,roof}$ and $\phi_{nY,roof}$ are the n^{th} mode shape components at the roof level in the X and Y directions, respectively.

● **Computing the elastic peak responses by using the elastic acceleration response spectra**

According to the response spectrum analysis (RSA) procedure, the peak seismic responses can be estimated by applying the complete quadratic combination (CQC) rules. If r_{io} is the peak values of the i^{th} mode's contribution $r_i(t)$, and r_{jo} is the j^{th} mode's contribution $r_j(t)$ to the total response $r(t)$, then the peak total response r_o can be estimated based on the CQC rule (Der Kiureghian, 1981; Chopra 2003) as:

$$r_o \approx \sqrt{\sum_{i=1}^N \sum_{j=1}^N \rho_{ij} r_{io} r_{jo}} \quad (10)$$

where N is the number of modes included. When the RSA procedure is adopted, it has been suggested that

the number of modes be determined to include at least 90% of the total building effective mass (ICBO 2006). Lopez and Cruz (1996) also proposed some empirical formulae to determine the minimum number of modes for seismic response computations.

Estimation of peak base shear

Substituting Equation (8) into Equation (10) and replacing regarded notations, Equations (11) and (12) for estimation of peak base shears can be established. The peak base shears, $V_{D,CQC}$ and $V_{EQ,CQC}$ can be computed from two acceleration response spectra $S_{a,des}$ (the smoothed design spectrum) and $S_{a,EQ}$ (obtained from the historical earthquake accelerations), respectively as:

$$V_{DXCQC} = \sqrt{\sum_{i=1}^N \sum_{j=1}^N \rho_{ij} (\mathbf{F}_{Xi} L_{Xi} S_{aXdes_i} + \mathbf{F}_{Yi} L_{Yi} S_{aYdes_i}) (\mathbf{F}_{Xj} L_{Xj} S_{aXdes_j} + \mathbf{F}_{Yj} L_{Yj} S_{aYdes_j})} \quad (11a)$$

$$V_{DYCQC} = \sqrt{\sum_{i=1}^N \sum_{j=1}^N \rho_{ij} (\mathbf{F}_{Xi} L_{Xi} S_{aXdes_i} + \mathbf{F}_{Yi} L_{Yi} S_{aYdes_i}) (\mathbf{F}_{Xj} L_{Xj} S_{aXdes_j} + \mathbf{F}_{Yj} L_{Yj} S_{aYdes_j})} \quad (11b)$$

$$V_{EQXCQC} = \sqrt{\sum_{i=1}^N \sum_{j=1}^N \rho_{ij} (\mathbf{F}_{Xi} L_{Xi} S_{aXEQ_i} + \mathbf{F}_{Yi} L_{Yi} S_{aYEQ_i}) (\mathbf{F}_{Xj} L_{Xj} S_{aXEQ_j} + \mathbf{F}_{Yj} L_{Yj} S_{aYEQ_j})} \quad (12a)$$

$$V_{EQYCQC} = \sqrt{\sum_{i=1}^N \sum_{j=1}^N \rho_{ij} (\mathbf{F}_{Xi} L_{Xi} S_{aXEQ_i} + \mathbf{F}_{Yi} L_{Yi} S_{aYEQ_i}) (\mathbf{F}_{Xj} L_{Xj} S_{aXEQ_j} + \mathbf{F}_{Yj} L_{Yj} S_{aYEQ_j})} \quad (12b)$$

where $S_{ai,des}$ or $S_{aj,des}$ is the spectral accelerations in the smoothed design spectrum, $S_{ai,EQ}$ or $S_{aj,EQ}$ is the spectral accelerations in the spectrum obtained from the historical earthquake accelerations. The subscripts X and Y in these parameters indicate the direction of the applied earthquake.

● **Computation of scaling factors for MMS methods**

In the current study, the MMS methods are developed to minimize the first few modal participating differences. The least square error fitting method is utilized to minimize the weighted sum of the square errors among the spectral responses of a given pair of scaled ground motions and those of the smoothed design response spectrum at the periods of interest. Therefore, the sum of the square differences ($error$)² can be expressed as:

$$(error)^2 = \sum_{i=1}^N \sum_{j=1}^N \left[\sqrt{W_{ij,X} \cdot W_{ij,Y} S_{ai,des} \cdot S_{aj,des}} \right. \\ \left. - SF \cdot \sqrt{W_{ij,X} S_{ai,EQ} \cdot S_{aj,EQ}} \cdot \sqrt{W_{ij,Y} S_{ai,EQ} \cdot S_{aj,EQ}} \right]^2 \quad (13)$$

where SF is the ground motion scaling factor and $W_{ij,X}$ and $W_{ij,Y}$ are the ij^{th} element of the modal correlation weighting factor matrices in the X and Y directions respectively, to be introduced in the next paragraph. The minimum error is achieved when the partial derivative of ($error$)² with respect to the scaling factor SF becomes zero:

$$\frac{\partial (error)^2}{\partial (SF)} = 0 \quad (14)$$

By taking the derivative of Equation (13) as illustrated in Equation (14), the scaling factors SF can be computed from using Equation (15) and the modal correlation weighting factors:

$$SF = \frac{\sum_{i=1}^N \sum_{j=1}^N \sqrt{W_{ij,X} \cdot W_{ij,Y} \cdot S_{aides} \cdot S_{ajdes} \cdot \sqrt{W_{ij,X} \cdot S_{aiXEQ} \cdot S_{ajXEQ}} \sqrt{W_{ij,Y} \cdot S_{aiYEQ} \cdot S_{ajYEQ}}}}{\sum_{i=1}^N \sum_{j=1}^N \sqrt{W_{ij,X} \cdot S_{aiXEQ} \cdot S_{ajXEQ}} \sqrt{W_{ij,Y} \cdot S_{aiYEQ} \cdot S_{ajYEQ}}} \quad (15)$$

Computation of the modal correlation weighting factor matrices

If the peak elastic base shear is chosen as the key design parameter, the weighting factors could be computed from:

$$W_{ij,X} = \frac{V_{ij,X}^2}{V_{DX,CQC}^2} = \frac{\rho_{ij} (\Gamma_{Xi} L_{Xi} + \Gamma_{Yi} L_{Yi}) (\Gamma_{Xj} L_{Xj} + \Gamma_{Yj} L_{Yj})}{\sum_{i=1}^N \sum_{j=1}^N \rho_{ij} (\Gamma_{Xi} L_{Xi} + \Gamma_{Yi} L_{Yi}) (\Gamma_{Xj} L_{Xj} + \Gamma_{Yj} L_{Yj})} \quad (16a)$$

$$W_{ij,Y} = \frac{V_{ij,Y}^2}{V_{DY,CQC}^2} = \frac{\rho_{ij} (\Gamma_{Xi} L_{Xi} + \Gamma_{Yi} L_{Yi}) (\Gamma_{Xj} L_{Xj} + \Gamma_{Yj} L_{Yj})}{\sum_{i=1}^N \sum_{j=1}^N \rho_{ij} (\Gamma_{Xi} L_{Xi} + \Gamma_{Yi} L_{Yi}) (\Gamma_{Xj} L_{Xj} + \Gamma_{Yj} L_{Yj})} \quad (16b)$$

Similarly, if the peak elastic roof displacement is chosen as the key design parameter, the weighting factors could be computed from:

$$W_{ij,X} = \frac{\rho_{ij} (\phi_{iXroof} (\Gamma_{Xi} + \Gamma_{Yi}) / \omega_i^2) (\phi_{jXroof} (\Gamma_{Xj} + \Gamma_{Yj}) / \omega_j^2)}{\sum_{i=1}^N \sum_{j=1}^N \rho_{ij} (\phi_{iXroof} (\Gamma_{Xi} + \Gamma_{Yi}) / \omega_i^2) (\phi_{jXroof} (\Gamma_{Xj} + \Gamma_{Yj}) / \omega_j^2)} \quad (17a)$$

$$W_{ij,Y} = \frac{\rho_{ij} (\phi_{iYroof} (\Gamma_{Xi} + \Gamma_{Yi}) / \omega_i^2) (\phi_{jYroof} (\Gamma_{Xj} + \Gamma_{Yj}) / \omega_j^2)}{\sum_{i=1}^N \sum_{j=1}^N \rho_{ij} (\phi_{iYroof} (\Gamma_{Xi} + \Gamma_{Yi}) / \omega_i^2) (\phi_{jYroof} (\Gamma_{Xj} + \Gamma_{Yj}) / \omega_j^2)} \quad (17b)$$

The sum of the W_{ij} elements (Equation (16) or (17)) in the modal correlation matrix should be equal to 1.0. Thus, modal weighting factors given Equation (16) can be applied in Equation (15) for computation of scale factors when the base shear is considered as the key design parameter, whereas Equation (17) can be applied when the roof displacement is the key parameter of interest. For the purpose of discussion, the method is identified as MMSV (V fort shear) or MMSD (D for displacement) when Equation (16) or Equation (17) is applied, respectively.

Conclusions

Among the four stated scaling procedures investigated in this thesis, it is clear that MMS procedures provide more peak elastic as well as inelastic seismic demands that are consistent with those obtained using the smoothed design spectra. This improvement in consistency has a great significance for the estimation of seismic demands of high-rise building structures.

The effectiveness of MMS procedures in estimation of peak story torsional moment, torsional angle and torsional drift was not investigated in this study. Further study is needed for evaluation of the stated problem.

References

- American Society of Civil Engineers (ASCE). (2006). "Minimum design loads for buildings and other structures." ASCE/SEI 7-05, American Society of Civil Engineers, Reston, Virginia.
- Baker J.W., 2007. Measuring bias in structural response caused by ground motion scaling, Proceedings of 8th Pacific Conference on Earthquake Engineering, Nanyang Technological University, Singapore.
- Chopra, A. K., 2003. Dynamic of structures: Theory and applications to earthquake engineering, Prentice Hall, 2nd ed., Englewood, Cliffs, N J.
- Der Kiureghian, A., 1981. A response spectrum method for random vibration analysis of MDF systems, *Earthquake Engineering and Structural Dynamics* 9, 419-435.
- FEMA. NEHRP. Recommended provisions for new building and other structures: training and instructional materials, FEMA 451B, Washington, DC, 2007.
- Haselton, C. B., 2009. Evaluation of ground motion selection and modification methods: predicting median interstory drift response of buildings, PEER 2009/01.
- Kurama, Y., and Farrow, K. (2003). "Ground motion scaling methods for different site conditions and structure characteristics," *Eq. Eng. and Str. Dyn.*, Vol. 32, No. 15, pp. 2425-2450.
- Sedarat H, Bertero VV. *Effect of torsion on the linear and non-linear seismic response of structure*. Report No. UCB/EERC 90-2, Earthquake Engineering Research Centre, College of Engineering, University of Berkeley, 1990.
- Shome, N. and Cornell, C.A., 1998. *Normalization and scaling accelerograms for nonlinear structural analysis*, Sixth U.S. National Conference on Earthquake Engineering (CD-ROM), Seattle, WA.
- Thanoon WA, Paul DK, Jaafar MS, Trikha DN. *Influence of torsion on the inelastic response of three-dimensional RC frames*. Finite Elements in Analysis and Design 2004; 40: 611-28.
- Yuan-Tao Weng, Keh-Chyuan Tsai, and Ya-Ran Chan (2010) "A Ground Motion Scaling Method considering Higher-mode Effects and Structural Characteristics," *Earthquake Spectra*, Vol.26 No.3, pp.841-867.

Study on Design Earthquakes for Kinmen, Matsu and Penhu Areas

Yu-Wen Chang¹, Wen-Yu Jean², Shyh-bin Chiou³

張毓文¹、簡文郁²、邱世彬³

Abstract

Observed from the earthquake events recorded by Taiwan's Central Weather Bureau during the past 100 years, it is obvious that the seismicity in the Taiwan Strait is lower than that in the Taiwan Island. Since low seismicity may cause high mathematical uncertainty in the seismic hazard analysis, the minimum seismic requirement specified in the design code for buildings in the Taiwan Island is also currently used for the design earthquake at Kinmen, Matsu, and Penhu areas. Recently, geological investigation result indicated that the Binhai fault is an active fault and dominates most of the seismic activities in the Taiwan Strait. Thus, the current design earthquake may not be appropriate and conservative for Kinmen, Matsu, and Penhu areas. This study aimed to modify the current seismic design earthquake for those areas. By establishing an earthquake catalogue for the Taiwan Strait from different earthquake data recorded in Taiwan, in Mainland China, and in Global network, the seismicity at the mentioned areas can be evaluated. Both the deterministic and probabilistic analyses results are taken into account to assess the seismic hazard at those areas. The results of this study can make the current seismic design code more comprehensive.

Keywords: Design earthquake, Kinmen, Matsu, Penhu, Binhai fault

Introduction

Taiwan is located at the convergent plate boundary where the Eurasian plate is eastward underthrusting and colliding with the Philippine Sea plate. This tectonic environment leads to high seismicity in and around the Taiwan Island. Thus, earthquake hazard mitigation is always an important issue in Taiwan. It is worth noting that Kinmen, Matsu and Penhu areas at the Taiwan Strait are seismicity inactive areas in which the assessment of seismic hazard still requires special care. High uncertainty on the estimate of reoccurrence rate may be induced in the seismic hazard analysis when such areas have low b -value at long return periods. Therefore, for the conservative design purpose, the minimum seismic requirement specified in the design code for buildings in the Taiwan Island is currently used for the design earthquake (i.e. 10% probability level of exceedance within 50 years, return period of 475 years) at Kinmen, Matsu and Penhu areas.

Table 1 lists the maximum seismic design accelerations for Kinmen, Matsu, and Penhu areas specified in the design codes of 1997, 2000 and 2005 versions as 0.2g, 0.23g and 0.2g, respectively. In addition, from the seismic design levels published by the Chinese government in 2001, as shown in the seismic hazard map of Fig. 1, it can be seen that the seismic design accelerations for those areas are varied from 0.15g to 0.2g. Although the seismic design requirements for Kinmen, Matsu, and Penhu areas in Taiwan are comparable to, and even more conservative than, those in China, the earthquake hazard and seismic demands are still necessary to be reviewed in a more proper and accurate manner for the low-seismicity areas.

This study aims at modifying the current seismic design earthquake for Kinmen, Matsu, and Penhu areas. According to the data of bottom topography, gravity, geomagnetism measurements and multichannel seismic detection collected and investigated in China, it is apparent that the Binhai

¹ Assistant Researcher, National Center for Research on Earthquake Engineering, ywchang@ncree.narl.org.tw

² Research Fellow, National Center for Research on Earthquake Engineering, wychien@ncree.narl.org.tw

³ Assistant Researcher, National Center for Research on Earthquake Engineering, sbchiou@ncree.narl.org.tw

fault was a recently active fault and dominates most of the seismic activities in the Taiwan Strait. Establishing an earthquake catalogue for the Taiwan Strait considering a sufficient number of damaging earthquakes recorded in Taiwan, Mainland China, and Global network, the deterministic and probabilistic seismic hazard analyses for those areas can be performed. The seismic hazard analysis results considering either of the aforementioned information are very beneficial for the further modification of the seismic design earthquakes for those areas.

Table 1 Seismic design accelerations for Kinmen, Matsu, and Penhu areas

Code Version	Area	PGA (or EPA)	Explanation
1997 yr	Kinmen Penhu Matsu	0.20g 0.18g 0.15g	Seismic design acceleration coefficient
2000 yr	Kinmen Penhu Matsu	0.23g	Seismic zone after 1999 Chi-Chi earthquake
2005 yr	Kinmen Penhu Matsu	0.20g	Design spectral response acceleration at 0.3 sec. is equal to 0.5g



Fig.1 Seismic hazard map in China that has seven seismic design levels.

Seismicity and tectonic features in Taiwan Strait

Tectonic features in Taiwan Strait

The seismic distribution in and around the Taiwan Island (including the Taiwan Strait) is shown in the geographical map of Fig. 2. Although the seismic activity is generally decreased from the Taiwan Island northwestward to the Fujian coastal area through the Taiwan Strait, it is not negligible that some high level activities in the Taiwan Strait are induced by the Binhai fault. The Binhai fault is a main thrust fault and extends generally in the NE direction. Its NE end starts from the sea area to the east of the Niushan Island, and its SW end is in the sea area of the eastern Xiongdi Islet. It is also a Quaternary boundary fault with a total length of more than 500 km between the South China continent and the sea basin of the Taiwan Strait, and stretches out roughly along the isobaths of 50 to 60 m.

Most of the seismic activities in the Fujian coastal region are induced by the Binhai fault. It was found that six historical earthquakes with the magnitude of greater than 6.0 occurred from 1185 to 1918 ruptured along the Binhai fault (Zhu et al., 2004). The location of the Binhai fault and the locations of the epicenters of those historical earthquakes are depicted in Fig. 2. Among the six historical earthquakes, the 1604 M7.5 Quanzhou earthquake is the most renowned because of its magnitude and location. Compared with the 1918 M7.3 earthquake, another research indicated that the 1067 Chaoshan Guangdong earthquake, which is excluded and had occurred prior to the six historical earthquakes aforementioned, might be one of the historical earthquakes that ruptured along the Binhai fault (Wen et al., 2005).

The magnitude and time characteristics of the Binhai fault from 1067 to 1918 are shown in Fig. 3, and from which the characteristic earthquake parameters and seismic hazard assessment for the Binhai fault can be better realized. It can be observed that the fracture behavior of the fault may be divided into three repeating earthquake sequences. Considering the historical earthquakes from 1185 to 1918, the estimated recurrence interval (T_r) is about 320 to 400 years, and the magnitudes ranges from 6.3 to 7.5. Therefore, $M_L 7.0$ - $M_L 7.5$ and 300 years are the characteristic magnitude and recurrence interval, respectively, of the Binhai fault for the deterministic and probabilistic seismic hazard analyses.

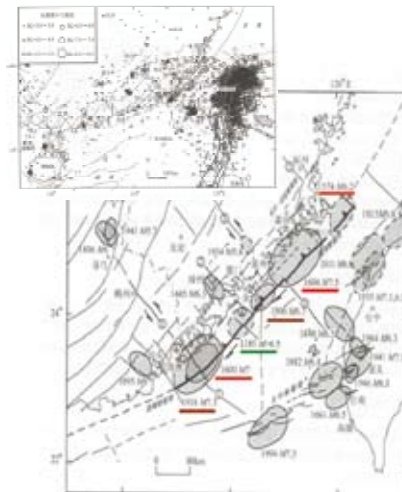


Fig. 2 Seismic distribution in Taiwan Strait and locations of epicenters of historical earthquakes related to Binhai fault (Zhu et al., 2004).

Earthquake Catalogue in Taiwan Strait

All the data used to establish a comprehensive earthquake catalogue for the Taiwan Strait in this study come from several sources: (a) the China Earthquake Data Center catalogue, which contains earthquake events with magnitude of greater than $M_L 4.0$ from 1832 to 1969; (b) the catalogue collected

by Wen *et al.* (1999) in which has all the historical damage earthquakes in the Taiwan Strait before 1900; (c) the catalogue composed of different earthquake data recorded in Taiwan, Mainland China and Global networks from 1901 to 2000 (Wen *et al.*, 1999); (d) the catalogue which includes earthquake data from 1604 to 1989 for seismic hazard assessment in Fuzhou City (Zhu *et al.*, 2004); and (e) the Taiwan Central Weather Bureau catalogue which contains earthquake events with magnitude of greater than $M_L 4.5$ from 1900 to 2008.

The records with same occur time, depth and magnitude information obtained from the difference sources aforementioned should not be repeatedly incorporated into the final earthquake catalogue for the Taiwan Strait. The final catalogue containing 105 earthquake events with magnitude of greater than 2.5 obtained from historical observations and instrumental reports after 1067, as shown in Fig. 4, is adopted for the further seismic hazard analysis.

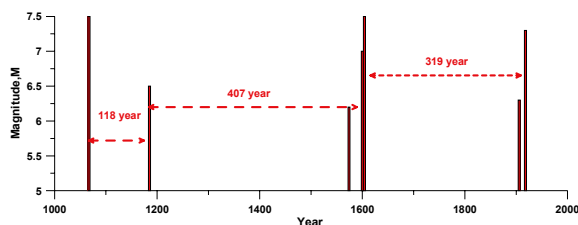


Fig. 3 Time-magnitude distribution of historical earthquakes related to Binhai fault.

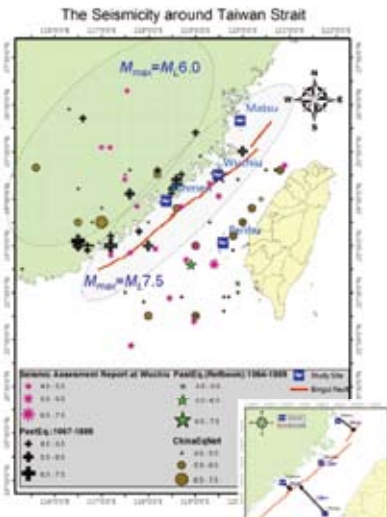


Fig. 4 Distribution of locations of epicenters of used earthquake data at Taiwan Strait

Seismic Hazard Assessment

The seismic hazard assessment depends on the information of how earthquakes are generated and how they recur in space and time at a given location. In this study, two approaches, deterministic and probabilistic approaches are used to assess the seismic hazard at Kinmen, Matsu and Penhu areas considering the Binhai fault.

Deterministic Approach (DSHA)

In the deterministic seismic hazard analysis (DSHA), the past seismicity with different extreme magnitudes is used to assess the seismic hazard at different design levels. It is obvious that most of the seismicity at the Taiwan Strait is related to the Binhai fault. In this study, referring to the six large paleo-earthquakes related to the Binhai fault with moment magnitude varying from $M_6.3$ to $M_7.5$ (Zhu *et al.*, 2004), $M_L 7.0$ and $M_L 7.5$ earthquakes are assumed to be plausible scenario earthquakes corresponding to the uniform seismic hazard level of 10% and 2% probability of exceedance within 50 years (*i.e.* corresponding to 475-year and 2500-year return periods, respectively).

The peak ground acceleration (PGA) and spectral acceleration values for the studied areas, as summarized in Table 2, are estimated using different ground motion attenuation relations on rock. It can be seen from the table that the PGA values corresponding to 475-year return period at Kinmen, Matsu and Penhu areas are 0.15~0.19g, 0.07g and 0.02g, respectively. Besides, the distance between each studied area and the Binhai fault is shown in Fig. 4. Since the distance from Penhu area to the Binhai fault is more than 120 km, the Binhai fault may not significantly affect the seismic hazard at Penhu area.

Table 2 DSHA results for Binhai fault

(a) 475-year Return period, $M_L 7.0$

Area	R(km)	PGA(g)	$S_{as}(g)$	$S_{al}(g)$	EPA(g)
Kinmen	25	0.185	0.389	0.217	0.155
	30	0.150	0.324	0.179	0.130
Kinmen Wuchiu	12	0.360	0.682	0.398	0.273
Matsu	55	0.067	0.158	0.084	0.063
Penhu	123	0.018	0.047	0.024	0.019

(b) 2500-year Return period, $M_L 7.5$

Area	R(km)	PGA(g)	$S_{as}(g)$	$S_{al}(g)$	EPA(g)
Kinmen	25	0.291	0.575	0.340	0.230
	30	0.245	0.497	0.291	0.199
Kinmen Wuchiu	12	0.493	0.886	0.548	0.354
Matsu	55	0.123	0.272	0.153	0.109
Penhu	123	0.037	0.093	0.050	0.037

Probabilistic Approach (PSHA)

In the probabilistic seismic hazard analysis (PSHA), the occurrence rate of source types can be assumed according to the information aforementioned. For the source areas, the recurrence rate of the probabilistic scheme in the Taiwan Strait, as shown in Fig. 4, is estimated using the earthquake catalogue of the Taiwan Strait. It is expected that the use of a more appropriate catalogue can produce better estimate of the overall earthquake process. The Gutenberg-Richter (GR) relation is adopted for the seismic occurrence model of the area sources.

Moreover, the maximum magnitude M_{max} can be defined using an arbitrary approach, which increases the maximum observed magnitude by 0.5 unit ($M_{max} + 0.5$, depending on the source zone). Thus, the maximum magnitudes of the two source zones at the Taiwan Strait are $M_L 6.0$ and $M_L 7.5$, respectively. The recurrence rate and magnitude of the characteristic earthquake of the Binhai fault can be analyzed. The earthquake characteristic of the Binhai fault is modeled using the stationary Poisson process with a constant occurrence rate equal to 0.011667 that accompanied the characteristic of magnitude from $M_L 7.0$ to $M_L 7.5$. The constant occurrence rate is determined from the repeating earthquake sequences along the fault, which occurs at an average of 3.5 times during 300 years.

The seismic hazard curves for Kinmen, Matsu, and Penhu areas, including PGA values and 5% damped acceleration response spectra at 0.3 and 1.0 sec., are calculated and illustrated in Fig. 6. The ground motion values for 475-year and 2500-year return periods is used to represent the seismic hazard at those areas, as summarized in Table 3. It is of no surprise that Wuchiu in Kinmen county has the highest hazard. It should be noted that the effect of the Binhai fault on the ground motion hazard in Wuchiu varies depending upon PGA levels. It is because that Wuchiu is closest to the Binhai fault. On the contrast, the seismic hazard for Penhu area, which is approximate to the seismic design requirement specified in the current design code, is lower than that for Kinmen area.

Table 3 Different return period design levels at each area in PSHA

Area	475-year			2500-year		
	PGA(g)	S_{a1} (g)	S_{a5} (g)	PGA(g)	S_{a1} (g)	S_{a5} (g)
Kinmen county						
Wuchiu	0.452	0.491	0.822	0.613	0.649	1.049
Lieyu	0.124	0.152	0.275	0.164	0.2	0.351
Jinning	0.137	0.166	0.299	0.18	0.218	0.381
Jincheng	0.152	0.183	0.327	0.2	0.24	0.417
Jinsha	0.151	0.182	0.327	0.199	0.239	0.416
Jinhu	0.177	0.211	0.375	0.233	0.276	0.476
Penhu county						
Penhu	0.184	0.203	0.38	0.317	0.339	0.606
Matsu county						
Matsu	0.087	0.109	0.20	0.118	0.146	0.263

Conclusion

This study proposed modifications for the current seismic design earthquake in Kinmen, Matsu, and Penhu areas. Both the deterministic and probabilistic analyses results are taken into account to assess the seismic hazard at those areas. The analyses results show that the current seismic design requirements for Kinmen, Matsu, and Penhu areas in Taiwan are comparable to, and even more conservative than,

those from the seismic acceleration estimations. On the contrast, the seismic hazard for Penhu area, which is approximate to the seismic design requirement specified in the current design code, is lower than that for Kinmen area. It implies that the earthquake hazard contribution from the Binhai fault can be enveloped in the current seismic design requirements. The results of this study can make the current seismic design code more comprehensive.

References

Seismic Ground Motion Parameter Zonation Map of China(中國地震動參數區劃圖), GB18306-2001.

Seismic Design Code for Building in Taiwan(建築物耐震設計規範及解說), the Architecture and Building Research Institute, Ministry of the Interior, July, 2005. (in Chinese)

Zhu J. F., X. W. Hsu, Z. L. Huang, C. C. Wu and X. K. Chang, Active Faults Exploration and Seismic Hazard Assessment in Fuzhou City(福州市活斷層探測與地震危險性評價), Science Press, 2004. (in Chinese)

Wen K. L., C. H. Lin, B. S. Huang and S.N. Cheng, The Seismic Assessment in Wuchiu (Phase I)(烏坵地區地震評估報告(第一階段研究)), Chinese Taipei Geophysical Society, 1999. (in Chinese)

Wen X. Z. and X. W. Hsu (2005), Analysis of the two historical earthquakes of 1067 and 1574 in the southeast coastal region of China (對東南沿海 1067 年和 1574 年兩次地震的分析), Seismology and Geology, Vol.27, No.1, pp1-10.(in Chinese)

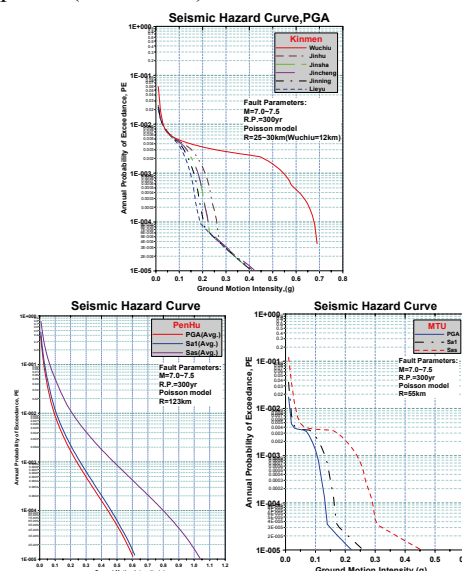


Fig. 6 Hazard curves for Kinmen, Matsu and Penhu areas. Plotted is the median annual probability of exceedance as a function of PGA and 5% damped acceleration response spectrum at 0.3 and 1.0 periods.

Application and Improvement of the Coefficient Method of Displacement

Yuan-Tao Weng¹, Shyh-Jiann Hwang²

翁元滔¹、黃世建²

Abstract

Knowledge of the inelastic displacement ratio, i.e. the ratio of the maximum inelastic to the maximum elastic displacement of an SDOF system, allows the computation of its maximum inelastic displacement directly from the corresponding elastic one. This study presents a simple and effective method for the inelastic displacement ratio estimation of a structure under cyclic earthquakes. Extensive parametric studies are conducted to obtain expressions for this ratio, in terms of the period of vibration, the viscous damping ratio, the strain-hardening ratio, the force reduction factor and the soil class. It is found that the post-stiffness ratio has a significant effect on the inelastic displacement ratio and hence on the maximum inelastic displacement of SDOF systems.

Keywords: Inelastic displacement ratio, performance-based seismic design, displacement coefficient method, strength degradation.

Introduction

The Coefficient Method of displacement is the primary nonlinear static procedure presented in FEMA 356 (ASCE, 2000). This approach modifies the linear elastic response of the equivalent SDOF system by multiplying it by a series of coefficients C_0 through C_3 to generate an estimate of the maximum global displacement (elastic and inelastic), which is termed the target displacement. The process begins with an idealized force-deformation curve (i.e., pushover curve) relating base shear to roof displacement. An effective period, T_e , is generated from the initial period, T_b , by a graphical procedure that accounts for some loss of stiffness in the transition from elastic to inelastic behavior. The effective period represents the linear stiffness of the equivalent SDOF system. When plotted on an elastic response spectrum representing the seismic ground motion, as peak acceleration, S_a , versus period, T . The assumed damping, often five percent, represents a level that might be expected for a typical structure responding in the elastic range. The peak elastic spectral displacement is directly related to the spectral acceleration by the relationship

$$S_D = \frac{T_e^2}{4\pi^2} S_a \quad (1)$$

The coefficient C_0 is a shape factor (often taken as the first mode participation factor) that simply converts the spectral displacement to the displacement at the roof. The other coefficients each account for a separate inelastic effect.

Based on the evaluation summarized in FEMA 440 document and available research data, improvements to the Coefficient Method of FEMA 356 have been developed and are presented in that document. Recommendations include several improved alternatives for the basic ratio of the maximum displacement (elastic plus inelastic) for an elastic perfectly plastic SDOF oscillator to the maximum displacement for a completely linear elastic oscillator that is designated as the coefficient C_1 in FEMA 356. FEMA 440 report also recommends that the current limitations (capping) allowed by FEMA 356 to the coefficient C_1 be abandoned. In addition, a distinction is recognized between two different types of strength degradation that have different effects on system response and performance. This distinction leads to recommendations for the coefficient C_2 to account for

¹ Associate Research Fellow, National Center for Research on Earthquake Engineering, ytweng@ncree.org.tw

² Professor, Dept. of Civil Engineering, Taiwan University, sjhwang@ntu.edu.tw

cyclic degradation in strength and stiffness. It is also suggested that the coefficient C_3 be eliminated and replaced with a limitation on strength.

In this study, the coefficients C_1 to C_2 are revised to be presented using constant-ductility format. The determination of the target displacement in the simplified nonlinear static procedure (NSP) known as the Displacement Coefficient Method is revised in this study. The target displacement, δ_t , which corresponds to the displacement at roof level, can be estimated as

$$\delta_t = C_0 C_1 C_2 S_a \frac{T_e^2}{4\pi^2} g \quad (2)$$

where C_0 is the fundamental modal participation factor, C_1 represents the approximate ratio of the maximum displacement of an elastic-perfectly-plastic SDOF oscillator model to that of a fully elastic counterpart. The proposed modification is based on the results of the simplified dynamic analyses conducted as a part of the evaluation database. The proposed relationship is a function of ductility (μ), period (T), and site class; The C_2 accounts for the change in maximum inelastic displacement for systems that exhibit cyclic degradation of stiffness and strength. The proposed modification is based on the results of the simplified dynamic analyses conducted as a part of the evaluation database. In many cases the data suggest that cyclic degradation does not increase maximum displacements. However, there are exceptions especially for short period, low strength structures.

Description of equivalent SDOF model

An elastoplastic SDOF system with linear hardening or softening and viscous damping is used to model the structure, as shown in Fig. 1. The statistical dynamic response of this system to actual seismic records will be investigated in the next section. The dynamic equilibrium equation of an SDOF system is given by

$$m\ddot{u} + c\dot{u} + k_T u = -m a_g \quad (3)$$

where m is the mass, u is the relative displacement, c is the damping coefficient, k_T is the tangent stiffness, and a_g is the acceleration of the ground motion, while upper dots stand for time derivatives. If the required yield force for a system with available ductility μ is denoted by f_y and the maximum force response of the corresponding linear elastic system by f_{el} (Fig. 1), the force reduction factor R can be defined as

$$R = f_{el} / f_y \quad (4)$$

Using traditional structural dynamics theory, SDOF systems are defined here by their elastic vibration period T , ranging from 0.1 s to 3.0 s, and viscous damping ratio ξ , assumed to be 1%, 2%, 5% and 10%. The yield force f_y can be expressed in terms of the yield displacement u_y and the elastic stiffness k_{el} as

$$f_y = k_{el} \cdot u_y \quad (5)$$

while the ductility μ is defined in terms of the maximum displacement u_{max} and the yield displacement u_y , as

$$\mu = u_{max} / u_y \quad (6)$$

Strain hardening or softening takes place after yielding initiates. The tangent stiffness is defined as the slope $k_T = H \times k_{el}$ of the second branch of the skeleton force-displacement relationship (Fig. 1). In this work seven different values of the post-yield stiffness ratio, $H = k_T / k_{el}$, are examined. These are 0%, which corresponds to an elastic-perfectly plastic model, 1%, 3% and 5% for the linear hardening model, and -1%, -3% and -5% for the linear softening model. Unloadings and subsequent loadings are assumed to be parallel to the original loading curve, as shown in Fig. 1.

Finally, the inelastic displacement ratio is defined as the maximum lateral inelastic displacement u_{max} divided by the maximum lateral elastic displacement u_{el} for a system with the same mass and initial stiffness (i.e., same period of vibration) subjected to the same earthquake ground motion. This ratio is given by

$$IDR = u_{max} / u_{el} = \mu / R \quad (7)$$

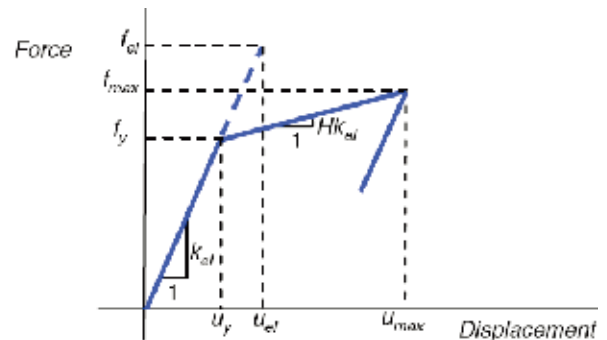


Figure 1 Bilinear elastoplastic model of an SDOF

As Figure 2 shown, in order to compute the coefficients C_1 and C_2 , an equivalent bilinear structural pushover curve model proposed to consider structural cyclic strength degradation.

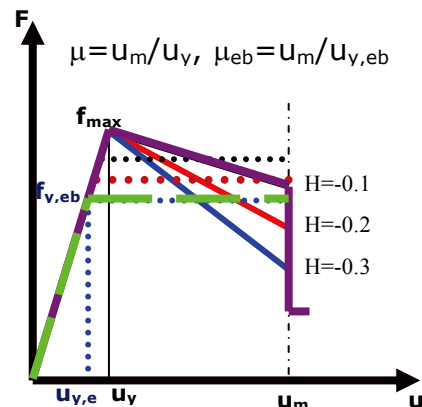


Figure 2 Equivalent bilinear structural pushover curve model

In order to evaluate the coefficient C_2 , the model shown in Figure 2 was considered. Use equal energy principle to idealize the pushover curve as a bilinear curve, and then compute the corresponding post-yield stiffness ratio H and ductility ratio. The C_2 coefficient which reveals cyclic stiffness and strength degradation effects can be computed as

$$IDR = (1 - \sqrt{1 - H}) \cdot \mu + \sqrt{1 - H} \quad (8)$$

In order to verify the feasibility of Eq. (8), a total of 112 real earthquake acceleration time-histories from around the world are used in this study. These accelerograms present maximum ground acceleration greater or equal to 0.10g and are recorded at sites ranging from hard rock to soft soil conditions according to the definitions of the United States Geological Survey (USGS) site classification system (Boore 1993). More specifically, 4 groups of 28 accelerograms are examined, which correspond to:

- hard rock site conditions with shear wave velocity $750 \text{ m/s} \leq V_S$ (soil type A).
- soft rock or very dense soil with shear wave velocity $360 \text{ m/s} \leq V_S < 750 \text{ m/s}$ (soil type B)
- stiff soil with shear wave velocity $180 \text{ m/s} \leq V_S < 360 \text{ m/s}$ (soil type C)
- soft soil with shear wave velocity $180 \text{ m/s} > V_S$ (soil type D).

The complete list of these earthquakes, which was downloaded from the strong motion database of the Pacific Earthquake Engineering Research (PEER) Center. The total sample of earthquakes can be characterized as fairly broad since it ranges in terms of maximum ground acceleration between 98 and 806 cm/s^2 , i.e., between 0.100g and 0.822g. The mean response elastic spectra ($\xi = 5\%$) for the four aforementioned groups and the whole sample are presented in Fig. 3. These spectra seem to be similar to the corresponding design spectra proposed by modern seismic codes with analogous site classification systems. Furthermore, this soil classification system is quite similar to EC8 provisions (ECS, 2003) since the only difference between the EC8 and USGS categorizations has to do with the characteristic shear wave velocity of hard rock, which is greater than or equal to 800 m/s and 750 m/s, respectively.

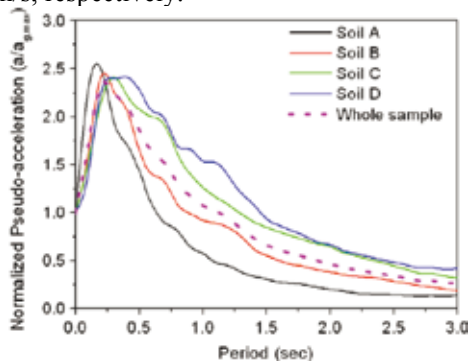


Figure 3. Acceleration spectra for the four groups of accelerograms.

Influence of various parameters

This section examines the influence of period of vibration, force reduction factor, site conditions, post-yield stiffness ratio and viscous damping ratio on the inelastic displacement ratios. These aspects are investigated for reasons of completeness as many of them have been also studied by several authors, but in the most cases separately and seldom simultaneously. The influence of soil types is typically shown in Fig. 4. It is evident that the inelastic displacement ratios are not significantly affected by local site conditions and can be practically neglected. This characteristic is in agreement with the observations of Miranda (2000).

Figure 5 shows the influence of post-yield stiffness ratio. It is evident that the decrease of this ratio leads to a significantly higher inelastic displacement ratio value and vice versa. Finally, as one can observe from Figs. 4-5, the inelastic displacement ratios are extremely dependent on the structural period of vibration, in any case. Concluding this section, it should be noted that despite the observed influence of the most critical parameters, i.e. post-yield stiffness ratio, force reduction factors and structural period on the inelastic displacement ratios, there are many seismic design codes which ignore them in the estimations.

Conclusions

This paper proposes a new method for evaluating the inelastic displacement ratios of SDOF systems on the basis of empirical expressions obtained after extensive parametric studies. The influence of period of vibration, force reduction factor, soil type conditions and post-yield stiffness ratio (hardening and softening) is carefully examined and discussed. The main innovation of this work has to do with the quantification of the seismic sequence effect directly onto displacement demands, a problem which has not been studied in the past. A detailed study of the influence of the various parameters of the problem on the inelastic displacement ratio leads to the following conclusions:

1. The increase of force reduction factors always leads to an increase of the inelastic displacement ratio and vice versa. Furthermore, these ratio values are extremely dependent on the structural period of the SDOF system, especially in the short-period range, say up to 0.5 s. In this case, the lower the period, the higher the inelastic displacement ratio. Additionally, the decrease of post-yield stiffness ratio leads to higher displacement demands and vice versa. This effect is more pronounced for negative values of this parameter, i.e., for softening behavior.
2. The local site conditions and the viscous damping ratio influence the inelastic displacement ratio slightly, and can be practically ignored.

- Currently available empirical and theoretical knowledge on nonlinear cyclic and in-cycle strength and stiffness degradation (Figure 6) should be investigated and documented.

References

Federal Emergency Management Agency. Prestandard and commentary for the seismic rehabilitation of buildings. Rep. FEMA 356, Washington (DC); 2000.

Federal Emergency Management Agency. Improvement of nonlinear static seismic analysis procedures. Rep. FEMA 440, Washington (DC); 2006.

Miranda E. Inelastic displacement ratios for structures on firm sites. J Struct Eng 2000;126(10):1150-9.

Boore DM. Some notes concerning the determination of shear-wave velocity and attenuation. In: Proceedings of geophysical techniques for site and material characterization. 1993. p. 129-34.

Pacific Earthquake Engineering Research Center. PEER strong motion database. [accessed 01.03.09] <http://peer.berkeley.edu/smcat>.

European Committee for Standardization. Eurocode 8: Design of structures for earthquake resistance. 2003.

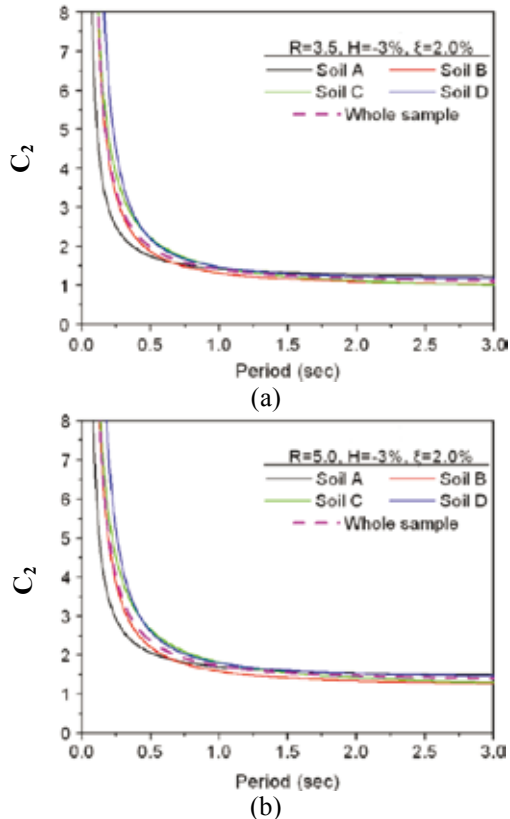


Figure 4. Influence of local site conditions.

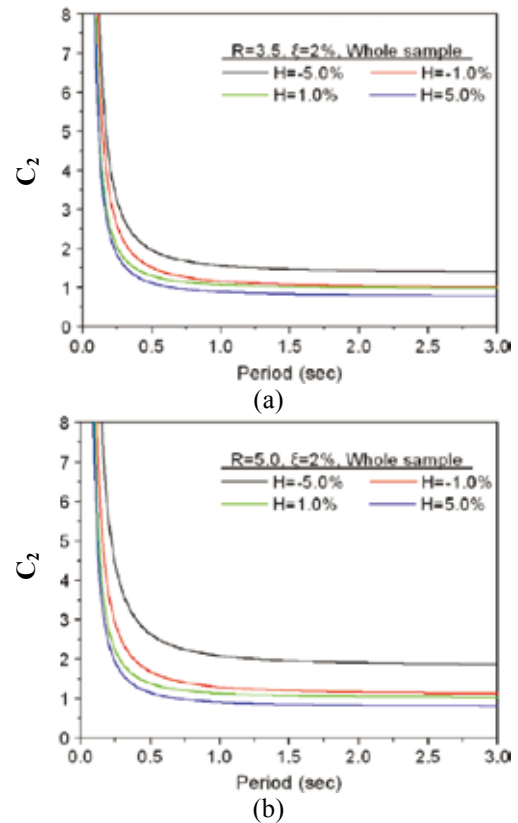


Figure 5. Influence of post-stiffness ratio.

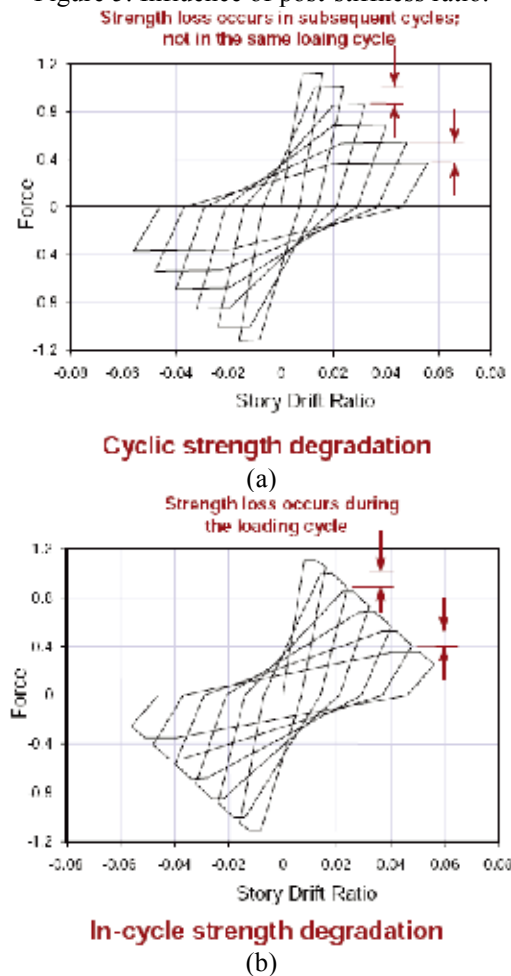


Figure 6. Types of degradation defined in FEMA-440

Seismic Evaluation Method of Geometrically Eccentric Reinforced Concrete Structure with Torsional Plastic Hinge

Lap-Loi Chung¹, Lai-Yun Wu², Chi-Hsiang Sun³, Kuan-Hua Lien³, Yao-Sheng Yang³,
Zhen-Hao Chen³, Guo-Luen Huang⁴, Yeong-Kae Yeh¹, Te-Kuang Chow⁵

鍾立來¹、吳賴雲²、孫啟祥³、連冠華³、楊耀昇³、
陳振豪³、黃國倫⁴、葉勇凱¹、周德光⁵

Abstract

The methods of pushover analyses are still not suitable for the seismic evaluation of eccentric structures. In this, such structures need to consider their members' torque effect. Thus, this study was tasked to develop torsional plastic hinges of structural members in simulating their torque behavior. The cracking torque and the nominal torsional moment strength were computed according to ACI 318-08 and reasonable reduction in torque strengths has been proposed under combined loadings. Cracking and ultimate torsional rigidities originated by Hsu (1984) was adopted. These rigidities are reasonable and conservative when compared with experimental results. Torsional plastic hinge was established according to the torque-twist relationship. In pushover analysis of a pure frame specimen, torsional effect becomes more obvious when the eccentricity increases. The initial stiffness increases with the eccentricity. The displacement corresponding to the 0.8 maximum base force decreases with the increasing eccentricity.

Keywords: pushover analyses, seismic evaluation of eccentric structures, torsional plastic hinge

Introduction

In typical pushover analysis, only the axial forces, shear forces and bending moments of reinforced concrete structures are focused and considered. However, eccentricity may be present or inherent to structures due to architectural (geometry) or usage reasons. In geometry, the structures in L-shape, convex or irregular shape may become eccentric. In usage, the mass may not be evenly distributed in structures such as library buildings. In this paper, torsional plastic hinge is proposed as addition to bending and plastic shear hinges in simulating the pushover properties of eccentric structures. The effectiveness of the proposed torsional plastic hinge was verified numerically using a pure frame (PF) specimen.

Torque Strength

The cracking torque T_{cr} and the nominal torsional moment strength T_n can be calculated from ACI Code (ACI Committee 318, 2008) respectively, as follows:

$$T_{cr} = \frac{1}{3} \sqrt{f'_c} \left(\frac{A_{cp}^2}{p_{cp}} \right) \quad (1)$$

$$T_n = \frac{2A_o A_t f_{yt}}{s} \cot \theta \quad (2)$$

where f'_c is the compressive strength of concrete; A_{cp} is the area enclosed by outer perimeter of concrete cross-section; p_{cp} is the outer perimeter of concrete cross section; and A_o is the gross area enclosed by shear flow path. The ACI Code permits A_o be taken as $0.85 A_{oh}$ in this study where A_{oh} is the area

¹ Research Fellow, National Center for Research on Earthquake Engineering, chung@ncree.org.tw.

^{2,3} Department of Civil Engineering, National Taiwan University

⁴ Department of Construction Engineering, National Taiwan University of Science and Technology

⁵ Assistant Technician, National Center for Research on Earthquake Engineering

enclosed by the centerline of the outermost closed transverse torsional reinforcement; A_t is the area of one leg of a closed stirrup within spacing s ; s is the center-to-center spacing of transverse reinforcement; f_{yt} is the yield strength of transverse reinforcement; and θ is taken to be 45° which is the same value used in this study.

Experimental results of 16 beams with monotonic pure torque load, 10 with repeated pure torque load, 8 with cyclic pure torque load, 19 with monotonic (M+T) combined loadings, 3 with monotonic (V+T) combined loadings, and 4 with monotonic (M+T+V) combined loadings --- a total of 60 specimens, were collected. Cracking and nominal torsional moment strength of the specimens were predicted by ACI 318-08 and compared with the experimental results to see whether the predicted ones are conservative or not. The prediction for beams with pure torsion was found to be conservative, but not for those with combined loadings.

Under combined loadings of shear and torsion, the cracking torque strength is overestimated if concrete was considered to contribute in torsion only. Since concrete resists both shear and torsion, the cracking torque strength T_{cr} has to be reduced. Part of the concrete is provided for shear resistance and the rest is provided for torsion. Eq. (1) was modified to give the reduced cracking torque strength T'_{cr} as follows:

$$T'_{cr} = \left(1 - \frac{V}{V_n}\right) \frac{1}{3} \sqrt{f'_c} \left(\frac{A_{cp}^2}{p_{cp}}\right) \quad (V < V_n) \quad (3a,3b)$$

$$T'_{cr} = 0 \quad (V \geq V_n)$$

where V is the shear force of structural member and V_n is the nominal shear strength. When $V \geq V_n$, all concrete contributed shear resistance only and no more torque, so $T'_{cr} = 0$.

Similarly, the nominal torsional moment strength will be overestimated if stirrup is considered to contribute in torsion only. Since stirrup resists both shear and torsion, the nominal torsional moment strength T_n has to be reduced. Shear force V is taken by concrete first and the rest of the shear force ($V - V_c$) is taken by stirrup. Because part of the stirrup has been provided for shear resistance, only the rest is provided for torsion resistance. Therefore, the reduced nominal torsional moment strength was modified from Eq. (2) as follows:

$$T'_n = T_n \quad (V \leq V_c)$$

$$T'_n = \left(1 - \frac{V - V_c}{V_s}\right) \frac{2(0.85A_{oh})A_t f_{yt}}{s} \cot \alpha \quad (V_c < V < V_n)$$

$$T'_n = 0 \quad (V \geq V_n) \quad (4a,4b,4c)$$

When $V \leq V_c$, all shear force is taken by concrete, so $T'_n = T_n$; when $V \geq V_n$, all stirrups contributed for shear resistance and no more torque can be taken, so $T'_n = 0$.

The reduced torque strengths of the 60 specimens were computed by Eq. (3) and Eq. (4). The results were compared with the experimental ones to check whether the formulae are conservative or not. In cracking torque strength, the average of the ratio of the predicted and experimental values decreases from 1.003 before reduction to 0.909 after reduction. In nominal torsional moment strength, the average of the ratio of the predicted and experimental values decreases from 1.071 before reduction to 0.991 after reduction. It shows that the cracking and ultimate torque strength become conservative after reduction.

Torsional Rigidity

Based from Hsu (1984), the torsional rigidity at cracking can be derived with the introduction of some variables and after some simplification as follows (Tavio and Teng, 2004):

$$(GC)_{cr} = \frac{4\mu E_s A_o^2 A_{cp}}{p_o^2 \left(\frac{1}{\rho_l} + \frac{1}{\rho_h}\right)} \quad (5)$$

where $(GC)_{cr}$ is the torsional rigidity at cracking; μ is the rigidity multiplier; E_s is the modulus of elasticity of steel; p_o is the perimeter of the centerline of shear flow; ρ_l is the ratio of area of distributed longitudinal reinforcement to gross concrete area perpendicular to that reinforcement; and ρ_h is the ratio of area of distributed transverse reinforcement to gross concrete area perpendicular to that reinforcement. A value of 1.5 for μ gives the best fit of the overall experimental data adopted from the literature.

When the reinforced concrete member reaches the ultimate state, the ultimate torsional rigidity is only a small part of the cracking one. Therefore, the ultimate torsional rigidity needs further simplification from the cracking torsional rigidity with the use of a multiplier of concrete strain, λ . This ultimate torsional rigidity is a lower bound for the torsional rigidity. A modified formula proposed by Tavio and Teng (2004) is as follows:

$$(GC)_n = \frac{4E_s A_o^2 A_{cp}}{p_o^2 \left(\frac{4n\lambda A_{cp}}{p_o t_d} + \frac{1}{\rho_l} + \frac{1}{\rho_h}\right)} \quad (6)$$

where $t_d = (4T_a)/(A_{cp} f'_c)$ is the thickness of the shear flow zone; T_a is the applied torque; $n = E_s/E_c$ is the moduli ratio; and a value of 4.0 for λ reflects better the torsional rigidity at the ultimate limit state.

Torque-Twist Relationship & Plastic Hinge

From the previous two sections, torque-twist relationship of a structural member is summarized in a diagram, as shown in Fig. 1. Point A is the origin (0, 0). Point B is $(\theta'_{cr}/H, T'_{cr})$ where θ'_{cr}/H is

$$\frac{\theta'_{cr}}{H} = \frac{T'_{cr}}{(GC)_{cr}} \quad (7)$$

The slope of line AB is the cracking torsional rigidity $(GC)_{cr}$ of Eq.(5). Point C is $(\theta'_n/H, T'_n)$ where θ'_n/H is

$$\frac{\theta'_n}{H} = \frac{T'_n}{(GC)_n} \quad (8)$$

The slope of line AC is the ultimate torsional rigidity $(GC)_n$ of Eq. (6). It is assumed in this study that when the member reaches the ultimate point, it cannot take torque anymore, so point D is $(\theta'_n/H, 0)$.

Torque-twist relationship in Fig. 1 was transformed into torsional plastic hinge curve shown in Fig. 2. Point A of the torsional plastic hinge curve is also the origin (0, 0). Since the elastic behavior was taken care by ETABS and the cracking torque strength was normalized to be unity, point B of the torsional plastic hinge curve is (0, 1). Point C of the torsional plastic hinge curve is $((\theta'_n - T'_n)/(GC)_{cr})/H, T'_n/T'_{cr}$. Because only the plastic behavior was considered, the elastic portion was subtracted from the twist corresponding to the nominal torsional moment strength to give $(\theta'_n - T'_n)/(GC)_{cr}/H$. The nominal torsional moment strength was normalized to T'_n/T'_{cr} . Point D of the torsional plastic hinge curve is $(\theta'_n/H, 0)$ where the axial bearing capacity of the member has been lost, so the Moment/SF is zero at point D. The end point, point E, of the torsional plastic hinge curve is $(10\theta'_n/H, 0)$ where the twist is ten times of point D to make the numerical convergence better and for it to have no difference to the pushover curve. The torsional plastic hinge curve described above is shown in Fig. 2.

Pushover Analysis of Eccentric Structure

The use of reduced cracking and the ultimate torque strengths requires the determination of individual corresponding shear forces, V . However, through equilibrium of forces, the shear forces corresponding to cracking and ultimate states cannot be obtained. Therefore, it is necessary to assume the corresponding shear forces of the member. The torsional plastic hinge is then assigned and pushover analysis is carried out. After pushover analysis, the shear forces corresponding to the cracking and ultimate torsion states are checked whether the

assumption is acceptable or not. If the shear forces output from pushover analysis are different from the assumed ones, the corresponding shear forces are updated. The process repeats iteratively until the difference is acceptable. The procedures for pushover analysis with consideration of torsional plastic hinges are as follows:

- (1) Establish ETABS model for the structure.
- (2) Calculate the flexural and shear plastic hinges of the structural members (Chung et al., 2009).
- (3) Assume the shear force $V = \min(V_m, V_n)$.
- (4) Calculate the torsional plastic hinges of the structural members.
- (5) Assign the plastic hinges to the structure in ETABS.
- (6) Check the shears V whether the assumptions are correct or not, if not, repeat step (4).
- (7) Obtain the pushover curve.

The effectiveness of the proposed torsional plastic hinge is verified numerically using the PF specimen. By varying the eccentricities from 0% to 20% in the transverse direction, the results of pushover analysis in the longitudinal direction were studied. The PF specimen (Fig. 3) was 330 cm in height. The footing was 350cm in width in the longitudinal direction, 450cm in length in the transverse direction, and 35cm in depth. The reinforcement and ties for the footing was a two-layer of D22@25cm and D13@50cm in both directions, respectively. The column was 30cm in depth in the longitudinal direction, 35cm in width in the longitudinal direction and 280cm in clear height. The reinforcements for the column were eight D16 in the longitudinal direction and D10@25cm in the transverse direction. The G1 beam was 50cm in depth, 30cm in width and 180cm in clear length. The reinforcements for the G1 beam were ten D19 in the longitudinal direction and D10@10cm in the transverse direction. The B1 beam was 50cm in depth, 30cm in width and 270cm in clear length. The reinforcements for the B1 beam were six D19 in the longitudinal direction and D10@20cm in the transverse direction. The floor slab was 300cm in width along the corridor, 340cm in length perpendicular to the corridor and 40cm in depth. The reinforcement and ties for the footing were two-layer D16@20cm and D13@40cm in both directions. Within the columns, beams and slabs, the average yield strength of reinforcement D10 was 4070kgf/cm², D13=3621kgf/cm², D16=3676kgf/cm² and D22=4747kgf/cm², while the average compressive strength of the concrete was 199.3kgf/cm².

The pushover curves in different eccentricities are shown in the Fig. 4. The initial stiffness was increased from 12229.4kgf/cm (without eccentricity) to 14965.9kgf/cm (with 20% eccentricity) because due to eccentricity, the push direction was

transferred from longitudinal to transverse direction. The maximum base force in different eccentricities was 18333kgf because the failure mode of the PF specimen was flexural. The displacement corresponding to the 0.8 maximum base force has been decreased from 13.2cm (without eccentricity) to 12.9cm (with 20 % eccentricity) due to the torsional effect.

Conclusions

This study aimed to develop the torsional plastic hinges for eccentric structural members to simulate their torque behavior. The cracking torque and the nominal torsional moment strength were computed according to ACI 318-08 and reasonable reduction in torque strengths is proposed under combined loadings. Cracking and ultimate torsional rigidities originated by Hsu (2004) was adopted. These rigidities are found to be reasonable and conservative when compared with experimental results. Torsional plastic hinge was established according to the torque-twist relationship. The effectiveness of the proposed torsional plastic hinge was verified numerically using the pure frame specimen.

References

- ACI Committee 318. (2008), *Building Code Requirements for Reinforced Concrete (ACI 318-08) and Commentary*, American Concrete Institute, Farmington Hills, Michigan.
- Hsu, T.T.C. (1984), *Torsion of Reinforced Concrete*, Van Nostrand Reinhold Company, New York.
- Tavio and Teng, S. (2004), "Effective torsion rigidity of reinforced concrete members," *ACI Structural Journal*, Vol.101, No. 2, pp.252-260.
- Chung, L.L., Yeh, Y.K., Chien, W.Y., Hsiao F.P., Shen, W.C., Chiou, T.C., and Chow, T.K. (2009), *Technology Handbook for Seismic Evaluation and Retrofit of School Buildings - Second Edition*, National Center for Research on Earthquake Engineering, Taiwan, NCREE 09-023.

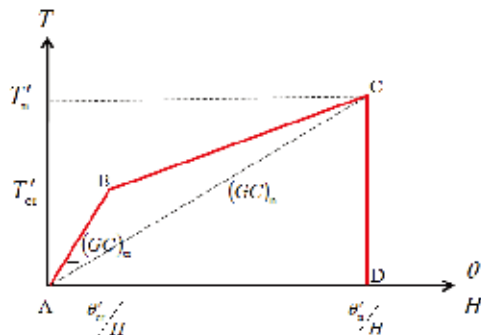


Fig. 1 Torque-twist relationship

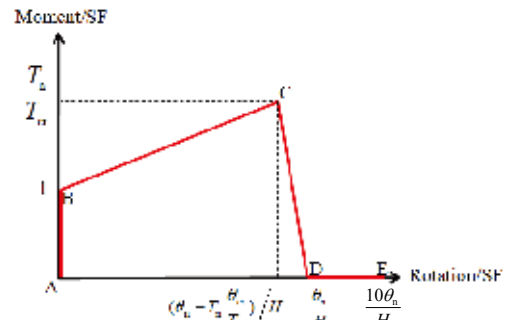


Fig. 2 Torsional plastic hinge curve

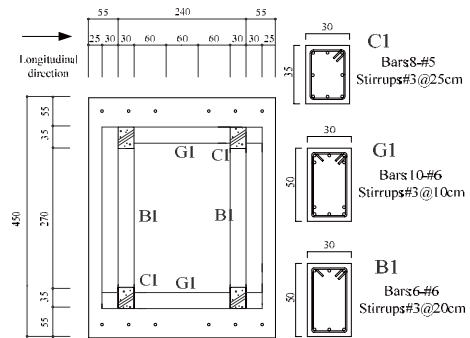


Fig. 3 PF specimen plane and cross section

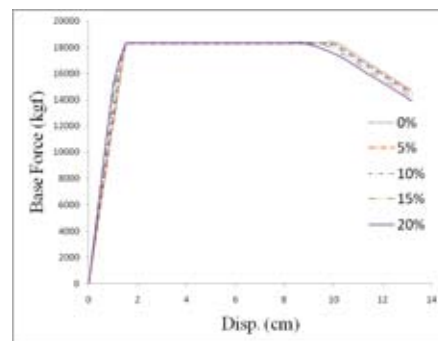


Fig. 4 Pushover curves with different eccentricities

Experimental and Numerical Study on Dynamic Collapse of Reinforced Concrete Frames

Chiun-lin Wu¹, Shyh-Jiann Hwang², Yuan-Sen Yang³ and Kenneth Elwood⁴

吳俊霖¹, 黃世建², 楊元森³, Kenneth Elwood⁴

Abstract

A good number of dynamic collapse experiments using NCREE's 5mx5m shaking table has been conducted in the past few years to study a complete spectrum of column failure modes, and to preliminarily investigate full range structural response up to the limit state of global collapse using two-bay-two-story concrete frames representing realistic proportioning and reinforcement detail of various structural components, including columns, beams, joints, and slabs. Such valuable long-term experimental and numerical study effort, promoting international collaborations, not only has led to the critically important verification of the accuracy of existing analysis methods and models, but also pinpoints future challenges and emerging research needs in the next few years. Overall, the studies proved that the updated provisions of ASCE/SEI 41-06 document appropriately yield a good match with test data while preserving a favorably moderate degree of conservatism; on the other hand, the 84th-percentile backbone curve produced by the Zhu et al. probabilistic model, among many others, oftentimes provides closest match with test data. Finally, OpenSEES based simulation employing Limit State material models usually provides satisfactory predictive results though further improvements are still needed before numerical predictions with comfortable confidence and conservatism can be reached.

Keywords: collapse, shaking table tests, concrete frames, column, beam, beam-column joint

Introduction

The loss of gravity load carrying capacity of reinforced concrete columns is the most critical factor leading to catastrophic structural collapse of buildings, and thereby causes tragic consequence of losses of lives; for instance, a large number of pancake type of building failures found in the 1999 Chi-Chi (Taiwan) and the 2008 Wenchuan (China) earthquakes, etc., which can be attributed to nonductile detailing fairly common in older concrete columns. To better understand full range structural behavior of a wide variety of concrete columns, a good number of collapse tests using a shaking table have been conducted during the past few years at the National Center for Research on Earthquake Engineering of Taiwan since 2004 to experimentally observe three major types of column failure mechanisms, i.e., flexure, flexure-shear and pure shear failures in a dynamic manner. The dynamic test data can serve as a great test bed for validating

numerical nonlinear simulation methods as well as existing simplified assessment models.

Characteristics of Concrete Frame Specimens and Input Motions

The test specimens were a single-story shear frame containing multiple columns (two, three, and four) interconnected at column top through a rigid beam to either allow or prohibit an alternative path for vertical load redistribution using different combinations of ductile and nonductile columns. The ones prohibiting vertical load redistribution using test frames having two identical concrete columns can be considered very similar to quasi-static reversed cyclic tests on double-curvature single column specimens.

On the other hand, four 1/2.25 scale specimen models representing two-bay-two-story reinforced concrete frames were built for the purpose of

¹ National Center for Research on Earthquake Engineering, Taipei, Taiwan, clwu@ncree.narl.org.tw

² Department of Civil Engineering, National Taiwan University, Taipei, Taiwan

³ Department of Civil Engineering, National Taipei University of Technology, Taipei, Taiwan

⁴ Department of Civil Engineering, University of British Columbia, Vancouver, Canada

studying complicated structural behavior under whole frame interaction during the full range of structural nonlinearity up to global collapse. These specimens were tested under high and low gravity loads to investigate the influence of axial loads on the collapse vulnerability of the structures. The test results led to a better understanding of component interaction between beams, columns, joints and slab participation after incipient failure took place until complete frame failure was observed. Such studies will lead to a better understanding of the behavior of existing reinforced concrete structures, and consequently, more cost-effective retrofit strategies

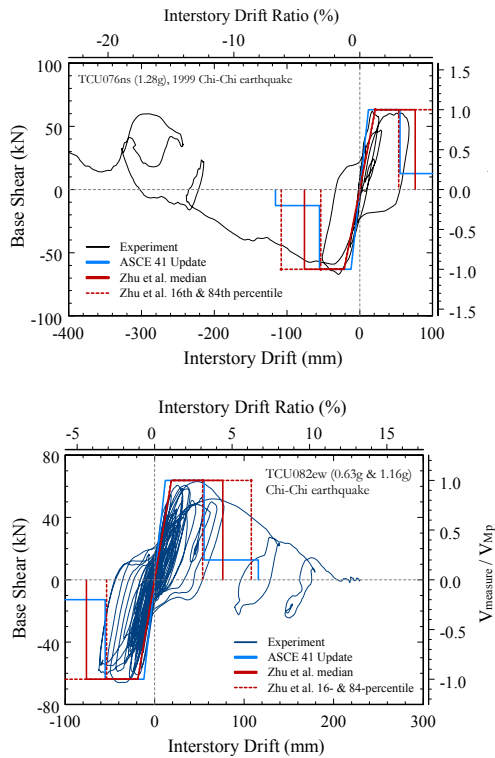


Fig. 1. Experimentally obtained hysteretic loops of flexure-shear critical columns in comparison with ASCE 41 models and probabilistic force-deformation curves subjected to TCU076ns (upper) and TCU082ew (lower).

The earthquake records selected as input table motions are representative of main characteristics of ordinary (TCU082ew, TCU047ns) and near-fault (TCU076ns) earthquake motions in central Taiwan. TCU076 and TCU082 were near-fault stations in the 1999 Chi-Chi earthquake, but the strong ground shaking recorded at station TCU082 did not contain velocity pulses or static fling step pulse, which might be observed in a near-fault site. In contrast, TCU076 motion contains dynamic velocity pulses. The occurrence frequency of velocity pulses in a near-fault zone remains a mystery due to the very limited near-fault motion data collected and research findings up to date. The static fling effect is beyond the scope of this study. Distinct from the narrow

band nature of intermediate-period velocity pulses existing in TCU076, TCU082 has broader frequency contents and excitation force was able to remain approximately at the same intensity level even when columns sustained initial damage and minor cracking such that the structural period already started to lengthen. TCU047 is considered as a commonly seen ordinary motion with wave trains mostly in high frequency range.

Research Findings

Hysteretic data collected from the shaking table tests are compared with existing predictive models. In addition to providing more reversed cyclic data, which is essential for validating existing analytical models, dynamic test results can also contribute to evaluating the ability of the models to predict dynamic structural response due to seismic excitations. Major differences between dynamic and static tests include the strain rate effect and varied loading history determined by dynamic response of the specimen to the input base motion. The experimental hysteretic loops shown in Figs. 1-3 represent frame base shear vs. frame lateral drift responses of flexure-shear, flexure, and shear critical columns, respectively, which are a direct summation of individual column hysteretic curves to remove the shear asymmetry due to frame action effect.

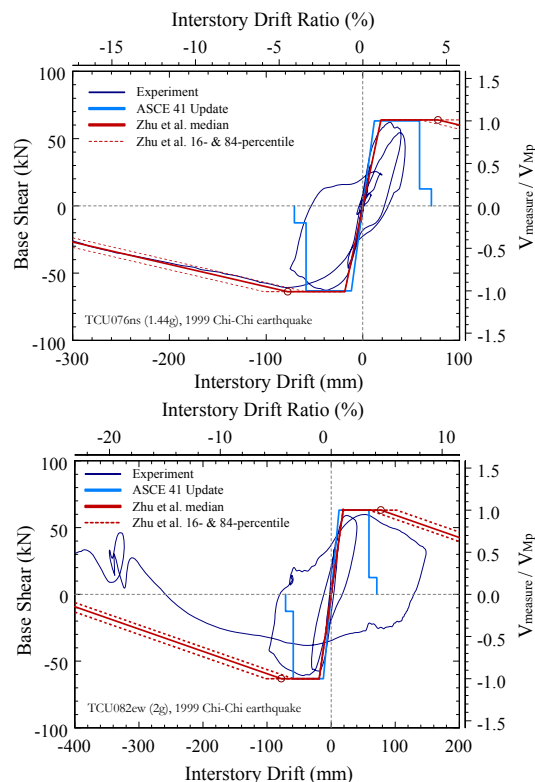


Fig. 2. Experimentally obtained hysteretic loops of flexure critical columns in comparison with ASCE 41 Update models and probabilistic force-deformation curves subjected to TCU076ns (upper) and TCU082ew (lower).

The ASCE/SEI 41-06 Update proposed the failure mode classification scheme for RC columns using a variable matrix containing nominal shear strength V_{41} , plastic shear demand V_{Mp} and the transverse reinforcement detailing. Its classification scheme successfully identifies all the observed failure modes of columns tested at NCREE. The column drift at flexural yield obtained from the Update assumes an effective flexural rigidity of $0.3E_cI_g$, which corresponds to only 60% of the value originally assumed in ASCE/SEI 41-06 (2007). The reduced stiffness incorporates the influence of bar slip prior to yielding of the longitudinal reinforcement and thereby provides a better agreement with the recorded data. The effective shear rigidity is assumed to be $0.4E_cA_g$. The second model included for comparison was the probabilistic backbone curve proposed by Zhu *et al.* (2007). The column classification method of that model also successfully identifies the observed column failure modes. The lateral drift ratio at flexural yield was considered as the sum of lateral displacements due to flexure, shear, and bar slip of the column divided by the clear column height. Median values were used to compute drifts at shear and axial failure of flexure-shear critical columns, and drifts at flexural failure of flexural columns. It should be mentioned that Zhu *et al.* (2007) does not propose assessment models for shear critical columns, so only the predictive curves from the ASCE/SEI 41-06 Update are reported in Fig. 3. The assessment models were derived from test data on isolated columns under reversed cyclic loadings of a lower strain rate than real earthquakes without loading pattern variation, which likely accounts for some of the discrepancy between calculated and measured values. Overall, the ASCE/SEI 41-06 Update appropriately yields a satisfactory match with column test data of flexure-shear and flexure failures while preserving a moderate degree of conservatism.

Fig. 1 compares the predictive flexure-shear backbone curves obtained from the ASCE/SEI 41-06 Update and Zhu *et al.* (2007) models with test data. The 16th-percentile curve of Zhu *et al.* (2007) coincides roughly with estimates from the ASCE/SEI 41-06 Update. The median flexural strength curves are presented in Fig. 2 as solid red lines. After the onset of flexural failure of flexural columns (shown as red hollow circles in Fig. 2), P- Δ effects will dominate the response; thereby strength degradation after that point was estimated using the measured initial axial load multiplied by the measured drift ratio as the slope of the post-peak descending branch (shown as inclined solid red lines) with its probability band (16th- and 84th-percentile values shown as dashed red lines) reported as well. Fig. 2 reveals that dynamic hysteretic response under TCU076 near-fault motion is very similar to a push over curve due to low-cycle failure, while dynamic hysteretic response under TCU082 motion is not

captured by the nonlinear static procedure due to the observed cyclic degradation of lateral strength, in which case time history analysis shall be desirable. Fig. 3 suggests that the ASCE/SEI 41-06 Update yields satisfactory shear strength estimates, but overestimates the effective shear stiffness. The experimental post-peak branch has a slower descending slope than estimate from the ASCE/SEI 41-06 Update because a higher longitudinal steel ratio of 3.2% was used. In case of 1.4% longitudinal steel ratio, pure shear failure caused a steeper drop of strength and no residual strength was observed according to other cyclic test data collected at NCREE.

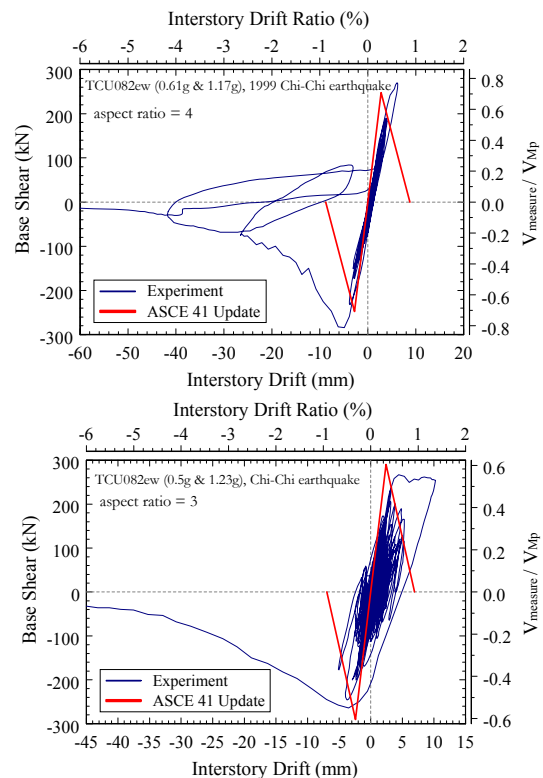


Fig. 3. Experimentally obtained hysteretic loops of shear critical columns in comparison with ASCE 41 Update models: aspect ratio = 4 (upper) and 3 (lower).

The capability of various nonlinear dynamic analysis models to capture the observed structural response was also preliminarily explored using OpenSEES as the analysis platform to facilitate comparison. Fig. 4 demonstrates the nonlinear time history analysis results using a detailed fiber section model, which shows the post-peak engineering conservatism inherited from cyclic test data, and modeling conservatism aiming to reduce the negative impact that may otherwise have arose due to lack of Knowledge on concrete fracture failure behavior. Fig. 5 demonstrates the nonlinear time history analysis results using Limit State material models to incorporate all the observed response characteristics that are reported above but cannot be effectively

represented by a traditional fiber section model. Generally speaking, OpenSEES based simulation employing Limit State material models provided satisfactory results though further improvements are still needed, particularly in the regard of backbone models, before numerical predictions with a satisfactory degree of confidence and conservatism can be reached.

Conclusions

A representative set of shaking table tests resulting in dynamic axial collapse of reinforced concrete frames covering a good variety of column failure modes has been studied. Strengths and drift capacities of the test frames were compared with values calculated using published analytical models. The models contained in the ASCE/SEI 41-06 Update (2007) standard produced reasonably close estimates of strength but moderately conservative estimates of deformation capacity for the columns tested. The probability-based model of Zhu et al. (2007) produced comparable predictive results with the ASCE/SEI 41-06 Update when mean minus one standard deviation deformation values were used in the analytical model. Subsequent studies will continue and focus on performance evaluation of the newly developed element models and dynamic simulation methods.

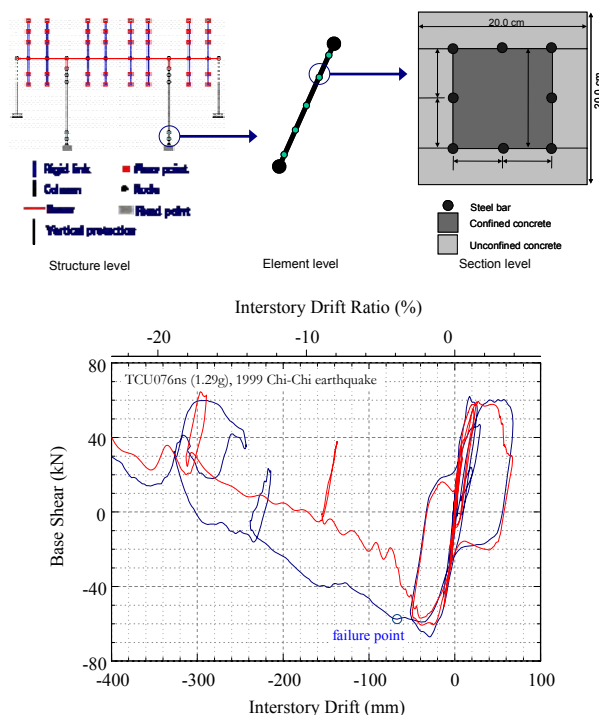


Fig. 4. Modeling two-column concrete frame specimens using OpenSEES detailed fiber section model (upper) and comparison of measured and calculated hysteretic responses (lower).

Behavior of specimen MUFS indicates that

inter-story drifts may not correlate well with shear failure of flexure-shear critical columns, where shear failure initiation appears to be more related to column end rotations than column drifts. As such, the development of existing simplified assessment models for concrete columns should be further improved by incorporating an additional format of evaluating column end rotation, in addition to column lateral drift, for better prediction of frame behavior. The interaction between unconfined joints and flexure-shear critical columns after incipient shear failure has developed, and slab participation within the range of severe structural nonlinearity both point out a valuable future direction of collapse studies.

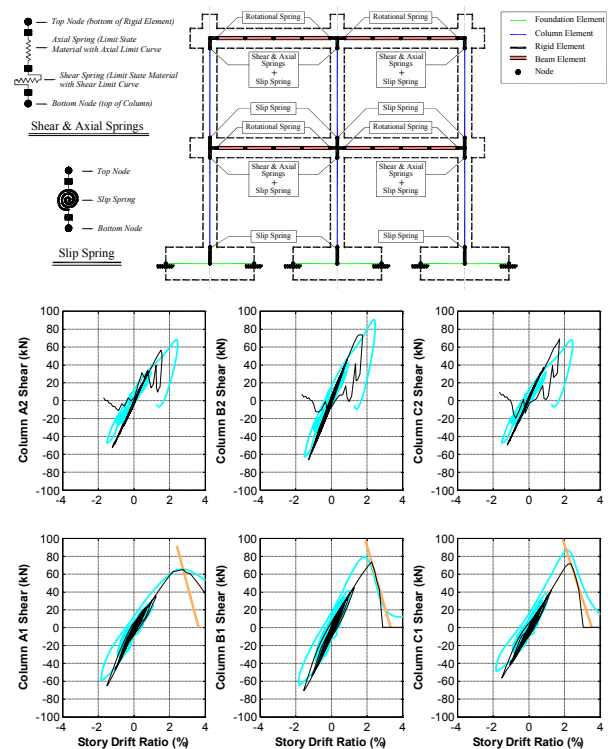


Fig. 5. Modeling two-bay-two-story concrete frame specimens using OpenSEES Limit State material models (upper) and comparison of measured and calculated hysteretic responses (lower)

References

ASCE/SEI 41-06 (2007). *Seismic Rehabilitation of Existing Buildings*, America Society of Civil Engineers, Reston, V.A.

Elwood K.J., Matamoros A.B., Wallace J.W., Lehman D.E., Heintz J.A., Mitchell A..D., Moore M.A., Valley M.T., Lowes L.N., Comartin C.D., Moehle J.P. (2007). "Update to ASCE/SEI 41 Concrete Provisions," *Earthquake Spectra*, **23**(3): 493-523.

Zhu L., Elwood K.J., Haukaas T. (2007). "Classification and Seismic Safety Evaluation of Existing Reinforced Concrete Columns," *Journal of Structural Engineering, ASCE*, **133**(9): 1316-1330.

Axial Loading Capacity of Retrofitted Full-scale Rectangular RC Columns

Min-Lang Lin¹ Ying-Han Wu² Chih-Tsung Lin³ Pei-Ching Chen⁴

Abstract

The performance of reinforced concrete columns subjected to axial force is relative to its confinement. Carbon fiber reinforced polymer (CFRP) wrapping, a generally adopted retrofit method, has been proven to have not effectively provided the required confining force due to the bulging effect on the column face. Therefore, this paper focused on the performance of the retrofitted full-scale rectangular RC columns using different retrofit schemes that include the proposed CFRP wrapping conjugated with CFRP anchors method. A total of 11 rectangular RC columns with low transverse reinforcement ratio were constructed. Among them, one was tested as benchmark; one was purposely constructed with larger transverse reinforcement ratio; five were retrofitted using CFRP wrapping and CFRP anchors; and the other four were retrofitted using different shapes of steel jacketing only or with adhesive anchors. All the specimens were subjected to monotonic incremental axial force until failure occurred. Results demonstrated that the ductility of the specimens retrofitted using CFRP wrapping with CFRP anchors has significantly improved compared with those retrofitted using CFRP wrapping only. On the other hand, the specimen with octagonal steel jacketing performed better not only on ductility but also on strength than all other specimens. Finally, a novel numerical model considering the contribution of the retrofit material will be proposed and validated in the future.

Keywords: Seismic retrofit, CFRP wrapping, CFRP anchor, octagonal steel jacketing

Introduction

Seismic retrofit of reinforced concrete (RC) members has become an important research issue in Taiwan since a number of RC buildings were severely damaged or had collapsed during the 1999 Chi-Chi earthquake. It has been observed that the lack of ductility capacity of the ground floor columns was the key factor among others for the collapse of the affected buildings. As a result, a large number of tests have been conducted at the National Center for Research on Earthquake Engineering (NCREE), Taiwan in the recent years to evaluate the effectiveness of various retrofit schemes on RC building columns, beams and walls (Tsai & Lin, 2002a; Tsai & Lin, 2002b).

Carbon fiber reinforced polymer (CFRP) wrapping has been widely used to retrofit the existing buildings because of its high tensile strength, slight weight, and convenient application. However, it has been observed that the external confinement provided by CFRP wrapping is ineffective due to the debonding between CFRP sheets and

RC surfaces. Therefore, CFRP wrapping conjugated with CFRP anchors retrofit method was proposed and validated in the previous studies (Lin et al., 2008; chen et al., 2010). Experimental results demonstrated that the seismic performance of rectangular RC columns and beams has been improved significantly by this retrofit method. Further researches on RC components retrofitted using CFRP wrapping and CFRP anchors are necessary to develop the theoretical model of retrofitted RC members. It is known that the relation between axial performance and confinement is the key factor to develop the numerical model of retrofitted RC members. Hence, a number of simple but representative axial tests for RC columns were conducted. In this paper, the axial performance of eleven RC columns retrofitted using several different schemes is compared and discussed.

¹ Associate Researcher, National Center for Research on Earthquake Engineering, mllin@ncree.narl.org.tw

² Graduate Student, Department of Civil Engineering, National Taipei University of Technology

³ Associate Professor, Department of Civil Engineering, National Taipei University of Technology

⁴ Assistant Researcher, National Center for Research on Earthquake Engineering

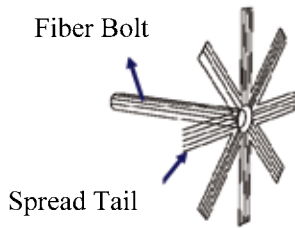


Fig. 1 Illustration of a CFRP anchor

Test Program

Specimen Design

Following the latest Taiwan Seismic Provisions for RC buildings, the equivalent transverse pressure can be expressed as (Tsai & Lin, 2002; Lin et al., 2009):

$$Q = \left\{ 0.3 f_c' \left(\frac{A_g}{A_{ch}} - 1 \right), 0.09 f_c' \right\}_{\max} \quad (1)$$

Considering the confinement provided by the external jacketing and anchors, Eq. 1 can be written as:

$$f_{am} = Q - \frac{A_{sh} f_{yh}}{s h_c} - \frac{2 f_{jd} t_f}{B} \quad (2)$$

where, A_{sh} is the total area of transverse reinforcements, f_{yh} is the yield stress of transverse reinforcements, s is the spacing of transverse reinforcements, h_c is the center-to-center distance of the transverse reinforcements, A_g is the cross-sectional area of the column, A_{ch} is the area enclosed by the transverse reinforcements, f_c' is the compressive strength of concrete, f_{am} is the confinement stress provided by anchors and f_{jd} is the design stress of CFRP.

Figure 1 illustrates a CFRP anchor. Since CFRP anchors are designed to provide additional confinement to satisfy the equivalent transverse pressure, the design procedures of CFRP anchors are documented in the works of Lin et al.(2009).

Specimen Preparation

Eleven specimens were designed based on the non-ductile type of reinforcement details. Among them, one was purposely constructed with larger transverse reinforcement ratio and marked R09TS8. Details of the other columns were made identical with Specimen R09BM, the benchmark specimen, made of 12-22mm diameter vertical bars. The spacing of 10mm diameter stirrups was 250mm. The column height was 1600mm, including the test region of 1000mm and two stiffened regions of 300mm at the bottom and at the top of the column. The stiffened region is for transferring the axial force to the test region without causing any failure at the end; as a result, the transverse reinforcement ratio of the stiffened region was designed larger than that of the test region. The column's cross-section is 450mm × 450mm. The fabrication details of the

specimens are shown in Fig.2. The tensile test results of reinforcements and the compressive test results of concrete cylinders are shown in Table 1.

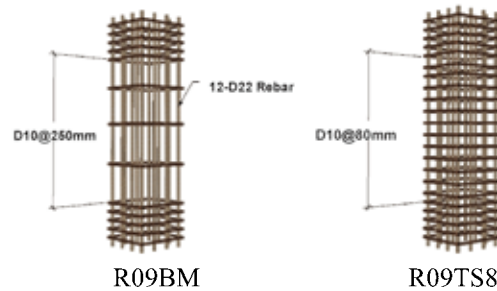


Fig. 2. Details reinforcement of specimens

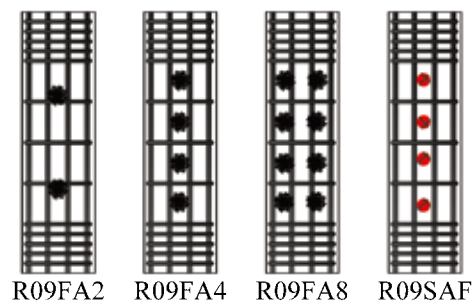


Fig. 3. Details anchors spacing of specimens

The above-mentioned ten RC columns with same reinforcement details were retrofitted using different schemes. Among them, five were retrofitted with CFRP wrapping and CFRP anchors. Specimens R09F2 and R09F4 were retrofitted using only CFRP wrapping with two and four wrapping layers, respectively. Specimens R09FA2, R09FA4 and R09FA8 were retrofitted with two layers of CFRP wrapping conjugated with two, four and eight CFRP anchors on each side of the column, correspondingly. The diameter of the fiber bolt was 20mm and the length was 170mm. The radius of the spread tail was 170mm. The remainder four specimens were retrofitted using steel jackets. The steel thickness of Specimen R09S3 and R09S6 were 3mm and 6mm respectively. Specimen R09SA4 was retrofitted using 3mm-thick steel with 16mm-diameter adhesive anchors. Specimen R09OS3 was retrofitted with 3mm-thick octagonal steel jacket. Figure 3 illustrates the details of anchor spacing on the specimens, and a brief instruction on each specimens is listed in Table 2.

Table 1 Properties of materials used in this study

Concrete 28' compressive strength (MPa)	22.1
D10 rebar tensile yield strength (MPa)	368
D22 rebar tensile yield strength (MPa)	478
Tensile modulus of CFRP (GPa)	279
A-36 steel plate yield strength (MPa)	252

Table 2 Instruction of the tested specimens

Specimen	Retrofit Scheme
R09BM	Bench mark specimen with low transverse reinforcement ratio
R09TS8	Bench mark specimen with high transverse reinforcement ratio
R09F2	2 layers of CFRP wrapping
R09F4	4 layers of CFRP wrapping
R09FA2	2 layers of CFRP wrapping with CFRP anchors 500mm spacing
R09FA4	2 layers of CFRP wrapping with CFRP anchors 250mm spacing
R09FA8	2 layers of CFRP wrapping with CFRP anchors 250mm spacing
R09S3	3mm thickness steel jacket
R09S6	6mm thickness steel jacket
R09SA4	3mm thickness steel jacket with adhesive anchors 250mm spacing
R09OS3	3mm thickness steel jacket

Test Setup

All the specimens were tested on the 6-DOF (degree-of-freedom) testing system called MATS or the Multi-Axial Testing System. Six compression dynamic actuators are of vertical single ended pancake type actuators with hydrostatic bearings at the interface with the platen. The full capacity of each dynamic actuator is 5000kN. Therefore, the total vertical force capacity can reach 60MN. In this paper, MATS was used to apply monotonic axial force on the specimens. The two post-tensioned A-shaped RC frames were interconnected by a steel concrete composite cross beam and RC reacting base. In this study, four high performance concrete (HPC) blocks were installed between the cross beam and the specimens. A rigid universal joint was fixed on the HPC blocks to transfer the axial force to the specimens without carrying any bending moment. Figure 4 shows the test setup.

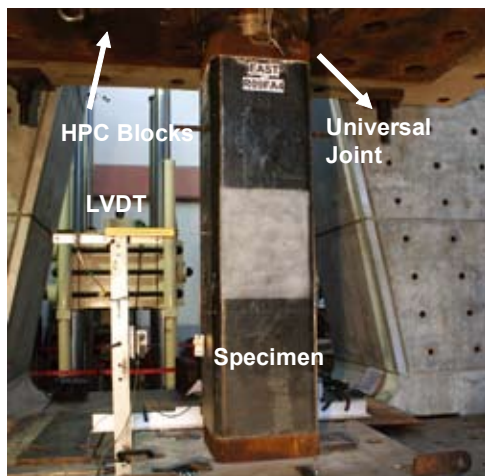


Fig. 4 Test setup

Test Results

Specimens R09BM and R09TS8 have the same performance. The concrete cover bulged and broke immediately after reaching the peak axial strength. The recorded axial strength of Specimen R09BM and Specimen R09TS8 was 6191kN and 6692kN, respectively. On the other hand, the ultimate axial deformation of the Specimens R09BM and R09TS8 was 12.1mm and 13.8mm, correspondingly. The strength of Specimen R09TS8 is slightly higher than that of Specimen R09BM.

Both the axial strength and deformation capacities were increased for the retrofitted specimens of R09F2 and R09F4. The ultimate axial deformation of these three specimens, namely, R09FA2, R09FA4 and R09FA8, has improved compared with those CFRP wrapped specimens without using CFRP anchors. The response of each CFRP wrapped specimen subjected to monotonic axial loading is shown in Fig. 5.

Comparing the specimens with steel jacket to Specimen R09BM, the extraordinary increase of axial strength may be due to the enlarged cross section after the non-shrinkage grout was filled in. On the other hand, the thickness of the steel jacket resulted to slight difference on the observed axial strength based on the results of the steel-jacketed specimens. Of these specimens, Specimen R09S3 has ruptured at its welding region whereas Specimen R09S6 has torn at its corner. Neither the strength nor the deformation capacity was improved by the application of adhesive anchors. On the other hand, the specimen retrofitted using octagonal steel jacketing, Specimen R09OS3, exhibited the best performance among all the retrofitted specimens. The response of each steel jacketed specimen is shown in Fig. 6.

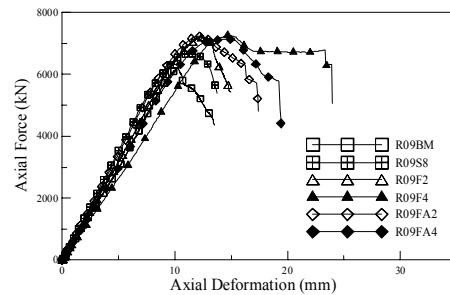


Fig. 5 Responses of specimens with CFRP wrapping

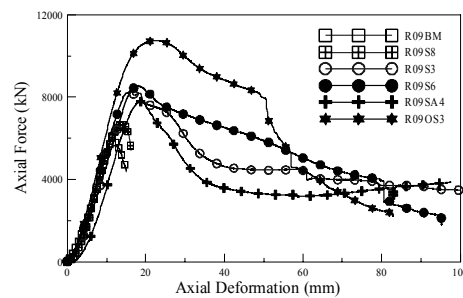


Fig. 6 Responses of specimens with steel jacket

In order to specify the effectiveness of each retrofit scheme, a confining ratio index, R , is defined as shown in

Eq. 3.

$$R = \frac{f_{ts} + f_{an} + f_{rf}}{Q} \quad (3)$$

where f_{ts} , f_{an} , and f_{rf} are the confinement stress provided by transverse reinforcement, anchors, and external jacketing, respectively. The relationship between the confining ratio and the ultimate strain that demonstrates the ultimate strain is proportional to the confining ratio on the premise that the same cross-sectional area is shown in Figure 7. The failure modes of the specimens are shown in Figure 8.

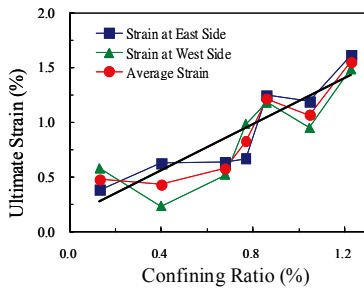


Fig. 7. Ultimate strain related to confining ratio

Conclusions

Eleven full-scale RC columns with different retrofit schemes have been tested in this study. The proposed CFRP anchors have been proven to provide additional confinement thus improve the axial strength and ductility of the RC columns. The results are helpful in developing a numerical model based on the contribution of confinement. Further researches on RC components retrofitted using CFRP wrapping and CFRP anchors will be continued to develop and refine the mechanical theorem and modified design criteria.

References

Tsai, K. C., and Lin, M.L., "Steel Jacket Retrofitting of Rectangular RC Bridge Columns to Prevent Lap Splice and Shear Failures," National Center for Research on Earthquake Engineering, Report No. 02-015, 2002a.

Tsai, K. C., and Lin, M.L., "Seismic Jacketing of RC Columns for Enhanced Axial Load Carrying Performances," National Center for Research on Earthquake Engineering, Report No. 02-016, 2002b.

Lin, M.L., Chen, P.C., Tsai, K. C., and Wu, Y.H., "Retrofit Tests on RC Columns Subjected to High Axial Force and Reverse-Curvature Moment," National Center for Research on Earthquake Engineering, Report No. 08-025, 2008.

Lin, M.L., Lin, C.T., Chen, P.C., Tsai, K.C., and Wu, Y.H., "Seismic Retrofit of Rectangle RC Columns Using CFRP Wrapping and CFRP Anchors," National Center for Research on Earthquake Engineering, Report No. 09-014, 2009.

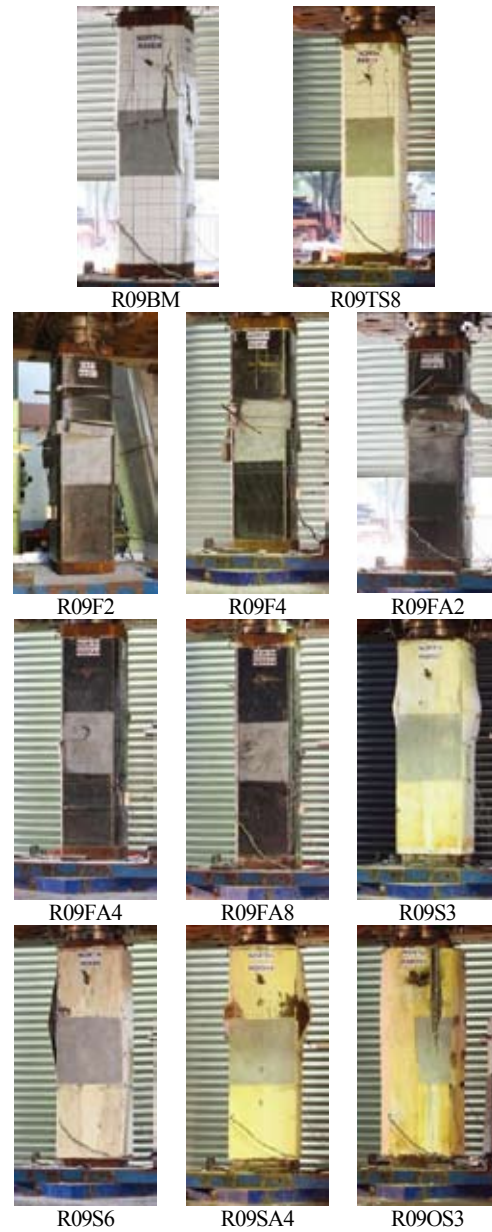


Fig. 8. Failure patterns of specimens

Inelastic Response Spectra for Two-Way Asymmetric-Plan Structures under Bi-Directional Ground Excitations

Jui-Liang Lin¹, Keh-Chyuan Tsai² and Wen-Chia Yang³

林瑞良¹、蔡克銓²、楊文嘉³

Abstract

It has been found that any one vibration “mode” of an inelastic multi-story asymmetrical building structure can be represented by a 3DOF modal system representing two modal translations and one modal rotation. This study introduces the inelastic response spectra, constructed from the inelastic 3DOF modal systems, specifically useful for multi-story two-way asymmetric-plan buildings subjected to bi-directional ground excitations. These spectra for asymmetrical structures are abbreviated as SAS. SAS provides the three-component inelastic peak modal responses of multi-story two-way asymmetric-plan buildings subjected to bi-directional ground excitations. In order to construct SAS, the independent elastic parameters of the 3DOF modal systems were identified and the inelastic 3DOF modal parameters versus the strength ratio relationships were established. The parametric study of the 3DOF modal parameters showed the ranges, the variation trends of these parameters.

Keywords: inelastic response spectra, asymmetric-plan structures, modal systems, modal response spectrum analysis

Introduction

Theoretically, vibration modes only exist in the elastic systems. Thus, the elastic dynamic structural responses can be conveniently computed by the modal analysis, combining all or the dominant modal responses using either modal response history analysis or modal response spectrum analysis procedures. Nevertheless, the pushover analysis is widely adopted by earthquake engineering researchers and practitioners. It often uses the first elastic modal properties of the original structure to relate the original MDOF system's base shear versus roof displacement response into the equivalent SDOF system response (ATC-40 1996). Chopra and Goel (2004) further proposed the modal pushover analysis (MPA) procedure, suggesting the feasibility of using more modes than just the first mode in the pushover analysis. Then, several dominant peak modal responses can be combined using procedures such as the SRSS or CQC combination rules to incorporate the

higher “modes” effects into the overall inelastic structural response computations. The peak modal responses can be obtained directly from the inelastic response history analysis of the corresponding “modal” systems. Or, it can be indirectly computed from using the inelastic response spectra through certain iteration process (ATC-40 1996). The pushover analyses suggested by ATC-40 and Chopra and Goel (2004) have been well investigated and adopted. It indicates that the inelastic structural responses can be estimated by considering either one “mode” or several “modes” of vibration.

While a two-way asymmetric-plan building pushed by using its modal inertia force vector, there are two base shears versus two roof translations and one base torque versus one roof rotation relationships simultaneously available (Lin and Tsai 2008). It has been confirmed that the stated three force-deformation curves presented in the acceleration-displacement-response-spectra (ADRS) format overlap when the original building is elastic.

¹ Associate Researcher, National Center for Research on Earthquake Engineering, jllin@ncree.narl.org.tw.

² Professor, Department of Civil Engineering, National Taiwan University, kctsai@ntu.edu.tw

³ Assistant Researcher, National Center for Research on Earthquake Engineering, wcyang@ncree.narl.org.tw.

However, these three pushover curves are very likely bifurcated when the original building becomes inelastic. This bifurcation is due to the non-proportionality between roof translations and roof rotation, which is a rather common physical phenomenon for inelastic asymmetric-plan building systems. Obviously, the SDOF modal system is only capable of describing one of the three force-deformation relationships. Thus, when the conventional inelastic response spectrum constructed from the SDOF modal systems is used to predict the seismic responses of an inelastic multi-story two-way asymmetric-plan structure, there would be no available information about the responses in the other two directions. Or otherwise, the responses in the other two directions may be inappropriately estimated if the same inelastic response spectrum is utilized. It is obvious that the more difference between these three pushover curves, the more errors in the prediction of the responses in the other two directions using the same response spectrum. Furthermore, the peak responses shown in the conventional inelastic response spectra are obtained without considering the translation-rotation interaction effects. The existence of the translation-rotation interaction effects in each vibration mode of asymmetric-plan structures will be demonstrated in the study. On the other aspect, the conventional inelastic response spectra are only applicable to structures under the excitation of one-component of ground motions. These issues in the application of the conventional inelastic response spectra arises from the fact that SDOF modal systems are incapable of simultaneously describing the three force-deformation relationships in each “vibration mode” of an inelastic two-way asymmetric-plan building.

In order to simultaneously describe the three force-deformation relationships of the original multi-story two-way asymmetric-plan building when it is pushed by using its modal inertia force vector, the three-degree-of-freedom (3DOF) modal system has been developed (Lin and Tsai 2008). The stated three force-deformation relationships are two roof translations versus two roof rotations relationships and one roof rotation versus one base torque relationship. It has been demonstrated that the elastic 3DOF modal system itself exhibits only one vibration mode, and the other two vibration modes are spurious, i.e. no any effect to its elastic dynamic responses. Thus, the elastic 3DOF modal system actually represents one single vibration mode of an elastic multi-story two-way asymmetric-plan building. Furthermore, the properly constructed inelastic 3DOF modal system can satisfactorily describe the bifurcation phenomenon observed in the pushover curves of the original multi-story two-way asymmetric-plan building when it is pushed by using its modal inertia force vector.

With the aim dealing with the aforementioned issues arising from using the conventional inelastic response spectra, the objective of this study is to

develop a new type of inelastic response spectra constructed from the 3DOF modal systems. It will be demonstrated that such a new type of inelastic response spectra can effectively predict the peak responses in the three directions for each vibration mode of the multi-story two-way asymmetric-plan buildings under the bi-directional ground excitations. In order to construct the new type of inelastic response spectra for asymmetrical structures (referred to as SAS hereafter), three prerequisite key tasks are completed. These three key tasks are 1) the identification of the independent elastic 3DOF modal parameters, 2) the establishment of the relationships between the strength ratio and the inelastic 3DOF modal parameters and 3) the verification of the ranges of the 3DOF modal parameter values.

Key parameters of the 3DOF Modal System

In order to construct SAS, it is necessary to identify the independent elastic 3DOF modal parameters as well as establish the relationships between the strength ratio and the inelastic 3DOF modal parameters. The results are briefly stated as follows.

The independent elastic 3DOF modal parameters are vibration period T_n , frequency ratios $\Omega_{\theta xn}$, $\Omega_{\theta zn}$, modal eccentricity e_{xn} and the normalized modal eccentricity ratio $|e_{zn}|/r_{xn}$. Given the values of these five elastic 3DOF modal parameters, all the other elastic 3DOF modal parameters can be determined by using Eqs. 1, 2 and 3 shown as follows:

$$\Omega_{\theta xn} = \sqrt{\left(1 + \frac{m_{xn}}{I_n} e_{zn} - \frac{m_{zn}}{I_n} e_{xn}\right) (1 - e_{zn})} \quad (1)$$

$$\Omega_{\theta zn} = \sqrt{\left(1 + \frac{m_{xn}}{I_n} e_{zn} - \frac{m_{zn}}{I_n} e_{xn}\right) (1 + e_{xn})}$$

$$T_n = \frac{T_{xn}}{\sqrt{1 - e_{zn}}} = \frac{T_{zn}}{\sqrt{1 + e_{xn}}} \quad (2)$$

$$m_{xn} + m_{zn} + I_n = 1 \quad (3)$$

The relationships between the strength ratio and the inelastic 3DOF modal parameters are shown as Eq. 4. That is, given the strength ratio, all the yielding moments of the three rotational springs in a 3DOF modal system can be determined by using Eq. 4.

$$M_{yxn} = \frac{S_{dn}^{elastic}}{R} (-1 + e_{zn}) k_{xn} \quad (4a)$$

$$M_{yzn} = \frac{S_{dn}^{elastic}}{R} (1 + e_{xn}) k_{zn} \quad (4b)$$

$$M_{y\theta n} = \frac{S_{dn}^{elastic}}{R} k_{\theta n} \quad (4c)$$

Bi-directional Ground Excitations

The synthetic ground excitation, i.e. $\Gamma_{xn}\ddot{u}_{gx} + \Gamma_{zn}\ddot{u}_{gz}$, shown at the right hand side of the 3DOF modal equation of motion indicates that the modal participation factors are involved. Thus, the specification of the bi-directional ground excitation for constructing SAS is different from that for constructing conventional response spectra. To get dimensionless coefficients, the synthetic ground excitation is further expressed as $\lambda(\gamma_{xn}\ddot{u}_{gx} + \gamma_{zn}\ddot{u}_{gz})$, where

$$\lambda = \sqrt{\Gamma_{xn}^2 + \Gamma_{zn}^2} \tag{5a}$$

$$\gamma_{xn} = \frac{\Gamma_{xn}}{\sqrt{\Gamma_{xn}^2 + \Gamma_{zn}^2}} = \frac{\sum_{j=1}^N \phi_{xn,j} m_{xj}}{\sqrt{\left(\sum_{j=1}^N \phi_{xn,j} m_{xj}\right)^2 + \left(\sum_{j=1}^N \phi_{zn,j} m_{zj}\right)^2}} \tag{5b}$$

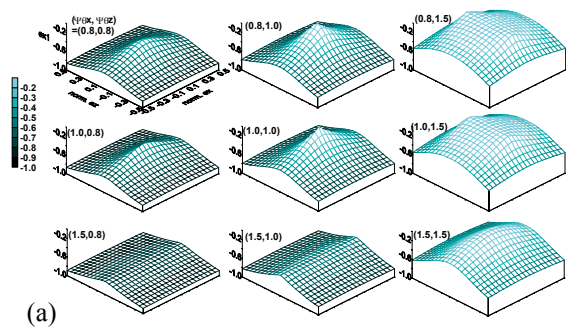
$$\gamma_{zn} = \frac{\Gamma_{zn}}{\sqrt{\Gamma_{xn}^2 + \Gamma_{zn}^2}} = \frac{\sum_{j=1}^N \phi_{zn,j} m_{zj}}{\sqrt{\left(\sum_{j=1}^N \phi_{xn,j} m_{xj}\right)^2 + \left(\sum_{j=1}^N \phi_{zn,j} m_{zj}\right)^2}} \tag{5c}$$

Equations 5b and 5c indicate that the γ_{xn} and γ_{zn} can be regarded as the ratios of the earthquake load resulting from the n -th vibration mode subjected to a single directional ground excitation to that being subjected to the bi-directional ground excitation when $\ddot{u}_{gx}(t)$ is the same as $\ddot{u}_{gz}(t)$. The γ_{xn} and γ_{zn} are referred to as the n -th modal excitation ratios in the X- and Z-directions, respectively. λ is a scaling factor. When the peak 3DOF modal responses are presented in terms of the corresponding peak elastic responses, λ vanishes and only γ_{xn} and γ_{zn} remain as the parameters required for the specification of bidirectional ground excitations.

Parametric study

The inelastic response spectra for two-way asymmetric-plan buildings can be constructed by using the 3DOF modal systems if the values of e_{xn} , $|e_{xn}|/r_{xn}$, $\Omega_{\theta xn}$, $\Omega_{\theta zn}$, α_{xn} , α_{zn} , $\alpha_{\theta n}$, R , γ_{xn} , γ_{zn} and the damping ratio ξ_n are given. The ranges of the values of strength ratio, R , and damping ratio, ξ_n , have been widely studied. However, the ranges of the values of e_{xn} , $|e_{xn}|/r_{xn}$, $\Omega_{\theta xn}$, $\Omega_{\theta zn}$, α_{xn} , α_{zn} , $\alpha_{\theta n}$, γ_{xn} and γ_{zn} are not clear. The study of the conventional response spectra only became meaningful after the ranges of the associated parameter values were well understood. Therefore, the goal of this section is to study the

ranges of the values of e_{xn} , $|e_{xn}|/r_{xn}$, $\Omega_{\theta xn}$, $\Omega_{\theta zn}$, α_{xn} , α_{zn} , $\alpha_{\theta n}$, γ_{xn} and γ_{zn} . Since parametric studies on elastic one-story asymmetric-plan buildings have been extensively conducted in the past, the ranges of the whole-structure parameter values for one-story systems are already available. In order to know the common values of the mentioned 3DOF modal parameters, their variations with respect to the changes of the whole-structure parameters for one-story asymmetric-plan buildings are investigated as follows. Figure 1 illustrates the variation of the values of the first modal eccentricities, i.e. e_{x1} , e_{z1} , of the one-story systems with an aspect ratio β equal to 0.5. In the figure, there are nine 3-dimensional plots representing the nine combinations of $\Psi_{\theta x}$ and $\Psi_{\theta z}$. The two abscissa of each plot are the values of \bar{e}_x and \bar{e}_z ranging from -0.5 to 0.5. In general, the surfaces representing the values of e_{x1} and e_{z1} look like concave or convex domes. Figure 1a shows the values of e_{x1} are always larger than -1. In addition, Fig. 1b shows the values of e_{z1} are always less than 1. Figure 1 evidently shows that the values of e_{x1} and e_{z1} increase as the frequency ratio $\Psi_{\theta z}$ increases. On the other hand, the values of e_{x1} and e_{z1} decrease as the frequency ratio $\Psi_{\theta x}$ increases. Figure 1 also shows that the variation for the values of e_{x1} and e_{z1} is more sensitive to the change of the normalized eccentricity \bar{e}_z than to the change of \bar{e}_x . Since the values of e_{x1} and e_{z1} are negative and positive, respectively (Figs. 1a and 1b), it clearly indicates that the first modal vibration period of a one-story system is elongated when compared with the X- and Z-translational vibration periods of the corresponding uncoupled one-story system. On the other hand, since the values of e_{x3} and e_{z3} are positive and negative, respectively (not shown in this paper), it indicates that the third modal vibration period of a one-story system is shortened when compared with the X- and Z-translational vibration periods of the corresponding uncoupled one-story system.



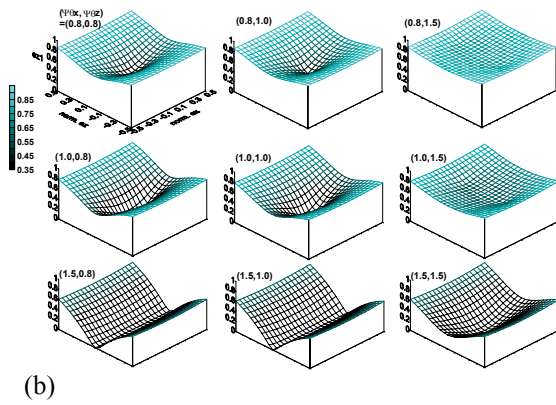


Fig. 1. The first modal eccentricities, (a) e_{xl} and (b) e_{zl} , of the one-story two-way asymmetric-plan buildings with aspect ratio $\beta=0.5$.

Selected Modal Parameter Values and Ground Motion Records

To sum up, there are 50 values of T_n , 3 values of $\Omega_{\theta xn}$, 3 values of $\Omega_{\theta zn}$, 2 values of $|e_{xn}|/r_{xn}$, 2 values of e_{xn} , 2 values of γ_{xn} , 2 values of R , 3 cases of the combinations of α_{xn} , α_{zn} and $\alpha_{\theta n}$ when $e_{xn} = -0.75$, and 6 cases of the combinations of α_{xn} , α_{zn} and $\alpha_{\theta n}$ when $e_{xn} = 6$. Therefore, there are a total of 32400 ($=50 \times 3 \times 3 \times 2 \times 2 \times (3+6)$) 3DOF modal systems have been considered in this study. Applying 40 pairs of ground motion records, it requires 1296000 ($=32400 \times 40$) times of nonlinear response history analyses.

Spectra for Asymmetric Structures

Figure 2 shows the mean ductility response spectra for the strength ratio equal to 3 and 6. Moreover, the mean values plus one standard deviation are also shown in Fig. 2. It is obvious that the ductility values approach the strength values when the vibration period is very large, which is the same as that observed in the conventional response spectra. Figure 2 shows that the three components of the mean ductility demands for $R = 3$ are close, i.e. $\mu_{xn} \approx \mu_{zn} \approx \mu_{\theta n}$. Nevertheless, μ_{xn} , μ_{zn} and $\mu_{\theta n}$ are quite different for $R = 6$. This implies that the conventional response spectra gradually become inadequate as the strength ratio increases. That is, it is insufficient to use a SDOF modal system for estimating the three different modal ductility demands of a substantially inelastic asymmetric-plan building. From the mean value plus one standard deviation (Fig. 2), it shows that the dispersion of the ductility demands as $R = 6$ is larger than that of $R = 3$. In short, the ductility demand as $R = 6$ is more sensitive to the variation of the 3DOF modal parameter values than the ductility demands as $R = 3$ are. Figure 2 also shows that the deviation of μ_{zn} is significantly larger than those of μ_{xn} and $\mu_{\theta n}$. This is because there are four selected values of α_{zn} widely ranging from -0.2 to

0.35. However, there are only one and two selected values of α_{xn} ($=0.05$) and $\alpha_{\theta n}$ ($=0.08$ and 0.3), respectively.

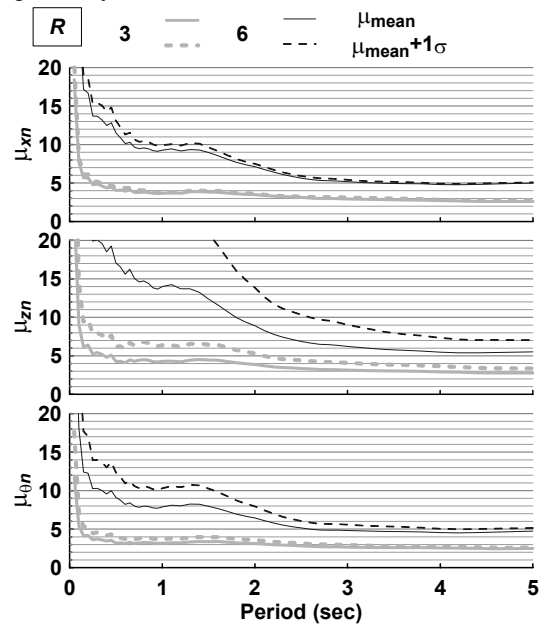


Fig. 2. The mean and the mean plus one standard deviation of the constant-strength SAS for all considered 3DOF modal systems under the excitation of the 40 pairs of ground motion records

Conclusions

For two-way asymmetric-plan buildings, the equal seismic displacement principle still holds for the three components of the modal response. As the strength ratio increases, the differences between μ_{xn} , μ_{zn} and $\mu_{\theta n}$ substantially increase at both short and intermediate vibration periods. Thus, this strongly suggests that the conventional response spectrum, which provides a same ductility demand for all three directions, would be insufficient to estimate the modal seismic demands in the three directions for inelastic two-way asymmetric-plan buildings.

References

Applied Technology Council (1996), "Seismic evaluation and retrofit of concrete buildings", *Report ATC-40*, Applied Technology Council, Redwood City, California.

Chopra, A.K. and Goel, R.K. (2004), "A modal pushover analysis procedure to estimate seismic demands for unsymmetric-plan buildings", *Earthquake Engineering and Structural Dynamics*, 33: 903-927.

Lin, J.L. and Tsai, K.C. (2008), "Seismic analysis of two-way asymmetric building systems under bi-directional seismic ground motions", *Earthquake Engineering and Structural Dynamics*, 37, 305-328.

Study on the Earthquake Damage Evaluation for RC Framed Buildings and on the School Building Damage Database

Yi-Hsuan TU¹, Lai-Cheng AO², and Wen-Yu JEAN³

杜怡萱¹、區麗貞²、簡文郁³

Abstract

Data collection is an important work in the earthquake reconnaissance. This paper aims at establishing an earthquake damage evaluation procedure that is objective and easy to use for low-rise RC and confined masonry buildings. Several current damage evaluation standards were reviewed and summarized to determine the evaluation factors. The relationships between evaluation factors and damage conditions were discussed by applying the presented procedure to three in-situ test specimens. The ability to distinguish medium damage states of the procedure was also verified by using the data of 10 school buildings damaged during recent moderate earthquakes. Twelve professionals with different backgrounds were asked to evaluate the damage state of the buildings with both their subjective judgment and the presented procedure. It was found that the damage state determined by the presented procedure showed less dispersion and stricter result than the subjective judgments.

Keywords: earthquake damage; damage evaluation; reinforced concrete; confined masonry.

Introduction

Making observations and keeping records of the damage and effects following a disaster are critical to managing emergency response activities in the short term and improving the understanding of natural hazards in the long term (<http://www.eeri.org/site/life-introduction>). Damage data has been widely used in earthquake-related researches, such as seismic assessment, loss estimation, and establishment of vulnerability function. The ATC-13 report (ATC, 1985) presented a methodology for estimating earthquake damage/losses by using existing damage data from California. However, it is usually difficult to apply the damage data out of the region where it was originally collected. The difficulty comes not only from the difference in structural characteristics of the building culture in different areas, but also from the difference in description and definition of damage. The definition of damage can be qualitative or quantitative, chosen by the research subjectively. Qualitative damage state could be simply expressed as

damaged/collapsed or subdivided into several discrete levels; quantitative damage index might be defined as cost/number/range of repair/replacement for individual building or the percentage for a category of buildings. A workshop hosted by EERI on collection & management of earthquake data (EERI, 2003) identified the needs of improving data collection, access, organization, and use. Creating a data dictionary so that different professions can use the same language to describe the same concept and defining guidelines for the collection process are included in the major issues drawn for data collection.

The authors have been establishing a databank for school buildings damaged during the Chi-Chi earthquake and studying on the motion-damage relationship by using the databank (Tu et al. 2009). A typical five-level qualitative standard, including slight, light, moderate, severe damage and collapse, was used to define the damage state of each building from the databank. However, it was found that the damage states of some buildings are questionable since the

¹ Assistant Professor, Department of Architecture, National Cheng Kung University, Taiwan, e-mail: yhtu@mail.ncku.edu.tw

² Master, Department of Architecture, National Cheng Kung University, Taiwan

³ Researcher, National Center for Research on Earthquake Engineering, wychien@ncree.narl.org.tw

original ones were made by subjective judgment. The relationship between damage state and the seismic capacity of a building is also unclear, causing uncertainties when the data is used for comparison with analytical models. Therefore, this research aims at establishing a new earthquake damage evaluation procedure for low-rise RC and confined masonry buildings. The presented procedure is expected to redefine the damage states with objective and clear languages, so that the error caused by subjective judgment can be reduced.

The Damage Evaluation Procedure

Several existing damage evaluation standards [1-3] for RC and confined masonry buildings were reviewed and compared. The damage evaluation is usually composed by two parts: the factors that describe the damage and the procedure that weighs the factors and determines the global damage state. Most damage evaluation standards use qualitative descriptions to define damage states. In some standards, quantitative factors, such as crack width or residual story drift are also used. The values of quantitative factors and the choice of qualitative factors were compared. Details of the comparison can be found in the master thesis of Ao (2010).

The number of damage states is not identical in every standard. However, 5-level is the most frequently used one, including in the EERI procedure (1996). The vertical members (RC columns/walls and masonry walls) are usually the major objects for evaluation. The reason might be their importance of vertical and horizontal load resisting. Vertical members are also easier to be observed, comparing to the beams that usually hide in ceilings.

In basis of the review, a new damage evaluation procedure was designed as a detailed evaluation that only applies to the most severely damaged members. The evaluation factors and procedure were integrated into a single form that can be printed on an A4-size paper. The evaluation factors were divided with main elements, including non-structural elements, RC beams/columns, masonry walls, and RC walls. Damages to non-structural elements were also considered in the evaluation for slight to moderate damage states.

Comparison with In-Situ Test

The presented evaluation procedure was applied to three specimens of in-situ push-over tests for school buildings by the National Center for Research on Earthquake Engineering (NCREE), including Kouhu elementary school (Jaung et al. 2008), Reipu elementary school (Chung et al. 2007), and Guanmiao elementary school (Chiou et al. 2008). The purpose of the comparison was to study the relationships between the evaluation factors and the capacity curves of the specimens and to check if the factors refer to the same damage states appear closely in the experimental damage progress. However, the crack width was not checked in the comparison. Because the crack width in the in-situ tests was observed when the specimens were under loading, it should be wider than the post-earthquake crack width and was not referable. Also, all the specimens were confined masonry buildings. Therefore, the factors of RC walls had no chance to be checked.

Figure 1 shows the relationships between the evaluation factors and the capacity curves of the in-situ specimens. For each evaluation factors, marks

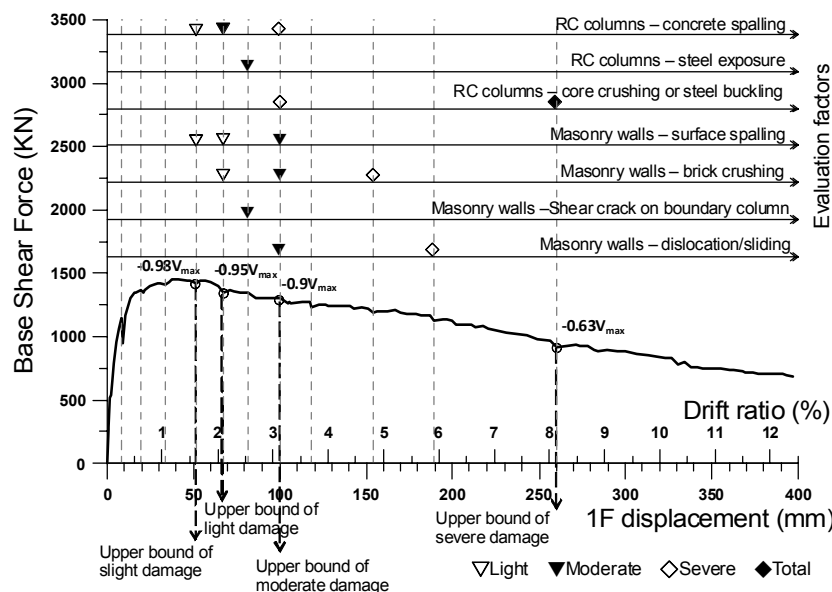


Figure 1. Relationships between the evaluation factors and the capacity curves of the in-situ specimens (Guanmiao elementary school)

Table 1. The base shear corresponding to damage states

Specimen \ Damage states	Upper bound of slight damage	Upper bound of light damage	Upper bound of moderate damage	Upper bound of severe damage
Kouhu elem. school	—	+0.92 V_{max}	- 0.65 V_{max}	—
Reipu elem. school	+0.96 V_{max}	V_{max}	- 0.97 V_{max}	- 0.77 V_{max}
Guanmiao elem. school	- 0.98 V_{max}	- 0.95 V_{max}	- 0.90 V_{max}	- 0.63 V_{max}

V_{max} : Maximum base shear

that represent different damage states (light/moderate/severe/total) were put along the drift/displacement axes where the damage conditions corresponding to the levels in the evaluation form were observed. The figures were supposed to be capable of determining the positions of the overall damage states, as the dotted lines show. For example, the first mark that represents severe damage appeared at the drift ratio of 2.86% in the Kouhu elementary school specimen (Figure 2(a)), meaning that the specimen stepped from moderate damage into severe damage at this drift. However, since the crack width factors were not considered in the evaluation, the determined damage state should be conservative. In other words, the determined damage states might appear earlier if the crack width was evaluated. Therefore, the dotted lines actually represent the possible upper bound of the damage states.

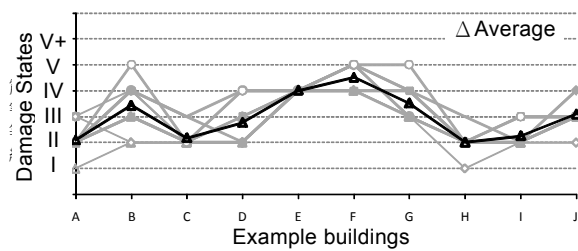
The marks that represent the same damage states were close to each other for the test results. The distributions of marks were reasonable. However, the positions of the damage states were found to be later than expected. Table 1 shows the base shear corresponding to the boundaries of damage states. The positive and negative values mean that it appeared before and after the maximum base shear, respectively. It indicated that the boundary between light and moderate damage states approximately corresponds to the maximum base shear. However, as mentioned above, the result might be conservative since the crack width was not considered in the evaluation.

Verification with Damaged Buildings

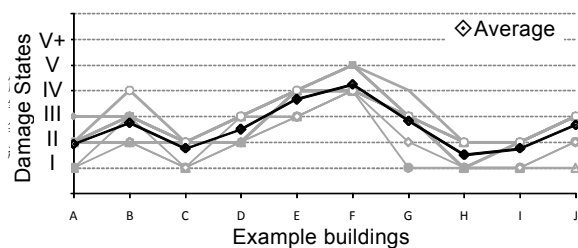
Ten school buildings damaged in recent moderate earthquake occurred in Taiwan were chosen as the examples for evaluation. Twelve professionals of architecture and structure engineering, including 3 architects, 3 structural engineers, and 6 researchers, were asked to evaluate the examples with provided damage pictures. Provided the presented evaluation forms, the evaluators were asked to check the boxes of the factors that correspond to their observation, but determine the overall damage state by their subjective judgments. After the forms were retrieved, another overall damage state was determined in accordance with the checked factors following the presented procedure. Figure 2 shows the comparison between the form-determined damage states and the

subjectively judged ones.

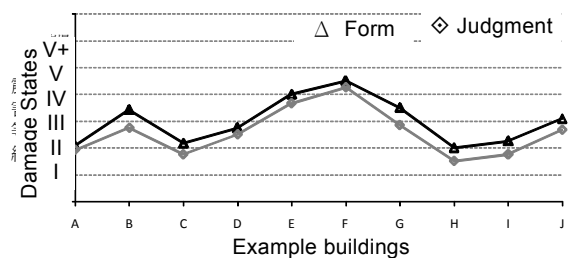
The grey lines in Figures 2(a) and 2(b) show the individual results and the black lines represent the average. There were obvious individual differences in both form-determined and subjectively judged damage states, but the form-determined results were more concentrated to one damage state than the subjectively judged results. The individual differences in form-determined results indicated that there might still be misinterpretation for the evaluation factors or the damage pictures provided. The averages of the two results were very close and the form-determined one was lightly stricter, as shown in Figure 2(c). Although the verification was made from a limited number of



(a) The form-determined damage states



(b) The subjectively judged damage states



(c) Comparison between average form-determined and average subjectively judged damage states

Figure 2. The comparison between form-determined and subjectively judged damage states

examples and evaluators, it suggested that the presented procedure is at least as efficient as the subjective judgment in distinguishing the medium damage states. Further detailed result and discussion can be found in the master thesis of Ao (2010).

Damaged School Building Database

Based on the proposed seismic damage evaluation procedure, the damage states of previous established databank of seismic damaged school buildings were revised. Six school buildings damaged during the 2009/11 Nantou ML6.2 earthquake were also added into this database. The number of seismic damaged school building database is 163. Among these, 74 building's damage states were revised. According to the shake-map estimation procedure proposed by NCREE, the PGA values were provided for each school building in both horizontal directions along the corridor and transverse to the corridor. This database should be variable for the studies on the fragility and seismic assessment for the low rise RC (school) buildings.

Conclusions

A new earthquake damage evaluation procedure is presented in this paper. On the basis of a review of the existing standards, the procedure was designed to be a simple evaluation form. The overall damage state, which was basically divided into 5 levels as in most standards, can be determined in few minutes by checking the evaluation factors corresponding to observed damage. In order to reduce the error from subjective judgment, the evaluation factors were expressed by quantitative values and concise qualitative words with clear definition.

The presented procedure was applied to three specimens of in-situ push-over tests for school buildings to study the relationships between evaluation factors and the capacity curves of the structures. The distributions of evaluation factors were found to be reasonable. However, the corresponding positions of the damage states on the capacity curves were later than expected. The capability of distinguishing the medium damage states of the procedure was also verified by using the data of 10 school buildings damaged during recent moderate earthquakes. Twelve professionals with different backgrounds were asked to fill the presented evaluation form and evaluate the damage state subjectively for the example buildings. The averages of the form-determined and subjectively judged results were found to be very close and the form-determined one was lightly stricter. It suggested that the presented procedure is applicable and efficient.

References

- Anagnostopoulos, S. and Moretti, M. (2008), Post-earthquake emergency assessment of building damage, safety and usability Part1: Technical issues, *Soil Dynamics and Earthquake Engineering*, **28**(3), 223-232.
- Ao, L. C. (2010), *Improvement of Earthquake Damage Evaluation Procedure for RC and Confined Masonry Buildings*, Master thesis, Department of Architecture, National Cheng Kung University, Tainan, Taiwan.
- Japan Building Disaster Prevention Association (1991), *Damage Evaluation Standard and Technical Instructions for Retrofit of Buildings Damaged by Earthquake (RC buildings)*, Japan Building Disaster Prevention Association, Tokyo. (in Japanese).
- Jean, W. Y., Lien, K. H., Chang, Y. W., Chung, L. L., and Hwang, S. J. (2008), The Fragility of Low-rise RC School Buildings in Taiwan, *Proceedings of the 9th National Conference on Structure Engineering*, Kaohsiung, Taiwan, Aug. 22-24, paper no. L-0289. (in Chinese).
- Tu, Yi-Hsuan, Lai-Cheng Ao, and Wen-Yu Jean (2010), Study on the Earthquake Damage Evaluation Procedure for RC and Confined Masonry Buildings, *Proceedings of the Twelfth Japan-Korea-Taiwan Joint Seminar on Earthquake Engineering for Building Structures (SEEBUS 2010)*, pp. 173-182, Kaohsiung, Taiwan, Nov. 26-27, 2010

Verification of Detailed Seismic Evaluation Method Using 921 Seismic Damage Records of School Buildings

Yeong-Kae Yeh¹, Fu-Pei Hsiao² and Li-Ming Tseng³

葉勇凱¹、蕭輔沛²、曾立明³

Abstract

Earthquakes are very common in Taiwan. In the past few large earthquakes, serious damages in school buildings were observed. Because of that, the National Center for Research on Earthquake Engineering (NCREE) has developed a detailed seismic evaluation method based on the nonlinear pushover analysis in selecting school buildings that need to be retrofitted. From 2005 to 2007, a series of *in situ* tests of school buildings has been performed by NCREE. The test results can be used to verify the accuracy of the nonlinear pushover analyses conducted. The 921 Earthquake's seismic damage database of school buildings in Nantou County has been established also at the research center. These damage data can be used to verify the detailed seismic evaluation method. In this report, the detailed seismic evaluation method for school buildings developed by NCREE will be discussed and verified using the real seismic damage data of school buildings in the 921 Earthquake.

Keywords: school buildings, detailed seismic evaluation, 921 Earthquake seismic damage database of school buildings

Introduction

Taiwan is located at the Circum-Pacific seismic zone. The occurrence of earthquakes has become part of the lives of the people in the island. In this, seismic capacities of school buildings are very important to ensure the safety of many teachers and students. As such, seismic upgrading of existing school buildings is an urgent relevant issue being done by the government. Because of the large number of elementary and secondary school buildings, and the limited budget and time for possible retrofitting, it is only necessary to set up a reasonable seismic evaluation and retrofit procedure. School buildings with insufficient seismic capacities must be identified and demolished or retrofitted.

Detailed seismic evaluation method is the last step to evaluate the seismic capacities of school buildings, thus the said method needs to have enough screening ability and safety factors. If the method is too conservative, school buildings with insufficient

seismic capacities can not be identified properly. If the method does not have enough safety factors, school buildings with insufficient seismic capacities may not get suitable retrofits.

NCREE has already developed a detailed seismic evaluation method for school buildings (Yeh *et al.*, 2009) and has provided a technology handbook (Chung *et al.*, 2009) to professional engineers. In this report, the detailed seismic evaluation method for school buildings developed by NCREE is further discussed and is verified by real seismic damage data of school buildings in the 921 Earthquake. The results show that the NCREE's established detailed seismic evaluation method has certain safety factor.

Detailed Seismic Evaluation Method

NCREE's detailed seismic evaluation method adopted the Capacity Spectrum Method of ATC-40 (ATC 1996) and suggested a set of nonlinear hinge properties of RC beams, columns, walls and brick

¹ Research Fellow, National Center for Research on Earthquake Engineering, ykyeh@ncree.narl.org.tw.

² Associate Research Fellow, National Center for Research on Earthquake Engineering, fphsiao@ncree.narl.org.tw.

³ Master, Department of Civil Engineering, Chung Yuan Christian University.

walls. By using structural analysis software, the nonlinear pushover analysis can be performed and the capacity curve of the building can then be constructed. The capacity curve can be transformed into a capacity spectrum and the performance curve can be set up consequently. After, according to the performance demand of the building, the peak ground acceleration (PGA) of the earthquake which the target building can sustain will be determined. If the computed PGA value is less than the PGA of the 475-year design earthquake, it means that the target building does not have enough seismic capacity and thus needs to be retrofitted. Otherwise, the target building has proven enough seismic capacity.

The capacity curve of a building represents its lateral load capacity and nonlinear displacement ability. The nonlinear behaviors of a building are produced by the nonlinear hinges of its structural elements. As the reinforced concrete (RC) column is subjected to lateral load, three damage modes may exist, *i.e.* flexural damage, flexural-shear damage and shear damage modes. These damage modes are dependent on the length-to-width ratio, material strength and reinforcement details of the column. The flexural-shear damage mode is frequently observed on the non-ductile columns of old existing school buildings. Because the column's inflection point position changes during the nonlinear deformation process of the structure, the damage mode can not be determined before the nonlinear analysis. In this, the moment hinges need to be set at both ends of the column to achieve possible flexural or flexural-shear damage mode, and the shear hinges need to be set at the center of the column to achieve possible shear damage mode.

The capacity spectrum assumes that every point at the curve is the response of an equivalent elastic system. This elastic system uses the secant stiffness of the curve as its equivalent stiffness and has its equivalent period and damping ratio. The response of this elastic system can be specified through the capacity spectrum. There exist relationships between capacity curve and capacity spectrum.

NCREE's detailed seismic evaluation method does not need an iteration procedure. Every performance point at the capacity spectrum is the intersection of capacity spectrum and design spectrum. The PGA of the design spectrum is identified as the performance ground acceleration. The relationship curve of the performance ground acceleration and the spectrum displacement or roof displacement is the so-called seismic performance curve.

According to the laboratory and *in situ* school building structural test results, NCREE has observed the damage conditions and the corresponding capacity curves from lateral pushover tests in defining the seismic performance demand of school buildings under the 475-year design requirement. For the

generally used school buildings, the life safety of teachers and students is the most concerned during an earthquake. As such, the seismic performance demand is aimed to limit the damage condition below moderate damage state. With the capacity curve, the strength criterion is that the allowable base shear must be smaller than the maximum base shear of the capacity curve, and the displacement criterion is that any inter-storey drift must be smaller than 2%. And to avoid local structural collapse, none of the load-bearing elements must lose their axial strength capacities. According to the seismic performance demand, the allowable roof displacement can be specified at the capacity curve, and the performance ground acceleration can be specified at the seismic performance curve.

921 Earthquake School Buildings' Damage Records and Detailed Seismic Evaluation Analyses

NCREE has undertaken a project that aimed to investigate the seismic data of damaged school buildings in the midland of Taiwan in the 921 Chi-Chi Earthquake. The collected structural drawings and school building damage records in the project established the "Chi-Chi Earthquake Damage Database of School Buildings in the Midland of Taiwan" (Tu *et al.*, 2007).

There are 188 secondary and elementary schools in the Nantou County and the total number of school buildings is not estimated exactly. In this database, the damage states of the damaged school buildings were classified into five levels.

In the damage database, there are 35 school buildings with enough materials such that NCREE was able to build their detailed seismic evaluation models. These buildings' damage states include micro damage (in 11 buildings), small damage (in 9 buildings), moderate damage (in 3 buildings), serious damage (in 7 buildings) and collapse damage (in 5 buildings).

The moderate damage state is almost equal to the seismic performance demand of the generally used school buildings. Thus, if the performance ground acceleration and the site peak ground acceleration of the 475-year design earthquake for each level of damage states are compared, the screening ability of the proposed detailed seismic evaluation method can be verified. For the school buildings which damage level are higher than or equal to moderate damage state, their performance ground acceleration should be less than the code's required site peak ground acceleration.

CDR is defined as the ratio of the seismic capacity of a school building to its seismic demand. The seismic capacity of a school building is defined as its performance ground acceleration, and the seismic

demand is defined as the site peak ground acceleration of 475-year design earthquake. If the CDR value is less than one, it means the school building does not have enough seismic capacity and needs to be retrofitted. From the detailed seismic evaluation results of the damaged school buildings, it is observed that all the school buildings with damage level higher than or equal to the moderate damage state have CDR values less than one. It shows that the NCREE's method has an excellent screening ability to identify which school buildings need to be retrofitted. If these school buildings indeed were screened by NCREE's method and have been retrofitted before the Chi-Chi earthquake occurred, they have a great chance to avoid the damage level higher than the moderate damage state in the Chi-Chi Earthquake. As shown in Fig. 1, the average CDR value of small or micro-damaged school buildings are all larger than 1 and the CDR value tends to smaller values as the damage state becomes more serious. Therefore, according to the previous analysis, the detailed seismic evaluation method developed by NCREE can screen the school buildings to be retrofitted with damage level higher than or equal to the moderate damage state.

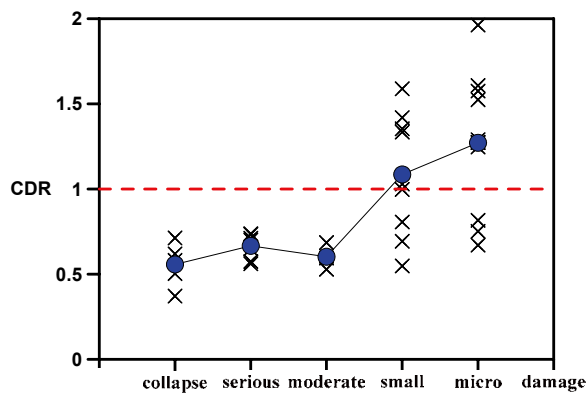


Fig. 1 Relationship of CDR and damage state

Verification of Detailed Seismic Evaluation Method of School Buildings

There are two ways to verify the detailed seismic evaluation method. One way is through the capacity curve. The other is through the performance ground acceleration. The former can be verified by the lateral pushover test data of *in situ* school buildings (Yeh *et al.*, 2008). With the nonlinear hinge properties suggested by NCREE, the capacity curves derived from nonlinear pushover analysis are more conservative than that from the lateral pushover test results. And, the latter can be verified by the damage records of school buildings in the real earthquakes.

In using the damage records of school buildings to verify the detailed seismic evaluation method, one needs to build the analysis model of the school buildings, the clear damage record descriptions, and the estimated site peak ground accelerations of the damaged school buildings. According to the database,

analysis models of 35 damaged school buildings have been built to obtain their required performance ground acceleration and corresponding damage levels. For the estimated site peak ground accelerations of the damaged school buildings during the Chi-Chi Earthquake, two estimated results were used in this report. One was estimated by Dr. Wen-Yu Chien of NCREE, and the other was estimated by Prof. Hung-Ming Chen of the National Taiwan University of Science and Technology (NTUST).

According to the seismic records of the Chi-Chi Earthquake, which were gathered at CWB's strong-motion earthquake accelerographs of the Nantou area, Dr. Chien derived the estimated site peak ground accelerations of damaged school buildings. If the estimated peak ground acceleration of the school building is smaller than its performance ground acceleration, the damage level of that school building should be less than the moderate damage state. If this statement is true, the performance ground acceleration is correctly estimated. CDR^*_1 is defined as the ratio of the performance ground acceleration of a school building to its estimated site peak ground acceleration by Dr. Chien. If the computed value is less than one, the damage level should be more serious than the moderate damage state, and the value should tend to smaller number as the damage state becomes more serious. As shown in Fig. 2, the average CDR^*_1 value of small or more seriously damaged school buildings are all smaller than one. It means that this detailed seismic evaluation method is conservative. But the relationship between CDR^*_1 and the damage level is not very clear. The CDR^*_1 values of collapsed and seriously damaged school buildings are not small enough.

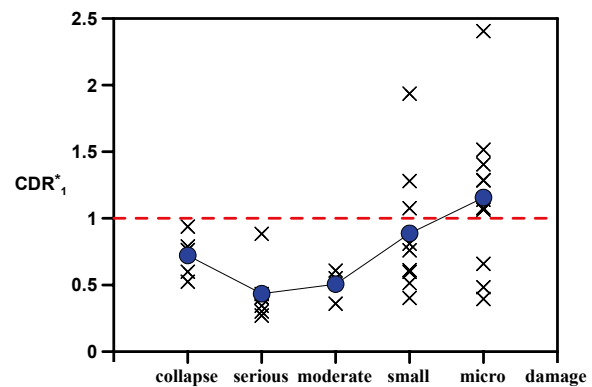


Fig. 2 Relationship of CDR^*_1 and damage state

From the peak ground accelerations of seismic records of the Chi-Chi earthquake which were gathered at CWB's strong-motion earthquake accelerographs of the Nantou area, Prof. Chen derived the estimated site peak ground accelerations of damaged school buildings. CDR^*_2 is defined as the ratio of the performance ground acceleration of a school building to its estimated site peak ground acceleration derived by Prof. Chen. If the value is found to be less than one, the damage level is

expected to be more serious than the moderate damage state, and this value should tend to smaller number as the damage state becomes more serious. As shown in Fig. 3, all the average CDR^*_2 values of damaged school buildings are smaller than one. It simply means that this detailed seismic evaluation method is very conservative. The corresponding relationship between CDR^*_2 and the damage level can be observed. The CDR^*_2 values of collapsed and seriously damaged school buildings are smaller than 0.371. Observing the damage levels, which are less than the moderate damage state and the CDR^*_2 values are larger than and close to 0.371, the safety factor can be estimated. The CDR^*_2 value of Ming-Chien Elementary School building B is 0.432 and its damage state is at moderate level. Thus, the safety factor is about 2.4 (that is the inverse of 0.432).

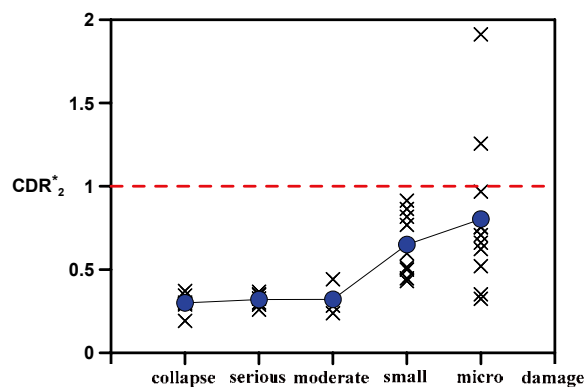


Fig. 3 Relationship of CDR^*_2 and damage state

Conclusions

This report discusses the detailed seismic evaluation method developed by NCREE to answer the following issues: 1) Does this method have the screen ability to identify the school buildings which are needed to retrofit?, 2) Does this method can estimate the damage state of damage school buildings in the earthquake?, and 3) Does this method have enough safety factor?

With the detailed seismic evaluation analyses of 35 damaged school buildings during the Chi-Chi earthquake, all the CDR values are smaller than one, if their damage levels are more serious than the moderate damage state. The evaluation method has been found to have the screening ability to identify the school buildings which needs to be retrofitted.

Based from the comparison of the performance ground accelerations and the estimated site peak ground accelerations of the damaged school buildings, the damage states were predicted conservatively. If the site peak ground acceleration is smaller than the performance ground acceleration, the damage level of that damaged school building is also less than the moderate damage state. And if the estimated site peak ground accelerations by Prof. Chen are adopted, the detailed seismic evaluation method developed by

NCREE has a safety factor of about 2.3.

References

- Applied Technology Council (ATC), (1996). *ATC-40 Seismic Evaluation and Retrofit of Concrete Buildings*, prepared by the Applied Technology Council, Redwood City, Calif.
- Chung, Lap-Loi, Yeh, Yeong-Kae, Chien, Wen-Yu, Hsiao, Fu-Pei, Shen, Wen-Cheng, Chiou, Tsung-Chih, Chow, Te-Kuang, Chao, Yi-Feng, Yang, Yao-Sheng, Tu, Yaw-Shen, Chai, Juin-Fu, Hwang, Shyh-Jiann and Sun, Chi-Hsiang, (2009). *Technology Handbook for Seismic Evaluation and Retrofit of School Buildings Second Edition*, Report NCREE-09-023, Taipei, Taiwan.
- Tu, Yi-Hsuan, Yeh, Pei-Lin and Liu, Tzu-Wei, (2007). *Chi-Chi Earthquake Damage Database of School Buildings in the Midland of Taiwan*, Report NCREE-07-023, Taipei, Taiwan.
- Yeh, Yeong-Kae, Shen, Wen-Cheng, Hsiao, Fu-Pei and Chow, Te-Kuang, (2008). *Verification of Pushover Analysis on In-Situ Test of School Buildings*, Report NCREE-08-031, Taipei, Taiwan.
- Yeh, Yeong-Kae, Hsiao, Fu-Pei, Shen, Wen-Cheng, Yang, Yao-Sheng and Hwang, Shyh-Jiann, (2009). *Seismic Evaluation of Reinforced Concrete Structure with Pushover Analysis*, Report NCREE-09-015, Taipei, Taiwan.

Seismic Upgrading Strategy for Near-Fault School Buildings

Fu-Pei Hsiao¹, Hui-Hsien Lo², Wen-Yu Jean³ and Shyh-Jiann Hwang⁴

蕭輔沛¹ 羅惠嫻² 簡文郁³ 黃世建⁴

Abstract

All types of school buildings were seriously damaged in Taiwan's 921 Chi-Chi earthquake. Seismic evaluation and retrofit of these numerous vulnerable school buildings has become an important issue to be resolved. The National Center for Research on Earthquake Engineering (NCREE), Taiwan assisted the Ministry of Education on the arrangement of programs to accelerate retrofit and rebuilding works of elementary school, junior high school, senior high school and vocational school buildings, as part of the project called, "Economic Recovery Act". Based on the database for seismic assessments and retrofits of school buildings, this study recommends a seismic upgrading procedure of near-fault school buildings. The proposed procedure can control effectively the seismic upgrading progress of near-fault school buildings. It also provides suggestions on the seismic retrofitting and reconstruction plans of near-fault school buildings to reduce damages and losses in a possible seismic event.

Keywords: school buildings, seismic evaluation, seismic retrofitting, near-fault effect

Introduction

The project entitled, "Accelerating old school buildings and related equipments' retrofitting and renovation" by the Taiwan's Ministry of Education is aimed to encourage public elementary school officials regarding the promotion of seismic evaluation and retrofit of buildings. Insufficient seismic capacities of prioritized schools require appropriate retrofitting to ensure the safety of teachers and students.

In August 2009, the Central Geological Survey of the Ministry of Economic Affairs, Taiwan has completed the investigation and identification of schools close to active earthquake faults. The survey indicates that there are 20 Holocene active faults in Taiwan (see Fig. 1). Some evidences show that these faults' activities have occurred in the last million years and the probability of future activity is relatively high. There are 39 schools whose distance from these Holocene active faults is within 100 meters, and there are 92 schools within 200 meters.

To prevent possible damages of schools near the traced active faults, the National Center for Research on Earthquake Engineering (NCREE), Taiwan held a consultation meeting to the respective school officials. The meeting initially developed principles and recommendations. The near-fault effect considered to be destructive for the school buildings is quite large. The seismic qualification criteria of school buildings near the active faults shall then be considered different from others. Moreover, the seismic retrofitting methods should also have special consideration of the schools. Project management can be recommended in these schools to reduce effectively the damages, which might be caused by the active faults.

This paper proposed a complete set of process for the examination and related seismic upgrading of schools near the traced active faults. This process can be used with current seismic evaluation and retrofitting mechanisms. It can be operated also in coordination with the results of the school seismic survey and school seismic database. It aimed to

¹ Associate Researcher, National Center for Research on Earthquake Engineering, fphsiao@ncree.narl.org.tw

² Assistant, National Center for Research on Earthquake Engineering, hhlo@ncree.narl.org.tw

³ Researcher, National Center for Research on Earthquake Engineering, wychien@ncree.narl.org.tw

⁴ Division Head, National Center for Research on Earthquake Engineering, sjhwang@ntu.edu.tw

reduce the damages of schools near the active faults.

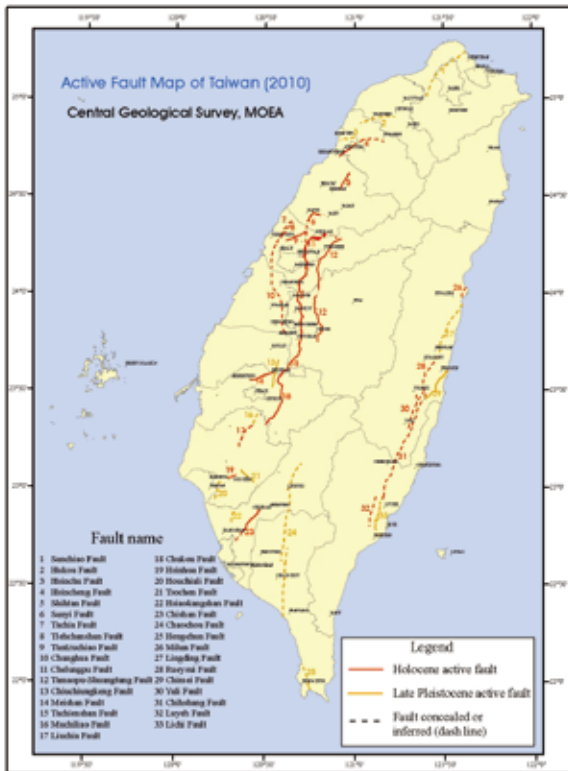


Fig. 1 Active faults map of Taiwan as of 2010

Characteristics of and Strategies for Near-fault Effects

The near-fault earthquake will lead to ground motion with pulse characteristics. At the same time, it also results to a large ground motion similar to the rapid whipping. After the pulse, it will produce a large permanent displacement.

During the Taiwan's 921 Chi-Chi earthquake, many seismic stations have measured and recorded the near-fault effects. Those records provide further understanding about the impact of the near-fault effects. There are many obvious differences between near-fault earthquakes and far-away-fault earthquakes. For example, the earthquake with the former could induce the hanging wall effect, the permanent displacement of the ground surface, and the whipping effect, and so on. At present, many scholars are doing several researches that include the characteristics of near-fault effects.

Because of the differences between near-fault earthquakes and distant-fault earthquakes, the former one causes more severe damages than the latter one. In order to prevent any future disasters caused by near-fault earthquakes, the strategies below may be considered.

1. Seismic retrofitting process

Based on the reconnaissance report of Jiashian Earthquake in Kaohsiung City on March 4, 2010, there was no structural damage observed on the school buildings of Yujing Industrial and Commercial Vocational School. This is possible because the buildings in the said school had been retrofitted prior to the earthquake (see Fig. 2).

After detailed assessments, some school buildings in Yujing Junior High School, Kaohsiung City were evaluated to have the need to undergo seismic retrofitting process. But prior to the Jiashian earthquake, these buildings were not retrofitted thus have led to serious damages as shown in Fig. 3. It can be said that the structural strength of those school buildings is not enough. They do need to be improved the seismic capacity by seismic retrofitting. Through seismic evaluation and retrofitting, buildings' structural capacities can be increased for those near the faults to improve their seismic resistance.

2. Increasing the structure's rigidity

In 921 Chi-Chi earthquake, from the reconnaissance report of Joyful-Blessing Community near Chelungpu fault in Taichung County, observations include visible permanent deformations and surface uplifts, but the buildings on both sides of the fault did not have serious damage nor did collapsed as shown in Fig. 4. These structures were found to have a considerable amount of walls, thus they have sufficient rigidities to resist surface deformation. Moreover, these buildings are structurally low-raised and small. Increasing the rigidity of a structure, such as using shear walls and raft foundation either in design or in retrofitting, may significantly improve the structural characteristics of a building. It will effectively reduce the disaster often caused by near-fault earthquakes.



Fig. 2 Photo of Yujing Industrial and Commercial Vocational School after Jiashian earthquake



Fig. 3 Photo of Yujing Junior High School after Jiashian earthquake



Fig. 4 Photo of Joyful-Blessing Community in Taichung County after the 921 Chi-Chi earthquake

Seismic Upgrade Procedures for Near-fault School Buildings

A near-fault earthquake produces ground motion with pulse characteristics. The resulting ground motion is similar to a rapid whipping. After the pulse happened, it results to a large permanent displacement.

For schools 200 meters away from Holocene active faults, their respective buildings must be governed with the following provisions for near-fault effects. The provisions consider appropriate near-fault adjustment factors to amplify seismic requirements. Seismic capacity indexes, I_s and CDR should be adjusted to $(I_s)^*$ and $(CDR)^*$, respectively.

1. The Taiwan Building Code of Seismic Design has clearly specified the near-fault adjustment factors for Holocene active faults, such as Shihtan Fault, Tuntzuchiaio Fault, Chelungpu Fault, Meishan Fault, Tachienshan Fault, Chukou Fault, Hsiahua Fault, Milun Fault, Yuli Fault, Chihshang Fault and Chimei Fault. School buildings can be accorded with the requirements of specification shown in Table 1.

2. The near-fault adjustment factors for Holocene active faults, which Taiwan Building Code of Seismic Design has not specified, should be referred to the provisions as follows:

(1) Rueysui fault (formerly known as the northern section of Yuli fault) and Luyeh Fault (announced as new Holocene active faults in 2010) also named as "Near Huadong Fault Adjustment Factor". The near-fault seismic adjustment factor of those faults should be set as $N_a = 1.42$, $N_v = 1.58$;

(2) Other Holocene active faults include Hsincheng Fault, Sanyi Fault, Tachia Fault, Tiehchanshan Fault, Changhua Fault, Tamaopu-Shuangtung Fault, Liuchia Fault and Chishan Fault. The near-fault seismic adjustment factors of those faults are in accordance with Chelungpu Fault, a more conservative value of $N_a = 1.30$, $N_v = 1.40$ (see Table 2).

3. If the Construction and Planning Agency of the Ministry of Interior (CPAMI), Taiwan would propose relevant specifications in the future, it shall comply with the stated provisions.

Table 1 Near-fault adjustment factors of design earthquake provided by the seismic design code

Fault name	Near-fault adjustment factor of design earthquake N_a	Near-fault adjustment factor of design earthquake N_v
Shihtan Fault	1.28	1.33
Tuntzuchiaio Fault	1.28	1.31
Chelungpu Fault	1.23	1.36
Meishan Fault	1.37	1.44
Tachienshan Fault	1.15	1.15
Chukou Fault	1.15	1.15
Hsiahua Fault	1.23	1.15
Milun Fault	1.42	1.58
Yuli Fault	1.42	1.58
Chihshang Fault	1.42	1.58
Chimei Fault	1.42	1.58

Table 2 Near-fault adjustment factors of design earthquake provided by the seismic design code

Fault name	Near-fault adjustment factor of design earthquake N_a	Near-fault adjustment factor of design earthquake N_v
Rueysui Fault	1.42	1.58
Luyeh Fault	1.42	1.58
Hsincheng Fault	1.30	1.40
Sanyi Fault	1.30	1.40
Tachia Fault	1.30	1.40
Tiehchanshan Fault	1.30	1.40
Changhua Fault	1.30	1.40
Tamaopu-Shuangtung Fault	1.30	1.40
Liuchia Fault	1.30	1.40
Chishan Fault	1.30	1.40

This paper presents a complete approach for school buildings that are near the traced Holocene active faults in Taiwan. The proposed procedure considers seismic capacity indexes (I_s)* and (CDR)*. Moreover, it should be accompanied with the process on seismic evaluation and retrofitting. With the suggestions on this paper, it is hoped that the retrofitting progress of near-fault school buildings can be controlled, as well as the upgrade of seismic capacities of those concerned school buildings.

If the near-fault school buildings have seismic retrofitting requirements, a retrofitted method using reinforced concrete shear wall with full-height configuration is suggested. In addition, the RC shear wall is appropriate to be constructed with a strip foundation.

The recommendations on the reconstruction of near-fault school buildings are as follows:

1. For near-fault school buildings, more detailed investigation shall be made. Subsurface investigation shall be carried out more carefully than the average school buildings. The investigation can be used for campus planning and as a reference for the configuration of school buildings. If necessary, it can adjust the usage of school buildings. For instance, low-density usage and plan for open spaces, grasslands, and playgrounds and so on can be considered.

2. If a school building needs to be reconstructed or renovated, it should be designed as a small, low-rise and rigid structure. The building shall be then lower than three stories. Each of the stories shall have no more than three classrooms on each floor. And the building shall be designed appropriately with shear walls and raft foundation.

Conclusion

This study was based on the relevant regulations of current Taiwan Building Code of Seismic Design, and provides suggestions on the retrofitting and/or the reconstruction of near-fault school buildings. It combines well the system of seismic evaluation and retrofitting and controls effectively the retrofitting progress of concerned structures. Further, it aimed to reduce earthquake damages of near-fault school buildings in the future.

References

- Central Geological Survey, Ministry of Economic Affairs, *Active faults map of Taiwan*, 2010.
- Chai, Juin-Fu and Loh, Chin-hsiung, "Consideration of the Near-fault Effect on Seismic Design Code for Sites near the Chelungpu Fault." (In Chinese)
- Wang, Hai-Yun and Xie, Li-li, "Characteristics of near fault strong ground motions," *Journal of Harbin Institute of Technology*, Vol.38, No.12, pp. 2070-2076, 2000.
- Construction and Planning Agency, Ministry of the Interior, *Seismic Design Specifications and Commentary*, Construction and Planning Agency, Ministry of the Interior, 2005. (In Chinese)

Pushover Analysis of Irregular Bridges

Hsiao-Hui Hung¹ Chang-Wei Huang² and Hao-Jen Liao

洪曉慧¹、黃仲偉²、廖皓荏³

Abstract

A rational seismic evaluation and design for a structure have to be based on the accurate prediction of its inelastic displacement demand and capacity. Therefore, displacement-based seismic evaluation and design has increasingly become the main stream for the design code of the next generation. Because nonlinear static pushover analysis can obtain failure mechanism and sequence of a structure which are both not easy to be obtained through strength-based design, and that two widespread-used commercial engineering softwares, ETABS and SAP2000, provide pushover analysis capacity, pushover analysis has become rapidly popular in the engineering community for seismic evaluation of various structures in recent years. However, the conventional single-mode pushover procedure provided by SAP2000 can only be applied reliably to a structure that is mainly controlled by first mode. For a complex structure where higher mode is important, single-mode pushover analysis cannot predict accurately the structure's nonlinear displacement. Moreover, the results of conventional pushover analysis depend on the choices of the single monitored point. For an irregular bridge, it is not easy to select the proper point to be monitored. Different choices of monitored point from different evaluators may lead to different seismic evaluation results for the same structure. This phenomenon is not acceptable. Therefore, to establish a generally acceptable pushover procedure that can reasonably consider the effects of all important modes is needed. The purpose of this current study aimed to clarify the scope of applicability for the conventional single-mode pushover analysis on the multi-span continuous bridge with different degrees of irregularities. A simple pushover procedure, which is more suitable for irregular bridge, has been proposed.

Keywords: nonlinear static pushover analysis, irregular bridge, monitored point

Introduction

Taiwan is located along the western ridge of the Pacific Ocean earthquake belt and thus suffers frequently from earthquake. Over the years, several earthquake events not only damaged the structures and caused life and property losses, but also impeded the development of the country. As such, the seismic design and evaluation of structures have become an essential issue for the sustainable development of Taiwan in recent years. As part of this, a rational seismic evaluation and design of a bridge has to be based on the accurate estimation of its inelastic deformation. Because pushover analysis has the ability to obtain these results, it has become rapidly an essential analysis tool for seismic design and

evaluation of bridges recently.

There are more than two thousands railway bridges and highway bridges in Taiwan. Many of which are irregular bridges in different forms. Some were widened to a larger road width in different time periods using different design codes. As a result, different types of bridge piers may exist in a bridge. Such type of bridge system is rather asymmetric and its first vibration mode cannot represent its overall vibration behavior. Therefore, seismic evaluation performed by the conventional single-mode pushover analysis becomes questionable. In order to overcome this problem, various improved multi-mode pushover analyses were developed during the last few years. However, most procedures were too complex and impractical in

¹ Associate Researcher, National Center for Research on Earthquake Engineering, hhung@ncree.narl.org.tw

² Assistant Professor, Department of Civil Engineering, Chung-Yuan University

³ Graduate Student, Department of Civil Engineering, Chung-Yuan University

practice. In addition, most of these refined methods were aimed at solving problems related to buildings, not to bridges. Due to the intrinsic differences of seismic responses between buildings and bridges, the procedure which can be applied reliably on buildings may not be as such reliable on bridges. For instance, it is reasonable to select the nodal point at the upper floor of a building as the monitored point. However, for a multi-span continuous bridge, the selection of monitored point for pushover analysis along the transverse direction is not that straightforward. Besides, the reliability of adopting the first vibration mode of a multi-span continuous bridge to be the distribution of lateral force still needs further investigation.

Conventional pushover is performed by applying a monotonically increasing invariant lateral forces pattern on the structure until a pre-determined target displacement on a pre-determined monitored point is reached. Based on the relationship between the recorded displacements at the monitored point and the total base shear, the seismic capacity of a structure can be obtained. Both the distribution of lateral forces and the calculation of target displacement are all based on the assumptions that structural behavior is influenced predominately by its fundamental mode. Obviously, this assumption is not accurate for irregular bridges where the higher modes are relatively important. Thus, to establish pushover analysis procedure which can reasonably take most of the important modes into account is urgent for seismic evaluation of irregular bridges.

Pushover Procedure

Conventional pushover analysis is a type of single-mode pushover analysis. For single-mode pushover, the structure is subjected to a monotonically increasing lateral force with an invariant spatial distribution, which is generally the fundamental modal load pattern. In this study, not only the fundamental modal load pattern was adopted, accumulated modal load pattern (Type 1), uniform modal load pattern (Type 2), and a type of lateral force pattern that is equal to the static seismic force defined by bridge design code in Taiwan (Type 3) were also adopted.

The accumulated modal load pattern (Type 1) is the combination of several important modal forces corresponding to an accumulated mass participation of more than 90% based on the Complete Quadratic Combination (CQC) method,

$$F_i = \sqrt{\sum_j \sum_l F_{ij} \rho_{jl} F_{il}}, \quad F_{ij} = \Gamma_j \phi_{ij} m_i \quad (1)$$

where F_{ij} is the modal nodal force applied on node i for mode j , ρ_{jl} is the cross-modal correlation coefficient, Γ_j is the modal participation factor for the j^{th} mode, and m_i is the mass of the node i . For uniform modal load pattern (Type 2), the lateral force can be written as,

$$F_i = m_i \zeta_i \quad (2)$$

where $\zeta_i = 1$ for the deck and $\zeta_i = z_i/z_p$ for the piers connected to the deck. In which, z_i is the height of point i above the foundation of the individual pier, and z_p is the height of the pier P (distance from the ground to the centerline of the deck). Lateral force pattern Type 3 can be obtained by multiplying nodal mass by the corresponding nodal displacement which is obtained by applying nodal weight in the transverse direction,

$$F_i = m_i u(\omega)_i \quad (3)$$

where $u(\omega)_i$ is the nodal displacement at node i obtained by applying nodal weight of a bridge in the transverse direction.

Pushover curve represents the relation between total base shear and displacement observed at a selected monitored point. In order to compare structural capacity to design earthquake demand, the pushover curve for a multi-degree-of-freedom (MDOF) system has to be converted to a capacity spectrum for an equivalent single-degree-of-freedom (SDOF) system. In literature, the capacity spectrum curve that relates the spectral acceleration $S_{a,k}$ to the spectral displacement $S_{d,k}$ can be obtained from the pushover curve ($V_{b,k}$ vs $\Delta_{r,k}$) by the following equation:

$$S_{a,k} = \frac{V_{b,k}}{M_n^* g}, \quad S_{d,k} = \frac{\Delta_{r,k}}{\Gamma_n \times \phi_{rn}} \quad (4)$$

In the above equation, $\Delta_{r,k}$ is the lateral displacement at monitored point r , $V_{b,k}$ is the total base shear, and k represents the analysis step. M_n^* is the effective modal mass of the fundamental mode n , also referred to as the mass of the equivalent SDOF system, Γ_n is the modal participation factor of the fundamental mode n , and ϕ_{rn} is the value of mode shape ϕ_n at the monitored point r . As can be seen, the curve obtained from Eq. (4) depends strongly on the selection of the monitored point r . Different choices of monitored point will lead to different capacity spectrum curves, and in turn lead to different seismic evaluation results for the same structure. In reality, a more rational way for deriving capacity spectrum curve should consider the displacement contributions from all important nodes. Accordingly, the concept of system displacement and system mass (Kowalsky, 2002) is recommended in the current study to calculate the equivalent SDOF capacity curve,

$$S_{a,k} = \frac{V_{b,k}}{M_{sys,k} g}, \quad S_{d,k} = \Delta_{sys,k} \quad (5)$$

where $M_{sys,k}$ and $\Delta_{sys,k}$ is the effective system mass and equivalent system displacement at analysis step k , respectively,

$$M_{sys,k} = \frac{\sum_i m_i \Delta_{i,k}}{\Delta_{sys,k}}, \quad \Delta_{sys,k} = \frac{\sum_i m_i \Delta_{i,k}^2}{\sum_i m_i \Delta_{i,k}} \quad (6)$$

The estimation of system displacement $\Delta_{sys,k}$ is based on the assumption that work done by the original MDOF bridge and the equivalent SDOF

structure is equal. The system effective mass $M_{sys,k}$ is similar to effective modal mass M_n^* , except that M_n^* only takes into account the fundamental mode shape in elastic state, whereas $M_{sys,k}$ is obtained from the instantaneous displacement profile of the structure at analysis step k . Thus, the value of $M_{sys,k}$ is not an invariant value as M_n^* does, but varies with the increase of time step. In Eq.(6), i represents every node of the structure regarded to be important, and m_i is the mass tributary to node i . For a bridge structure, the important nodes can be the deck nodes that are located immediately above piers.

By superposing the capacity spectrum with the demand spectrum, the performance point where capacity equals demand can be obtained. However, because nonlinear demand spectrum depends on damping ratio, while damping ratio depends on nonlinear deformation of the structure, this process needs repetition. In order to prevent repetition, a modified seismic evaluation method proposed by Sung *et al.* (2006) was adopted in this study to calculate the performance point.

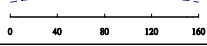
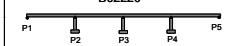
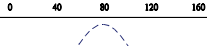
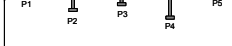
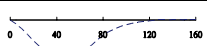
Case Study

In order to identify the feasibility of the conventional single-mode pushover analysis for bridges and to recommend a reasonable procedure, all of the mentioned pushover procedures as well as inelastic dynamic analysis were performed on a set of continuous bridges with piers of different heights. Taking the results of inelastic dynamic analysis as reference values, the accuracy of each pushover analysis procedure for irregular bridges can be identified. The bridge configurations considered are listed in Table 1, which consists of five types of four-span continuous bridges with different pier heights. The length of each span was 40 m, the total length was 160 m, and the superstructure mass was 15 ton/m all throughout. The bearing systems were pin supports at the intermediate piers P2, P3 and P4, and roller supports at expansion joints P1 and P5. All piers were circular RC columns with a diameter of 2.5 m. Also, all have the same reinforcement details of 74-D32 longitudinal reinforcing bars, and were transversely reinforced with 19mm bar hoop spaced at 8 cm. However, the pier heights were varied to cover both regular and irregular bridges. These bridges were named as B22222, B02220, B22132, B02130 and B01234, in which each number represents the height of pier from P1 to P5. Numbers 1, 2, 3, 4 represent 5 m, 10 m, 15 m and 20 m, respectively, whereas 0 represents abutment.

For a continuous bridge, the effect of irregularity due to unequal pier heights mainly reacts on the transverse response. As a result, only the analysis along transverse direction is included. By a standard modal analysis, the transverse modal properties for each bridge type are also given in Table 1. In which, T is the vibration period, and α is the modal mass

participation factor.

Table 1 Schematic representation of analyzed bridges

Bridge configurations	Modal properties	Mode shape for transverse mode
 B22222	Mode 1 $T = 0.521$ sec $\alpha = 90.10\%$	
 B02220	Mode 1 $T = 0.459$ sec $\alpha = 69.93\%$	
 B22132	Mode 1 $T = 0.555$ sec $\alpha = 20.45\%$	
 B02130	Mode 1 $T = 0.339$ sec $\alpha = 33.16\%$	
 B01234	Mode 1 $T = 1.086$ sec $\alpha = 41.89\%$	
	Mode 2 $T = 0.299$ sec $\alpha = 46.94\%$	
	Mode 1 $T = 0.491$ sec $\alpha = 21.55\%$	

Results and Discussions

In the current study, static pushover analysis was carried out using Sap 2000N. Superstructures were simulated by elastic beam elements, and the nonlinear behavior of piers was modeled by M3 hinge. Following the procedure mentioned previously, the capacity spectra developed by different pushover procedures and the performance point corresponding to a design earthquake ($S_{DS} = 0.856$, $S_{D1} = 0.6588$) can be obtained. Based on the spectral displacement and spectral acceleration at the performance point, the lateral displacements at deck's level under the design earthquake can be obtained from Eq. (4) or (5) for the single monitored point case and the multiple monitored points case, respectively. The calculated transverse displacement profiles from different methods are given in Fig. 1. In order to realize the performance of different pushover procedures, inelastic dynamic analysis was also performed. The results of dynamic analysis shown in Fig. 1 are the average displacements at deck nodes obtained by applying three code-compatible artificial earthquakes on the bridge. Moreover, considering the results of inelastic dynamic analysis as reference values, the error ratios for different pushover procedures were also calculated and are listed in Table 2.

The effect of lateral force patterns on the transverse displacement profiles can be observed in Fig. 1. As can be observed, single-mode pushover can only capture the displacement profile of bridges B22222, B02220 and B01234 observed by dynamic analysis. As for bridges B22132 and B02130, the results obtained by single-mode pushover are completely different from the profiles obtained by dynamic analysis. This observation concludes that

conventional single-mode pushover analysis cannot accurately capture the development of displacement profile for irregular bridges. On the other hand, all the other three lateral force patterns incorporated with multiple monitored points perform better than the single-mode pushover analysis in predicting the displacement profiles. Among these three methods, uniform modal force (Type 2) performs best.

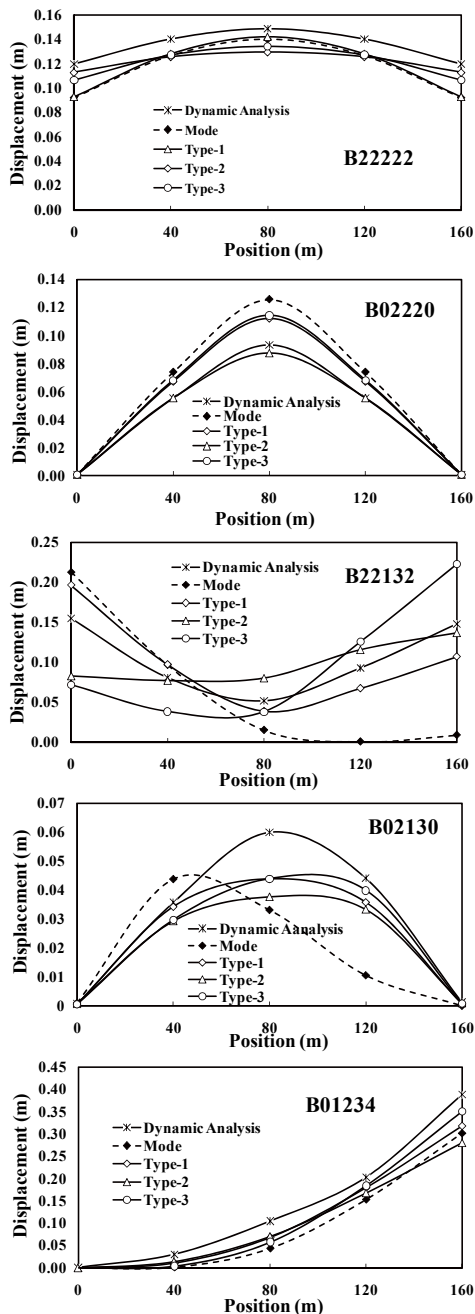


Fig. 1 Displacement distribution of the superstructure

The same results can be observed from the error ratios for different pushover procedures given in Table 2. As can be seen, the error ratios of the conventional single-mode pushover are all larger than that of the other procedures. The smallest error ratio that the single-mode method has is 14.48%. This is because B22222 has a modal mass

participation factor of the first mode reaching 90.10% and can be regarded as a rather regular bridge. As for the other three procedures, the uniform modal force (Type 2) performs best for different bridges and provides the smallest average error ratio.

Considering the selection of monitored points, obviously, the procedure using multiple monitored points can achieve better results as can be seen in Table 1. The major influence of monitored points is on the capacity spectrum, whereas capacity spectrum is the basis of seismic evaluation. For the case with single monitored point, the evaluation results will depend on the selection of the monitored point. However, it is not easy to select a proper monitored point for an irregular continuous bridge, thus the said procedure is not feasible for irregular bridges. On the other hand, if all of the important nodes are taken as the monitored points, the arbitrary selection of monitored point can be prevented. Therefore, the procedure that considers displacements of multiple monitored points is a more rational approach in the performance evaluation of irregular bridges.

Table 2 Average error ratios of different pushover procedures

Lateral force pattern	Average error ratio (%)			
	Mode	Type 1	Type 2	Type 3
Monitored point	single	multiple	multiple	multiple
B22222	14.48	13.41	9.23	10.07
B02220	33.73	21.02	2.28	22.76
B22132	70.67	25.46	27.53	43.95
B02130	55.72	16.57	26.47	17.93
B01234	50.31	32.03	31.91	37.91
average	44.98	21.70	19.48	26.52

Conclusions

Two key factors in the pushover analysis procedures include the selection of lateral force pattern and of monitored points. In this study, the effects of different load patterns of lateral forces and monitoring points on the seismic evaluation are discussed. According to the results, pushover analysis using uniform modal force incorporated with multiple monitored points that include all the deck nodes immediately above each pier has been recommended.

References

Kowalsky, M. J., "A displacement-based approach for the seismic design of continuous concrete bridges," *Earthquake Engineering and Structural Dynamics*, 31, pp. 719-747. (2002).

Sung Yu-Chi, Su Chin-Kuo, Wu Chuan-Wei, Tsai I-Chau, *Performance-Based Damage Assessment of Low-Rise Reinforced Concrete Buildings*, *Journal of the Chinese Institute of Engineers*, 29(1), pp. 51-62. (2006)

Bridge Load Testing in the Malingkeng Qidu Road Section of Freeway No. 3 near Xizhi, Keelung

Zheng-Kuan Lee¹

李政寬¹

Abstract

A landslide occurring at 2:33 p.m. on April 25, 2010 near the 3.25 kilometer mark of Freeway No. 3, close to the Malingkeng Qidu Road Section, blocked both lanes of the freeway. The huge amounts of soil and rock deposited by the landslide buried the road embankment and some of a bridge. After the incident occurred, the Taiwan Area National Freeway Bureau, MOTC quickly performed emergency repairs on this road section. In order to ease public misgivings concerning the integrity of the repaired elevated roadway, the Freeway Bureau accordingly engaged CECI Engineering Consultants, Inc. and the National Center for Research on Earthquake Engineering (NCREE) to draft a load testing plan.

Keywords: landslide, bridge loading test

Introduction

A landslide occurring at 2:33 p.m. on April 25, 2010 near the 3.25 kilometer mark of Freeway No. 3, close to the Malingkeng Qidu Road Section, blocked both lanes of the freeway. The huge amounts of soil and rock deposited by the landslide buried the road embankment and some of a bridge. Most of the debris buried the embankment, and only a small amount of debris covered the bridge. The bridge section consequently suffered less damage than had originally been expected. The most severe damage to the bridge affected the main northbound roadway and ramp (see Fig. 1 and Fig. 2). The most significant damage included damage to the cantilever slab outside of the first span box girder near the bridge abutment on the northbound main lanes (Fig. 3), the displacement of the northbound ramp abutment supports (Fig. 4), and damage to the abutment backwall.



Figure 1: Aerial photograph of landslide

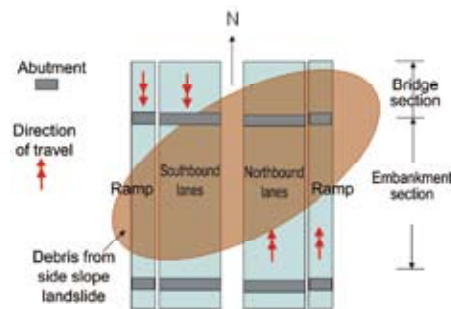


Figure 2: Distribution of landslide debris



Figure 3: Damage to the outer box girder



Figure 4: Displacement and damage to supports

¹ Associated Researcher, National Center for Research on Earthquake Engineering, zklee@ncree.narl.org.tw

Emergency Road-opening Repairs by the Taiwan Area National Freeway Bureau

As part of its plan to quickly restore use of the main lanes of the freeway, the Taiwan Area National Freeway Bureau, MOTC first performed emergency repairs to the destroyed abutment back wall and box girder outer cantilever slab. Figures 5 and Figure 6 show the repaired abutment back wall and box girder outer cantilever slab. The ramp (northbound) connecting with Expressway No. 62 will be repaired after the main traffic lanes have been fully repaired and are open to traffic.



Figure 5: Repair of the abutment back wall



Figure 6: Repair of the cantilever slab

Load Testing Project

To confirm the effectiveness of repairs to the elevated roadway, and ease public misgivings concerning the integrity of the repaired elevated roadway, the Freeway Bureau accordingly engaged CECI Engineering Consultants, Inc. and the National Center for Research on Earthquake Engineering (NCREE) to assist with the implementation of a load testing project. Vehicle load testing was performed on the southbound lanes on May 18, and on the northbound lanes on May 23. Vehicle load testing to measure the effect of the maximum live load on the displacement of bridge piers (abutments) was conducted on May 27.

Plan of the Loading Test

In accordance with the testing plan drafted by CECI Engineering Consultants, dump trucks with a weight of approximately 26.5 tons each were used to supply the testing load. Three trucks were used on each lane, and a total of nine trucks provided the load on all three lanes. The arrangement of the dump trucks

and locations of girder displacement monitoring instruments are shown in figures 7 and 8 respectively:

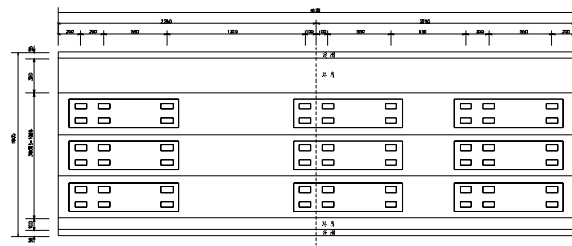


Figure 7: Maximum live load testing

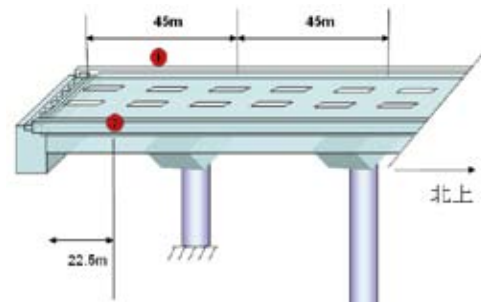


Figure 8: Micrometers to monitor girder displacement

Repeated Girder Loading/Unloading Test of Northbound Lanes

The procedures for the repeated girder loading/unloading test using maximum live load were as shown in Fig. 9. This figure shows the displacement of girder center points, which indicates that the girders have a nearly completely elastic response.

Repeated girder Loading/Unloading Test of Northbound Lane Cantilever Slab outside of the Box Beam

To confirm the effectiveness of repairs to the cantilever slab, repeated loading and unloading of the repaired section was performed using dump trucks weighing approximately 26.5 tons each (see Fig. 10). The data in this figure is the displacement response of the cantilever slab. The data indicates that the structural load of the repaired section has a nearly elastic response.

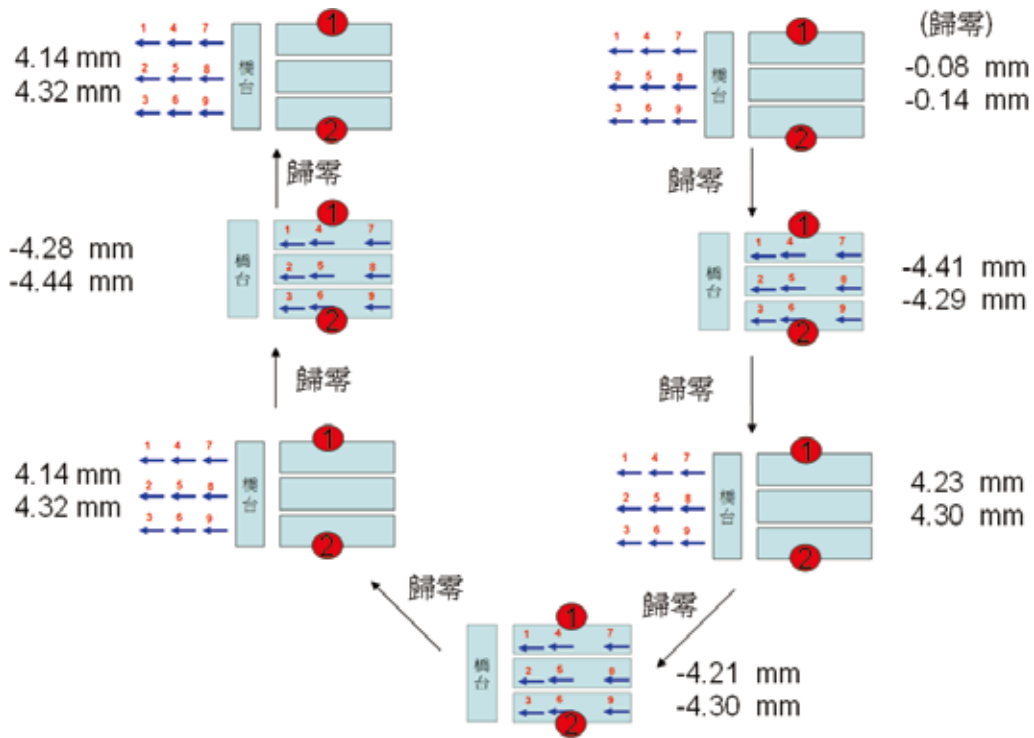


Figure 9: Measurement of the displacement of girder center points during repeated loading and unloading

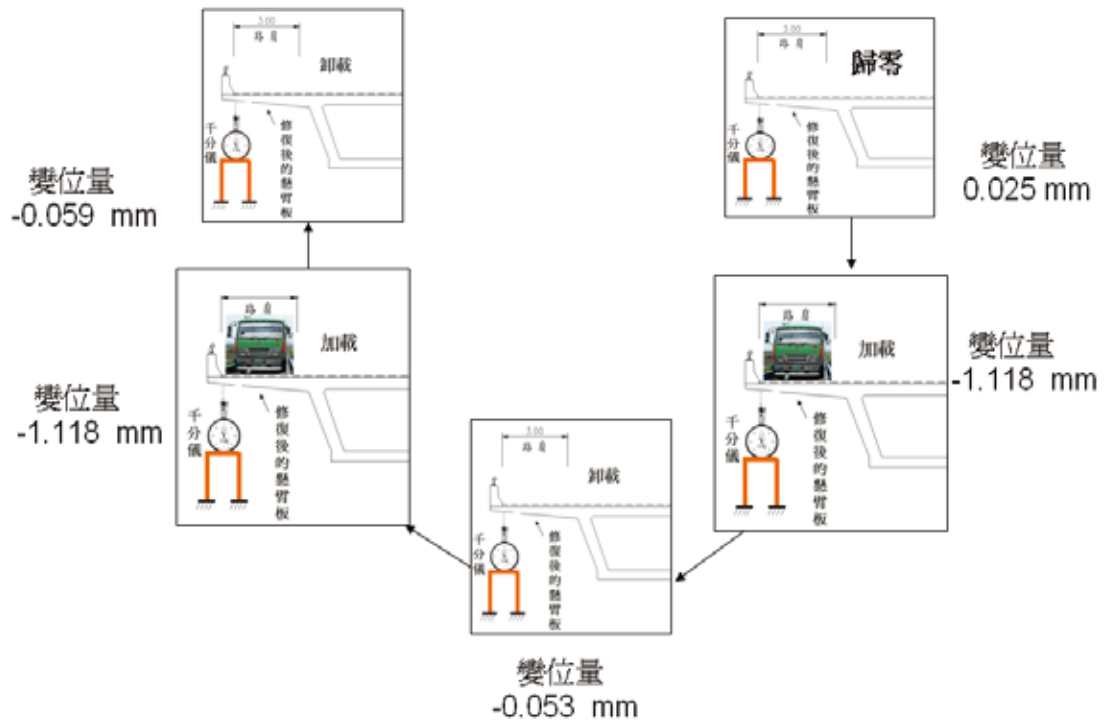


Figure 10: Measurement of the displacement response during process of repeated loading and unloading of repaired outer cantilever slab

Numerical Modeling Simulated Loading of Northbound Lane Girders

CECI Engineering Consultants used a numerical model of the original design to simulate maximum live load testing as shown in Fig. 7. When three dump trucks were used in each lane, for a total of nine dump trucks on all three lanes, and each dump truck weighed approximately 26.5 tons, the structural response shown in Fig. 11 resulted. It can be seen that the largest vertical displacement of approximately 0.48 cm, which was in the first span, was slightly greater than the experimental value of 0.43 cm.

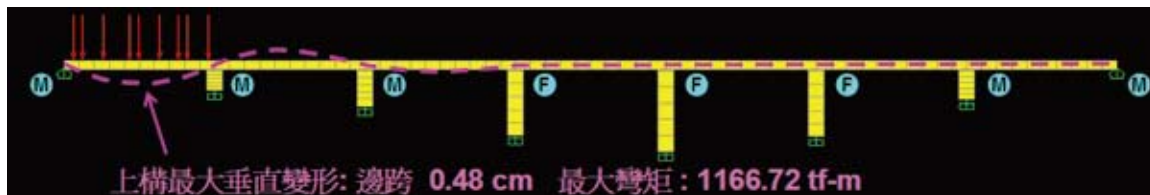


Figure 11: Numerical modeling of maximum live load

Loading Analysis of Cantilever Slab outside of the Box Beam

The weight of one 26.5-ton dump trucks was converted to an equal, evenly-distributed load in a model of the original cantilever slab design (see Fig. 12). A vertical displacement of $\Delta = 1.26$ mm was obtained, which was slightly greater than the experimental value of 1.12 mm (obtained during the repeated loading/unloading process).

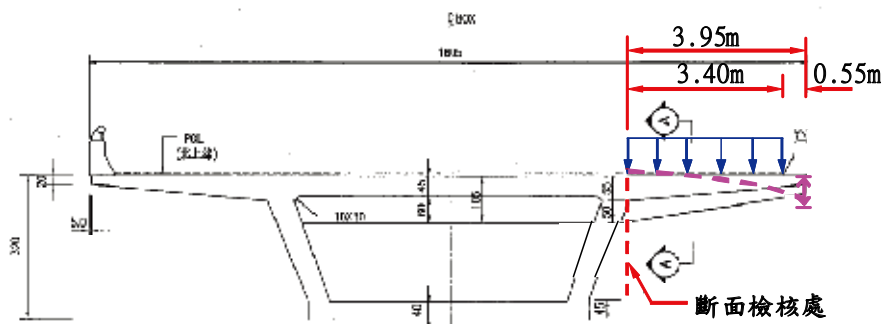


Figure 12: Displacement analysis when the load of one dump truck is applied to the cantilever slab

Conclusions

After repair, load testing of the girders and cantilever slab showed that there was no significant residual displacement of the bridge structure during the loading and unloading process, and displacement was quite close to the design response. This indicates that the deformation of the bridge structure in response to the planned live load is uniformly within the elastic range. Therefore, after the loading test, the road is open to the public on 1, June, 2010.

Seismic Behavior of Scoured Bridges (I)

Kuo-Chun Chang¹, Shiou-Chun Wang², Kuang-Yen Liu³, Tzou-Shin Ueng⁴,
Chia-Han Chen⁵, and Cheng-Hsing Chen⁶

張國鎮¹、王修駿²、劉光晏³、翁作新⁴、陳家漢⁵、陳正興⁶

Abstract

In order to study the seismic behavior and soil-structure interaction of scoured bridges, shaking table tests were conducted on a model piled bridge foundation placed in the biaxial laminar shear box at the National Center for Research on Earthquake Engineering (NCREE), Taiwan. The model included a lumped mass representing the superstructure, a steel column, and a footing supported by an aluminum pile. The pile tip was fixed at the bottom of the shear box to simulate a pile embedded in a firm stratum. Strain gauges and accelerometers were placed on the pile surface to observe its behavior during the tests. Accelerations and displacements at various depths of soil specimen and settlement of the ground surface after each shaking were also measured. The model was subjected to one- and two-dimensional shakings, including white noise acceleration, sinusoidal acceleration and earthquake records. The performance of the model piled bridge foundation at various scouring conditions is discussed in this report.

Keywords: scouring effect, piled bridge foundation, soil-structure interaction, shaking table test

Introduction

The river-crossing type of bridges usually suffers the obvious local scour effect during heavy rains and typhoons, thus leading to bridge foundation being exposed. This exposure of the bridge foundation, commonly built on piles, might possibly cause the bridge pier footing to be inclined and be damaged by the forces of flowing water. Furthermore, the more is exposed on the length of the foundation piles, the less is the foundation's seismic performance, which might greatly affect the structure and will tend to cause the bridge's collapse. Only few attempts have been made so far to study scoured bridges. Most of the earlier studies were performed using analytical approaches (Priestley et al., 1996). Recently, with the advances in experimental techniques, soil-structure interaction experiments became the focus of several studies including series of tests performed on a large

centrifuge by Abdoun et al. (2003) and tests performed on a shaking table by Tokimatsu et al. (2005), and Chen & Ueng (2010). All of these studies focused on the soil-pile interaction.

However, the relevant researches are not comprehensive enough to provide confidence in assessing the seismic capacity of the scoured piled bridge foundation. In order to have a better understanding of the effects of scouring on the seismic behavior of a bridge, more experimental data and different modeling approaches are required. Therefore, in this study, a series of shaking table tests of a model piled bridge foundation were conducted.

Experimental Studies of a Scoured Piled Bridge Foundation

¹ Professor, Dept. of Civil Engineering, National Taiwan University, kcchang@ncree.narl.org.tw

² Ph.D. Candidate, Dept. of Civil Engineering, National Taiwan University, d96521009@ntu.edu.tw

³ Associate Researcher, National Center for Research on Earthquake Engineering, kyliu@ncree.narl.org.tw

⁴ Professor Emeritus, Dept. of Civil Engineering, National Taiwan University, ueng@ntu.edu.tw

⁵ Assistant Researcher, National Center for Research on Earthquake Engineering, chiaham@ncree.narl.org.tw

⁶ Professor, Dept. of Civil Engineering, National Taiwan University, chchen2@ntu.edu.tw

Test Specimens

Four different conditions of the model piled bridge foundation were constructed for the shaking table tests. The model was set up with instrumentation inside the shear box as shown in Fig. 1. The pile was modeled by an aluminum alloy pipe, 1,300 mm in length, outer diameter of 50.5 mm, wall thickness of 2.5 mm, and yield strength $f_y=147.15$ MPa. The footing was made of A36 steel plate, 300×300 mm in size, 50 mm in thickness, and 0.346 kN in weight. Above the steel plate, there was a column made of an A36 steel pipe, 2.5 mm thick, 600 mm in length, with an outer diameter of 48.6 mm, wall thickness of 2.5 mm, and yield strength $f_y=250.16$ MPa. A lumped mass representing the superstructure was fixed on the top of the column and weighs about 2.45 kN.

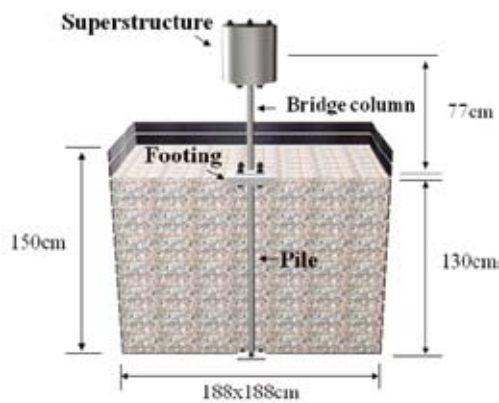


Fig. 1 Test specimens

Strain gauges and accelerometers were placed at different locations to measure the bending moment and accelerations along the pile and the column. The pile was fixed at the bottom of the shear box to simulate the condition of a pile foundation embedded in firm stratum. Clean and dry silica sand from Vietnam was used in the test. The soil was modeled by five layers of silica sand which were prepared using compaction method soon after the modeled pile has been placed in position and instrumentations were attached in the shear box. The sand was rained down into the shear box to design the weight requirement and then was compacted to a pre-determined depth (relative density = 50%) of each layer. The size of sand specimen is 188 cm × 188 cm in plane and about 130 cm in height before the shaking tests. There were four different heights of sand specimens used: 130 cm, 128.5 cm, 113.5 cm and 97 cm, as shown in Fig. 2. The test cases were named as SBF-O, SBF-NC, SBF-S3D, SBF-S6D and SBF-WS. In which, “SBF” stands for cases with soil-bridge-foundation: “O”, “NC”, “S3D”, “S6D” and “WS” denote cases of the soil in contact with the footing plate, non-contact between the soil and the footing plate, scoured depth at 3 times the outer diameter of the pile, scoured depth at 6 times the outer diameter of the pile, and without soil, respectively.



Fig. 2 Sand heights in different test cases

Test Setup

To study the behavior of the bridge foundation under different scouring conditions, a series of shaking table tests were conducted as shown in Fig. 3. Figure 4 illustrates the layout of the instrumentation on the model. During the test, accelerations and displacements at the center of the lumped mass, accelerations and displacements of the footing, and strains and accelerations at different levels on the pile and column were measured. In addition, the frame movements at different depths of the laminar shear box were recorded using displacement transducers and accelerometers to evaluate the responses of the sand specimen. The height of the sand surface after each test was obtained in calculating the settlement and density of the sand specimen.



Fig. 3 Instrumentation of the tests on the shaking table

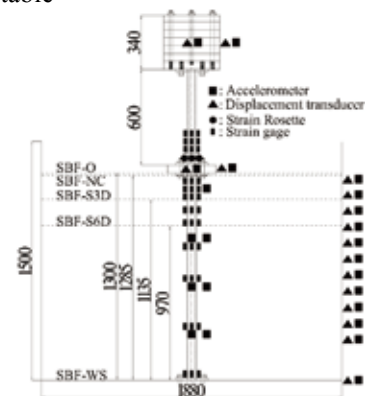


Fig. 4 Layout of instrumentation

Test Input Motions

Table 1 shows the input motions in the shaking table tests including sinusoidal accelerations and earthquake accelerations. Shaking table tests were first conducted on the bridge piled foundation model without sand specimen to evaluate the dynamic characteristics of the model itself. Sinusoidal and white noise accelerations with amplitudes from 0.03 to 0.05 g were applied in x-direction and y-direction. The model structure in the dry sand specimen was then tested under one-directional and two-directional sinusoidal (1~8 Hz) accelerations. The input ground motions included the 1940 El Centro earthquake, the 1999 Chi-Chi earthquake (TCU068) and the artificial earthquake acceleration, a code-compatible design earthquake acceleration of Chi-Chi earthquake (TCU068) in Taiwan. White noise accelerations were also applied in both x and y directions to investigate the dynamic characteristics of the model and the sand specimen after every several shakings.

Table 1. Test input motions

Input Motion	X-Direction (NS)	Y-Direction (EW)	XY-Direction (2D)
	PGA (g)	PGA (g)	PGA (g)
White Noise	0.03~0.05	0.03~0.05	0.03~0.05
Sine Wave	0.03 (1Hz~8Hz)	0.03 (1Hz~8Hz)	0.03 (1Hz~2Hz)
El Centro	0.1~0.2	0.1	0.1
TCU068	0.1~0.15		
Artificial TCU068	0.1~0.2		

Preliminary Test Result

In order to understand the dynamic characteristics of the test model, system identification was conducted first. Initial dynamic characteristics of the test model at different scouring conditions were identified using 0.03~0.05 g white noise excitations listed in Table 2. The transfer functions at the center of the lumped mass (roof) of the test model structure at different test cases subjected to a 0.03 g white noise excitation are shown in Fig. 5. It can be observed that the first modal (predominant) frequency of the test model decreases from 2.038 Hz to 0.488 Hz as the scouring depth increases.

Table 2. Transfer functions of the test model structures subjected to 0.03 g white noise excitation

White Noise 0.03 g X-direction		
Test Specimens	1st Mode from T.R. (Hz)	Period (s)
SBF-O	2.038	0.49
SBF-NC	1.560	0.64
SBF-S3D	1.320	0.76
SBF-S6D	0.977	1.02
SBF-WS	0.488	2.05

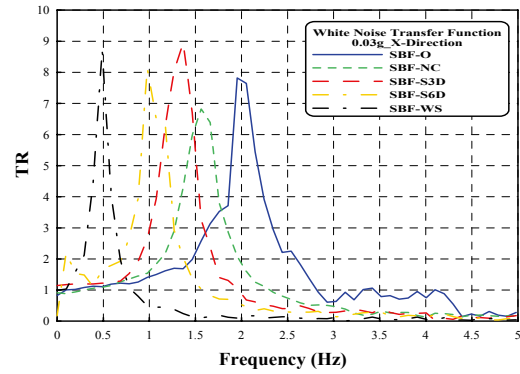


Fig.5 Transfer functions of the test model structures subjected to 0.03 g white noise excitation

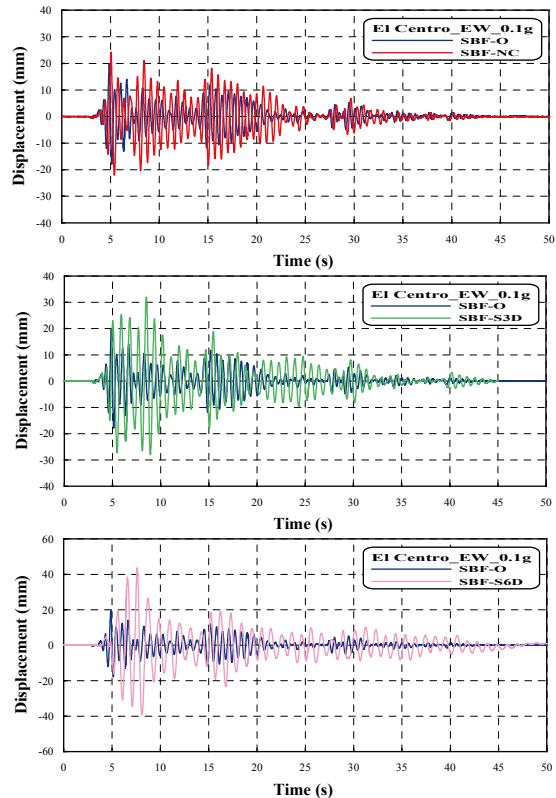


Fig. 6 Comparison of time histories of relative displacement of the model subjected to 0.1 g El Centro earthquake

The time history responses under 0.1 g El Centro earthquake of each specimen are shown in Fig. 6 and Fig. 7. It can be seen that the maximum value of the displacement time history response increases from 19.9 mm to 43.5 mm as the scouring depth increases. The relationship between the maximum roof responses of the piled bridge foundation and the scouring depth is shown in Fig. 8. It can be seen that the displacement has increased due to the scouring effect. Figures 6 to 8 show a significant change of behavior of the model structure between cases SBF-O (with contact between footing plate and soil) and SBF-NC (without contact between footing plate and soil) of approximately the same scoured depth

for the case subjected to 0.1 g El Centro earthquake excitation. The maximum moment distributions under 0.1 g El Centro earthquake of each specimen are shown in Figs. 9 and 10. It can be seen that the maximum moment response of the pile increases with increasing scoured depth.

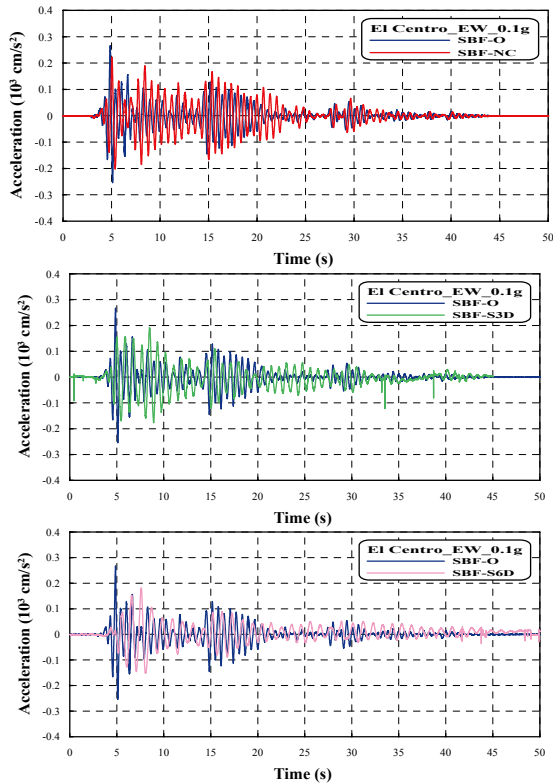
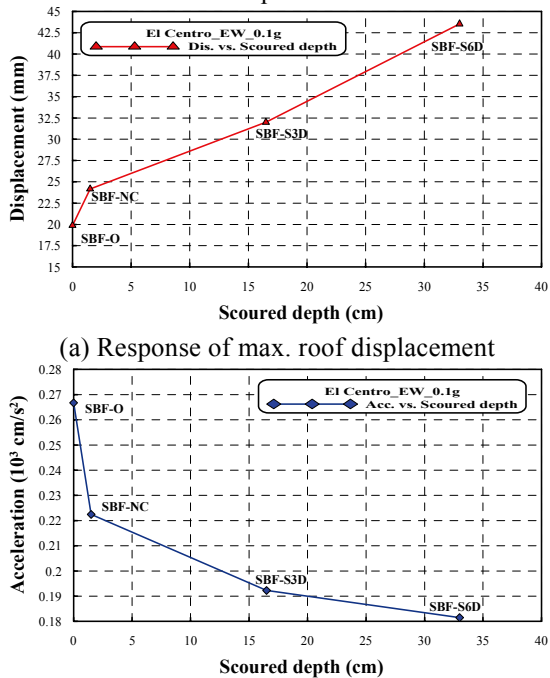


Fig. 7 Comparison of time histories of absolute acceleration of the model subjected to 0.1 g El Centro earthquake



(a) Response of max. roof displacement
(b) Response of max. roof acceleration
Fig. 8 Response of test model structures subjected to 0.1 g El Centro earthquake excitation

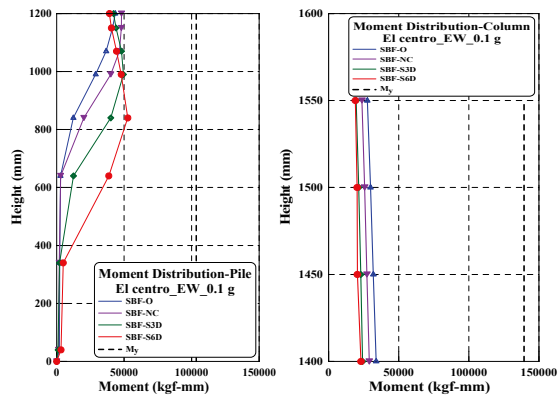


Fig. 9 Moment envelope of model pile subjected to 0.1 g El Centro earthquake excitation (left)

Fig. 10 Moment envelope of model column subjected to 0.1 g El Centro earthquake excitation (right)

Summary

In this study, a series of shaking table tests on a model piled bridge foundation at various scoured depths were conducted. The results of the experiments show that the frequency of the model piled bridge decreases with increase of scoured depth. The contact effect of footing plate on dynamic behavior of the model piled bridge foundation appeared to be significant. The maximum displacement response of the column's top increases with increasing scoured depth, while the acceleration changes according to the characteristic of the model foundation and the input motions. Also, it can be noted that the contact condition is an important factor on the responses of the piled bridge foundation.

References

- Abdoun, T., Ricardo Dobry, Thomas D. O'Rourke, S. H. Goh (2003), "Pile Response to Lateral Spreads: Centrifuge Modeling", ASCE, Journal of Geotechnical and Geoenvironmental Engineering, Vol 129, No.10, pp.869-878.
- Chen, C.H. and Ueng, T.S. (2010). "Behavior of Model Piles in a Liquefiable Soil in Shaking Table Tests," 5th International Conference on Recent Advances in Geotechnical Earthquake Engineering and Soil Dynamics, San Diego, CA, Paper No. 8.04.
- Priestley, N. M. J., Seible, F. and Calvi, G. M. (1996), Seismic design and retrofit of bridges, John Wiley & Sons
- Tokimatsua, K., Hiroko Suzuki, Masayoshi Sato (2005), "Effects of Inertial and Kinematic Interaction on Seismic Behavior of Pile with Embedded Foundation", Soil Dynamics and Earthquake Engineering, 25, pp.753-762.

A Study on the Simplified Seismic Evaluation and Preliminary Design Method for Critical Equipment

Juin-Fu Chai¹ and Fan-Ru Lin²

柴駿甫¹、林凡茹²

Abstract

Due to the variety in the categorization of nonstructural components and medical equipment in a hospital, before embarking on seismic design, the critical and/or vulnerable nonstructural items should be identified and prioritized. In this study, consulting with the constructors and hospital facility managers, the procedures and accompanied tools including the screening criteria, simplified seismic evaluation form, design requirements and appropriate seismic restraints are proposed and recommended for the nonstructural components and equipment in a hospital. Furthermore, some critical and vulnerable medical equipment items were chosen for shaking table tests to verify the application of proposed simplified evaluation forms and recommended seismic restraints. Based on the modeled specimens of medical equipment, the test results revealed that restraint devices actually contribute to decrease displacement response, but it increases acceleration response of the equipment due to the impact effect. Besides, damages of adhesive layer between restraint devices and equipment or anchors at partition wall appeared under larger earthquakes. Based on the test results, the simplified evaluation form and seismic restraints were modified to be applicable for free-standing medical equipment, and further, the pull-out strength of partition wall and the adhesive strength of non-destructive devices were taken for the next research subjects for seismic design of medical equipment.

Keywords: freestanding medical equipment, shaking table test, simplified evaluation form, simplified seismic design

Introduction

Due to the interruption of traffic after earthquakes, it is necessary that medical equipment and medicine supplies of a hospital within the affected area should be self-sufficient for at least 72 hours. However, from the experiences of the Hanshin-Awaji earthquake in Japan (1995) and the Chi-Chi Earthquake in Taiwan (1999), medical equipment (e.g. medicine cabinets and X-ray machines) was damaged seriously, and hence it resulted to significant shortage of emergent medical capacities of hospitals. Currently, the Department of Health (DOH) in Taiwan has completed the simplified evaluation of seismic capacity, electrical and mechanical systems of DOH hospitals, but the specific seismic capacity of medical equipment was not considered yet. For large hospitals, a lot of medical equipment is attached to different

types of structures with miscellaneous attachment types. Therefore, both the efficiency and accuracy should be considered for the simplified evaluation of seismic capacity and simplified seismic design of medical equipment.

In this study, in cooperation with a large hospital (hereinafter referred to as N Hospital), the installation manual for nonstructural components in a hospital and the practical suggestions are proposed and integrated with the construction plan to promote the seismic performance of nonstructural components in the new hospital building (under construction). Considering a great quantity and variety of hospital inventories, the first step in this study is to define the selection criteria to identify the critical and seismic vulnerable nonstructural components, and then, to define the installation types to meet the operational requirement. The seismic vulnerability and associated seismic

¹ Research Fellow, National Center for Research on Earthquake Engineering, chai@ncree.narl.org.tw

² Assistant Research Fellow, National Center for Research on Earthquake Engineering, frlin@ncree.narl.org.tw

demand can be determined by the developed simplified seismic evaluation and design programs, and further, the design parameters for anchors and some non-destructive seismic restraint devices can be calculated directly by the programs. In addition to the traditional attachments, the auxiliary non-destructive seismic restraint devices were also proposed for general nonstructural components. Furthermore, some critical and vulnerable medical equipment items were chosen for shaking table tests to verify the application of proposed simplified evaluation and design forms as well as the recommended seismic restraints.

Survey of Critical Medical Equipment

Considering a great quantity and variety of hospital inventories, the first step in this study is to define the selection criteria to identify the critical and seismic vulnerable nonstructural components, and then, to define the installation types to meet the operational requirement. The seismic vulnerability and associated seismic demand can be determined by the developed simplified seismic evaluation and design programs, and further, the design parameters for anchors and some non-destructive seismic restraint devices can be calculated directly by the programs. In addition to the traditional attachments, the auxiliary non-destructive seismic restraint devices were also proposed for general nonstructural components. Furthermore, some critical and vulnerable medical equipment items were chosen for shaking table tests to verify the application of proposed simplified evaluation and design forms as well as the recommended seismic restraints.

By the supports of the N Hospital, the survey questionnaire for the critical categories of medical equipment after a catastrophic earthquake was answered by head nurses (Fig.1). Basic features of critical medical equipment in nine medical spaces in the N Hospital were identified, and could be classified into three attachment types, i.e. wheel movable, freestanding, and desktop ones. Vulnerable items among the critical equipment were then identified by simplified evaluation forms. The simplified design forms were presented for non-destructive seismic restraint devices as well.

According to the results of questionnaires and simplified evaluation forms, nine vulnerable medical equipment items were chosen for shaking table tests. Non-destructive seismic-restraint devices were also proposed for each equipment item. Test results revealed that restraint devices actually contribute to decrease displacement response (Fig.2), but it also increases acceleration response of the equipment. Besides, damages of adhesive layer between restraint devices and equipment or anchors at partition wall appeared under larger earthquakes (Fig.3). Therefore, the pull-out strength of partition wall and the adhesive strength of non-destructive devices might be the next

research subjects for seismic design of medical equipment.

Simplified Seismic Design Programs

In general, the installation types for nonstructural items are considered to meet the operational requirement. For seismic consideration, it is required to improve the seismic capacity of installation devices for nonstructural components, and meanwhile, not to obstruct the functionality of nonstructural components and equipment. The seismic restraint devices for general nonstructural components can be divided into four categories according to different installation types, where the component can be rigidly mounted, vibration isolated, suspended or classified as portable ones.

Based on the *Seismic Design Code for Buildings in Taiwan* (2005) and other references, the seismic demand on attachments of nonstructural components and medical equipment can be automatically calculated by MS Excel software. In addition, as shown in Table 1, a simplified seismic design form for post-installed anchorage was presented according to ACI 318-02 (2002). Based on the determined design parameters (e.g. number of anchors at each support, anchor size, and embedded depth), the attachments of equipment can be designed to satisfy the specified seismic demands. However, the support of medical equipment may be not designed with bolt holes in advance and it is unlikely to drill holes at the shell of equipment. In view of this situation, the additional non-destructive seismic restraint devices should be considered, and hence, the simplified seismic design forms for such devices for medical equipment were presented in this study. One example for the Z-shape stopper is illustrated in Table 2.

Pull-out and Shaking Table Tests

Based on the survey questionnaires and simplified evaluation for medical equipment at each critical medical space in the N Hospital, all medical equipment can be classified into three categories according to its type of attachment, namely, freestanding items (e.g. safety cabinet), wheel movable items (e.g. medical trolley, micro-selectron, pharmaceutical refrigerator, mass infuser, hyperbaric oxygen capsule, dialysis machine), and desktop items (e.g. gamma counter). Meanwhile, more vulnerable medical equipment in each category was subjected to shaking table tests. In this study, as summarised in Table 3, Z-shape stoppers and some auxiliary non-destructive seismic restraint devices, such as brakes and adhesive belts (such as Thumb Lock), were proposed and designed for equipment according to its daily use. In addition, the tensile strength of adhesive and clasp belts were confirmed by pull-out tests. The test results show that most damages occurred at the

adhesive layer between restraint devices and equipment or at the anchors on partition wall.

The input excitation that is compatible with the Required Response Spectrum (RRS) as specified by AC-156 can be determined from the time histories of floor response acceleration at ChiaYi Potz Hospital in Chi-Chi Earthquake. The amplitude of input time histories was scaled linearly to the design earthquake with PGA of 0.32g. The N Hospital is a 10-story building, and most of critical medical equipment is located from B1F to 3F, therefore, the RRS for shaking table tests were classified into two groups with $z/h=0$ and $1/3$, respectively, according to their location.

For the equipment items without seismic restraint devices, most responses in shaking table tests were quite consistent with the response identified by the simplified evaluation form (i.e. fixed well, rocking, sliding or overturning). Based on the test results, it can be observed that seismic restraint devices efficiently decreased displacement responses and possibilities of overturning or bumping with other items. However, restraint devices would inevitably increase the acceleration responses of equipment items. Take dialysis machine and mass infuser as examples, Thumb Lock or belt devices can decrease the amount of sliding displacement, but result in a sharp increase of response acceleration because of the impact force. To reduce impact force and to avoid resonance of internal components in medical equipment, using ductile restraint devices or adding energy-dissipating devices (such as rubber pads) are suggested. In addition, the fundamental frequencies of medical equipment with restraint become generally higher than those without any restraint.

Conclusions

In cooperation with the N Hospital, the survey questionnaire for the critical categories of medical equipment after a catastrophic earthquake was answer by head nurses. Basic features of critical medical equipment in nine medical spaces in the N Hospital

were identified, and could be classified into three attachment types, i.e. wheel movable, freestanding, and desktop ones. Vulnerable items among the critical equipment were then identified by simplified evaluation forms. The simplified design forms were presented for non-destructive seismic restraint devices as well.

According to the results of questionnaires and simplified evaluation forms, nine vulnerable medical equipment items were chosen for shaking table tests. Non-destructive seismic-restraint devices were also proposed for each equipment item. Test results revealed that restraint devices actually contribute to decrease displacement response, but it also increases acceleration response of the equipment. Besides, damages of adhesive layer between restraint devices and equipment or anchors at partition wall appeared under larger earthquakes. Therefore, the pull-out strength of partition wall and the adhesive strength of non-destructive devices might be the next research subjects for seismic design of medical equipment.

References

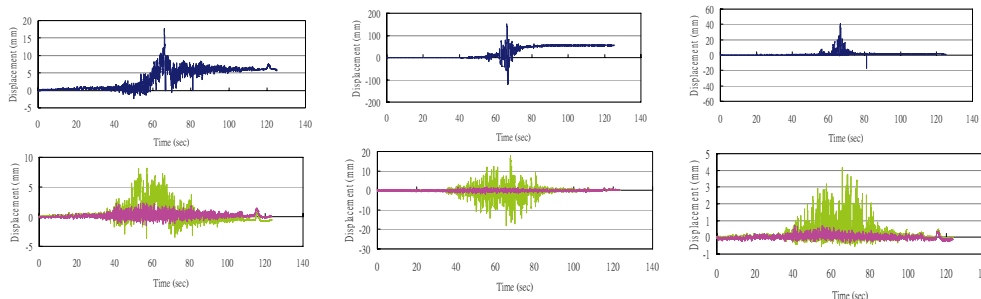
Chai, J-F., Yao George C. and Lin, Fan-Ru, (2008). "Simplified Study on the Seismic Design of Nonstructural Components in a Hospital", NCREE, Taiwan, NCREE-09-018 (in Chinese).

ACI Committee 318, (2002). "Building Code Requirements for Structural Concrete (ACI 318-02) and Commentary (ACI 318R-02)," American Concrete Institute, Detroit.

ASCE/SEI 7-05, Minimum Design Loads for Buildings and Other Structures, American Society of Civil Engineers, 2006.

FEMA 356, prestandard and commentary for the seismic rehabilitation of buildings, Federal Emergency Management Agency (FEMA), Washington, D.C, November 2000.

SB 1953 Regulations, Title 24, Part 1, California Building Standards Administrative Code , Chapter 6, OSHPD, 2001



* device A: top/bottom stoppers; device B: bottom stoppers

Fig.2 Relative displacement between the top and bottom of the safety cabinet specimen



Fig.1 Examples of critical medical equipment selected from questionnaire results

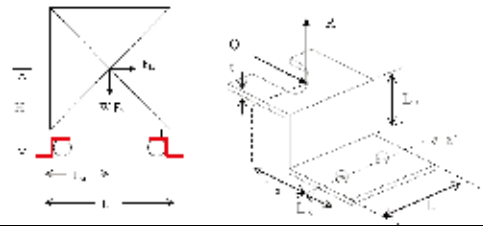


Fig.3 Failure of seismic restraint devices: pull out of expansion anchor (left), loosen belt (middle), and failure of adhesive layer attached on the table (right)

Table 1: Simplified seismic design form for anchorage

No.		03	05
Equipment Name		Safety Cabinet	Refrigerator
Evaluate Results	Y: seismic design required; N: not required	Y	Y
	Response of equipment	Rocking	Rocking
Horizontal seismic force (kgf)		166.3	216.0
Vertical seismic force (kgf)		83.2	108.0
Number of total attachments		3	2
Number of attachments at short side		1	1
Number of anchor bolts at one attachment		2	3
Spacing of anchor bolts at one attachment (inch)		5	2
Size of anchor bolt (M8, M10 ...)		M8	M8
Embedded depth of anchor bolt (inch)		2	2
Concrete strength f'_c (psi)		2000	2000
Maximum shear force at one attachment (kgf)		55.44	108
Maximum tensile force at one attachment (kgf)		139.8	276.8
Maximum normal force at one attachment (kgf)		523.7	462.9
$(V/V_a)^{5/3} + (N/N_a)^{5/3}$		0.4	0.63
Seismic capacity of attachment		OK	OK

Table 2: Seismic design form of non-destructive seismic restraint devices (Z-shape stopper)



No.		03	05
Equipment Name		Safety Cabinet	Refrigerator
Width L1 (cm)		130	125
Height L2 (cm)		12	15
Distance L3 (cm)		7	6
Distance L5 (cm)		2.5	4
Height of mass center: H_G (cm)		350	106
Distance L_G at short side (cm)		38	38
Distance L at short side (cm)		76.5	77
Allowable bending stress of stopper (kgf/cm ²)		2400	2400
Size of anchor bolt (M8, M10,...)		M8	M8
Thickness of stopper plate (cm)		0.15	0.19
Tensile force for each bolt (kgf)		265.6	230.6
Tensile force for each bolt (kgf)		27.7	36.0
$(V/V_a)^{5/3} + (N/N_a)^{5/3}$		1.00	0.41
Seismic capacity of attachment		OK	OK
Desig n results	Thickness of plate (cm)	0.2	0.2
	Bolt / embedded depth	M8/ 2in.	M8/ 2 in.

Table 3: Proposed seismic restraint devices for the medical equipment

Medical Equipment	Bearing	seismic restraint devices A	seismic restraint devices B
safety cabinet	adjustable glides	top/bottom stoppers	bottom stoppers
pharmaceutical refrigerator	iron casters	against the wall / Thumb Lock	against the wall
medical trolley supporting defibrillator	rubber casters	diagonal braking trolley/ defibrillator restrained by Thumb Lock	diagonal braking trolley / defibrillator restrained by plastic clasps and cable
micro-selectron mass infuser	medical equipment casters	against the wall / Thumb Lock	Braking casters
hooded ball casters	hooded ball casters	Thumb Lock	alternative devices (metal clasps and cable)
dialysis machine	hooded ball casters	Thumb Lock	alternative devices (metal clasps and cable)
gamma counter	rubber glides	Thumb Lock	angles and rubber pads

Development of Raw Data Storage Module on a Structural Health Monitoring Prototype

Ming-Yi Shen¹, Tzu-Kang Lin² and Kuo-Chun Chang³

沈明毅¹、林子剛²、張國鎮³

Abstract

Recently, structural health monitoring (SHM) has become an important issue in civil engineering. As structures and facilities of high-technological industries may be seriously damaged during a major earthquake, which will surely create a huge loss in the country's economy, researchers start to develop customized SHM system for these industries. To enhance the function of the SHM prototype developed in 2010, a raw data storage module has been proposed in this study to back up and support real-time processing.

Keywords: structural health monitoring, raw data storage

Introduction

Various structures are usually damaged or collapsed unexpectedly due to aging or external loadings. As no significant phenomenon was observed on these structures before the catastrophe, the structural health monitoring (SHM) concept started to play an important issue in civil engineering as various algorithms and techniques have been proposed in the last few decades (Farrar et al., 2000).

With the development of SHM technique, research on raw data storage was also conducted for establishing the database required by scenario simulation (Fergus, 2003). As the on-site SHM system may be malfunctioned by the harsh environment faced, it is necessary to develop a robust raw data storage mechanism.

SHM Prototype

Traditionally, monitoring data are transmitted back to the monitoring center, and data processing is then completed. As data transmission needs to be implemented before the diagnosis, the system may become unstable or time-consuming. To solve this problem, a novel concept of in situ processing has been proposed. An SHM prototype was successfully established in 2010 to rapidly evaluate the health condition of structures by the vibration signals

received.

The SHM algorithm is composed of AR-ARX Expression Array and Bayesian Classification. By the processor installed on the prototype, large data flow can be simplified to a simple SHM condition index and be transmitted back to the monitoring center through wireless protocol.

High portability of the SHM system can be achieved easily. As shown in Fig. 1, the SHM prototype was based on a platform of NI CompactRIO 9074. With the support of customized software, the SHM algorithm can be optimized with the independent and parallel-processing characteristics.



Fig. 1 SHM prototype

¹ Undergraduate student, National Taiwan University Civil Engineering, ckwuda@gmail.com

² Associate Research Fellow, National Center for Research on Earthquake Engineering, tklin@ncree.org.tw

³ Professor, National Taiwan University Civil Engineering Department, ciekuo@ntu.edu.tw

Raw Data Storage Module

The raw data storage module was developed to enhance the performance of the SHM prototype, where the feasibility of real-time processing has been demonstrated in 2010. The NI 9215 Input Module with 16-bit resolution and four 100 kS/s channels was chosen as the analog input for data acquisition. The operating temperature ranges from -40 to 70 °C.



Fig. 2 NI 9215 Module

Regarding the raw data storage module, the NI 9802 SD Card Module was selected with 4 GB storage capacity and a sustained data write/read speeds of 2 MB/s. To protect the data recorded, a special mechanism was designed to absorb 50 g shock and 5 g vibration ratings. The operating temperature also ranges from -40 to 70 °C.



Fig. 3 NI 9802 Module

To obtain a stable data acquisition rate, the Field-programmable Gate Array (FPGA), advantageous for high precision and parallel processing, was applied in programming, and a reliable 200Hz was achieved. The annoying time delay problem faced in sampling of the original prototype was solved to support the utilization of NI 9802. The SD Card Method in FPGA I/O Method Node was used with the FPGA I/O Property Node in design of program. The data acquired by NI 9215 was deposited into the SD Card following the steps of Open File Method, Write Method, and Close Method.

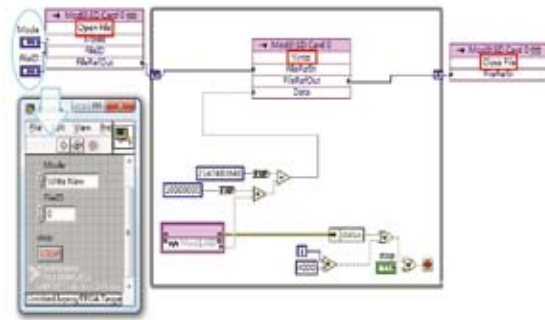


Fig. 4 The FPGA methods

Due to the restriction of format being supported by NI 9802, the raw data are deposited in 16-bit digital format. Meanwhile, as FPGA can only process integer, shifting and zooming were applied on original vibration data of floating format for later reformatting.

The function of loop number in the program designed can be used with versatile purposes. In this research, the loop number was used to control the data point collected in a single file and the time to trigger overwrite.

By using the “Case Structure” in the LabView software, the “False” signal is transmitted to the “Case Structure” when the loop number is smaller than the preset number, and a new signal is sent to the part “Mode” to open a new file with the command “Write New.” On the other hand, the “True” signal is submitted to the “Case Structure” to overwrite the file with the command “Write Over.”

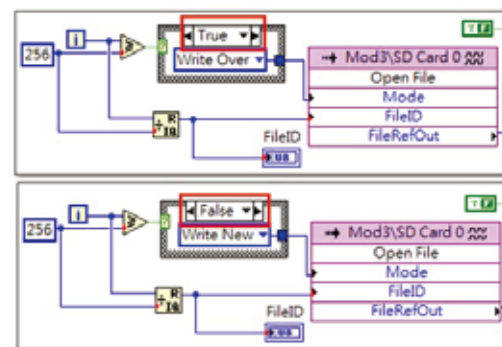


Fig. 5 Function of overwriting

The basic concept of the mobile SHM module designed was to process data collection and algorithm diagnosis in parallel. The recorded raw data can be accessed easily by utilizing the memory card treated as an on-site backup mechanism. Therefore, the conversion of compressed raw data is not included in the LabView-based software. The data is decoded independently by a post-processing software to meet the portability requirement.

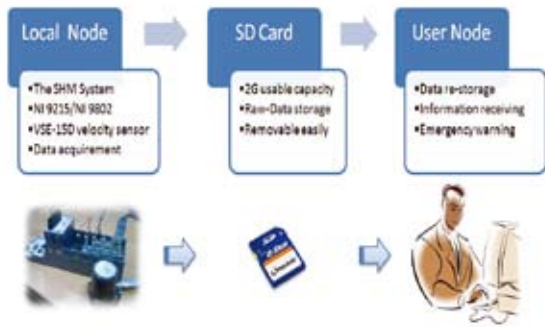


Fig. 6 Concept of Raw Data Storage System

As shown in Fig. 7, the 16-byte binary file deposited in the on-site memory card cannot be used directly for damage assessment as the vibration signal is represented by 16 characters, which hinders the health monitoring task. To solve this, a customized Matlab-based program shown in Fig. 8 was used to convert the raw data into practical vibration signals with techniques of shifting and zooming. A file in the commonly seen text format is shown in Fig. 9 to demonstrate the final performance of the system.

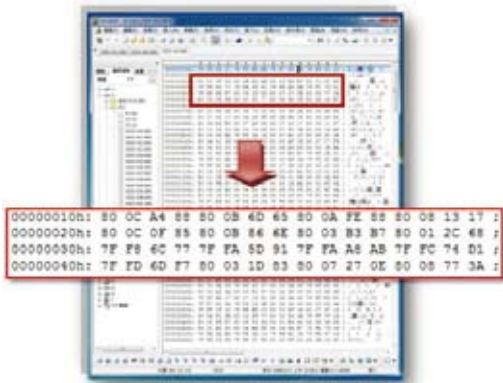


Fig. 7 Original data from the bin file



Fig. 8 The Matlab decoding program



Fig. 9 the vibration data in text form

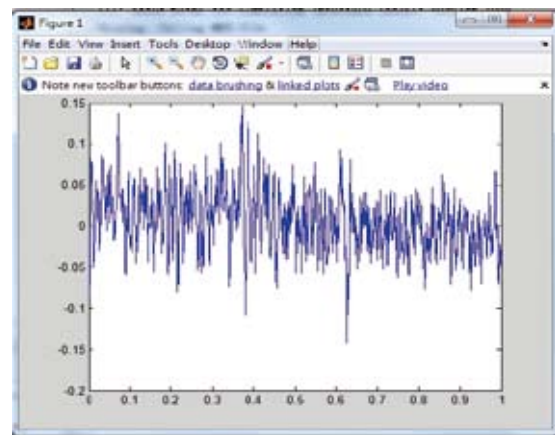


Fig. 10 Vibration Converted by Matlab-based Program

System Performance Verification

To verify the performance of the proposed system, the data recorded by the mobile SHM module was compared with signals from SPC-51, an industrial product of Tokyo Sokushin Co., Ltd. with high precision and reliability on instrumentation. However, the poor portability and no real-time processing function becomes the main drawback that needs to be improved.



Fig. 11 SPC-51 System

In order to fairly compare the performance between the two systems, same type of sensors were used to monitor the structural response of

identically-located measurement, and recorded data were evaluated in both time and frequency domains.



Fig. 12 Comparison in time domain

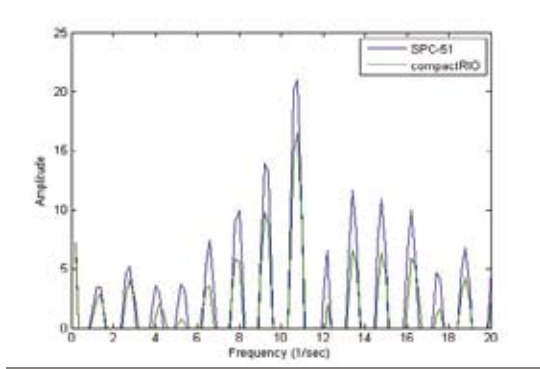


Fig. 13 Comparison in frequency domain

As shown above, high capability of the proposed SHM system can be expected in time and frequency domains. The result strongly supports the applicability of the SHM system developed for its instrumentation and raw data storage.

Conclusion

A novel SHM module has been proposed in this research. With the newly-developed module, vibration data can be precisely recorded with high reliability, portability, and precision, while the raw data can also be processed on site. A mechanism was also built for rapid conversion and real-time processing of highly compressed data to useful information.

References

- C. R. Farrar, Duffey T. A., S. W. Doebling and Nix D. A., “A Statistical Health Monitoring Recognition Paradigm for Vibration-base Structural Health Monitoring”, Proceeding 2nd International Workshop on Structural Health Monitoring , Stanford, CA, September 8-10, pp 764-773.(2000)
- Fergus, Adrian; “Long-term storage of chromatographic data”; Source: Scientific Computing and Instrumentation, v 20, n 2, p C/20-C/22+C/25, January 2003

Analytical and Experimental Studies on Seismic Behavior of Mid-Story Isolated Buildings (II)

Shiang-Jung Wang¹, Kuo-Chun Chang², Jenn-Shin Hwang³, Jia-Yi Hsiao⁴ and Ying-Chen Hung⁵

汪向榮¹、張國鎮²、黃震興³、蕭佳益⁴、洪瑩真⁵

Abstract

This study aims to investigate the discrepancies of dynamic characteristics and seismic responses in base-isolated and mid-story isolated buildings through a series of shaking table tests. The system identification results indicate that a mid-story isolated structure has less fundamental modal quantities, including effective vibration frequency, damping ratio and participation mass ratio, than a base-isolated structure. It is particularly evident when the isolation system is designated at a higher story or when the substructure below the isolation system is not sufficiently stiff. Besides, it can be found from the test results that there exists obviously a phase lag of larger than 90 degrees between the seismic responses acting at the isolated superstructure and substructure when the peak seismic responses occur at the isolation system. Therefore, the influence of higher modes on the seismic responses of mid-story isolated buildings should be paid more attention. Acknowledging the contribution of higher modes to the mid-story isolation design, the peak seismic responses of the test structures are predicted by multiple and simplified modal response spectrum analysis procedures in which a sufficient number of higher modes and only one representative residual mode are taken into account, respectively. Based on the comparison between analytical and experimental results, it is disclosed that for the preliminary mid-story isolation design prior to performing nonlinear response history analyses, the modal response spectrum analysis procedure considering a sufficient number of higher modes is more applicable than that considering only one representative residual mode.

Keywords: mid-story isolation, higher modes, equivalent linear, modal response spectrum analysis

Introduction

The mid-story seismic isolation design method, in which the isolation system is incorporated into the mid-story rather than the base of the building, is recently gaining popularity for the seismic protective design of buildings. In the past decade, the effectiveness of mid-story isolation design in reducing seismic demand of the superstructure above the isolation system has been proved numerically (Ogura *et al.*, 1999). The dynamic characteristics and seismic responses of mid-story isolated buildings have been investigated numerically using various simplified structural models (Koh and Kobayashi, 2000;

Murakami *et al.*, 2001; Wang *et al.*, 2011). Among these proposed models, the simplified structural model in which three lumped masses were respectively assigned at the substructure below the isolation system, super-floor above the isolation system and superstructure, comprehensively considered the effects arising from both the substructure and superstructure on the modal quantities and dynamic responses of a mid-story isolated building (Wang *et al.*, 2011). Assuming the first modal frequency ω_1 be very close to the effective isolated frequency ω_{iso} and employing an equivalent linear model composed of effective stiffness and equivalent damping ratio to represent the hysteretic behavior of the isolation

¹ Associate Research Fellow, National Center for Research on Earthquake Engineering, sjwang@ncree.narl.org.tw.

² Director General, National Center for Research on Earthquake Engineering, kcchang@ncree.narl.org.tw.

³ Deputy Director General, National Center for Research on Earthquake Engineering, jshwang@ncree.narl.org.tw.

⁴ Graduate Student, Dept. of Construction Engineering, Taiwan University of Science and Technology, willy.shiau@gmail.com.

⁵ Graduate Student, Dept. of Civil Engineering, National Taiwan University, r97521207@ntu.edu.tw.

system (Kelly, 1990), the first modal damping ratio ζ_1 and the first modal participation mass ratio L_1 can be approximated by (Wang *et al.*, 2011)

$$\zeta_1 = \frac{\xi_{iso}}{\left(1 + \frac{2(1+r_{sup})}{r_{sub}} \left(\frac{\omega_{iso}}{\omega_{sub}}\right)^2 + \frac{2r_{sup}}{1+r_{sup}} \left(\frac{\omega_{iso}}{\omega_{sup}}\right)^2\right)} \quad (1)$$

$$L_1 = \frac{r_{sub} + 2(r_{sub} + r_{sup} + 1) \left(\frac{\omega_{iso}}{\omega_{sub}}\right)^2 + \frac{2r_{sub}r_{sup}}{1+r_{sup}} \left(\frac{\omega_{iso}}{\omega_{sup}}\right)^2}{(1+r_{sub}+r_{sup}) \left(\frac{r_{sub}}{1+r_{sup}} + 2 \left(\frac{\omega_{iso}}{\omega_{sub}}\right)^2 + \frac{2r_{sub}r_{sup}}{(1+r_{sup})^2} \left(\frac{\omega_{iso}}{\omega_{sup}}\right)^2\right)} \quad (2)$$

where $r_{sub} = m_{sub}/m_{iso}$; $r_{sup} = m_{sup}/m_{iso}$; $\omega_{sub} = \sqrt{k_{sub}/m_{sub}}$; $\omega_{iso} = \sqrt{k_{iso}/(m_{iso} + m_{sup})}$; $\omega_{sup} = \sqrt{k_{sup}/m_{sup}}$; $\xi_{iso} = c_{iso}/[2\omega_{iso}(m_{iso} + m_{sup})]$; m_{sub} , m_{iso} and m_{sup} = correspondingly the seismic reactive masses of the substructure, super-floor and superstructure; k_{sub} and k_{sup} = the elastic lateral stiffnesses of the substructure and superstructure, respectively; k_{iso} = the effective lateral stiffness of the isolation system; and c_{iso} = the equivalent viscous damping coefficient of the isolation system.

It can be found from equations (1) and (2) that both ζ_1 and L_1 are more significantly affected by the masses and lateral stiffnesses of the substructure than those of the superstructure. The increases in r_{sub} and $\omega_{sub}/\omega_{iso}$ result in the increase of ζ_1 and the reduction of L_1 . Besides, from the maximum seismic responses calculated using the response spectrum analysis under decoupling approximation, it is seen that the maximum inertia force exerting at the substructure is primarily attributed to the higher mode responses rather than to the fundamental mode response. It is also found that the maximum inertia force acting at the substructure due to the higher mode responses contributes significantly to the maximum base shear force.

In order to demonstrate the analytical results obtained from the previous research (Wang *et al.*, 2011), and to investigate the discrepancies of dynamic characteristics and seismic responses in base-isolated and mid-story isolated buildings, a series of shaking table tests on scaled down steel structural models with base and mid-story isolation systems were performed in this study. In addition, since the dynamic behavior of a mid-story isolated structure may not be identical to, or even becomes more complex than, that of a base-isolated structure, two modal response spectrum analysis procedures appropriately considering the contribution of higher modes were used to predict the peak seismic responses of the test structural models. Based on the comparison of test results and numerical predictions by these two analysis procedures, the feasibility of the modal response spectrum analysis procedures for the preliminary design of mid-story isolated buildings is explored thoroughly.

Test Structural Models

The superstructures of three seismically isolated structural models, Specimens A, B and C, as shown in Fig. 1, are all identical but isolated at the base of the superstructure, at the top of a one-story substructure, and at the top of another two-story substructure, respectively. Therefore, Specimen A is a conventional base-isolated building while Specimens B and C are the so-called mid-story isolated buildings. The test specimens are assumed as 1/4 scale-down models. The four floors from bottom to top of the superstructure are sequentially denoted as SUP-1, SUP-2, SUP-3, and ROOF. In addition, the floor of the substructure of Specimen B is denoted as SUB-1 and the two floors from top to bottom of the substructure of Specimen C are sequentially denoted as SUB-1 and SUB-2. The isolation system is composed of four high damping rubber bearings (HDRB). Three earthquake records, denoted as 921TCU047, I-ELC270 and KJM000, are selected for the earthquake inputs.



Fig. 1 Photos of Specimens A, B and C

Test Results

Assuming the hysteretic behavior of HDRBs being represented by an equivalent linear model, the modal quantities of all the specimens are identified using the system realization using information matrix (SRIM) (Juang, 1994), as summarized in Table 1. It is seen that the effective higher modes of Specimens B and C are the third mode and the second mode, respectively. Furthermore, the mid-story isolation design (e.g. Specimen B or C) has more significant participation of higher modes, higher fundamental modal period and less fundamental modal damping ratio than the base isolation design (e.g. Specimen A). It is particularly evident when the isolation system is designated at a higher story or the substructure is more flexible (e.g. Specimen C). The first modal damping ratios and the first modal participation mass ratios of Specimens B and C are also calculated respectively using equations (1) and (2), as summarized in Table 1. It is observed that the predicted values are very comparable to, as well as more conservative than, the identified results.

Table 1 Identified modal quantities of specimens

Input Excitation	300% 921TCU047			200% I-ELC270			100% KJM000		
	A	B	C	A	B	C	A	B	C
Modal Natural									
Period (sec)	1 st Mode	0.71	0.82	0.90	0.66	0.75	0.87	0.84	0.85
	2 nd Mode	0.11	0.11	0.22	0.11	0.11	0.22	0.11	0.11
	3 rd Mode	-	0.09	0.13	-	0.09	0.14	-	0.09
Modal Damping Ratio (%)	1 st Mode	17.92	16.70	13.74	19.13	16.07	14.57	18.28	17.38
	2 nd Mode	2.54	2.24	8.07	2.05	1.85	8.48	0.40	1.70
	3 rd Mode	-	7.00	3.33	-	6.22	1.21	-	5.30
ζ_1 Calculated Using Equation (1)		16.14	13.72	10.09	17.37	14.65	14.40	18.00	16.40
									11.14

Modal Participation	1 st Mode	99.88	77.16	67.63	99.75	76.47	67.91	99.84	76.19	66.42
Mass Ratio (%)	2 nd Mode	0.01	2.41	14.96	0.11	1.39	13.98	0.16	3.90	17.48
ξ_1 Calculated Using Equation (2)	3 rd Mode	-	19.51	2.73	-	15.94	0.09	-	15.67	3.94
		-	74.44	61.13		74.73	62.41	-	74.37	60.96

The peak seismic responses subjected to different earthquake excitations are summarized in Table 2. The comparison of peak seismic responses in Specimens A, B and C subjected to the entire earthquake tests is shown in Fig. 2. It can be seen that the peak acceleration responses at the superstructures of Specimens B and C are somewhat enlarged compared with those of Specimen A. Nevertheless, the excellent seismic performance is exhibited by Specimens B and C since the story drift response is still concentrated at the isolation layer and the acceleration response transmitted to the superstructure can be reduced effectively compared with the ground excitation. Moreover, it is found that the maximum deformation response (or the peak shear force response) of the isolation system is increased when the isolation system is installed at a higher story or when the substructure is more flexible. It is because that the fundamental modal damping ratio of a mid-story isolated building becomes smaller with a more flexible substructure. In addition, the significant phase lag existing between the displacement responses at the superstructure and substructure may not be negligible. It is reasonable that the peak story drift response ratios and peak acceleration response ratios are almost reduced with increasing PGA scales.

Table 2 Peak seismic responses of specimens

Input Excitation	300%			200%			100%			
	921TCU047			I-ELC270			KJM000			
Test Specimen	A	B	C	A	B	C	A	B	C	
Maximum Deformation of HDRB (mm)	43.0	45.1	65.1	33.7	38.5	53.8	48.3	54.6	58.0	
Ratio of Peak Acceleration to PGA	ROOF	0.39	0.59	0.42	0.53	0.74	0.61	0.50	0.51	0.65
	SUP-3	0.28	0.32	0.38	0.47	0.60	0.54	0.44	0.48	0.51
	SUP-2	0.26	0.34	0.38	0.41	0.52	0.54	0.39	0.37	0.39
	SUP-1	0.33	0.48	0.37	0.47	0.66	0.51	0.40	0.39	0.48
	SUB-1	-	0.97	0.82	-	0.94	0.97	-	0.76	0.95
	SUB-2	-	-	1.00	-	-	1.27	-	-	-
Peak Shear across Isolation System (kN)	46.8	46.9	68.6	44.8	44.9	55.2	52.8	53.3	58.6	
Peak Base Shear (kN)	46.8	84.0	89.4	44.8	53.4	76.2	52.8	69.1	85.9	

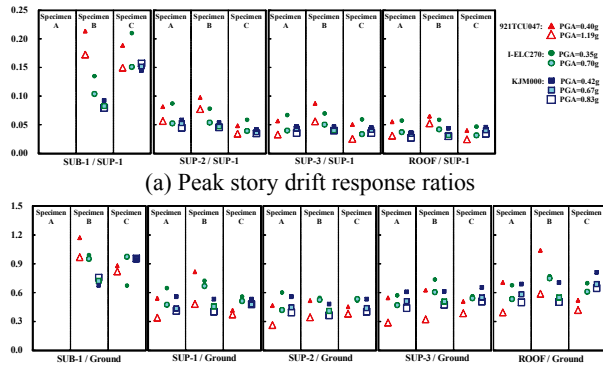


Fig. 2 Comparison of peak story drifts and accelerations at different stories

The force and displacement responses vertically distributed along each floor of Specimen C at different

moments are depicted in Fig. 3. It can be seen that there exists a phase lag of larger than 90 degrees between the seismic responses acting at the substructure and superstructure when the peak seismic responses occur at the superstructure and isolation system. Furthermore, when the peak seismic responses occur at the substructure, the inertia force responses acting at the superstructure are very limited compared with those at the substructure. Consequently, for the mid-story isolation design, the seismic response acting at the superstructure is mainly attributed to the fundamental mode response, while the higher mode responses contribute significantly to the seismic responses acting at the substructure. Test results reveal that the assumption of a single degree-of-freedom system for the superstructure of a mid-story isolated building (*i.e.* the isolation system is the only lateral deformation system as the base isolation design) may not be conservative especially when the substructure is not sufficiently stiff.

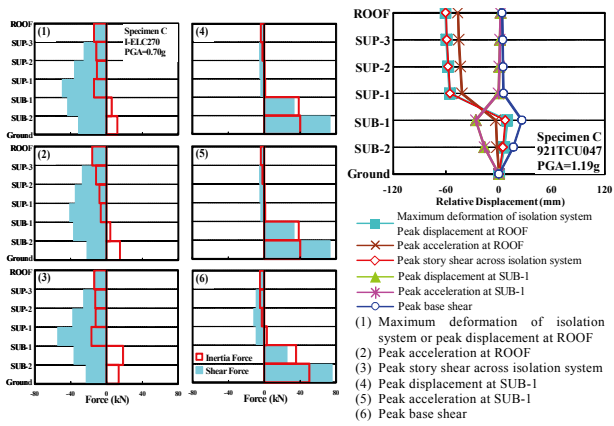


Fig. 3 Vertically distributed force and displacement responses at different instants

Modal Response Spectrum Analysis

Two analysis procedures, (1) multiple modal response spectrum analysis (denoted as MMRSA) and (2) simplified modal response spectrum analysis (denoted as SMRSA), are used in this study to approximate the maximum inelastic responses of test structures under the earthquake tests by the maximum elastic responses obtained from an equivalent linear structural model. In MMRSA, assuming the necessary modal characteristics being rationally substituted by the system identification results, a sufficient number of modes are considered to obtain a combined modal mass participation of at least 90% of the actual mass of a mid-story isolated building. In SMRSA (Ramirez *et al.*, 2000), the fundamental mode and a residual mode that could approximately account for the contribution of higher modes of a mid-story isolated building are considered. It is assumed that the effective period and damping ratio of the representative residual mode are respectively estimated by the vibration period and damping ratio corresponding to the identified effective higher mode. Under the condition that the mode shapes are normalized so that the amplitude is equal to

1 at the roof level, the modal characteristics of the representative residual mode for a mid-story isolated building, including the effective residual modal seismic weight W_R , residual modal participation factor Γ_R and residual mode shape ϕ_{iR} , can be mathematically determined by

$$W_R = W - W_1 \quad (3)$$

$$\Gamma_R = 1 - \Gamma_1 \quad (4)$$

$$\phi_{iR} = \frac{1 - \Gamma_1 \phi_{i1}}{1 - \Gamma_1} \quad (5)$$

where W_1 = the effective fundamental modal seismic weight; Γ_1 = the fundamental modal participation factor; and ϕ_{i1} = the fundamental mode shape.

The comparison of test results and analytical results by MMRSA and SMRSA on the peak displacement, acceleration and story shear force responses at different floors of Specimen B is illustrated in Fig. 4. It is found that the peak seismic responses predicted by MMRSA are comparable with the test envelopes. It is evident that the peak acceleration and story shear force responses at some floors of the superstructure predicted by SMRSA are less than those by MMRSA, while those responses at the substructure predicted by SMRSA are much larger than those by MMRSA. In other words, the adoption of SMRSA may be too rigorous for the substructure but not conservative for the superstructure. The significant difference of peak acceleration and story shear force responses by MMRSA and SMRSA may be caused by the inappropriate approximation of the representative residual mode shape in SMRSA.

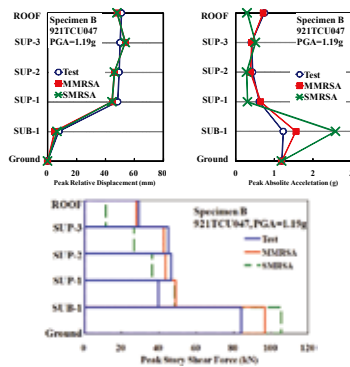


Fig. 4 Comparison of test and analytical results

Conclusions

The dynamic behavior of a mid-story isolated structure becomes more complex than that of a base-isolated structure in which the superstructure can be rationally assumed as a single degree-of-freedom system assigned above the isolation system. From the comparison of the shaking table test results between base-isolated and mid-story isolated structural models, it is disclosed that a mid-story isolated building has less fundamental modal quantities, including effective vibration frequency, damping ratio and participation mass ratio, than a base-isolated building. It is particularly evident when the isolation system is

designated at a higher story or when the substructure is not sufficiently stiff. It is also seen that the seismic response acting at the superstructure is mainly attributed to the fundamental mode response, while the higher mode responses contribute significantly to the seismic responses acting at the substructure. Therefore, the maximum deformation and peak shear force responses of the isolation system are increased when the isolation system is installed at a higher story or when the substructure is more flexible. Considering the contribution of higher modes, two modal response spectrum analysis procedures, as alternatives to the equivalent lateral force design procedure, are adopted to predict the peak seismic responses of the test structural models. It is found that the peak seismic responses of a mid-story isolated building can be well captured by the multiple modal response spectrum analysis procedure rather than the simplified modal response spectrum analysis procedure in which only a residual mode is considered. Consequently, the modal response spectrum analysis procedure considering a sufficient number of modes is applicable for the preliminary design of mid-story isolated buildings.

References

- Ogura, K., Takayama, M., Tsujita, O., Kimura, Y. and Wada, A., (1999). "Seismic Response of Mid-Story Isolated Buildings", *Journal of Structural and Construction Engineering*, Architectural Institute of Japan. 516, 99-104.
- Koh, T. and Kobayashi, M., (2000). "Vibratory Characteristics and Earthquake Response of Mid-Story Isolated Buildings", *Memoirs of the Institute of Sciences and Technology*, Meiji University. 39(12), 97-114.
- Murakami, K., Kitamura, H. and Matsushima, Y., (2001). "The Prediction for Seismic Responses of The Two-Mass Model with The Mid-Story Isolation System", *Journal of Structural and Construction Engineering*, Architectural Institute of Japan. 549, 51-58.
- Wang, S.J., Chang, K.C., Hwang, J.S. and Lee, B.H., (2011). "Simplified Analysis of Mid-Story Seismically Isolated Buildings", *Earthquake Engineering and Structural Dynamics*. 40(2), 119-133.
- Kelly, J.M., (1990). "Base Isolation: Linear Theory and Design", *Earthquake Spectra*. 6(2), 223-244.
- Juang, J.N., (1994) "Applied System Identification", Prentice Hall, New Jersey.
- Ramirez, O.M., Constantinou, M.C., Kircher, C.A., Whittaker, A.S., Johnson, M.W. and Gomez, J.D., (2000). "Development and evaluation of simplified procedures for analysis and design of buildings with passive energy dissipation systems", Report No. NCEER-00-0010, National Center for Earthquake Engineering Research, State University of New York at Buffalo, New York.

Evaluation of the Maximum Sliding Displacements of Unanchored Equipment under Seismic Excitations

Keng-Chang Kuo¹ Hung-Wei Chiang² Pei-Yang Lin³ and Fan-Ru Lin⁴

郭耕杖¹、江宏偉²、林沛暘³、林凡茹⁴

Abstract

The main objective of this study was to evaluate the maximum sliding displacements of unanchored equipment placed on the ground or floor during earthquakes. Shaking table tests were conducted to investigate the sliding responses of unanchored equipment. In the tests, steel frames were used to represent equipment and were placed on plastic floors connected to the shaking table. The base of steel frames adopted three types of materials: rubber, plastic, and Teflon, corresponding to high, medium, and low coefficients of friction, respectively. It is observed that the maximum sliding displacement may result from a single predominant sliding incident or multiple sliding incidents due to the effects of stick-slip phenomenon. This paper presents a simple formula using rectangular pulse as input to estimate the maximum sliding displacement of unanchored equipment under earthquakes. From a comparison to the test results, the formula gives reasonable predictions of the maximum sliding displacement. Nevertheless, evaluation of the sliding displacement due to the stick-slip effects needs further study.

Keywords: hospitals, nonstructural components, sliding

Introduction

Experience reveals that damage to medical equipment of hospitals in a seismic event, not only causes monetary loss but also affects medical services (Lin et al., 2009). In hospitals, a great deal of medical equipment cannot be anchored for aesthetic and practical reason and are thus prone to high risk of seismic damage. Of particular interest in this paper is the unanchored equipment undergoing sliding-dominated response under seismic excitations. Excessive sliding displacements may cause unanchored objects to collide with surrounding objects or to fall off a table. Increasing the friction force on the contact surface or providing sufficient space around the unanchored objects can prevent damage due to excessive sliding. Thus, the evaluation of the maximum sliding displacement is important.

Considering the limits of *in situ* surveys on equipment, this paper proposes a simple method to

predict the maximum sliding displacement of unanchored equipment using static friction coefficient and excitation intensity of input motion. Applicability of the method was verified by the results of shaking table tests.

Experimental Evaluation of the Maximum Sliding Displacements of Equipment

Shaking table tests were conducted at the National Center for Research on Earthquake Engineering (NCREE) in Taiwan to investigate the sliding responses of unanchored equipment. In the tests, steel frames, 30cm in width and in depth and 20cm in height, were used to represent equipment (Fig. 1) and were placed on plastic floors connected to the shaking table. The base of the steel frames adopted three types of materials: rubber, plastic, and Teflon, corresponding to high, medium, and low coefficients of friction, respectively. The static friction coefficients

¹ Associate Research Fellow, National Center for Research on Earthquake Engineering, kckuo@ncree.narl.org.tw

² Assistant Research Fellow, National Center for Research on Earthquake Engineering, hwchiang@ncree.narl.org.tw

³ Research Fellow, National Center for Research on Earthquake Engineering, pylin@ncree.narl.org.tw

⁴ Assistant Research Fellow, National Center for Research on Earthquake Engineering, frlin@ncree.narl.org.tw

for these three types of base materials were 0.75, 0.43 and 0.27 obtained from simple pull tests. For each interface condition, nine steel frames placed on the plastic floor were subjected to seismic motions simultaneously (Fig. 2). Seven acceleration time histories from past recorded earthquakes were input uniaxially and horizontally, including four ground motions and three floor responses (see Table 1). In order to initiate the sliding behavior of the rubber-base specimen, the input accelerations were scaled to 1g, except those for the input of Kobe and TCU129.

The sliding responses of the specimens are illustrated in Figs. 3-5. The displacement results were obtained by averaging the displacements of all the nine steel frames. For some cases such as the input of Kobe, the specimen slid forward and backward in one direction with respect to its original location, while for most cases, the specimens slid in two directions. Under the input of El Centro and TCU129, for all the three types of specimens, the maximum sliding displacements resulted from a single predominant sliding incident. In contrast, under the input of CHY1, the maximum sliding displacement resulted from specimens moving in several steps. The multiple sliding incidents were caused by the effects of stick-slip phenomenon (Chaudhuri et al., 2005). Figure 6 shows the relation of the maximum sliding displacements and the excitation intensities of the input motions. It is observed that peak velocity is a better parameter to estimate the maximum displacements than peak acceleration. Thus, this study has adopted peak velocity for the theoretical evaluation of the maximum sliding displacements discussed in the next section.



Fig. 1 Steel frame used in the shaking table tests.



Fig. 2 For each contact surface condition, nine specimens were subjected to the input motions simultaneously.

Table 1 Input motions for the shaking table tests.

No.	Type	Name	Target PA. (g)	Achieved PA. (g)
1	Ground motion	El Centro	1.00	1.08
2		Kobe	0.81	0.84
3		TCU129	0.98	1.08

4	Floor response	TCU014	1.00	1.01
5		TCU3	1.00	0.94
6		CHY1	1.00	0.90
7		HWA0	1.00	1.07

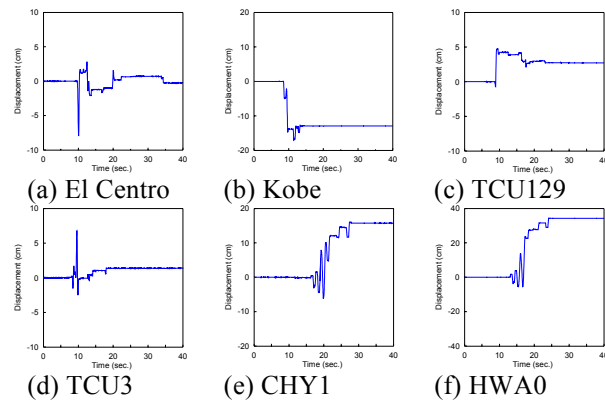


Fig. 3 Time histories of sliding displacements of the Teflon-base specimens.

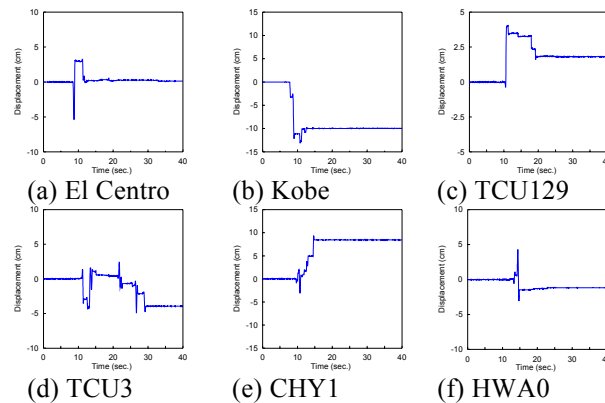


Fig. 4 Time histories of sliding displacements of the plastic-base specimens.

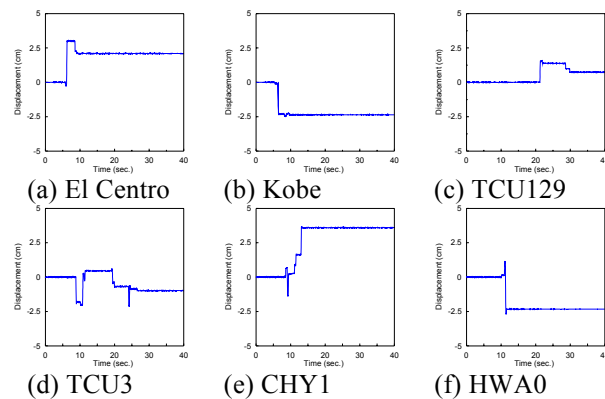


Fig. 5 Time histories of sliding displacements of the rubber-base specimens.

Derivation and Verification of the Theoretical Evaluation of the Maximum Sliding Displacements

In the theoretical evaluation, this study adopted a rectangular acceleration pulse for the input motion, with peak value A of the original acceleration time

history. The duration of the pulse is calculated by dividing V with A , where V is the peak velocity. As kinetic friction coefficient is not readily obtained from simple pull tests for *in situ* surveys, only static friction coefficient μ_s (hereafter μ) is used to describe the resistance force of the contact surface of the sliding object. No distinction is made between static and kinetic friction coefficients. The acceleration pulse is assumed to be an impulsive force applied to the resting object. Thus, the initial sliding velocity is calculated as $v_s = A \cdot T_p = V$ when the input acceleration is greater than the frictional force of the contact surface. Then, the sliding object stops due to friction force after a certain duration and the maximum displacement is obtained based on energy equilibrium.

$$D = \frac{V^2}{2\mu g} \quad (1)$$

The required minimum input velocity corresponding to the input acceleration that initiates the sliding behavior of the object is given by Eq. 2.

$$V_0 = \frac{\mu g}{2\pi F_e} \quad (2)$$

where $F_e = \frac{A}{2\pi \cdot V}$ is the equivalent dominant frequency used as a simple index to represent the main frequency contents of the input motion. Therefore, the theoretical evaluation of the maximum displacements of unanchored equipment under earthquakes proposed in this paper can be arranged as follows:

$$D = \begin{cases} \frac{V^2}{2\mu g}, & V \geq \frac{\mu g}{2\pi F_e} \\ 0, & V < \frac{\mu g}{2\pi F_e} \end{cases} \quad (3)$$

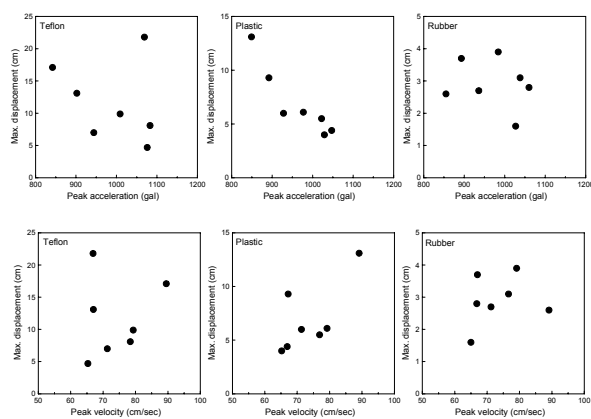


Fig. 6 The relationship among the maximum sliding displacement, and the peak acceleration (top) and velocity (bottom) of the input motions.

Figure 7 illustrates the comparison of the predicted and test results of the maximum sliding displacements for the three types of specimens. In the figure, the ●

and ○ symbols represent the test results for the input of ground motions and the floor responses, respectively. The asterisk (*) beside the symbols denotes that the maximum sliding displacement resulted from multiple sliding incidents. The predicted results, obtained by Eq. 3, are shown with the solid lines, and the dotted lines represent the predicted results modified by multiplying a certain factor as discussed in the succeeding paragraphs. For the Teflon-base specimen, the predicted results are conservative as the solid line is above most of the test results except for those with the asterisks. For the rubber-base specimen, the theoretical equation underestimates the test results. This is due to the difference between the static and kinetic friction coefficients. As an object slides with low velocity, the kinetic friction coefficient becomes lower (Chaudhuri et al., 2005). In Fig. 8, the rubber-base specimen shows a lower sliding velocity compared to the Teflon-base one. Therefore, a lower kinetic friction results in less conservative estimates which were obtained using static friction coefficient. Figure 9 illustrates the ratio of the test results to predicted ones. For the cases that the maximum displacements resulted from multiple sliding incidents, shown with the asterisks in Fig. 7, the average of the ratio is 1.8. For the other cases, the theoretical evaluation shows reasonable applicability. In order to better estimate the maximum displacements resulted from multiple sliding incidents, the estimates obtained by Eq. 3 were multiplied by 1.8. Therefore, using the original and modified estimates, shown with the solid and dotted lines in Fig. 7, a reasonable predicted range of the maximum sliding displacement is provided. Nevertheless, in application, a minimum safety distance of 5cm is recommended regardless of the predicted values.

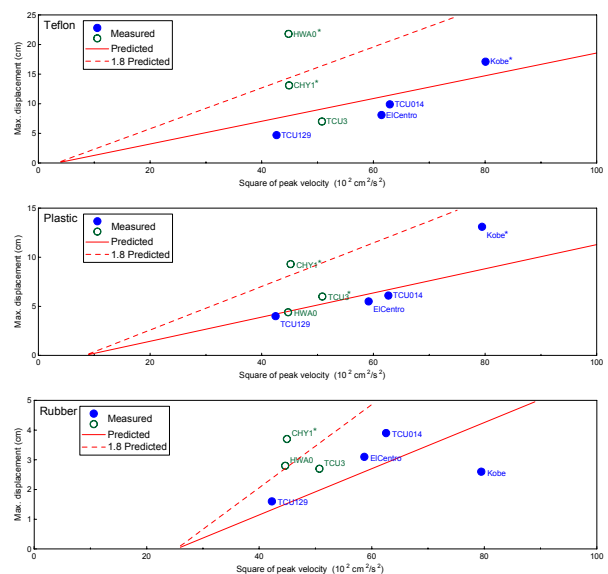


Fig. 7 Comparison of the predicted and test results of the maximum sliding displacements: Teflon- (top), plastic- (middle), and rubber-base specimens (bottom).

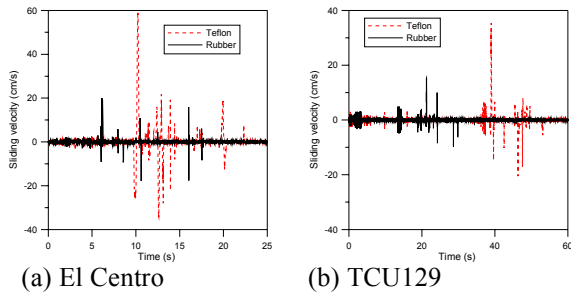


Fig. 8 Comparison of the sliding velocity of the Teflon- and rubber-base specimens under the input of (a) El Centro and (b) TCU129.

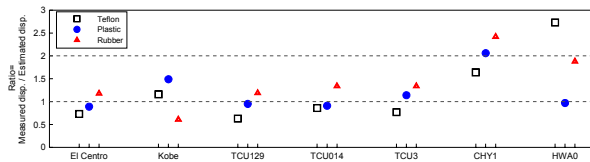


Fig. 9 The ratio of the test results to the theoretical predictions.

Conclusions

In this study, the maximum sliding displacement of unanchored equipment was investigated experimentally. Using acceleration pulse as input, theoretical evaluation of the maximum displacement was proposed. From the comparison of the predicted and test results, the evaluation was modified to better estimate the results due to multiple sliding incidents. Using the original and modified estimates, a reasonable predicted range of the maximum sliding displacement is obtained.

References

- Lin, F.R., and Yao, G.C. (2009), "Characteristics and seismic retrofit of critical nonstructural components of hospitals," *The Magazine of the Chinese Institute of Civil and Hydraulic Engineering*, 36(4), 59-70 (in Chinese).
- Chaudhuri, S.R., and Hutchinson, T.C. (2005), "Characterizing frictional behavior for use in predicting the seismic response of unattached equipment," *Soil Dynamics and Earthquake Engineering*, 25(7), 591-604.

Experimental Study on Seismic Performance of Equipment with Vibration Isolation Devices(II)

Jenn-Shin Hwang¹, Fan-Ru Lin² and Min-Fu Chen³

黃震興¹、林凡茹²、陳閔富³

Abstract

In recent major earthquake events in Taiwan, several damaged spring isolated equipment cases were observed and showed high vulnerability of spring isolators. Recognizing the particular significance of the spring isolators in affecting the earthquake resistant capacity of critical mechanical/electrical systems, such as emergency power supply, water supply and air conditioning system, the purpose of this research is to study the seismic behaviour of the spring isolators in comparison with the Isolation/Restraint system which is composed of spring isolators and snubbers. A diesel generator was used as test specimen to observe realistic seismic responses of spring isolated equipment. Shaking table tests were conducted to study elastic and inelastic behaviour of spring isolators. Testing results were preliminarily analyzed to investigate damage states and dynamic characteristics of spring isolators, and the appropriateness of the dynamic amplification factor for spring isolated equipment was discussed as well.

Keywords: Mechanical and electrical equipment, vibration isolation device, seismic performance

Introduction

The past investigations indicate that the dominant failure mode of most vibration isolation devices is the pop-up condition of the inside spring, as presented in Fig. 1. It can be deduced that, in addition to insufficient strength of the vibration isolation device itself, the significant overturning behavior due to inappropriate arrangement of the equipment mounted on vibration isolation devices (e.g. improper aspect ratios) may result in the failure mode aforementioned.



Fig. 1 Damaged vibration isolation devices due to earthquake.

It is a recognized fact that to maintain functionality

of an important building after an earthquake struck, both structural components and critical Mechanical/Electrical systems (M/E systems) should have well seismic performance. However, several damaged cases during Chi-Chi and Hwa-Lien earthquakes, showed that spring isolated equipment, such as cooling towers, generators, and pumps, may be the seismic resistant weakness of M/E systems (Fig. 2). In Taiwan, the spring isolator products are generally designed according to the weight and operating frequency of the equipment. Earthquake resistant capacity of vibration isolated equipment is seldom considered in practice.



Figure 2. Leakage damage of a spring isolated cooling tower after Hwa-Lien earthquake

¹ Deputy Director General, National Center for Research on Earthquake Engineering, jshwang@ncree.narl.org.tw.

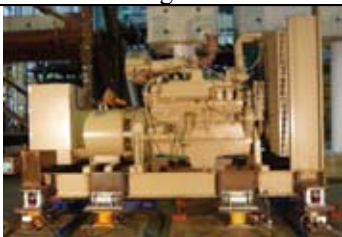
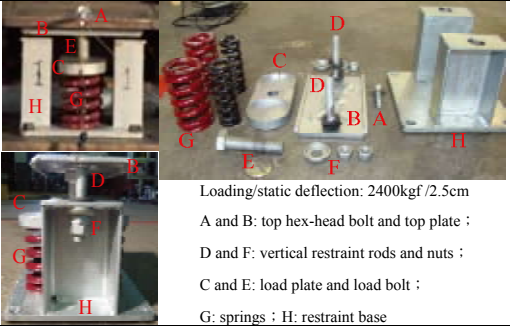
² Assistant Researcher, National Center for Research on Earthquake Engineering, frlin@ncree.narl.org.tw

³ Assistant Researcher, National Center for Research on Earthquake Engineering, mfchen@ncree.narl.org.tw

In order to improve the seismic resistant capacity of spring isolated equipment, this study investigated the present seismic performance of spring isolated equipment in the first place. As shown in Table 1, a 600kW diesel generator was used as testing specimen to observe seismic behaviour of spring isolator under realistic loading distribution. Meanwhile, the reason for choosing a generator was that it is a major equipment to maintain emergency power supply after a strong earthquake. The spring isolated system (I/ system) and Isolation/Restraint system (I/R system) were designed according to the operating frequency and weight of the generator by Taiwanese manufacturer. The I/ system was composed of four spring isolators, and the I/R system was composed of I/ system and additional four snubbers.

As shown in Table 1, the spring isolator can be separated into eight parts. Component A and B are used to connect equipment to the isolated system. Component C and E are used to transfer vertical loading to the springs. Component D, F and H are designed to prevent extremely large vertical vibration when isolated equipment initially starts. Due to lack of consideration for lateral resistance mechanism, lateral gaps exist among components. One is between the vertical restraint rod and restraint base, which is about 5mm and filled with an unfixed thin rubber pad. The other gap is about 2mm and between the top hex-head bolt and top plate. These two components are connected by a washer and resist shear force by friction.

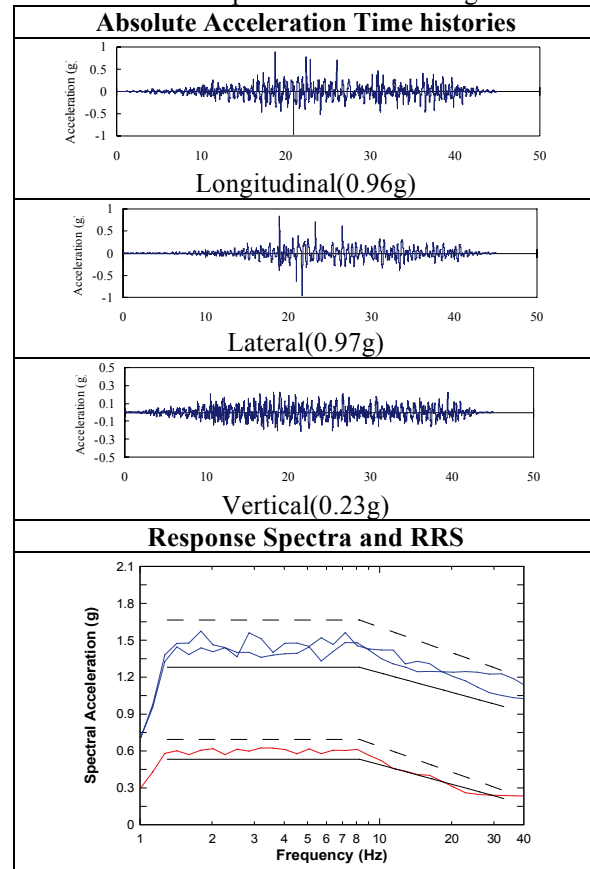
Table 1. Test specimen and components of the associated I/R system.

Diesel generator	
	
Spring Isolator Components	
	
<p>Loading/static deflection: 2400kgf /2.5cm A and B: top hex-head bolt and top plate ; D and F: vertical restraint rods and nuts ; C and E: load plate and load bolt ; G: springs ; H: restraint base</p>	
Snubber	
	

Experimental Procedures

In shaking table tests, triaxial artificial input motions were compatible to RRS (Required Response Spectra) complied with AC-156. Considering the applicability for generators in Taiwan, the design spectral response acceleration parameter (SDS) of input motions was selected to be 0.8, and the position of equipment was assumed at basement or at roof level. For the case at roof level, ZPA (i.e. Zero Period Acceleration) of input motions in the horizontal and vertical directions were respectively equal to 0.96g and 0.21g according to design codes. Table 2 depicts maximum values, response spectra and RRS of the triaxial artificial input motions at roof level.

Table 2. Artificial input motions of shaking table tests.



Experimental Results and Observations

From observation of the shaking table tests, spring isolators were damaged due to the failure of the connections between vertical restraint rods and top plates. As shown in Table 1 and Table 3, vertical restraint rods and top plates were shallowly thread connected. In the shaking table test under 100% scale of triaxial artificial motion at roof level. Although minor damages were observed, the failure of I/ system was major caused by the separation of vertical restraint rods from top plates of spring isolators.

In shaking table tests, system identification was

executed by both impulse tests and sine sweep survey tests. Table 4 illustrates the results of system identification tests for I/ and I/R systems. Under small excitation in system identification tests, due to the gaps (about 2mm) between lateral restraint rubber pads and stopper plates of snubbers, the fundamental frequencies in horizontal directions of I/R system were slightly larger than those of I/ system. The snubbers in I/R system were designed to accommodate limited free vertical movement by hinge mechanism, thus fundamental frequencies in vertical direction of I/ system and I/R system were the same under small excitation.

Table 3. Shaking table test results: generator with I/ system; 100% triaxial artificial motion (at roof level)

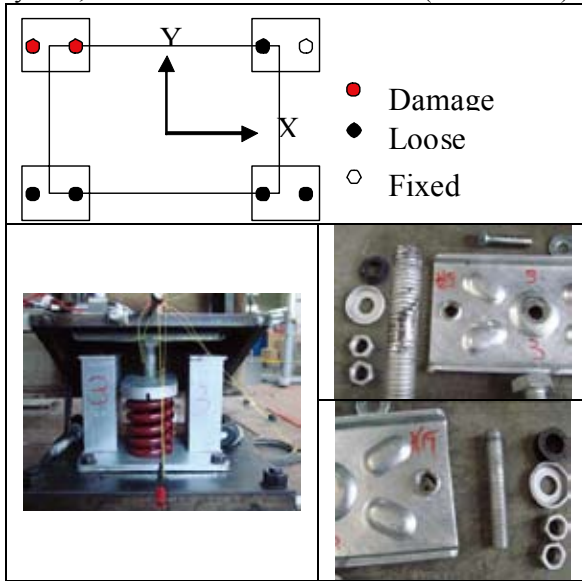
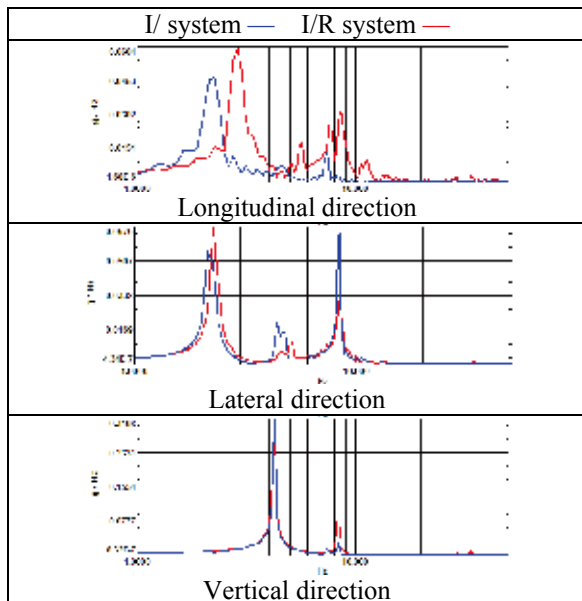


Table 4. FFT of Acceleration Response of spring isolators



In artificial input motion tests, the generator with I/ system were damaged under a 100% scale of triaxial artificial motion at roof level. Table 6 depicts the force-displacement curves of spring isolators at the same position of I/ and I/R system under triaxial artificial motion tests. In order to clearly compare dynamic responses of both systems, the spring isolator of I/ system showed in Table 5 and Table 6 were minor damaged with loosened vertical restraint rods. Comparing with I/ system, the dynamic responses of the spring isolator of I/R system remained in elastic stage in the triaxial artificial motion test. Its lateral force-displacement curves showed that horizontal responses were mostly in the first part of the elastic stage due to limited lateral displacements constrained by snubbers.

Table 5. Responses of spring isolators in shaking table tests.

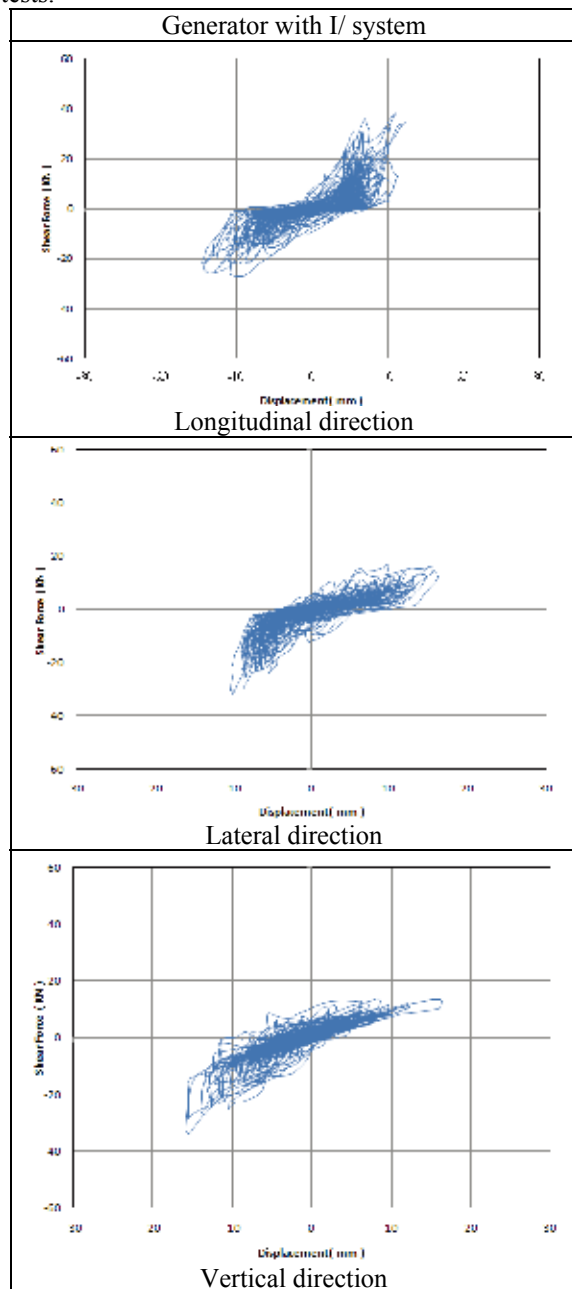
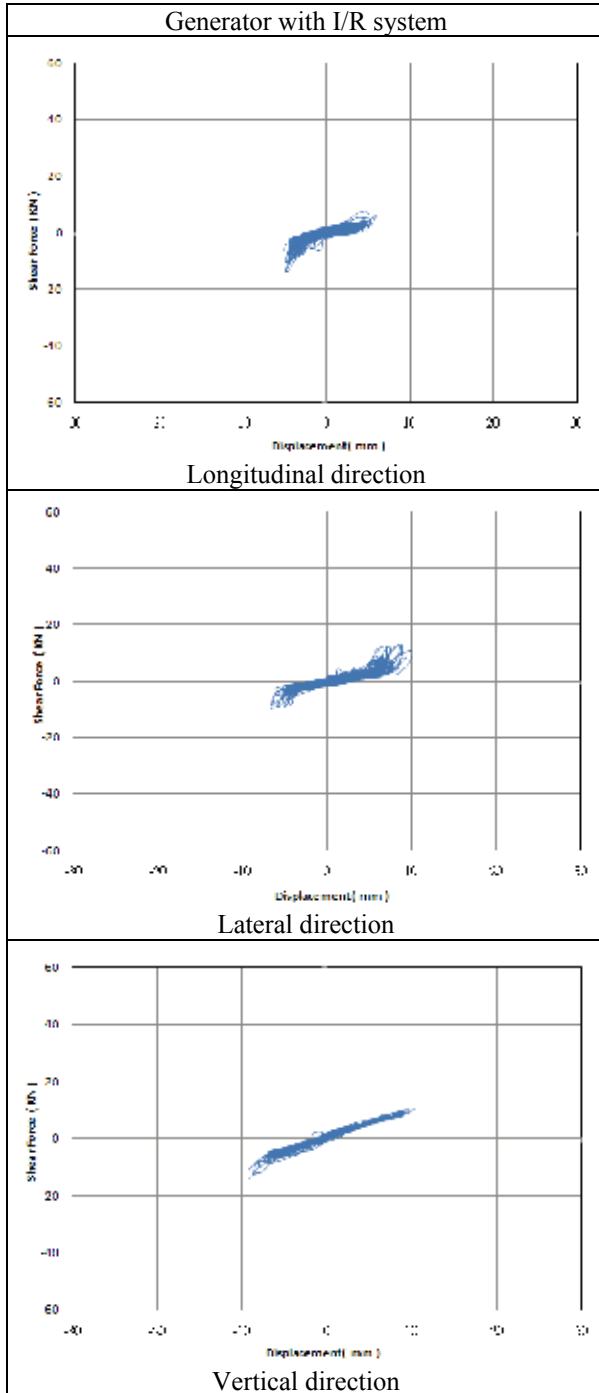


Table 6. Responses of spring isolators in shaking table tests.



Comparison With Design Codes

Component amplification factor a_p is based on the flexibility of the component and attachments. In both Taiwanese Building Code and ASCE 7-05, the value of a_p for spring isolated components is 2.5. As shown in Figure 3, most a_p values of I/ and I/R systems exceeded 2.5, especially in the lateral and vertical responses. Since the effect of impact responses wasn't significant on the RMS of acceleration response histories, most a_p values of I/R system in lateral directions were smaller than the a_p values of I/ systems.

However, several excessively vertical responses of I/R system occurred in small scale of input motions.

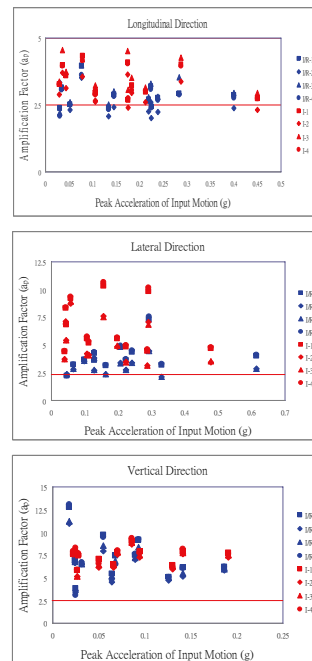


Fig. 3 Amplification factors of spring isolators of I/ or I/R systems in shaking table tests

Conclusions

In this paper, shaking table tests for the spring isolated generator with or without snubbers were briefly discussed. From test results, the mainly failure cause of spring isolators was the damage of connections between vertical restraint rods and top plates. In shaking table tests, extremely high vertical acceleration responses occurred in both I/ and I/R system, which were induced by the impact response among the components of spring isolators in I/ system, and by the constraint from the vertical movement limitation of snubbers in I/R system. Most amplification factor values obtained from shaking table tests were much larger than the value from design codes. Overall, the results of this study point out a need to improve earthquake resistant mechanism for spring isolated components.

References

- Saeed Fathali, and Andre Filiatrault, (2007) "Experimental Seismic Performance Evaluation of Isolation / Restraint Systems for Mechanical Equipment, Part1: Heavy Equipment Study" , MCEER-07-0007.
- Hwang J.S., and Chen M.F. (2008), "A Study on Cyclic Loading Tests of Vibration Isolations Mechanical/Electrical Equipment" ,Taiwan.
- Hwang J.S., and Chen Y. (2009), "Cyclic Behavior of Vibration Isolation Systems of Mechanical/Electrical Equipment" ,Taiwan.

Seismic Behaviors of High-Strength RC Columns under High Axial Loads

Ker-Chun Lin¹, Shyh-Jiann Hwang² and Fong-Chan Chang³

林克強¹、黃世建²、張豐展³

Abstract

In this paper, five full-scale high-strength RC columns were tested to assess interstory drift capacities under high axial force of $0.6 A_g f'_c$. A prescribed amount of confined reinforcements meeting the ACI 318 Code requirements was also designed for all specimens. But an upper limitation of 700 MPa stipulated by ACI design code for the confined reinforcements was used instead of their design yield stress. There were a total of five full-scale square columns of 600 x 600 mm tested at the MATS facility of the National Center for Research on Earthquake Engineering (NCREE), Taiwan. Concrete strengths of 70 MPa for Specimens B1, B3 and B5 and 100 MPa for Specimens B2 and B4 were used. All specimens adopted reinforcement grades of SD685 for main bars and SD785 for transverse stirrups and ties. The confined reinforcement details, including spacing, number of ties in each level, and end bent degree of the tie hooks, were elucidated as well.

Keywords: high-strength reinforced concrete column, confined reinforcements, high axial force, interstory drift ratio

Introduction

Appropriate amount of transverse reinforcements of columns are able to effectively provide confinement to increase their capacities of axial and flexural deformations. However, the ACI 318 Code (ACI 2008), being one of the most common reinforced concrete design code in practice around the world, recommends that an amount A_{sh} of transverse reinforcement for a rectangular column should be greater than larger one of Equation (1) and (2).

$$A_{sh} = 0.3 \left(sb_c \frac{f'_c}{f_{yt}} \right) \left(\frac{A_g}{A_{ch}} - 1 \right) \quad (1)$$

$$A_{sh} = 0.09 sb_c \frac{f'_c}{f_y} \quad (2)$$

where f'_c and f_{yt} are the design compressive strength of concrete and yield strength of transverse reinforcement, respectively. A_g is the gross area of the

column and A_{ch} and b_c is the cross-sectional area of the column and the dimension of the column member measured outside-to-outside edge of transverse reinforcements, respectively. And, s means the center-to-center spacing of transverse reinforcements. The amount of transverse reinforcements specified in the above two equations are constant value that depends on dimensions of the column and the material strengths of concrete and transverse reinforcement. It has nothing to do with the demand axial force on the column. This design concept of column member on confinement issue is different from some other design codes and reports, for instance, the Standards Association of New Zealand (NZS, 2006), the Canadian Standards Association (CSA, 2004), and the ACI report ITG-4.3R-07 (ITG 4, 2007) whose amount of transverse reinforcement for confinement increases as column's axial force increases. Related study results by Elwood *et al.* (2009) analyzed experimental data from 145 columns subjected to different axial loads and showed that deformation capacity of column had experienced a decreasing trend as axial load

¹ Researcher, National Center for Research on Earthquake Engineering

² Professor, Department of Civil Engineering, National Taiwan University

³ Graduated student, Department of Civil Engineering, National Taiwan University

increases. In other words, for columns with equal deformation demand, their confining reinforcements when subjected to higher axial load needed more than one under lower axial load. According to a previous study, also, a qualified deformation capacity of 3% radian of interstory drift angle for column member was implicated. To contrast with the research results, obviously, the required transverse reinforcement of ACI 318 Code as described in Equations (1) and (2) that do not vary with the axial force of the column should be further investigated. Figure 1 presents the results of comparison on the required confining reinforcements recommended by different codes or reports described previously, i.e. ACI 318, NZS CAS and ITG. A square column of 24 in x 24 in (600 mm x 600 mm) was assessed and two combinations of concrete and reinforcement material strengths ($f'_c = 5$ ksi, $f_{yt} = 60$ ksi and $f'_c = 12$ ksi, $f_{yt} = 100$ ksi) were considered. As shown in the Figure 1, comparing with CAS and NZS, the required confining reinforcement of ACI 318 Code under high axial load is significantly less.

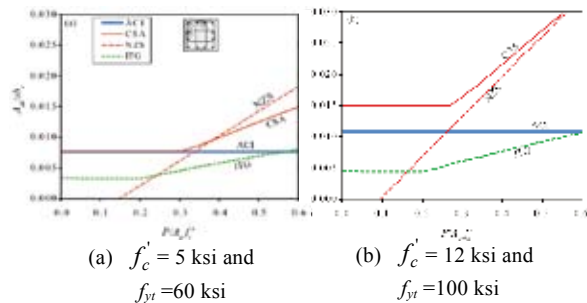


Figure 1 Comparisons on the required amount of confining reinforcement in varying axial load among ACI 318, CAS, NZS and ITG (Elwood *et al.* 2009).

A large difference in the required amount of confining reinforcement between the ACI and the other three provisions shown can be observed as the demand of axial load gets higher. Compared with NZS, the amount prescribed by ACI 318-08 was insufficient for the axial loads more than around $0.25 A_g f'_c$ and $0.35 A_g f'_c$.

Experimental Programs

A total of five full-scale high-strength columns subjected to the high axial load of $0.6 A_g f'_c$ were carried out at the National Center for Research on Earthquake Engineering (NCREE), Taiwan. The experiments utilized the multi-axial testing system (MATS) facility in applying the fixed high axial load and increasingly reversed lateral displacements simultaneously. The MATS facility has sufficient capacities of 60 MN (vertically) and 8 MN (horizontally) in providing the required up to around 20MN axial force and maximum 3MN predicted lateral force of the column specimens. The other

related specifications regarding the MATS facility can be referred to the literature written by Lin *et al.* (2007). The relationships among axial load, deformation capacity and amount of transverse reinforcement of column were concerned in this paper.

Parameters of specimens

The amount of confining reinforcement of column based on Equations (1) and (2) as stipulated in the ACI 318-08 is a basic design criterion. Based on the same amount of confining reinforcement, two parameters, i.e. layer spacing of transverse reinforcement and numbers of ties on each layer, were adjusted to study their significant influence on confinement effects. Varying bent degree of tie ends was also performed in this paper. Two types of bent details of tie ends, namely (1) 135-degree hook on one end and 90-degree hooks on the other end and (2) 180-degree hook on both ends were considered. In addition, two high-strength concrete materials of 70 and 100 MPa were used in the five specimens.

Specimen Specifications

In this study, a 600-mm square column section 1800 mm long was selected as test specimens. SD685 type of reinforcements for main bars and SD785 for transverse steel bars were used in all the five specimens. Two types of concrete compressive strength of 70 MPa (for Specimens B1, B3, and B5) and 100 MPa (for Specimens B2 and B4) were adopted. A concrete cover of 40 mm required in ACI 318-08 for column member cast in field was used. All specimens had similar arrangement of the 16-#8 main bars and identical flexural strength.

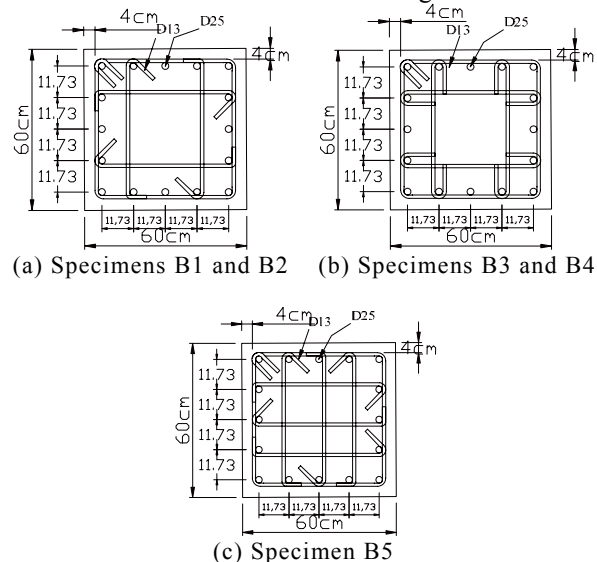


Figure 2 Sections of test specimens

According to Equations (1) and (2), the required volumetric ratios $A_{sh} / s b_c$ of the confining

reinforcement for 70 and 100 MPa concrete strengths were 0.886% (Specimens B1, B3, and B5) and 1.27% (Specimens B2 and B4), respectively. Three cross-sectional configurations were implemented in this study as shown in Figure 2. Figure 2(a) and (b) showed that two ties were arranged in two directions each layer. The type of tie configuration for Specimens B1 and B2 shown in Figure 2(a) was one end for 135° hook and the other end for 90° hook. For Specimen B5 as shown in Figure 2(c), there were three ties whose both ends were made as 90° and 135° hooks were used in two directions each layer for. For all the specimens, the stirrups and ties of column used #4 deformed bar (nominal area of 127 mm²). The required spacing of the confining reinforcement with and without a limitation of 700 MPa stipulated in ACI 318-08 Code was calculated and presented in Table 1. The final design spacing in all the specimens was based on the calculated results whose yield strength of the confining reinforcement adopted 785 MPa. The spacing of Specimens B1 and B3, Specimens B2 and B4, and Specimen B5 was 110 mm, 80 mm and 140 mm, respectively.

Table 1 Design results of specimens

Spec.	f'_c (MPa)	ACI s (mm) ($f_{yt}=785\text{MPa}$)	ACI s (mm) ($f_{yt}=700\text{MPa}$)	Design s (mm)
B1	70	110	97	110
B2	100	77	68	80
B3	70	110	97	110
B4	100	77	68	80
B5	70	138	121	140

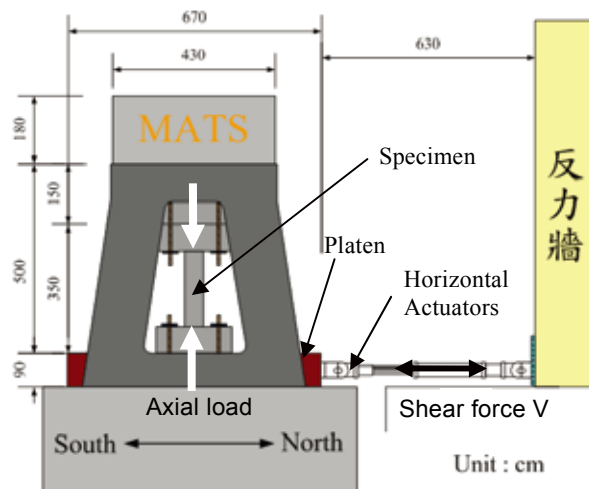


Figure 3 Experimental setup of this study

Experimental Setup

For each of the specimens, there were top and bottom footings as adapters to fix to top cross beam and bottom platen of the MATS, exception column specimen of 600 mm in square section and 1800 mm in height. The top and bottom footings are 900 x 1500 x 85 mm and 110 x 2000 x 85 mm, respectively. The experimental setup shows in Figure

3. Double-curvature behavior of column was considered in this study.

The axial load of $0.6 A_g f'_c$ was sustained during the test. The axial load was computed using the result of compressive strength of the 28-day cured 100 x 200 mm concrete cylinder specimens. The average 28-day compressive strengths of 79.2 and 98.9 MPa were obtained and used as inputs for the 70 and 100 MPa grade concrete, respectively. Therefore, the fixed axial loads for Specimens B1, B3, B5 and Specimens B2, B4 were around 17.1 MN and 21.4 MN, respectively. The horizontal actuators adopted displacement-control scheme to apply increasingly reversed cyclic loading.

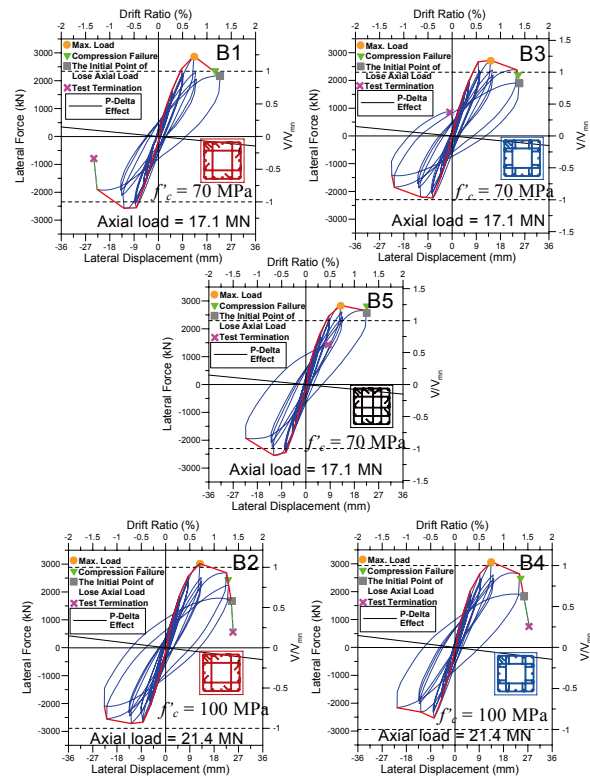


Figure 4 Horizontal force versus horizontal deformation relationships for all the specimens

Table 2 Experimental results of shear and deformation for all the specimens

Spe.	f'_{ce} (MPa)	$\frac{P}{A_g f'_{ce}}$	V_m (kN)	θ_m (% Rad.)	V_p (kN)	θ_p (% Rad.)	$\frac{V_p}{V_m}$
B1	85.1	0.56	2866	0.73	2173	1.27	0.76
B3	83.1	0.57	2724	0.80	2380	1.34	0.87
B5	83.4	0.57	2835	0.72	2649	1.25	0.93
B2	111.8	0.53	3017	0.71	2687	1.26	0.89
B4	113.9	0.52	3072	0.75	2642	1.33	0.86

Experimental Results

Figure 4 presents the hysteresis loops of column shear versus horizontal deformation for all five specimens. Additional initial test results are summarized in Table 2. In Table 2, the f'_{ce} is the

actual concrete strength at test day. Ratios of applied axial load to actual $A_g f'_c$ ranged from 0.52 to 0.57. V_m is the maximum shear of the column during the test and θ_m is its corresponding drift angle. The V_p referred to the maximum shear of column at post-peak stage and the corresponding drift angle is teamed as θ_p .

Deformation Responses

According to the results on deformation responses, under high axial load, the valid experimental drift angles, when drift angle and its corresponding strength is larger than and equal to 75% of the maximum test strength, ranged from 1.27 to 1.34. None of the specimens had the deformation capacity of 3% drift angle. The result also demonstrated that when subjected to about $0.6 A_g f'_c$ axial load, the columns with amount of the confining reinforcement based on Equations (1) and (2) proposed by ACI have experienced a rapid decay in strength over the peak point and are not able to provide the 3% radian drift angle. In other words, in order to obtain significant ductility, the required amount of confining reinforcement for a column member depends on the quantity of the axial load of the column. Therefore, the design concept proposed by the current ACI 318-08 Code that the amount of confining reinforcement of column has nothing to do with the axial load of column should be appropriately improved.

Strength Responses

Figure 4 shows that the entire test responses for all the five specimens were similar. As shown in Table 2, the maximum shear of column occurred at about 0.75% radian of drift angle for all specimens. However, it can also be observed that the strength responses decayed less than 75% of the maximum strength as the drift angle exceeded around 1.35% radian. Furthermore, for Specimens B1, B3 and B5 ($f'_c = 70\text{MPa}$), a difference on their maximum strengths was limited. Similarly, for Specimens B2 and B4, where f'_c was 100MPa, the difference on their maximum test strengths was not more than 2%. To compare strength differences of the two types of concrete (Specimens B1 and B2, and Specimens B3 and B4), it was found that though the actual concrete strength ratios of Specimens B3 and B4 to Specimens B1 and B2 were 1.31 and 1.37, respectively, the increased percentages of maximum shear were just 1.05 and 1.23, correspondingly. This result seemed to implicate that for high-strength reinforced concrete members, strength increase of concrete could not proportionally provide the member's strength.

Conclusions

To summarize the test results, some conclusions and recommendations were drawn as follows.

1. Test results showed that under high axial load, the deformation capacities of the column were around 0.75% radian drift angle at the maximum strength and around 1.3% radian for effective drift angle. These deformation capacities are significantly less than 3% radian.
2. Based on 3% radian demand of interstory drift angle for the column members, these experimental results demonstrated that the required amount of confining reinforcement proposed in ACI 318-08 was obviously insufficient when the column experiences high axial load demand.
3. For various concrete strength specimens, though concrete strength increased 1.31 and 1.37 times, the corresponding strength increases on the five columns were 5% and 23% only, respectively. Therefore, the predicted strength model of column used in practice and is applied to high-strength concrete material should be revised appropriately.
4. Test results presented that Specimens B1 and B3 or Specimens B2 and B4 with same amount of steel confining reinforcement but different types of tie bent had identical strength and deformation responses.

References

- ACI Committee 318, Building Code Requirement for Structural Concrete (ACI 318-08) and Commentary (ACI 318R-08), American Concrete Institute, Farmington Hills · Mich. · 2008.
- Canadian Standards Association, "Design of Concrete Structures," CSA A23.3-04, Mississauga, Canada, 2004.
- Elwood, K. J., Maffei, J. M., Riederer, K. A., and Telleen, K., "Improving Column Confinement—Part 1: Assessment of design provisions, and Part 2: Proposed new provisions for the ACI 318 Building Code" Concrete International, V. 31, No. 11, Nov. 2009, pp. 32-48.
- Innovative Task Group (ITG) 4, 2007, "Report on Structural Design and Detailing for High-Strength Concrete in Moderate to High Seismic Applications – ACI ITG-4.3R-07" American Concrete Institute, Farmington Hills, USA.
- Ker-Chun Lin, Der-Hong Lin, and Keh-Chyuan Tsai, "Analysis and Design of a Multi-Axial Testing System (MATS) at National Center for Research on Earthquake Engineering," Proceedings of 2007 ANCER Meeting, May 29-30, 2007, Hong Kong, Paper No.35.
- Standards Association of New Zealand, "Concrete Design Standard, NZS3101:2006, Part 1" and "Commentary on the Concrete Design Standard, NZS 3101:2006, Part 2," Wellington, New Zealand, 2006.

Optimal Design Formulae for Nonlinear Friction Pendulum Tuned Mass Dampers

Lap-Loi Chung¹ Lai-Yun Wu² Mei-Chun Lin³ Kuan-Hua Lien³ Hsu-Hui Huang³ and Yong-An Lai³

鍾立來¹、吳賴雲²、林美君³、連冠華³、黃旭輝³、賴勇安³

Abstract

The present study aimed at developing optimal design formulae of nonlinear friction pendulum tuned mass damper (FPTMD) for damped main systems under the acceleration response quantity being minimized. The FPTMD has the following properties: (1) the mass slides on the spherical surface so that the space to accommodate the FPTMD is much less than the suspension type; (2) the restoring force is provided by the spherical surface so that no extra spring is needed; and (3) the vibration energy is dissipated by the friction mechanism of the interface between the mass and the spherical surface. Direct search technique was used to obtain the optimum friction coefficient and tuning frequency ratio of the FPTMD for which the response of a damped single degree-of-freedom (SDOF) main system subjected to white-noise random excitation is minimized. Optimal design formulae for FPTMD were then obtained by a sequence of curve-fitting techniques. The feasibility of the proposed optimal design formulae is illustrated numerically using Taipei 101 structure implemented with FPTMD as a reference.

Keywords: optimal design formulae, friction pendulum tuned mass damper (FPTMD), nonlinear, friction

Introduction

In this paper, optimal design of a structure implemented with an FPTMD is proposed (Mokha et al., 1991). Restoring force is provided by the spherical surface of the TMD when the mass slides away from the lowest point of the spherical surface. Small angle of sliding is assumed so that the restoring force is linear (Tsopelas et al., 1996). Energy is dissipated due to the nonlinear friction force of the contact interface between the mass and the sliding surface.

The present study aimed at developing optimal design formulae for FPTMD of damped main systems under the acceleration response quantity being minimized. Direct search technique was used to obtain the optimum friction coefficient and tuning frequency ratio of an FPTMD for which the response of a damped single degree-of-freedom (SDOF) main system subjected to white-noise random excitation is

minimized. Optimal design formulae for these optimum parameters were then obtained by a sequence of curve-fitting techniques. The feasibility of the proposed optimal design formulae is illustrated numerically using Taipei 101 structure implemented with FPTMD as a reference.

Motion Equation

After an FPTMD is attached to the SDOF structure, as shown in Fig. 1, it becomes a 2DOF system. The equation of motion of the nonlinear system can be expressed as

$$\mathbf{M}\ddot{\mathbf{x}}(t) + \mathbf{C}\dot{\mathbf{x}}(t) + \mathbf{K}\mathbf{x}(t) = \mathbf{B}_1 u(t) + \mathbf{E}_1 w(t) \quad (1)$$

where

$\mathbf{M} = \begin{bmatrix} m_d & 0 \\ 0 & m_s \end{bmatrix}$ is the mass matrix of the system;

¹ Research Fellow and Adjunct Professor.

² Professor

³ Doctoral Candidate

$\mathbf{C} = \begin{bmatrix} 0 & 0 \\ 0 & c_s \end{bmatrix}$ is the damping matrix of the system;

$\mathbf{K} = \begin{bmatrix} k_d & -k_d \\ -k_d & k_d + k_s \end{bmatrix}$ is the stiffness matrix of the

system; $\mathbf{x}(t) = \begin{bmatrix} x_d(t) \\ x_s(t) \end{bmatrix}$ is the displacement vector of

the system; $\mathbf{B}_1 = \begin{bmatrix} -1 \\ 1 \end{bmatrix}$ is the TMD internal loading

vector; $\mathbf{E}_1 = \begin{bmatrix} 0 \\ 1 \end{bmatrix}$ is the primary structural external

loading vector; $u(t)$ is the friction force provided by the TMD; and $w(t)$ is external disturbances.

The solution of motion equation can be expressed in discrete-time fashion as first-order difference equation,

$$\mathbf{z}[k+1] = \mathbf{A}_d \mathbf{z}[k] + \mathbf{B}_d u[k] + \mathbf{E}_d w[k] \quad (2)$$

where $\mathbf{z}[k] = \begin{bmatrix} \mathbf{x}[k] \\ \dot{\mathbf{x}}[k] \end{bmatrix}$, $\mathbf{A}_d = e^{\mathbf{A}\Delta t}$,

$$\mathbf{B}_d = \mathbf{A}^{-1}(\mathbf{A}_d - \mathbf{I})\mathbf{B}, \quad \mathbf{E}_d = \mathbf{A}^{-1}(\mathbf{A}_d - \mathbf{I})\mathbf{E},$$

$$\mathbf{A} = \begin{bmatrix} \mathbf{0} & \mathbf{I} \\ -\mathbf{M}^{-1}\mathbf{K} & -\mathbf{M}^{-1}\mathbf{C} \end{bmatrix}, \quad \mathbf{B} = \begin{bmatrix} \mathbf{0} \\ \mathbf{M}^{-1}\mathbf{B}_1 \end{bmatrix},$$

$$\mathbf{E} = \begin{bmatrix} \mathbf{0} \\ \mathbf{M}^{-1}\mathbf{E}_1 \end{bmatrix}.$$

Assuming that the kinetic friction coefficient is equal to the static one, the maximum friction force can be expressed as

$$|u[k]|_{\max} = \mu N \quad (3)$$

where $N = m_d g$ is the normal force of the contact interface and g is the acceleration due to gravity.

Assuming that the $(k+1)$ -th step of the TMD relative velocity is zero, i.e. non-slip state, then the friction force of the k step can be estimated as

$$\hat{u}[k] = -(\mathbf{d}_1^T \mathbf{B}_d)^{-1} \mathbf{d}_1^T (\mathbf{A}_d \mathbf{z}[k] + \mathbf{E}_d w[k]) \quad (4)$$

When the friction force is less than the maximum static friction force $\hat{u}[k] < \mu N$, the FPTMD is in the stick state and the friction force can be expressed as

$$u[k] = \hat{u}[k] \quad (5)$$

And, when the friction force is larger than the maximum static friction force $\hat{u}[k] \geq \mu N$, the FPTMD is in the sliding state, thus the friction force can be expressed as

$$u[k] = \mu m_d g \operatorname{sgn}(\hat{u}[k]) \quad (6)$$

Structural acceleration is expressed as

$$\ddot{x}_s[k] = -m_s^{-1} c_s \dot{x}_s[k] - m_s^{-1} k_s x_s[k] + m_s^{-1} u[k] + m_s^{-1} w[k] \quad (7)$$

Optimal Design Formulae

The mass ratio is defined as $R_m = m_d/m_s$, the frequency ratio is defined as $R_f = f_d/f_s$ and the normalized friction coefficient is defined as $\bar{\mu} = \mu \cdot g / (f_s \cdot |\dot{x}_s|_{\text{RMS, without TMD}})$.

where $|\dot{x}_s|_{\text{RMS, without TMD}}$ is the root mean square velocity of the main system without TMD.

It is extremely difficult to determine the exact closed-form expressions for optimum nonlinear TMD parameters. However, explicit mathematical expressions corresponding to the optimum parameters of nonlinear TMD system obtained by numerical searching technique are useful for engineering applications. Ten white-noise wind forces, six structural damping ratios ξ_s (0, 1, 2, 3, 4 and 5%), five mass ratios R_m (1, 2, 3, 4 and 5%) were used to determine the optimum parameters by direct search technique (Wright 1995). A curve-fitting scheme was adopted to develop the optimum design formulae for normalized friction coefficient and frequency ratio of nonlinear the TMD,

$$\bar{\mu}^{\text{opt}} = (1.4682 + 0.8724\xi_s - 0.1197\xi_s^2) + (-9.9468 + 1.9064\xi_s + 0.4116\xi_s^2)R_m \quad (8)$$

$$\frac{R_f^{\text{opt}}}{R_m} = \exp \left[\begin{array}{l} (0.0295 - 0.0107\xi_s + 0.0028\xi_s^2) + \\ (-0.9941 - 0.0034\xi_s + 0.0007\xi_s^2) \ln(R_m) \end{array} \right] \quad (9)$$

Numerical Verification

The Taipei 101 holds the title of the world's second tallest building (for now) at 508 m high. Because the TMD is hung from the 92nd floor, in order to turn the structure into SDOF structure as shown in Table 1, the first mode shape is normalized such that the component at the 92nd floor is unity. After reduction, the first modal mass m_s was 5371.7 tonf-sec²/m, the first modal frequency f_s was 0.14251 Hz, and the first modal stiffness $k_s = m_s (2\pi f_s)^2$ is 4036.8 tonf/m. The first modal damping ratio ξ_s was assumed as 2% so that the first modal damping coefficient can be obtained as $c_s = 2m_s (2\pi f_s) \xi_s = 192.4$ tonf-sec/m (Wu *et al.*, 2005).

The Taipei 101 was turned into a SDOF structure and implemented with an FPS-type TMD. The mass of the TMD is $m_d = 67.146$ tonf-sec²/m so that the

mass ratio is 1.25%. The Taipei 101 structure was excited by external wind force with return period of half a year (Fig. 2).

Optimum design parameters for the nonlinear TMD from the direct search method and the optimal design formulae are listed in Table 2. Optimal frequency ratio (R_f^{opt}) from the design formula is 0.9915 times that from the direct search method but optimal friction coefficient (μ^{opt}) from the design formula is 0.7778 times that from the direct search method. Maximum displacement and acceleration of the main system with TMD from design formulae are, respectively, 1.1107 and 1.0288 times those from the direct search method (Figs. 3 and 4). Both of them can make the maximum acceleration of the structure less than 5 gal to fit the specification. It is observed from the acceleration ratios that effectiveness of both TMDs designed from the direct search method and the design formulae are similar since the effectiveness is sensitive to frequency ratio and not that sensitive to fixed friction coefficient. The relative displacement of the TMD from design formulae (0.3564 m) is larger but the damping force of the TMD from design formulae (0.5967 tonf) is smaller as compared with the TMD from the direct search method (0.3120 m and 0.7718 tonf) (Table 2 and Fig. 5).

Conclusion

In this paper, optimal design formulae for a TMD with nonlinear friction were established. Given the structural damping ratio, the root-mean-square of structural velocity without TMD and mass ratio, optimal design parameters (normalized friction coefficient and frequency ratio) can be computed from the proposed formulae. The feasibility of the proposed optimal design formulae is illustrated numerically by using Taipei 101 structure implemented with FPTMD as a reference.

References

Mokha, A.S., Constantinou, M.C., Reinhorn, A.M., and Zayas, V. (1991), "Experimental study of friction pendulum system isolation system", *Journal of Structural Engineering* 117: 1201-1217.

Tsopelas, P., Constantinou, M.C., Kim, Y.S., and Okamoto, S. (1996), "Experimental study of FPS system in bridge seismic isolation", *Earthquake Engineering and Structural Dynamics* 25: 65-78.

Wright, M.H. (1995), "Direct search methods: once scorned, now respectable in numerical analysis", *Pitman Research Notes in Mathematics*, Addison Wesley Longman Limited, 191-208.

Wu, L.Y., Chung, L.L., Chen, J.C., and Huang, G.L. (2005), "Control simulation for Taipei 101 with

wind excitation", 7th Conference on Structural Engineering. (in Chinese)

Table 1. Taipei 101 SDOF parameters

Parameter	Value
Mass(m_s)(tonf-sec ² /m)	5371.7
TMD mass(m_d)(tonf-sec ² /m)	67.278
Stiffness(k_s)(tonf/m)	4306.8
Damping ratio(ξ_s)	0.02
Frequency f_s (Hz)	0.1425

Table 2. Taipei 101 with optimal TMD

Parameter and Response	Without TMD	Direct search	Design formulae
Frequency ratio (R_f^{opt})	—	1.0197	1.0110
Friction coefficient (μ^{opt})	—	1.17×10^{-3}	0.91×10^{-3}
Acceleration ratio (R_a)	—	0.6888	0.7014
Maximum displacement (cm)	8.7	5.69	6.30
Maximum acceleration (cm/sec ²)	7.3	4.16	4.28
Maximum relative displacement for TMD (cm)	—	31.20	35.64
Maximum damping force for TMD (tonf)	—	0.7718	0.5967

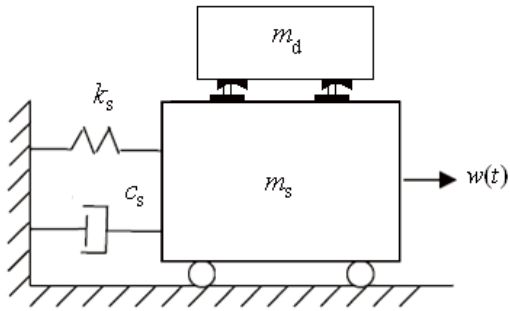


Fig. 1 System model of nonlinear TMD attached to SDOF structure.

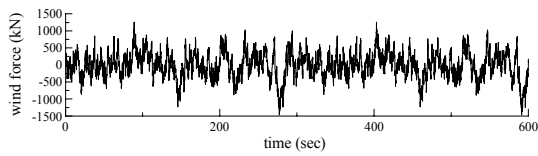
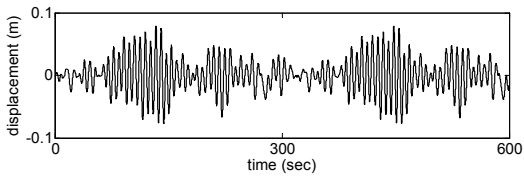
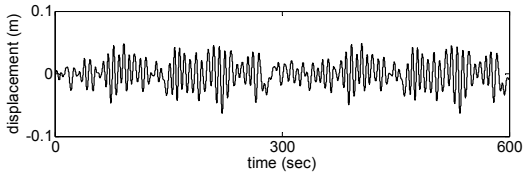


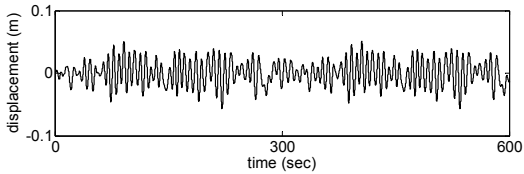
Fig. 2 External wind force with return period of half a year.



(a) Without TMD

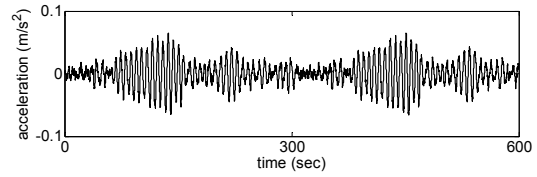


(b) Design formulae

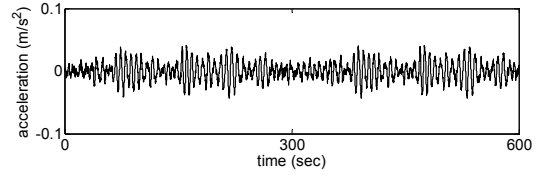


(c) Direct search

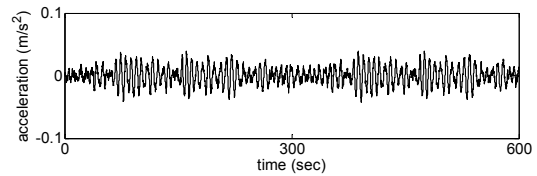
Fig. 3. Displacement time histories for Taipei 101



(a) Without TMD

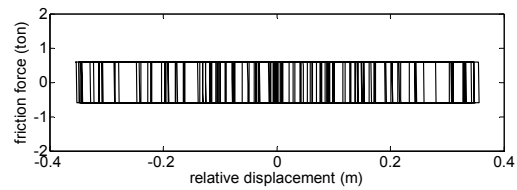


(b) Design formulae

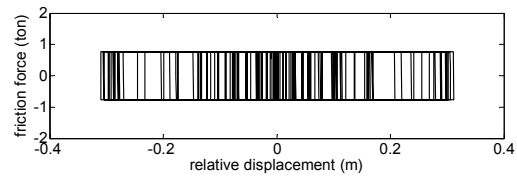


(c) Direct search

Fig. 4. Acceleration time histories for Taipei 101



(a) Design formulae



(b) Direct search

Fig. 5. Hysteresis loops for Taipei 101

Optimal Design of Bidirectional Friction Pendulum Tuned Mass Damper with Varying Curvature

L.L. Chung¹, L.Y. Wu², T.H. Lin³, M.C. Lin⁴, P.S. Kao⁵ and K.H. Lien⁶

鍾立來¹、吳賴雲²、林廷翰³、林美君⁴、高培修⁵、連冠華⁶

Abstract

In this paper, a bidirectional friction pendulum tuned mass damper (BFPTMD) has been proposed to reduce the structural response of a building. The BFPTMD was designed such that the curvature varies with the orientation. Therefore, the bidirectional frequencies of the TMD can be tuned with the structural frequencies even though they are different in the two horizontal directions. The design parameters of BFPTMD were optimized such that the sum of squares of structural response is minimized by direct search method in MATLAB. Finally, the BFPTMD was implemented on the structure of Taipei 101 simplified as single degree-of-freedom (SDOF) system in the two horizontal directions. The analytical result shows that when structural bidirectional natural frequencies are different, the vibration reduction of the TMD with varying curvature is better than the one with fixed curvature.

Keywords: bidirectional friction pendulum tuned mass damper (BFPTMD), bidirectional structural frequencies, varying curvature

Introduction

Friction pendulum is a system that has a curved surface with friction interface to restore the position of the mass and thereby to dissipate energy. Through various experiments and analyses, friction pendulum system (FPS) has become very common nowadays for base isolation in earthquake engineering. FPS is further developed for vibration suppression with the so-called tuned mass damper (TMD). Chung (2008) provided the theorem of optimal design of friction pendulum tuned mass damper (FPTMD) and confirmed the damper's ability to successfully reduce vibration. However, research results on FPTMD need further refinement since the traditional fixed-curvature FPTMD cannot be tuned with different natural frequencies of a bidirectional structure at the same time. In this study, BFPTMD with varying curvature has been proposed to allow frequencies of the TMD be tuned with different natural frequencies of a structure in the two horizontal directions. At first, the equation of the curved surface with varying curvature was developed and the mechanical behavior of the varying-curvature BFPTMD was described. The

dynamic behavior of a bidirectional structure with BFPTMD was analyzed and the optimal design parameters for the BFPTMD were found by direct search method. To test the system, BFPTMD was implemented on the structure of Taipei 101 and its usefulness has been confirmed.

Equation of Motion

The equation of the curved surface of a BFPTMD can be expressed as

$$z_d = R - \sqrt{R^2 - r_d^2} \quad (1)$$

where $r_d = \sqrt{x_d^2 + y_d^2}$; $R = \frac{R_x x_d^2 + R_y y_d^2}{x_d^2 + y_d^2}$ is the varying radius of curvature.

The restoring force of TMD is related to the maximum slope of the curved surface, and the vector of maximum slope has an angle θ with x_d - y_d plane. From Fig. 1, it gives

$$\tan \theta = s_{\max} = \sqrt{s_x^2 + s_y^2} \quad (2)$$

¹ Research Fellow, National Center for Research on Earthquake Engineering, chung@ncree.org.tw.

² Professor, Department of Civil Engineering, National Taiwan University, lywu@ntu.edu.tw

³ Graduate Student, Department of Civil Engineering, National Taiwan university

where $s_x = \frac{\partial z_d}{\partial x_d}$ is the slope of the curved surface in x_d - z_d plane; $s_y = \frac{\partial z_d}{\partial y_d}$ is the slope in y_d - z_d plane.

When the restoring force of TMD is projected on the x_d - y_d plane, the angle φ between the restoring force and the x_d -axis is

$$\tan \varphi = \frac{s_y}{s_x} \quad (3)$$

The restoring force is decomposed into two components $F_{rx}(t)$ and $F_{ry}(t)$ in x_d direction and y_d direction, respectively, as

$$\begin{aligned} F_{rx}(t) &= F_{r\theta}(t) \cos \theta \cos \varphi \\ F_{ry}(t) &= F_{r\theta}(t) \cos \theta \sin \varphi \end{aligned} \quad (4)$$

where $F_{r\theta}(t) = m_d g \sin \theta$ is the restoring force at a point on the curved surface.

When BFPTMD is attached to a bidirectional structure, it becomes a four-degree-of-freedom system. The restoring force provided by the TMD is decomposed into two parts: the linear one and the nonlinear one. The former is further incorporated with the structural stiffness to form the stiffness matrix of the system. The equation of motion of the system can be expressed as

$$\mathbf{M}\ddot{\mathbf{x}}(t) + \mathbf{C}\dot{\mathbf{x}}(t) + \mathbf{K}\mathbf{x}(t) = \mathbf{B}\mathbf{F}'_r(t) + \mathbf{B}\mathbf{F}_f(t) + \mathbf{E}_1\mathbf{w}(t) \quad (5)$$

where $\mathbf{M}_{(2n+2) \times (2n+2)} = \begin{bmatrix} \mathbf{M}_d 2 \times 2 & \mathbf{0}_{2 \times 2n} \\ \mathbf{0}_{2n \times 2} & \mathbf{M}_s 2n \times 2n \end{bmatrix}$ is the mass matrix; $\mathbf{C}_{(2n+2) \times (2n+2)} = \begin{bmatrix} \mathbf{0}_{2 \times 2} & \mathbf{0}_{2 \times 2n} \\ \mathbf{0}_{2n \times 2} & \mathbf{C}_s 2n \times 2n \end{bmatrix}$ is the damping matrix; $\mathbf{K} = \begin{bmatrix} \mathbf{K}_d & -\mathbf{K}_d \\ -\mathbf{K}_d & \mathbf{K}_d + \mathbf{K}_s \end{bmatrix}$ is the stiffness matrix; $\mathbf{x}_{(2n+2) \times 1}(t) = \begin{bmatrix} \mathbf{x}_d 2 \times 1(t) \\ \mathbf{x}_s 2n \times 1(t) \end{bmatrix}$ is the displacement vector; $\mathbf{B}_{(2n+2) \times 2} = \begin{bmatrix} -\mathbf{I}_{2 \times 2} \\ \mathbf{I}_{2 \times 2} \\ \mathbf{0}_{(2n-2) \times 2} \end{bmatrix}$ is

location matrix for the nonlinear part of the restoring force of TMD and the friction force;

$\mathbf{F}'_r(t) = \begin{bmatrix} F'_{rx}(t) \\ F'_{ry}(t) \end{bmatrix} = \begin{bmatrix} F_{rx}(t) - k_{dx} x_d(t) \\ F_{ry}(t) - k_{dy} y_d(t) \end{bmatrix}$ is the nonlinear part of the restoring force of the TMD;

$\mathbf{F}_f(t) = \begin{bmatrix} F_{fx}(t) \\ F_{fy}(t) \end{bmatrix}$ is the friction force vector of the

TMD; $\mathbf{E}_1 = \begin{bmatrix} \mathbf{0}_{2 \times 2} \\ \mathbf{I}_{2 \times 2} \end{bmatrix}$ is the external loading vector;

and $\mathbf{w}(t)_{2n \times 1}$ is the wind force vector that

influences directly the structure but not the TMD, thus the elements of matrix \mathbf{E}_1 are zero corresponding to the TMD and one corresponding to the structure.

The motion equation (5) can be expressed as a first-order differential equation

$$\dot{\mathbf{z}}(t) = \mathbf{A}\mathbf{z}(t) + \mathbf{B}_c\mathbf{F}'_r(t) + \mathbf{B}_c\mathbf{F}_f(t) + \mathbf{E}\mathbf{w}(t) \quad (6)$$

where $\mathbf{z}(t) = \begin{bmatrix} \mathbf{x}(t) \\ \dot{\mathbf{x}}(t) \end{bmatrix}$ is the state

vector, $\mathbf{A}_{2(2n+2) \times 2(2n+2)} = \begin{bmatrix} \mathbf{0} & \mathbf{I} \\ -\mathbf{M}^{-1}\mathbf{K} & -\mathbf{M}^{-1}\mathbf{C} \end{bmatrix}$ is the

system matrix, $\mathbf{B}_c 2(2n+2) \times 2 = \begin{bmatrix} \mathbf{0} \\ \mathbf{M}^{-1}\mathbf{B} \end{bmatrix}$ is the

location matrix for the nonlinear part of the restoring force of TMD and the friction force, and

$\mathbf{E}_{2(2n+2) \times 2} = \begin{bmatrix} \mathbf{0} \\ \mathbf{M}^{-1}\mathbf{E}_1 \end{bmatrix}$ is the loading location matrix.

After solving equation (6), it gives the state-space equation of the discrete-time system as

$$\mathbf{z}[k+1] = \mathbf{A}_d\mathbf{z}[k] + \mathbf{B}_d\mathbf{F}'_r[k] + \mathbf{B}_d\mathbf{F}_f[k] + \mathbf{E}_d\mathbf{w}[k] \quad (7)$$

where $\mathbf{A}_d = e^{\mathbf{A}\Delta t}$ is the discrete-time system matrix;

$\mathbf{B}_d = \mathbf{A}^{-1}(\mathbf{A}_d - \mathbf{I})\mathbf{B}_c$ is the discrete-time location matrix for the nonlinear part of the restoring force of the TMD and the friction force; and $\mathbf{E}_d = \mathbf{A}^{-1}(\mathbf{A}_d - \mathbf{I})\mathbf{E}$ is the discrete-time loading location matrix.

Assuming the velocities of the bidirectional FPS type TMD relative to the structure are zero in both directions at the $(k+1)$ -th step, then the friction force vector at the k -th step can be estimated as

$$\hat{\mathbf{F}}_f[k] = -(\mathbf{D}_1\mathbf{B}_d)^{-1}\mathbf{D}_1(\mathbf{A}_d\mathbf{z}[k] + \mathbf{B}_d\mathbf{F}'_r[k] + \mathbf{E}_d\mathbf{w}[k]) \quad (8)$$

where $\mathbf{D}_1 = \begin{bmatrix} \mathbf{0}_{2 \times 2} & \mathbf{0}_{2 \times 2} & \mathbf{I}_{2 \times 2} & -\mathbf{I}_{2 \times 2} \end{bmatrix}$; and

$\hat{\mathbf{F}}_f[k] = \begin{bmatrix} \hat{F}_{fx}[k] \\ \hat{F}_{fy}[k] \end{bmatrix}$ is the estimated friction force vector.

To determine whether the resultant of the estimated friction force is correct by comparing it with the maximum static friction force, the procedure can be described in two situations as follows:

(a) $|\hat{F}_f[k]| < F_{f,\max}[k]$, so the BFPTMD is actually in stick state, the resultant of the friction force is the same with the estimated one

$$|F_f[k]| = |\hat{F}_f[k]| \quad (9)$$

(b) $|\hat{F}_f[k]| \geq F_{f,\max}[k]$, so the BFPTMD is sliding in the k -th step, the resultant of the friction force is the maximum static friction force as

$$|F_f[k]| = F_{f,\max}[k] \quad (10)$$

where $|\hat{F}_f[k]| = \sqrt{(\hat{F}_{fx}[k])^2 + (\hat{F}_{fy}[k])^2}$ is the resultant of the friction force; and $F_{f,\max}[k] = \mu N \cos \theta$ is the maximum static friction force. The resultant of the friction force is further decomposed into two components in the two horizontal directions.

$$\mathbf{F}_f[k] = \begin{bmatrix} F_{fx}[k] \\ F_{fy}[k] \end{bmatrix} = \begin{bmatrix} |F_f[k]| \frac{\hat{F}_{fx}[k]}{|\hat{F}_f[k]|} \\ |F_f[k]| \frac{\hat{F}_{fy}[k]}{|\hat{F}_f[k]|} \end{bmatrix} \quad (11)$$

Numerical Verification

Taipei 101 holds the title as the world's second tallest building at 508 m at the time of this report. After model reduction, the first modal mass m_s was 5371.7 tonf-sec²/m, the first modal frequency f_{sx} was 0.14251 Hz, and $f_{sy} = 1.2f_{sx}$ was assumed such that the first modal stiffnesses were $k_{sx} = m_s \omega_x^2 = 4036.8$ tonf/m and $k_{sy} = 5168.2$ tonf/m. It was assumed that the first modal damping ratio ξ_s is 2% such that the first modal damping coefficient can be obtained as $c_{sx} = 2m_s \omega_x \xi_s = 192.4$ tonf-sec/m and $c_{sy} = 230.9$ tonf-sec/m. Before installing the TMD onto the Taipei 101, the peak acceleration response was 6.54 gal in the x-direction, 6.91 gal in the y-direction (refer to Figs. 2 and 3). Both the two directions are over 5 gal and therefore requirement of comfort was not satisfied. For this reason, the dynamic behavior of installing the BFPTMD onto Taipei 101 should be simulated to confirm the feasibility of BFPTMD. The mass of the TMD required for Taipei 101 is 660 ton, thus the mass ratio R_m is 1.25% ($m_d = 67.278$ tonf-sec²/m).

The sum of squares of structural responses was used as a cost function for optimal design of TMD,

$$J = \sum_{k=1}^{k_1} x_n^2[k] \quad (12)$$

The design parameters of BFPTMD were optimized by direct search method in MATLAB, and the cost function becomes the sum of structural responses in both x and y directions,

$$R_d = \frac{\sqrt{\sum_{k=1}^{k_1} (x_s^2[k] + y_s^2[k])_{\text{with TMD}}}}{\sqrt{\sum_{k=1}^{k_1} (x_s^2[k] + y_s^2[k])_{\text{w/o TMD}}}} \quad (13)$$

For the FPTMD system with fixed curvature, the optimal displacement ratio R_d was 0.7791, the optimal curvature radius R was 11.7128m, the optimal friction parameter μ was 0.0014, and the peak acceleration responses in x and y directions were 0.0424 m/sec² and 0.0501 m/sec² (see Fig. 2 and Fig. 3), respectively.

And for the BFPTMD with varying curvature, the optimal displacement ratio R_d was calculated as 0.7494, the optimal curvature radius in x-direction R_x was 12.0700m, the optimal curvature radius in y-direction R_y was 9.7163m, the optimal friction parameter μ was 0.00133, and the peak acceleration responses in x and y directions were 0.043 m/sec² and 0.0441 m/sec² (see Fig.2 and Fig.3), respectively. Finally, the analytical result shows that the vibration reduction of the BFPTMD with varying curvature is better than that of the FPTMD with fixed curvature.

Conclusions

This paper discusses the observed vibration reduction of the varying-curvature BFPTMD in a bidirectional structure. It has been assumed that the frequencies in the two horizontal directions of the Taipei 101 were different by 20%. If there is no TMD to reduce the vibration, the acceleration responses are over 5 gal in both x and y directions. If a fixed-curvature FPTMD is installed, it cannot be tuned at the same time with the different frequencies of a bidirectional structure because of its fixed frequency. As a result, the requirement of comfort in one of the directions was not satisfied. When a varying-curvature BFPTMD is attached onto a bidirectional structure, the structural response in both the two directions can be reduced because this type damper can be tuned with the bidirectional structural natural frequencies. Moreover, the analytical result shows that the vibration reduction of the BFPTMD with varying curvature is better than that of the FPTMD with fixed curvature if the natural frequencies of the structure are different in the two horizontal directions.

References

- Tsopelas P., Constantinou MC., Kim YS., and Okamoto S. "Experimental study of FPS system in bridge seismic isolation." *Earthquake Engineering and Structural Dynamics*. Vol. 25, pp. 65-78 (1996).
- Mokha, A.S., Amin, N., Constantinou, M.C., and Zayas, V., "Seismic isolation retrofit of large historic building," *Journal of Structural Engineering*, ASCE, Vol. 122, No. 3, pp. 298-308 (1996).
- Chung L.L., Wu L.Y., Chen H.H., Huang H.H.,

Chang C.H., Lin T.H., "Optimal Design of Friction Pendulum System Typed Tuned Mass Damper", National Center for Research on Earthquake Engineering, 2008, NCREE 08-018. (in Chinese).

Zayas, V., Low, S.S., and Mahin, S.A., "A simple pendulum technique for achieving seismic isolation," Earthquake Spectra, Vol. 6, No. 2, pp.317-331 (1990).

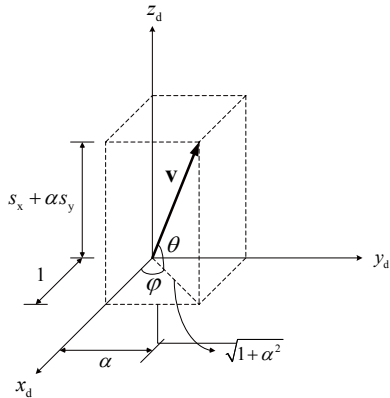


Fig.1 Vector space of slope of curved surface

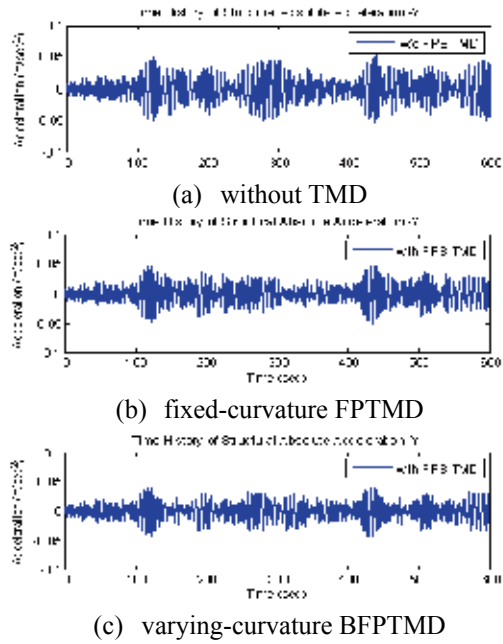


Fig. 3 Time histories of structural acceleration in y-direction ($f_{sy} = 1.2f_{sx}$)

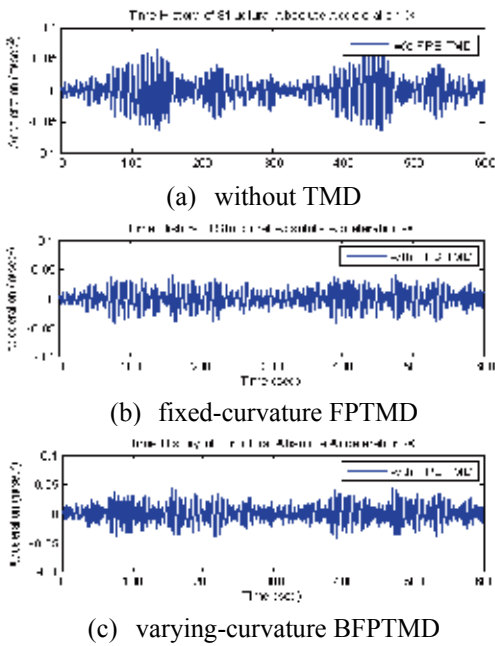


Fig. 2 Time histories of structural acceleration in x-direction ($f_{sy} = 1.2f_{sx}$)

Study on Eccentric Rolling Isolation System with Additional Friction Damping

Cho-Yen Yang¹, Cheng-Hsin Hsieh², Lap-Loi Chung³, Lai-Yun Wu⁴ and Hung-Ming Chen⁵

楊卓諺¹、謝姪馨²、鍾立來³、吳賴雲⁴、陳鴻銘⁵

Abstract

Passive isolation system is simple and effective to reduce the seismic ground acceleration. However, the responses may be magnified due to resonance for the conventional and linear passive isolation systems under near-fault earthquake. The nonlinear isolation system may avoid this situation. The proposed eccentric rolling isolation system (ERIS) with additional friction damping was investigated. The isolation performances of the ERIS were compared with a corresponding linear-restoring isolation system (linear system), which was established by the linearized frequency and the same optimization of friction parameters for energy-dissipating. If the resonance sine wave is considered, the response of the ERIS is magnified but much more slightly when compared to that of the linear system. In far-field El Centro earthquake, the two isolation systems were both found to be effective on acceleration and displacement. The nonlinear behavior of the ERIS is more obvious under near-fault Chi-Chi earthquake because of the occurrence of large displacement due to the near-fault excitation. This behavior implies more reduction in the response of acceleration. When the amplitude of the Chi-Chi earthquake becomes larger, the linear system becomes ineffective but the ERIS still works effectively. Consequently, the advantages and effectiveness of the ERIS with additional friction damping is further explained in this study.

Keywords: nonlinear, eccentricity, rolling, isolation, seismic

Introduction

Recently, several researches show that the responses of those linear isolation systems may be amplified under near-fault earthquake. The amplification effect of the linear system under near-fault earthquake can be attenuated by an appropriate damping device. Interestingly, the nonlinear stiffness isolation system is another possible way to alleviate the response under resonance. Therefore, Chung and his co-workers proposed the nonlinear rolling isolation system (Chung *et al.*, 2009). In their study, the isolation object (mass) was pinned eccentrically on the circular isolator. The dynamic

behaviors of this isolator without damping were investigated numerically through free vibrations and forced vibrations considering various eccentricities. From simulations, the behaviors of the proposed isolator were nonlinear due to the eccentricity. The fundamental frequency of the isolation system varies with the amplitude of the rolling angle, *i.e.* the restoring force of the isolator is nonlinear. Consequently, the eccentric isolator performs better than a corresponding linear system without damping. The advantage of this eccentric isolator due to nonlinearity has been observed. However, a well-designed isolation system should possess energy-dissipating ability. The absence of damping

¹ Ph.D. Student, Department of Construction Engineering, National Taiwan University of Science and Technology, d9405004@mail.ntust.edu.tw

² Graduate student, Department of Civil Engineering, National Taiwan University, r97521249@ntu.edu.tw

³ Research Fellow, National Center for Research on Earthquake Engineering, chung@ncree.narl.org.tw

⁴ Professor, Department of Civil Engineering, National Taiwan University, lywu@ntu.edu.tw

⁵ Associate Professor, Department of Construction Engineering, National Taiwan University of Science and Technology, hungming@mail.ntust.edu.tw

may imply that responses may not decay when the excitation ends. The energy-dissipating effect was not considered in their study. As such, the proposed nonlinear isolator still needs further advancements. Hence, in this research, the eccentric rolling isolator with friction damping was considered. In order to guarantee that the advantage of both nonlinearity in ERIS and the additional friction damping is not contradictory, the nonlinear behavior of the ERIS with additional friction damping was investigated and served as the main objective of the research. First, the eccentricity was selected by a familiar isolation frequency. Based on this selected eccentricity, the stiffness of the corresponding linear isolation system can be calculated by the linearized frequency. For the two isolation systems, the friction parameters including the normal force for ERIS and the passive friction coefficient for the linear isolation system were designed by the same optimization procedure. Then the behaviors of the two isolation systems with friction damping were simulated numerically through free vibration and forced vibration cases. Finally, the performances were compared under seismic excitations of varying amplitudes.

Numerical Simulation

From Figs. 1 and 2, the schematic diagrams show the whole scenario of the eccentric rolling isolation system with a friction damper on each isolator. The mass m represents that of the superstructure or any expensive facility. The isolation object was pin-connected eccentrically to the circular isolator. The link between the mass and the pin was considered as rigid. The distance between the center of circular isolator and the pin is denoted as αR . The eccentricity α describes the location of the pin on the circular isolator of radius R . The dynamic behavior is nonlinear for the eccentric rolling isolation system while the eccentricity (α) is greater than zero and smaller than unity ($0 < \alpha < 1$). The additional friction damper was installed on the rigid bar with distance αR from the pin (see Fig. 2), *i.e.* the friction damper is located at the center of circular isolator if the system is in the state of the lowest position. The μ_d is the friction coefficient between the circular isolator and the friction damper. The normal force N of the friction damper can be tuned by the bolts. The equation of motion of the proposed isolation system under ground acceleration \ddot{X}_g was obtained and is expressed as

$$(mR^2 + m\alpha^2R^2 - 2m\alpha R^2 \cos \theta)\ddot{\theta} + m\alpha R^2 \sin \theta \cdot \dot{\theta}^2 + mg\alpha R \sin \theta - f_r\alpha R = -[mR - m\alpha R \cos \theta]\ddot{X}_g \quad (1)$$

where θ is the only one degree-of-freedom of rolling angle and f_r is the friction force modeled

from Coulomb's model with maximum friction force equal to $\mu_d N$. The linearized frequency shown in equation (2) is obtained by assuming the free vibration in equation (1) has a small displacement.

$$f_0 = \frac{1}{2\pi} \sqrt{\frac{mg\alpha}{(mR^2 + m\alpha^2R^2 - 2m\alpha R^2)}} = \frac{1}{2\pi(1-\alpha)} \sqrt{\frac{\alpha g}{R}} \quad (2)$$

This linearized frequency was assigned to be the frequency of the linear isolation system in the succeeding numerical comparisons. Once the eccentricity (α) and the radius of circular isolator are decided, the linearized frequency is determined. The stiffness of the corresponding linear isolation system was calculated by $k = m(2\pi f_0)^2$.

The typical isolation period is 2-3 seconds (Naeim and Kelly, 1999; Yang *et al.*, 2005), which can be expressed as 0.33 to 0.5 Hz. When the eccentricity (α) equals to 0.3, the linearized frequency (f_0) from equation (2) is 0.39 Hz, which belongs to the range of 0.33-0.5 Hz. Therefore the eccentricity of 0.3 was selected. The other parameters of the eccentricity rolling isolation system are: $m=1$ (ton), $R=1$ (m) and $\mu_d=0.1$. However, the normal force N of the friction damper should be designed. Herein, the original far-field El Centro earthquake with peak ground acceleration (PGA) equal to 3.42 (m/sec²) was selected to be the design earthquake. The normal force N was optimized by minimizing the absolute acceleration of the mass block under El Centro earthquake excitation. The optimal normal force N occurs at 12 kN. For the corresponding linear isolation system, the mass is the same with ERIS. The stiffness of the linear isolation system can be converted then by $k = m(2\pi f_0)^2$. In this linear system, the friction is provided by the self-weight multiplied by a friction coefficient (μ_i). Therefore, the optimal friction coefficient was optimized at μ_i of 0.053 under the design El Centro earthquake.

The frequency of the sine wave is in the range between 0.1 to 3 times the linearized frequency with amplitude equal to 0.1 g. The simulation results are shown in Figs. 3 and 4. The performances of the two isolation systems are very close when the frequency ratio is smaller than 0.75 or larger than 1.25. The two isolation systems are effective only when the frequency ratio is larger than 1.5. When the frequency ratio is close to 1 ($f_{ext} = f_0$), the resonant effect for the ERIS is much smaller than the linear isolation system. In other words, the isolation system may fail when subjected to resonant sinusoidal excitation.

The two systems were numerically simulated

subjected to different amplitudes of the El Centro earthquake. The simulation results are shown in Figs. 5 and 6. In Fig. 5, the maximum displacements of the two isolation systems increase with the increasing of the amplitude from 0.05 to 1 g. In this amplitude range, the two curves of maximum displacement are very close. Moreover, the relation between the excitation amplitude and the acceleration ratio is shown in Fig. 6. In this, the acceleration ratio is defined as the maximum absolute acceleration of the mass divided by the maximum ground acceleration. In Fig. 6, the two curves of acceleration ratios are not always close with the increase of excitation amplitude. Generally, the two curves are close if the amplitude is smaller than 0.45 g. Once the amplitude becomes larger than 0.45g, the acceleration ratio for the ERIS is lower than that of the linear system. From these results, the ERIS may perform better than the linear system under some seismic loadings like the El Centro earthquake with large amplitude. The maximum displacements in the two systems may be close but the acceleration of the ERIS is smaller.

In addition, the two isolation systems were simulated under various amplitudes of the Chi-Chi earthquake. The simulation results demonstrated in Figs. 7 and 8 refer to responses on maximum displacement and acceleration ratio. In this case, the overturn may occur at the ERIS, so the amplitude is bounded by a maximum of 0.8 g. From Fig. 7, the variations of the maximum displacement of the two systems are similar. The maximum displacements of both systems increase as with the amplitude. In Fig. 8, the performances of the two isolation systems are close when the amplitude is smaller than 0.15 g. However, the acceleration of the ERIS is much smaller than the linear system when the amplitude becomes larger than 0.15 g. For example, when the amplitude equals to 0.8 g, the maximum absolute acceleration of the linear system and the ERIS are 16 and 4 (m/sec²), respectively. This shows that the ERIS is much better than the linear system when the amplitude is large enough. Figure 8 also shows that the linear system is ineffective when the amplitude is larger than 0.35 g. And, it is slightly effective when the amplitude is smaller than 0.35 g. In the view point of the ERIS, the acceleration ratios are all smaller than 1 except at 0.05 g. Generally, the acceleration decreases as amplitude increases. From the discussion above, when the amplitude is larger than 0.15 g, ERIS performs similar to the linear system on displacement response but is much better in acceleration response.

Conclusions

Based from simulation results, the proposed eccentric rolling isolation system with additional friction damping was investigated. In resonant sine wave, the responses of the linear system become larger and larger divergently due to resonance. However, the responses of the ERIS are amplified but

not divergent. And although ERIS is amplified, the amplification is still much more slightly compared with the linear system. In far-field El Centro earthquake, both systems are effective. The nonlinear behavior of the ERIS is not clear under El Centro earthquake because the displacement is not large enough. Also, the robustness of the two isolation systems under various amplitudes of the El Centro earthquake was also verified. The acceleration ratios of the two isolation systems are smaller than 0.4 when the amplitude is larger than 0.15 g. When the external excitation changes to near-fault Chi-Chi earthquake, the nonlinear behavior of ERIS is found to be more evident. This behavior of ERIS implies that its acceleration ratio is much smaller than the linear system. The relationship of excitation amplitude and performance also shows that the displacements of the two systems are close no matter what value of amplitude is. But ERIS performs better than the linear system regarding acceleration response. This advantage of ERIS can be observed easily when the excitation amplitude becomes larger and larger.

References

Chung L.L., Yang C.Y., Chen H.M. and Lu L.Y. (2009), "Dynamic behavior of nonlinear rolling isolation system," *Structural Control and Health Monitoring*, Vol. 16, pp. 32-54.

Naeim, F., Kelly J. M. (1999), "Design of Seismic Isolated Structures: from theory to practice," John Wiley & Sons.

Yang, Y. B., Lu L.Y., Yau J.D. (2005), "Structure and Equipment Isolation Vibration and Shock Handbook," edited by C. W. de Silva, CRC Press, Taylor & Francis Group Chapter 22.

Chopra A.K (1995), "Dynamic of Structures: Theory and Applications to Earthquake Engineering."

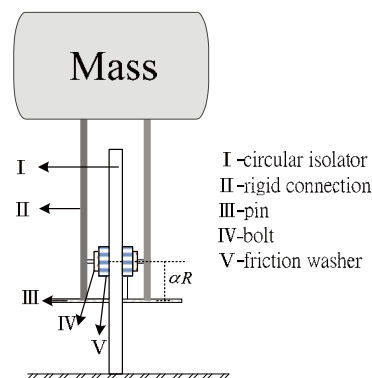


Fig. 1 Side view of ERIS

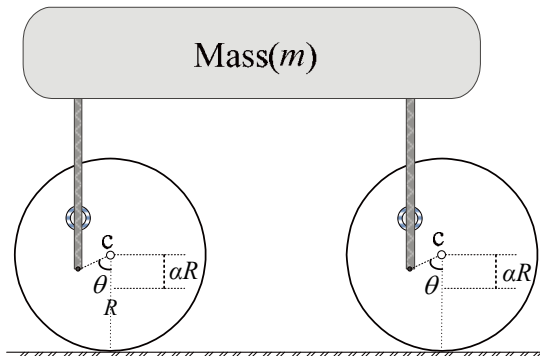


Fig. 2 Front view of ERS

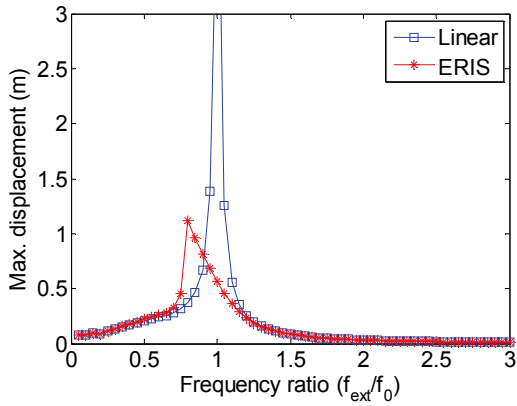


Fig. 3 Max. disp. vs. frequency ratio

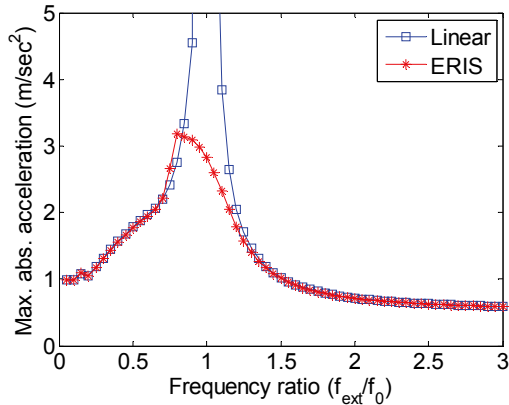


Fig. 4 Max. abs. acceleration vs. frequency ratio

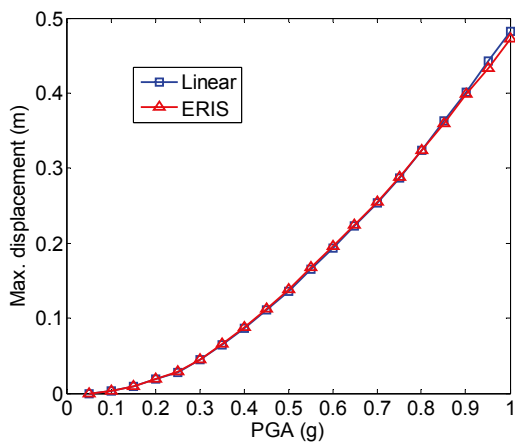


Fig. 5 Max. disp. vs. PGA (El Centro)

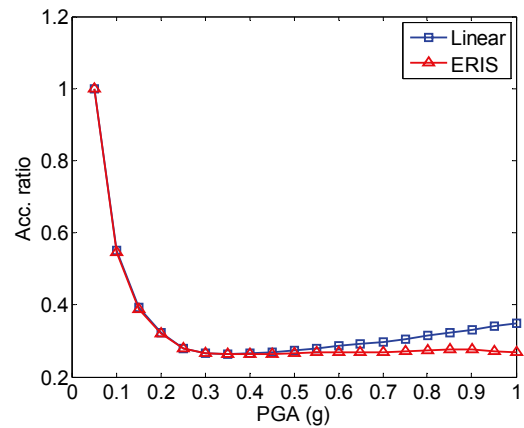


Fig. 6 Acceleration ratio vs. PGA (El Centro)

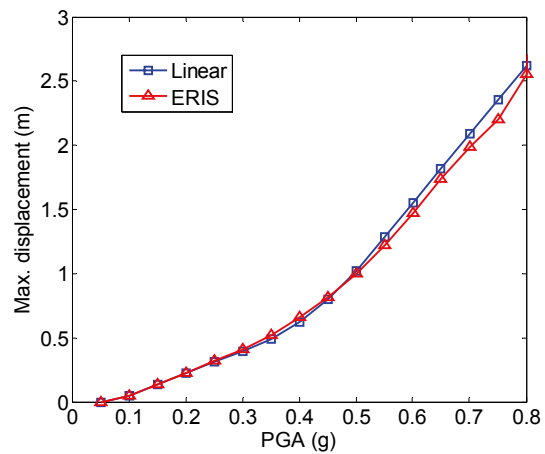


Fig. 7 Max. disp. vs. PGA (Chi-Chi)

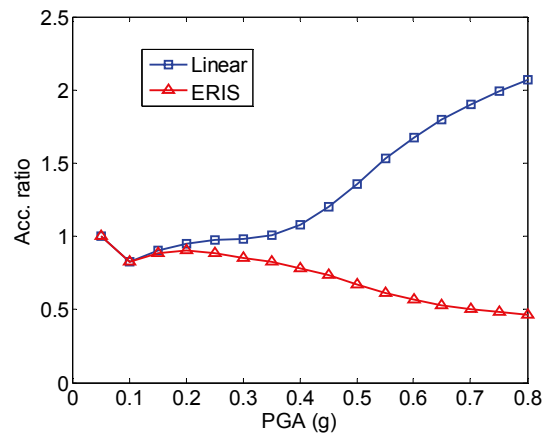


Fig. 8 Acceleration ratio vs. PGA (Chi-Chi)

Decentralized Control using Smart Control Device

Shieh-Kung Huang¹ Kung-Chun Lu² and Chin-Hsiung Loh³

黃謝恭¹、盧恭君²、羅俊雄³

Abstract

Depending on the large dimension and high degree-of-freedom of the real structure, the communication between sensors and controller becomes very complicated in control system. To overcome this, researchers proposed the concept of decentralized control. Incorporating with decentralized sliding mode control (DSMC), the smart control device (SCD) has been developed to enhance the reliability of semi-active control system and to reduce the cabling problem. This SCD integrates the measurement system, the computation system, and the control system. According to the feedback of LVDT, PAC evaluates the control command and output to MR Damper to mitigate the structure responses.

Keywords: decentralized control, semi-active control, MR damper

Introduction

Smart structure implies the ability of structure to sense, diagnose, and actuate in order to perform its functions (close-loop smartness). In a close-loop structure, sensor outputs are processed by the controller to generate actuator commands. Thus, a close-loop smart structure requires a controller. In conducting structural control there are three major systems that need to be integrated: (1) the sensing system, (2) the controller, (3) the actuation system.

One of the key functionalities required for a structure to be termed “smart” is the ability to sense. Civil engineering structure, such as tall buildings and long span bridges, involve a large number of degrees of freedom. As the results, static output feedback controllers that utilize only the measured information from a limited number of sensors are more desirable. Another key functionality is actuation. In practical application, the Magneto-Rheological (MR) dampers which are low power consumption, high reliability, and fail-safe operation, make the semi-active control technique become the one of the most attractive and promising approaches for the mitigation of structural response during seismic events. Dyke et al. used the acceleration feedback and MR damper to control the structural responses and have obtained a very good result. The last key functionality required for a smart

structure is the control algorithm. Because of the high dimensionality of the finite element model of the real structural system, the multiple input and outputs (MIMO), and the complex performance criteria, it is difficult to design a controller so as to achieve the desired control effectiveness for a large-scale structure. Therefore, the concept of decentralized control has been proposed to replace the global control system with several local control systems. Yang et al. had carried out a systematic investigation for the application of sliding mode control applied to building structures. Demonstration of decentralized sliding mode control of structure using MR dampers had been studied and verified using shaking table test by (Lu et al.).

The objective of this report was to develop a smart control device that integrates the measurement system, the computation system, and the control system. Verification of this smart control device has been conducted on the shaking table at the National Center for Research on Earthquake Engineering (NCREE) by mounting the smart control device in a 6-story 1/4-scale steel frame. The control effectiveness was also verified through shaking table test.

Smart Control Device

SCD (smart control device) integrates the

¹ Research Assistant Fellow, National Center for Research on Earthquake Engineering.

² Doctor, Department of Civil Engineering, National Taiwan University.

³ Professor, Department of Civil Engineering, National Taiwan University.

measurement system, the computation system, and the control system into a device. This device can overcome the cabling problem, reduce the real-time computation, and enhance the control reliability. In this report, SCD was combined with LVDT (Linear Variable Displacement Transformers), PAC (Programmable Automation Controller), and MR Damper (Magneto-Rheological Damper), as shown in Figure 1

The LVDT implemented here was Temposonics II manufactured by MTS Systems Corporation. This LVDT has +/- 50mm in measurement range and +/- 10V in signal range, respectively. It is a low non-linearity and high resolution LVDT, so it becomes the best choice for implementing SCD. One MR Damper was used also in SCD. This MR Damper (RD-1005-3) was provided by LORD Corporation. The maximum output force of this damper is 3kN, maximum input voltage is 0.8V, maximum input current is 2.0A, and the maximum stroke is +/-20mm. The performance test of RD-1005-3 is shown in Figure 2.

The key component of SCD is the Driven Box, which has five major functions: a. To supply power, b. To collect data, c. To output command, d. to process control algorithm, e. To update control algorithm and control parameters by the user. In order to offer these functions, the Driven Box includes the following components: power supply, power management, signal condition, VCCS (voltage-controlled current source), and PAC, as shown in Figure 3.

The power supply, NES-100-24, was provided by Mean Well Corporation. The NES-100-24 is a switch power supply and has an input current of 60Hz, 110V, 2.5A. The output current of the power supply is +24VDC, 4.5A. Power management was used to regulate the +24VDC power into +/-15VDC for LVDT. The DCW08B-15, also provided by Mean Well Corporation, is a dual-output, switch-mode regulator. The signal condition is the interface between LVDT and PAC, and converts the signal

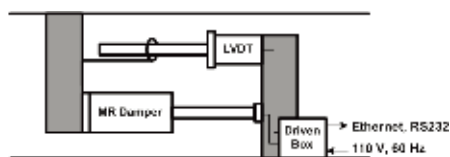


Figure 1: The components of SCD

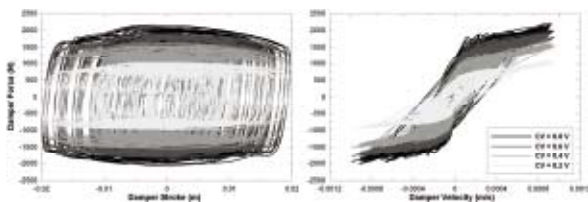


Figure 2: Performance test of RD-1005-3

range of the LVDT into the dynamic range of ADC (Analog to Digital Converter) in PAC. The VCCS is

an analog amplifier used to control the current applied to MR Damper. With VCCS, output current from Driven Box depends on the command voltage regardless of the damper resistance. The VCCS selected in this report was Model 4122Z DC Brush Servo Amplifier which was manufactured by Copley Controls Corporation. This VCCS operates from +22 to +90VDC unregulated power (+24VDC in this case), and outputs 10A continuous, 20A peak.

The PAC in the Driven Box was CompactRIO (NI cRIO-9072). The CompactRIO, designed by National Instruments, is operated by +24VDC unregulated power. This cRIO-9072 has 266 MHz industrial real-time processor for control and 1M gate FPGA for custom I/O timing. In order to collect signals from LVDT and send command to VCCS, both ADC module and DAC module should be implemented, such as NI 9215 and NI 9269. Moreover, the cRIO-9072 has 10/100BASE-T Ethernet port or RS232 serial port to communicate with the host PC. Using NI LabVIEW software, host user can monitor all the data or change the parameters through these communication ports.

Control Algorithm

To avoid the major difficulties in the structural control system, only the story drift was measured within the hardware design of SCD. Therefore, the concept of decentralized control was proposed. In this report, the theory of SMC (sliding mode control) is presented to implement decentralized control.

The SMC designs the controllers to drive the response trajectory in to the sliding surface where the motion on the sliding surface is theoretically stable. For linear structures, the sliding surface can be represented as a linear combination of the state vector, such as

$$S = PZ = 0$$

where **S** is sliding variable vector, **P** is parameter matrix, and **Z** is state vector. In decentralized SMC (DSMC), *i*-th sliding variable, S_i , is a function of x_i and \dot{x}_i , such as

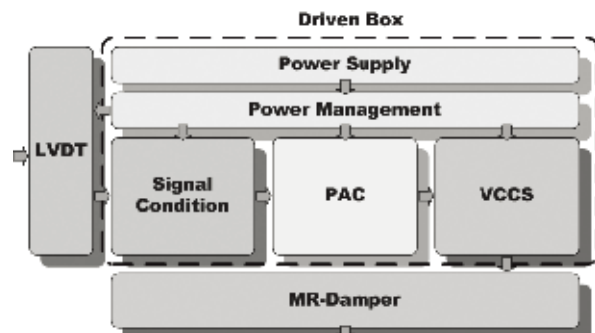


Figure 3: Components of Driven Box

$$S_i = \alpha_i x_i + \dot{x}_i$$

Based on the theory of SMC, the Lyapunov function can be expressed as

$$V = \frac{1}{2} S^T S$$

The derivative of the Lyapunov function can be obtained by defining $\lambda = S^T P B$ and $G = -(PB)^{-1} P(AZ + E)$

$$\dot{V} = \lambda(U - G) = \lambda U - \lambda G = \dot{V}_1 - \dot{V}_0$$

$$\dot{V}_1 = \lambda U = \sum_{i=1}^r \lambda_i u_i \quad \text{and} \quad \dot{V}_0 = \lambda G = \sum_{i=1}^r \lambda_i G_i$$

Therefore, to design a sliding mode controller, it is necessary to guarantee that $\dot{V}_1 \leq 0$. One possible design can be obtained by minimizing \dot{V}_1 in above equations. Hence, the minimization of \dot{V}_1 depends on the signs of λ_i and u_i . Based on this criterion, the following control law is proposed

$$[\lambda_i > 0] \oplus [\dot{x}_i > 0] \begin{cases} \text{if true, } \rho_i = \rho_{\min} \\ \text{if false, } \rho_i = \rho_{\max} \end{cases}$$

where \oplus represents the exclusive-or operator, ρ_i is command voltage. Furthermore, the relative story velocity can be calculated from story drift using finite difference method. Assuming \hat{x}_i is story drift of previous step and Δt is sampling time of story drift, thus the control law can be rewritten as

$$[[(\Delta t \alpha_i + 1)x_i - \hat{x}_i] > 0] \oplus [(x_i - \hat{x}_i) > 0]$$

$$\Rightarrow \begin{cases} \text{if true, } \rho_i = \rho_{\min} \\ \text{if false, } \rho_i = \rho_{\max} \end{cases}$$

Obviously, only story drift is required in this equation, and the control law is consistent now with the design of SCD, now.

Experimental Setup

To verify the efficiency of the smart control device, a 1/4 scaled 6-story steel structure was designed and constructed at the National Center for Research on Earthquake Engineering (NCREE), as shown in Figure 4. This 6-story scaled structure was a single bay with a 1.5m x 1.0m floor area and 1.0m story in height. The size of beams was 50mm x 50mm in L-section, and the size of column was 1000mm x 150mm in rectangular section (the thickness was 25mm). The dimension of floor was 1500mm x 1000mm x 100mm, and the dimension of base plate was 1700mm x 1700mm. All the connections of beam, column, and floor were welded, but the V-shape bracings were connected to the floor using bolt. Based on the analysis, the identified first six modal frequencies were 1.05Hz, 3.50Hz, 6.12Hz, 8.99Hz, and 11.91Hz.

As mentioned previously, the MR Dampers play the role of the actuator in SCD, thus the V-shape bracings were bolted in each story to provide support for MR dampers. Moreover, considering that the V-shape bracings were rigid, the LVDT was installed on the bottom of the bracings using C-clamp to feedback the story drift. In this report, the SCD was embedded individually on the first and third floors. Figure 5 shows the installation of the MR Damper and LVDT in the first floor.

There were eight cases designed for experiment, such as un-control, passive-on control, SCD1, SCD2, SCD3, SCD4, SCD5, and SCD6, designed for control experiment. The tested structure was subjected to the North-South earthquake of El Centro, Kobe, and TCU076 (Chi-Chi earthquake) in each case. For the case of passive-on control, the MR dampers of first and third floors were applied with the maximum command voltage. For the cases of SCD, the α values in DSMC of first and third floors were the same.

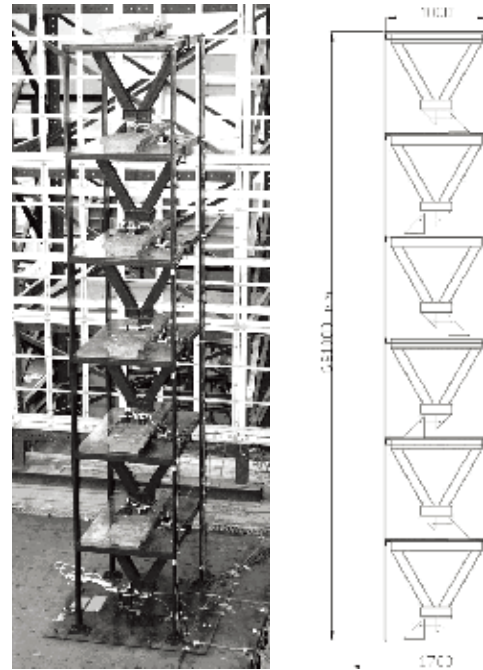


Figure 4: Photo and schematic diagrams of 6-story steel structure

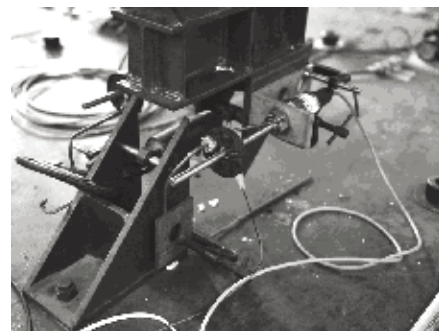


Figure 5: Photos of MR Damper and LVDT

Verification and Result

To verify the accuracy of SCD, the measured story drift and output command voltage of SCD in the first floor was compared with the data recorded by NCREE's data acquisition system (NCREE DAQ), as shown in Figure 6. This figure can show that the design of SCD was quite correct.

The control results of 150gal El Centro and Kobe earthquakes are shown in Figure 7. The x-axis indicates seven control cases (without the un-control case). The y-axis in the same figure is the ratio of the maximum response within six floors divided by the case of un-control. Generally, the acceleration responses decreased as the control cases, but the displacement responses were kept or decreased depending on the inputS earthquake. However, the ratio on passive-on control seems to be better than the SCD. The reason was that the SCD used only two story drift signals as a feedback and had difficulty in controlling the all the responses of tested structure. Different with SCD, the passive-on control used the whole hysteresis loop to dissipate energy and reduce most response. To show the advantage of SCD, it is necessary to compare the results of each floor. Figure 8 shows the control result of 150gal El Centro and TCU076. In this figure, the SCD1, SCD2, and SCD3 had excellent results in the floors with installed the SCD.

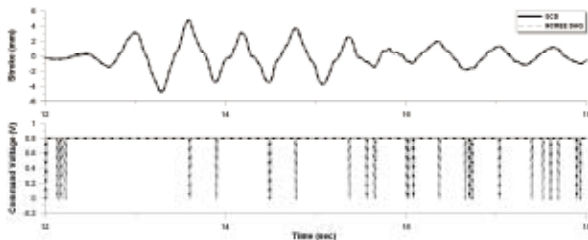


Figure 6: Comparison of measured story drift and command voltage

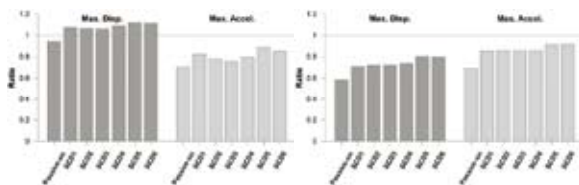


Figure 7: Comparison of control results

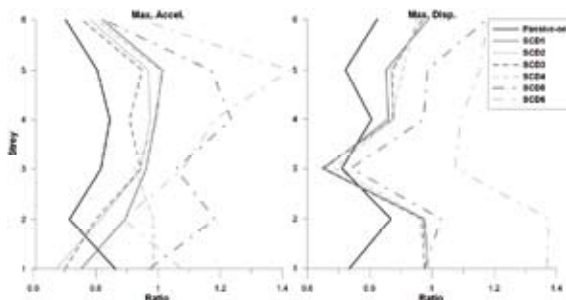


Figure 8: Control results of each floor

Conclusions

The object of this report was to develop a smart control device (SCD) that integrates the measurement system, the computation system, and the control system by combining the LVDT, PAC, and MR damper. Incorporated with decentralized sliding mode control, the SCD can enhance the reliability of semi-active control system and reduce the cabling problem. Conducting the shaking table test of a 1/4-scaled 6-story steel frame at the NCREE, the device was tested and verified. Moreover, the control effectiveness and reliability of SCD were strictly tested, and excellent results were obtained.

References

- S. J. Dyke, B. F. Spencer, P. Quest, M. K. Sain, D. C. Kapari and T. T. Soong, "Acceleration feedback control of MDOF Structures," J. Engng. Mech. ASCE, 122, 1996, 907-918.
- S. J. Dyke, B. F. Spencer, M. K. Sain, and J. D. Carlson, "Modeling and control of magnetorheological dampers for seismic response reduction," Smart Mater. Struct., 5, 1996, 565-575.
- J. N. Yang, J. C. Wu, A. M. Reinhorn and M. Riley, "Control of sliding-isolated buildings using sliding-mode control," J. Struct. Engrg. ASCE, 122(2), 1996, 83-91.
- J. N. Yang, J. C. Wu, A. K. Agrawal and S. Y. Hsu, "Sliding mode control with compensator for wind and seismic response control," Earthquake Engng. and Struct. Dyn., 26(11), 1997, 1137-1156
- K. C. Lu, C. H. Loh, J. N. Yang and P. Y. Lin, "Decentralized sliding mode control of a building using MR dampers," Smart Mater. Struct., 17, 2008.

Verification of Predicted Structural Response by Scenario-based Technique

Bing-Yun Wu¹ and Tzu-Kang Lin²

Abstract

As many structures had collapsed and were severely damaged by the 921 Chi-Chi earthquake, similar situation may inevitably happen again in Taiwan where earthquake occurs frequently. To avoid the collapse of a building during an earthquake, a real-time system called, the “Earthquake Early Warning System (EEWS)”, which can efficiently and accurately predict the structural response when earthquake happens, has been established. In this study, scenario-based and regression methods were verified by a benchmark test on shaking table to check the feasibility of the system by comparing the predicted amplitude coefficients with those obtained from tests.

Keywords: Earthquake Early Warning System, scenario, regression

Introduction

Due to the different wave speed of pressure (P) wave and shear (S) wave, there will always be a time difference between their reaching times. Recently, the concept of a real-time called, the “Earthquake Early Warning System (EEWS)” has been proposed based on the time delay characteristic of P-wave and S-wave. Meanwhile, estimation of the peak structural response is also an important issue. It was anticipated that the peak structural response can also be roughly predicted by the proposed early warning system. By knowing earthquake characteristics such as the earthquake magnitude, and the peak ground acceleration (PGA), along with other parameters (e.g. the distance between the structure and earthquake epicenter) and including them into the real-time EEWS system with scenario-based simulation technique, the amplification coefficient for each floor of a building can be easily obtained.

Regression Analysis

Regression analysis is commonly referred to as a statistical method for analyzing data. The main purpose of using regression analysis is to find the specific relationship between data, or the correlation between two or multiple parameters. Furthermore, a

mathematical model can be built up to predict specific interested variables through investigating required parameters. In this study, the regression analysis method was conducted together with a scenario-based technique in predicting the roof amplification factor of a structure under an earthquake. Since the developed regression model was based on the earthquake data collected recently, the method can be expected to be reliable with high precision for response estimation.

To discuss the relationship between the independent earthquake characteristic variables and the structural response variables, the Response Surface Methodology (RSM) was conducted. The RSM is an extended application of combined mathematics and statistics, and it is used during the design of experiments to optimize the design variables.

First, an unknown objective function should be assumed where

Y is the structural response; X_1, X_2, \dots, X_n are the independent variables, and ε is the error. The optimized design variable values and the regression model can be established by using a large amount of records from the database.

Generally, two common RMSs are used for the design purpose. One is the approximation of lower

¹ Graduate student, National Taiwan University Civil Engineering, ckwuda@gmail.com

² Researcher, National Center for Research on Earthquake Engineering, tklin@ncree.org.tw

order polynomial, which is called the first-order model:

$$Y = \alpha_0 + \sum_{i=1}^N \alpha_i x_i \quad (1)$$

Another one is the polynomial with higher order, which is the second-order model:

$$Y = \alpha_0 + \sum_{i=1}^N \alpha_i x_i + \sum_{i=1}^N \alpha_{ii} x_i^2 + \sum_{i<j} \alpha_{ij} x_i x_j \quad (2)$$

The interaction model and pure quadratic model are the other two options for regression analysis:

The mathematical form of the interaction model can be expressed as

$$Y = \alpha_0 + \sum_{i=1}^N \alpha_i x_i + \sum_{i<j} \alpha_{ij} x_i x_j \quad (3)$$

The expression for the pure quadratic model is shown below

$$Y = \alpha_0 + \sum_{i=1}^N \alpha_i x_i + \sum_{i=1}^N \alpha_{ii} x_i^2 \quad (4)$$

The model includes a constant (α_0), first order terms (α_i), interaction terms (α_{ij}), and second order terms (α_{ii}). Both interaction model and pure quadratic model are parts of second order regression models. There is no second order term in intersection models and no intersection term in pure quadratic models. A comparison of the four regression model mentioned was conducted in this study in order to determine the most effective regression model. The most suitable model chosen was then used to formulate a proper regression formula.

Shaking Table Test

Previous research has used the data of strong-motion seismograph network records to do the scenario-base and the regression analyses. The roof amplified coefficient by regression formula was verified with satisfactory result in 2010, the statistics-based technique was further improved by an experiment this year. In this study, the earthquake was simulated by the shaking table at the National Center for Research on Earthquake Engineering (NCREE), Taiwan to test the eight-story benchmark structure and to immediately analyze the fourth floor and roof level amplification coefficients relative to the ground. The resulting value was then compared with the predicted value to check the accuracy of the proposed method. The module can be integrated into the proposed

real-time EEWs.

In order to measure the full response of the eight-story benchmark structure on the shaking table during earthquake simulation, nine linear variable displacement transducers (LVDTs) and nine accelerometers were installed as shown in Fig. 1. When different earthquake time histories are simulated on the shaking table, the response of each story due to the earthquake can be collected by the installed sensor. The measured value was then compared to the predicted values that result from the regression formula, thus the accuracy of prediction can be estimated.



Fig. 1 LVDTs and accelerometers on the eight-story structure

Regression Formula and Test Result

As shown in previous research report, to obtain the roof amplification coefficient regression formula of a specific building, the strong-motion seismograph network records from Taiwan's Central Weather Bureau (CWB) and the simulated response of the roof using finite element analysis were used. In this study, 90 time histories with different PGA values and earthquake characteristics were first used to excite the eight-story benchmark structure on the shaking table, and then regression analysis with amplification coefficient of fourth and eighth floors concerned were executed. Parameters used in the regression formula

include the distance of the building from the earthquake epicenter and the peak ground acceleration. The regression formula obtained is expressed below:

The regression formula for the fourth floor:

$$\begin{aligned} Amp_4 = & 2.35172 - 4.832 \times 10^{-3} D \\ & + 1.597 \times 10^{-3} P - 3.527 \times 10^{-5} DP \\ & + 6.017 \times 10^{-5} D^2 - 2.996 \times 10^{-6} P^2 \end{aligned} \quad (6)$$

The regression formula for the eighth floor:

$$\begin{aligned} Amp_8 = & 2.72958 + 1.142 \times 10^{-3} D \\ & + 2.44 \times 10^{-3} P - 5.423 \times 10^{-5} DP \\ & + 5.795 \times 10^{-5} D^2 - 3441 \times 10^{-6} P^2 \end{aligned} \quad (7)$$

Where D represents the distance of the structure from the epicenter (km) and P indicates the peak ground acceleration (PGA).

In the regression formula, Amp_4 and Amp_8 mean the predicted value of amplification coefficient relative to ground for the fourth and eighth story, respectively. After establishing the regression formula of the specimen, the parameters were then used to estimate the required amplification coefficients.

A series of shaking table tests was then conducted to collect the earthquake response of the benchmark structure. Seismic parameters achieved on the shaking table were used in the regression analysis, and the amplification factors from ten test cases were then rapidly estimated and compared with the real amplification coefficients derived from the measured PGA values for evaluating the precision of the proposed method.

Table 1 shows the comparison among the estimated amplification coefficients of the fourth floor. It is shown that only 1 case has an error more than 40% among the ten test cases. After removing the said case that has an error more than 40%, it can be observed that there is only a minimum of 1% error and a maximum of 18% error among the remaining nine cases.

Similarly, Table 2 shows the comparison among estimated amplification coefficients of the eight-story as obtained from the shaking table test. The measured values are larger than one compared to the fourth floor's value. Moreover, the estimated values follow the trend in Table 1, and the estimated errors on the response of the eighth floor are small. Even though the largest error was 24% and some are more than 20%, the result is still acceptable. In view of the rapid estimation of the amplification coefficients, the developed regression formula is adequate, but improvements should still be made.

In Table 3 and 4, the comparison of the earthquake intensity on the fourth and eighth floors is shown. There are only two cases that do not match the

prediction in Table 3. However no significant differences were observed between the PGA value and the estimated value. It can be inferred that the misclassification is mainly caused by the value near the boundary of two intensity levels. In Table 4, two cases were estimated to be level higher than the achieved intensity with the remaining estimations correct. The errors can be inferred as the same reason discussed earlier. By comparing the intensity estimates of the fourth and eighth floors, as the intensity estimated is correct or higher, the regression formula can provide an acceptable and conservative estimation.

Table 1. Comparison of regression amplification coefficients and errors on the 4th floor

	amp_4F	Regression amp_4F	error
CHY004	2.17	2.22	2%
CHY104	1.89	2.21	17%
HAW006	2.53	2.21	-13%
ILA030	2.13	3.01	41%
ILA051	3.06	2.77	-9%
TAP008	3.63	3.76	4%
TAP020	4.00	3.41	-15%
TAP051	3.90	3.86	-1%
TCU071	1.98	2.30	16%
TCU138	2.75	2.27	-18%

Table 2. Comparison of regression amplification coefficients and errors on the 8th floor

	amp_8F	Regression amp_8F	error
CHY004	3.32	3.16	-5%
CHY104	2.62	2.90	11%
HAW006	2.87	2.94	2%
ILA030	3.51	4.36	24%
ILA051	4.57	4.07	-11%
TAP008	6.43	5.81	-10%
TAP020	5.05	5.01	-1%
TAP051	5.93	6.31	6%
TCU071	2.52	3.04	21%
TCU138	3.76	2.98	-21%

Table 3. The comparison of 4th floor intensity

	pga_4F (gal)	Estimated pga_4F (gal)	Practical Intensity	Estimated Intensity
CHY004	212.66	217.91	5	5
CHY104	168.56	197.09	5	5
HAW006	233.24	203.49	5	5
ILA030	190.12	268.72	5	6

ILA051	260.68	236.37	6	5
TAP008	362.6	376.34	6	6
TAP020	368.48	314.31	6	6
TAP051	408.66	404.96	6	6
TCU071	180.32	209.76	5	5
TCU138	247.94	204.29	5	5

Table 4. Comparison of 8th floor intensity

	pga_8F (gal)	Estimated pga_4F (gal)	Practical Intensity	Estimated Intensity
CHY004	325.36	309.85	6	6
CHY104	233.24	258.87	5	6
HAW006	264.6	270.90	6	6
ILA030	312.62	389.00	6	6
ILA051	390.04	347.12	6	6
TAP008	642.88	580.32	6	6
TAP020	465.5	461.90	6	6
TAP051	622.3	661.22	6	6
TCU071	229.32	277.17	5	6
TCU138	339.08	268.59	6	6

Conclusions

In this study, regression formulas for amplification coefficients based on the shaking table test and as confirmed through a benchmark structure were established. Since most of estimated amplification coefficients are close to the predicted values, the developed expressions are acceptable. The future works shall focus on the enhancement of the accuracy of estimation. Furthermore, the regression formulas obtained from the experiments are currently based on the 90 cases received from the shaking table test. The extension of regression database is necessary to improve the credibility and reliability of the system.

References

MATLAB. *User's Guide*. The MathWorks, Inc.: Natic, MA, 1992

On-line Structural Damage Localization and Quantification Using Wireless Sensors

Ting-Yu Hsu¹, Shieh-Kung Huang², Kung-Chung Lu³, Chin-Hsiung Loh⁴

Abstract

In this paper, a wireless sensing system was designed to realize on-line damage localization and quantification of a structure using the frequency response function change method (FRFCM). Data interrogation algorithms were embedded in the computational core of the wireless sensing units to extract necessary structural features, i.e. the frequency spectrum segments around eigenfrequencies, automatically from measured structural response for the FRFCM. Instead of the raw time history of the structural response, the extracted compact structural features were transmitted to the host computer. As a result, with less data transmitted between the wireless sensors and host computer, the energy consumed by the wireless transmission was reduced. To validate the performance of the proposed wireless sensing system, a six-storey steel building with replaceable bracings in each story was instrumented with the wireless sensors for on-line damage detection during shaking table tests. The accuracy of the wireless sensing system employed was verified by comparison of data recorded using a traditional wired monitoring system. The results demonstrate that by taking advantage of collocated computing resources in wireless sensors, the proposed wireless sensing system can locate and quantify damage with acceptable accuracy and high energy efficiency.

Keywords: damage detection, wireless sensors, frequency response function

Introduction

Since the mid-1990s, a number of research teams in both the academe and the industry have proposed an impressive array of wireless sensing unit prototypes for structural health monitoring (Lynch and Loh2006). One of the advantages of wireless structural monitoring systems is that they are inexpensive to install because extensive wiring is no longer required between the sensors and the central data acquisition system. Also, the wireless sensing network is not simply a substitute for traditional tethered monitoring system but is also a decentralized architecture offering parallel processing of measured data. The collocated computational power endows wireless sensing systems with great potential for research community to discover. However, one of the remaining limitations of current wireless sensing systems is the finite energy sources used to power such devices in the field because portable batteries

with limited operational duration are still the most-likely power source for the system's sensor nodes. Since wireless radio consumes large amount of electrical energy, energy can be saved by minimizing the use of the wireless communication channel, especially when far-reaching communication ranges are required. Therefore, minimizing the need to transfer long time-histories of structural response data by programming wireless sensing units to locally interrogate their data first seems an appropriate solution to improve the overall energy efficiency of the wireless structural monitoring system.

In this paper, the authors proposed to integrate the frequency response function change method (FRFCM) (Hsu and Loh 2009) with wireless sensing systems to not only detect the presence and location of damage but also to estimate the extent of damage, i.e. Level 3 damage detection. The integration of the FRFCM with a wireless sensing system was realized and then validated via a six-storey steel building on a shaking

¹ Associate Research Fellow, National Center for Research on Earthquake Engineering, dysheu@ncree.narl.org.tw.

² Assistant Research Fellow, National Center for Research on Earthquake Engineering, sghuang@ncree.narl.org.tw.

³ PhD, National Taiwan University, d95521003@ntu.edu.tw

⁴ Professor, National Taiwan University, loh0220@ntu.edu.tw

table. The energy efficiency gained by the proposed wireless sensing system to detect damage is also illustrated.

Implementation of the FRFCM on A Wireless Sensing System

The prototype of wireless sensing unit developed by Wang (2007) was employed to realize the on-line damage detection. This prototype has been applied successfully to both structural health monitoring (Lu *et al.* 2008) and structural control (Wang *et al.* 2007).

The frequency response function change method (FRFCM) derived from the equations of motion of a shear building subjected to ground motion both before and after damage is capable to detect the location and extent of damage (Hsu 2010). The damage identification equation of the FRFCM can be expressed as

$$\boldsymbol{\tau}_d(\omega)\Delta\boldsymbol{\kappa} = (-\omega^2\mathbf{M} + i\omega\mathbf{C}_1 + \mathbf{K})(\mathbf{T}_d(\omega) - \mathbf{T}(\omega)) \quad (1)$$

where \mathbf{M} , \mathbf{C}_1 and \mathbf{K} denotes the $n \times n$ mass, damping and stiffness matrices, respectively; $\mathbf{T}(\omega)$ and $\mathbf{T}_d(\omega)$ denote the frequency response function matrix between the input ground acceleration vector and the response displacement vector of the intact and damaged system, respectively; $\Delta\boldsymbol{\kappa}$ denotes the variation of stories' stiffnesses of a shear building as

$$\Delta\boldsymbol{\kappa} = [\Delta k_1 \quad \Delta k_2 \quad \dots \quad \Delta k_n]^T \quad (2)$$

and $\boldsymbol{\tau}_d(\omega)$ denotes the matrix composed of components in $\mathbf{T}_d(\omega)$ as

$$\boldsymbol{\tau}_d(\omega) = \begin{bmatrix} T_{d1}(\omega) & T_{d1}(\omega) - T_{d2}(\omega) & & & 0 \\ 0 & T_{d2}(\omega) - T_{d1}(\omega) & & & \\ & & \ddots & & \\ & & & T_{d(n-1)}(\omega) - T_{d(n-2)}(\omega) & T_{d(n-1)}(\omega) - T_{dn}(\omega) \\ 0 & & & 0 & T_{dn}(\omega) - T_{d(n-1)}(\omega) \end{bmatrix} \quad (3)$$

where $T_{dp}(\omega)$ presents the p^{th} component in $\mathbf{T}_d(\omega)$.

The only unknown in equation (1) is the vector $\Delta\boldsymbol{\kappa}$. The system matrices of the intact system, *i.e.* mass matrix, damping matrix and stiffness matrix, and the FRFs both before and after damage are required to solve equation (1). In order to obtain the well-estimated system matrices of the intact system, one can construct a finite element model of the structure and modify it to acquire well-estimated system matrices by model updating techniques. Alternatively, the subspace identification technique proposed by Xiao *et al.* (2001) is a very useful tool to obtain the well-estimated system matrices directly from measured data.

For a certain frequency ω_j , there are $2n$ equations (both real parts and imaginary parts) with n unknowns of the stories' stiffness variations. To reduce the error due to noise in measured signals, it is suggested to use m different frequencies around each eigenfrequency and get $2n \times m$ equations for each eigenfrequency because the signal-to-noise ratio around structural eigenfrequencies is higher. And the predicted variations of stories' stiffness are determined as weighted mean of the results obtained using frequencies around each eigenfrequency according to a "results similarity criterion". It has been shown that more reliable results can be obtained using this criterion without the interference of numerical errors caused by measurement noise (Hsu 2010).

With the system matrices and also the FRFs of the intact system written in the host computer of a wireless sensing system, the rest information needed for damage detection of the monitored structure are some segments of FRFs around the structural eigenfrequencies. On the other hand, because each wireless sensing unit is equipped with a computation core which enables it to transform the measured time history to the Fourier spectrum and also identify the possible structural eigenfrequencies, the segments of FRFs around the structural eigenfrequencies can be calculated and transmitted automatically to the host computer. Therefore, the FRFCM was chosen to be integrated with the wireless sensing system to realize on-line damage localization and quantification.

The on-line damage detection procedure and data broadcast between the sensing unit and the host computer are described as follows (see Fig. 1): After the acceleration time-history $y_i(t)$ is measured in the i^{th} WSU, the Fourier spectrum $Y_i(\omega)$ is calculated by an embedded FFT algorithm. A set of p eigenfrequencies of the structure in the i^{th} WSU, $\bar{\omega}_i = [\bar{\omega}_{i1}, \bar{\omega}_{i2}, \dots, \bar{\omega}_{ip}]$, is determined by an embedded peak-picking algorithm which selects the peaks of the Fourier spectrum smoothed by an embedded smoothing algorithm. The frequency set $\bar{\omega}_i$ selected in each WSU is then transmitted wirelessly to the host computer. The most probable set of the system eigenfrequencies $\bar{\omega}_{\text{system}}$ is decided by taking the median of each set of peaks in the host computer and then broadcasted to all the n WSUs. The i^{th} WSU then transmit a set of Fourier spectrum $\tilde{Y}_i(\bar{\omega}_{\text{system}})$ around the system eigenfrequencies back to the host computer. Note that the frequency set $\bar{\omega}_{\text{system}}$ contains not only the system eigenfrequencies $\bar{\omega}_{\text{system}}$ but also 10 adjacent frequencies around them. After the host computer receives the selected frequency spectrum segments from all the WSUs, the FRF segments are estimated by dividing cross-power

spectrum between the structural response and input excitation by the auto-power spectrum of the input excitation. With the system matrices and FRFs of the structure in reference state written in the host computer, the variations of stories' stiffness matrices $\Delta\mathbf{k}$ can be calculated using these FRF segments by equation (1). Since the necessary information for FRFCM to detect damage of the structure could be accessed automatically right after a ground excitation, e.g. passing of a train or occurrence of an earthquake, on-line damage detection could be achieved.

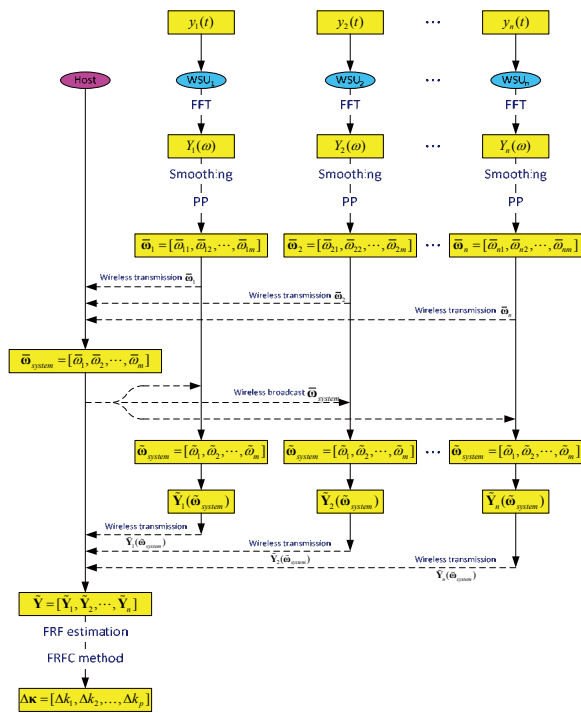


Fig. 1 Implementation of the FRFCM on a wireless sensing system.

Experimental Validation

A 1/4-scale six-storey steel building structure (Figure 3) was employed to perform experimental validation of the proposed wireless on-line damage detection operation scheme. The said six-storey structure consisted of a single bay with 1.0m×1.5m floor area and uniform 1.0-m storey height. The size of column and beam was 150mm×25mm (rectangular section) and 50mm×50mm (L-section), respectively. The beam-floor connection was welded, while the floor-beam connection and the floor-column connection were bolted. The dead load was simulated by lead-block units fixed on the steel plate of each floor, and the total mass of each floor of the target structure was 862.85 kg, except the mass of the roof floor which was 803.98 kg. The stiffness of the bracing system was controlled by a small connecting plate (named as “CP”) whose size was 100mm×10mm with clear height of 196mm.

To imitate damage of the structure, the connecting plates of some of the stories were removed. Because

the connection of the connecting plates was designed as bolted, the bending shape of the plate should be between single-curvature and double-curvature. The storey's stiffness reduction ratios after the connecting plate were removed assuming the behavior of the plates as single-curvature and double-curvature were calculated. The mean value of these two values was -37.3% and was chosen as a reference value to check with the experimental results.

In order to investigate the feasibility of the proposed wireless sensing system, a total of four different damage cases under El Centro earthquake excitation in the x-direction were studied. Case W1 was the baseline test and no damage was introduced. Case W2 was another baseline test to see if the FRFCM may give false alarm. Case W3 and Case W4 simulated the single and multiple damages, respectively, by removing the connecting plates in the designated stories. The peak ground acceleration was controlled to be less than 0.05 g because larger excitation may loosen the bolted connecting plates, which could make the extent of damage unpredictable. Note also that in real application where structure's behavior under strong earthquakes may become nonlinear, only the response in the end of the whole time-history should be used to estimate the damage.

The mass matrix was assumed diagonal with the lumped value of story mass. The stiffness and damping matrices of the structure in Case W1 were identified from measured data using the subspace identification technique with the diagonal mass matrix. The FRFs of the six-storey steel building structure in Case W1 and also the system matrices of the same structure identified using the data in Case W1 were already written in the host computer. The adjacent 11 FFT results around the six most probable eigenfrequencies were utilized to calculate FRFs right after the host computer received them from wireless sensing units. Therefore, on-line detection of the stiffness variation ratio of each storey was implemented by integrating FRFCM with the wireless sensing system.

Comparing to the stories' stiffness which can be estimated using the components in the identified stiffness matrix of the structure at the reference state, the stories' stiffness variation ratios can be estimated without establishing a finite element model of the structure. The results are plotted in Fig. 2 with bars marked as “Wireless On-line”. For Case W2 with no damage, no stiffness variations of any storey should be identified. For Case W3 and Case W4, stories with connecting plates removed should have stiffness variation ratio close to the reference value, while other stories should have no stiffness variations. For all the three cases, the damage locations were detected successfully with error of stiffness variation ratio less than 15 %. For the bars in Fig. 2 marked as “Wireless Off-Line”, the FRFs of the six-storey steel building structure after being damaged were obtained using

FFT results of the wireless-measured time history calculated in the host computer, instead of the wireless-calculated FFT results calculated in the wireless sensing units. Little improvement of the results was achieved if FFT results were obtained using the DFT algorithm in the Matlab software. This demonstrated the robustness of the algorithms embedded in the WSUs. However, if the FRFs of the test structure after being damaged are obtained using FFT results of the wired-measured time history in the host computer, the results of damage localization and quantification improved a lot (marked as “Wired Off-line” in Fig. 2). It was concluded that much less error was obtained if wired-measured data were used. The difference between wireless and wired data that causes moderate error in the estimation of stiffness variation ratio may be mainly contributed by the hardware difference, *i.e.* power supply devices of sensors, type of sensors and data acquisition system, etc. Nevertheless, the feasibility of the proposed idea to integrate the FRFCM with WSS to take advantage of collocated computing resources in wireless sensing units was verified.

The energy consumed by the wireless transmission of raw time history data E_1 is compared to the total energy E_2 required by the FRFCM including the computation of the embedded algorithm in WSUs (except the energy for recording raw time history data) and also the wireless transmission between WSUs and the host computer. If E_2 is less than E_1 , then there is an advantage of energy efficiencies contributed by the integration of FRFCM and WSS. In this study, the energy consumption E_1 is estimated as 2.94J which is only about 47% of the energy E_2 estimated as 6.27J.

Conclusions

A wireless sensing system for structural health monitoring application has been developed in this research. The wireless sensing system was integrated with the FRFCM in order to take advantage of collocated computing resources of wireless sensing systems and to reduce the energy consumed by wireless sensing units at the same time. The major achievement of the proposed wireless sensing system was the accomplishment of performing Level 3 damage detection automatically, *i.e.* on-line damage localization and quantification. In order to validate the proposed approach, a six-storey steel building structure instrumented with the developed wireless sensing units was tested on a shaking table. The experimental results demonstrate that the proposed approach works well for both single and multiple damage scenarios. The possibility of energy efficiency gained by the proposed approach was illustrated using the experimental case study where more than 50% energy is saved, as an example.

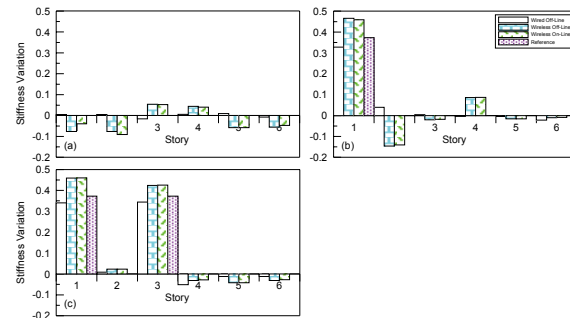


Fig. 2 Comparison among identified stories stiffnesses variation ratio obtained by wireless on-line, wireless off-line and wired off-line. (a) Case W2; (b) Case W3; (c) Case W4.

References

- Hsu T. Y., (2010) *Damage Detection of Civil Infrastructures Including Treatment of Nonlinear Environmental Effects*. Ph. D. Thesis, National Taiwan University.
- Hsu T. Y. and Loh C. H., (2009) “Damage detection using frequency response functions under ground excitation.” *Proc. of the 16th Int'l SPIE Symposium on Smart Structures and Materials and Nondestructive Evaluation and Health Monitoring*, March 2009, San Diego, CA, USA.
- Lu K.C., Loh C.H., Yang Y.S., Lynch J.P., Law K. HJ., (2008) “Real-time structural damage detection using wireless sensing and monitoring system,” *Smart Structures and Systems*, Vol. 4, No. 6, 759-778.
- Lynch J. P. and Loh K. J., (2006) “A Summary Review of Wireless Sensors and Sensor Networks for Structural Health Monitoring,” *The Shock and Vibration Digest*, 38(2), 91-128.
- Wang Y., (2007) *Wireless Sensing and Decentralized Control for Civil Structures: Theory and Implementation*. Ph. D. Thesis, Stanford University.
- Wang, Y., Swartz, R.A., Lynch, J.P., Law, K.H., Lu, K.-C. and Loh, C.-H. (2007). “Decentralized civil structural control using real-time wireless sensing and embedded computing,” *Smart Structures and Systems*, 3(3): 321-340.
- Xiao H., Bruhns O. T., Waller H., Meyers A., (2001) “An input/output-based procedure for fully evaluating and monitoring dynamic properties of structural systems via a subspace identification method.” *Journal of Sound and Vibration*, 246(4), 601-623

Theoretical and Experimental Study on the Dynamic Characteristic of Stayed Cable

Shieh-Kung Huang¹ Pei-Yang Lin² and Chin-Hsiung Loh³

黃謝恭¹、林沛暘²、羅俊雄³

Abstract

This report aimed to develop a numerical model of a stay cable interacted with deck, and to examine the vibration suppression technique of the stayed cable subject to external loading. First, a numerical model based on finite difference method and finite element method has been developed. For the vibration control of cable, a Magneto-Rheological (MR) damper was used as a control device. The MR damper can be achieved either through the passive control strategy or the semi-active control strategy. To verify this, a scaled-down cable structure was designed and constructed in NCREE. The DSMC algorithm using MR damper was studied to reduce the cable vibration under different excitation frequencies.

Keywords: cable vibration, semi-active control, stay-cable, MR damper

Introduction

Because of economic advantages and aesthetic qualities, cable-stayed bridges have been increasing popularity over the last three decades. However, vibrations of stay cables under specific loading always induce large vibration amplitude. This phenomenon is well known as a rain-wind vibration, and has been observed from a number of cable-stayed bridges. Unfortunately, the stay cables are flexible and have low inherent damping. This extremely low damping, typically in the order of a fraction of percent, is insufficient to mitigate vibrations. Sometimes, it may lead to fatigue in the cables and their anchors. To avoid these, many researchers have investigated in several ways, nevertheless, it is commonly recognized that the vibrations can be eliminated by providing mechanical dampers.

Compare to passive dampers, many researches have shown that semi-active dampers could provide much damping. Semi-active dampers offer not only the reliability of passive dampers but also the versatility and adaptability of active systems. Furthermore, Magneto-Rheological dampers (MR dampers) can be recognized as fail-safe devices because it became passive dampers when control system was malfunction. MR dampers are made from

MR fluids, which are typically consist of micron-sized, magnetically polarizable particles dispersed in a carrier medium such as water, oil or silicone. Most conveniently, these dampers can achieve the required forces in a few milliseconds for transition. Therefore, the MR dampers have been widely used to enhance the damping of cables in several researches.

Vibration control of the stay cables presented in most researches considered that the suspended cables had fixed connections at both ends. However, the span of cable-stayed bridges was much longer than other type of bridges, such as beam bridges and truss bridges. Theoretically, the vibration of deck should be slightly large and its ends are hard to consider as fixed. In this study, a numerical model of a stay cable interacted with deck was developed. To verify this, a scaled-down specimen was designed and constructed at National Center for Research on Earthquake Engineering (NCREE), Taiwan. A small shaker was mounted onto the cable to generate the sinusoidal excitation with different amplitudes and frequencies. From the results, vibration suppression can be examined for research on cable control.

Modeling of Cable-Deck

Considering an inclined cable shown in Figure 1,

¹ Research Assistant Fellow, National Center for Research on Earthquake Engineering.

² Research Fellow, National Center for Research on Earthquake Engineering.

³ Professor, Department of Civil Engineering, National Taiwan University.

for numerical analysis, the suspended cable typically has some assumptions that: (1) the cable has a uniform cross section; (2) the sag-to-length ratio is small and the tension-to-weight ratio is high; (3) the cable vibrates only in the xy-plane. Irvine recommended a simple procedure for the effect of inclination that only the component perpendicular to the cable chord was used in evaluation, as shown in Figure 1. Therefore, the equation of motion can be derived from Eq. (1) using Galerkin method or finite difference method.

$$\mathbf{M} \ddot{\mathbf{x}} + \mathbf{C} \dot{\mathbf{x}} + \mathbf{K} \mathbf{x} = \mathbf{F}$$

In Galerkin method, Pacheco et al. proposed sinusoidal shape functions to obtain the optimal damping for the suspended cable attached to a damper. For good convergence, Johnson et al. introduced the simple deformation due to a static force at the damper location as the first shape function. The advantage of Galerkin method is its excellently low order, even the number in units place. Finite difference method, proposed by Tabatabai et al., discretized the differential equation and approximated the solutions using finite governing equations. The feature of this method is its ability to account for both sag-extensibility and bending stiffness effects of suspended cable. To verify the dynamic characteristics of the numerical models simulated from these two methods, Loh and Huang carried out a laboratory test in NCREE. Figure 2 indicated that both these two methods can perfectly simulate the sag effect.

Different with Galerkin method, finite difference method directly uses dimensional quantities while deriving the equation of motion. Certainly, finite difference method can easily assemble with finite

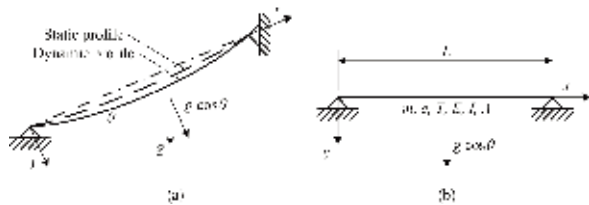


Figure 1: Schematic diagram of inclined cable

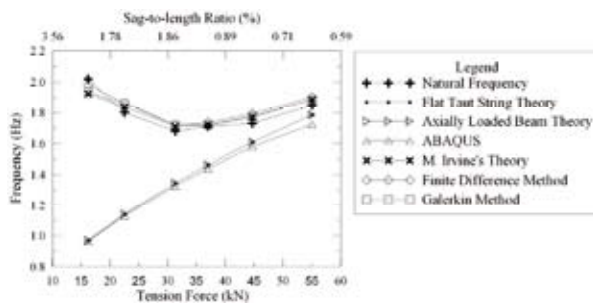


Figure 2: Estimated nature frequency of stay cable using different approaches

element model built for other components of cable-stayed bridges, such as deck model and pylon

model. In addition, the finite difference method allow engineer to apply various boundary conditions at both ends.

Due to the fact that the deck, girder, pylon and pier components of cable-stayed bridges are ideally stiffer than suspended cables, the beam-column element used in finite element method was considered in this study. Therefore, the equation of motion of these components can be derived based on stiffness matrix of uniform beam. Through four processes of finite element method (1. discretization, 2. interpolation, 3. element formulation, 4. assembling), the cable models and the deck models can be combined easily. Affirmably, this hybrid model combined from the finite element method and finite difference method can have excellent accuracy on dynamic characteristics of cable-stayed bridge.

Control of Cable Vibration

Because of the high dimensionality of the structural system, the multiple inputs and outputs, and the complex performance criteria, it is difficult to design a controller so as to achieve the desired control effectiveness for a full-scale structure. Therefore, the concept of decentralized control has been proposed. Yang et al. used the concept of sliding mode control (SMC) and applied it to a 1/4-scale six-story steel frame. Certainly, it can be applied to the stay cable interacted with deck.

The theory of SMC is to designs the controllers in driving the response trajectory in to the sliding surface where the motion on the sliding surface is theoretically stable.

$$\mathbf{S} = \mathbf{P} \mathbf{Z} = 0$$

where \mathbf{S} is sliding variable vector, \mathbf{P} is parameter matrix, and \mathbf{Z} is state vector. In decentralized SMC, i -th sliding variable, S_i , is a function of x_i and \dot{x}_i , such as

$$S_i = \alpha_i x_i + \dot{x}_i$$

Based on the theory of SMC, the Lyapunov function can be expressed as

$$\mathbf{V} = \frac{1}{2} \mathbf{S}^T \mathbf{S}$$

The derivative of the Lyapunov function is obtained by defining $\lambda = \mathbf{S}^T \mathbf{P} \mathbf{B}$ and $\mathbf{G} = -(\mathbf{P} \mathbf{B})^{-1} \mathbf{P} (\mathbf{A} \mathbf{Z} + \mathbf{E})$

$$\dot{\mathbf{V}} = \lambda (\mathbf{U} - \mathbf{G}) = \lambda \mathbf{U} - \lambda \mathbf{G} = \dot{\mathbf{V}}_1 - \dot{\mathbf{V}}_0$$

$$\dot{\mathbf{V}}_1 = \lambda \mathbf{U} = \sum_{i=1}^r \lambda_i u_i \quad \text{and} \quad \dot{\mathbf{V}}_0 = \lambda \mathbf{G} = \sum_{i=1}^r \lambda_i G_i$$

Therefore, to design a sliding mode controller, it

is necessary to guarantee that $\dot{V}_1 \leq 0$. One possible design is obtained by minimizing \dot{V}_1 in above equations. Hence, the minimization of \dot{V}_1 depends on the signs of λ_i and u_i . Based on this criterion, the following control law is proposed

$$[\lambda_i > 0] \oplus [\dot{x}_i > 0] \begin{cases} \text{if true, } \rho_i = \rho_{\min} \\ \text{if false, } \rho_i = \rho_{\max} \end{cases}$$

where \oplus represents the exclusive-or operator, and ρ_i is command voltage. Furthermore, the relative velocity can be calculated from stroke using finite difference method. Assuming \hat{x}_i is stroke of previous step and Δt is sampling time of stroke, the control law can be rewritten as

$$[(\Delta t \alpha_i + 1)x_i - \hat{x}_i > 0] \oplus [(x_i - \hat{x}_i) > 0] \Rightarrow \begin{cases} \text{if true, } \rho_i = \rho_{\min} \\ \text{if false, } \rho_i = \rho_{\max} \end{cases}$$

Obviously, only stroke is required in this equation, and the control law is decentralized sliding mode control (DSMC).

Although the semi-active device is restricted to exert dissipative force, from the performance test of MR dampers, it can be observed that the hysteresis loops of damper will sometime reach across the non-dissipative area. Therefore, the damper force can be considered as a feedback to ensure dissipation:

$$[(\Delta t \alpha_i + 1)x_i - \hat{x}_i > 0] \oplus [u_i > 0] \Rightarrow \begin{cases} \text{if true, } \rho_i = \rho_{\min} \\ \text{if false, } \rho_i = \rho_{\max} \end{cases}$$

This equation can be also identified as DSMC because only local measurement is used to evaluate the control command. Furthermore, if α is designated with a small value, the first term will have the same sign with the relative velocity of damper and the control law becomes a well-known control algorithm, maximum energy dissipation (MED), which was proposed by Dyke et al.

Experimental Setup

A scaled-down specimen was designed and constructed in NCREE. The upper end of the suspended cable was anchored to the reaction wall and lower end was anchored to the steel deck. Figure 3 shows the schematic diagram of experimental specimen.

The suspended cable of the specimen has one steel strand with seven steel wires. The area of cross section is 140 mm^2 , and the yielding stress is 1670 N/mm^2 . The upper and lower ends were inclined around 24.3 degree. Assuming the mass of steel deck is uniform

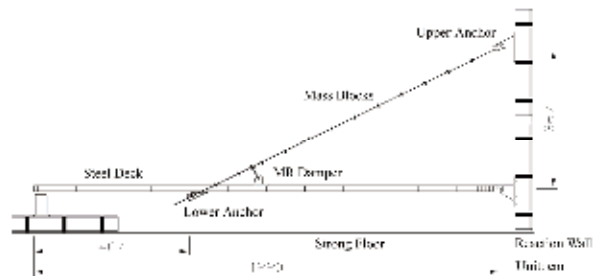


Figure 3: Schematic diagram of specimen

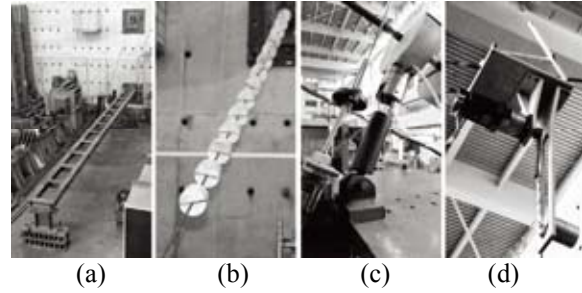


Figure 4: Photos of experimental specimen
(a) Stay Cable Interacted with Deck (b) Mass Blocks
(3) MR Damper (4) Shaker

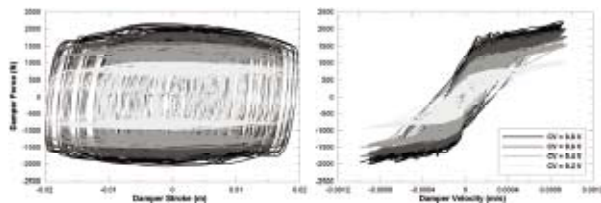


Figure 5: Voltage dependent force-displacement and force-velocity relationship of MR damper

distribution, the tension force can be roughly estimated using force balance, as 22.35kN . To maintain a similar dynamic characteristic, a total of 16 sets of mass block were used in this report and each mass block weights 17kg . The steel deck was consisted of two wide flange beams in longitudinal direction. To constrain these beams and construct a plane, 13 struts were welded in lateral between the beams. Thus, the steel deck had a size of $12\text{m} \times 0.75\text{m}$ in plane surface and $750\text{mm} \times 175\text{mm}$ in cross-section. Furthermore, the lower anchor of the cable was bolted onto the base and was considered as a rigid connection. The mass of the deck was estimated to be about 1.208 tons. The photos of the specimen are shown in Figure 4a and Figure 4b.

To mitigate the vibration, one MR damper was attached perpendicularly to the suspended cable on 12% of total length from lower end, as shown in Figure 4c. This MR damper can also be used to generate control force for control system. This MR Damper (RD-1005-3) is provided by LORD Corporation. The maximum output force of this damper is 3kN , maximum input voltage is 0.8V , and the stroke is $\pm 20\text{mm}$. The performance test was conducted under random stroke with constant voltage. Therefore, the force-displacement and force-velocity relationships of the MR damper are shown in Figure 5.

Experimental Results

In developing a numerical model for the specimen, determination of the model order is one of the most important processes. Through some analyses for convergence of modal frequencies, the determined order of the finite element model in this study was 75 nodes. The cable model and the deck model of the specimen were modeled by 102 and 50 DOFs, respectively. The cable and the deck were assembled at node 11. Using eigenvalue analysis, the identified first five natural frequencies were 1.73Hz, 3.41Hz, 5.15Hz, 6.9Hz, 8.69Hz, and 10.52Hz, respectively. To verify this numerical model, the free vibration response of the stay cable and the steel deck were collected. The initial displacement was applied at the middle point of the suspended cable. Hence, the Fourier spectrum and free vibration response are shown in Figure 6. The spectrum and response of numerical model (represented as FE Model) is also plotted in this figure. The FE Model had an excellent result in simulating of the stay cable interacted with deck, although the sag effect was considered.

According to the result presented in above sections, the MED seems to be a special case of DSMC-2. Theoretically, the feedback control cannot have the present state without estimator. Therefore, the MED may not be the best case of DSMC because the feedback signal was the past state. In this section, eight designed parameters were examined and compared. The index of these cases was calculated using following equation

$$Index_{case} = E \left[\frac{\max(A_{i,case})}{\max(A_{i,base})}, \frac{\max(D_{i,case})}{\max(D_{i,base})} \right]$$

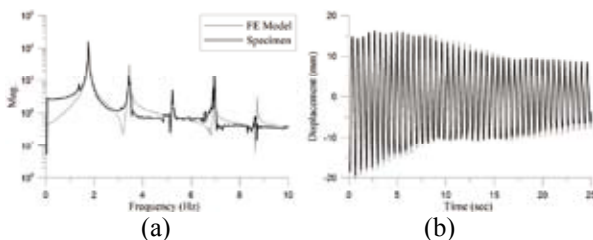


Figure 6. Experiment and simulation result
(a) Fourier spectrum (b) Free vibration response

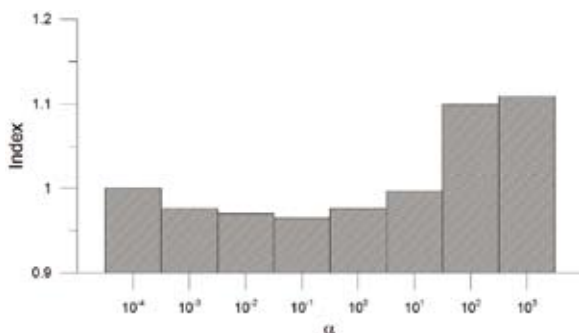


Figure 7. Index under designed parameters

where A_i and D_i are the response of i -th accelerometer and LVDT, respectively. The $\alpha = 0.0001$ was selected as a based case because it is very similar to MED. The results are shown in Figure 7. The best result was $\alpha = 0.1$ because the phase of command voltage modified by $[(\Delta t \alpha_i + 1)x_j - \hat{x}_j]$ forced the MR damper to dissipate most energy.

Conclusions

In this study, a numerical model combined from the finite element method and finite difference method was developed and verified. Using this model, the design parameters of control were selected through simulation. Moreover, the decentralized sliding mode control with stroke and force feedback was proposed for passive or semi-active control strategies of the stay cable interacted with deck. The controller embedded within DSMC not only modulated the MR damper to avoid lock-up situation, but also modified the phase of command voltage to urge dissipation. According the result collected from a scaled-down cable specimen in NCREE, the control effect was also verified. The decentralized sliding mode control algorithm using MR damper has efficiently reduced the cable vibration under different command voltages as well as different excitation frequencies.

References

- Irvine, M., [Cable structures], Dover Publications Inc., New York (1992).
- Pacheco, B. M., Fujino, Y., and Sulekh, A., "Estimation Curve for Modal Damping in Stay Cables with Viscous Damper," *J. Struct. Engrg.*, 119(6), 1961-1979 (1993).
- Johnson, E. A., Baker, G. A., Spencer, B. F., and Fujino, Y., "Mitigating Stay Cable Oscillation using Semiactive Damping," *Smart Struct. and Matls.* 2000, Proc. of SPIE, 3988, 207-216 (2000).
- Mehrabi, A. B. and Tabatabai, H., "Unified Finite Difference Formulation for Free Vibration of Cables," *J. of Struct. Engrg.*, 124, 1313-1322 (1998).
- Tabatabai, H. and Mehrabi, A. B., "Design of Mechanical Viscous Dampers for Stay Cables," *J. Bridge Engrg.*, 5(2), 114-123 (2000).
- Huang, S. K., Loh C. H., and Lin P. Y., "Damping Identification of Cable Vibration with and without MR Dampers," *Int. Conference of Struct. Health Monitoring*,
- Yang, J. N., Wu, J. C., Agrawal, A. K., and Hsu, S. Y., "Sliding Mode Control with Compensator for Wind and Seismic Response Control," *Earthquake Engrg. & Struct. Dyn.*, 26(11), 1137-1156 (1997).
- Wu, J. C., Yang, J. N., and Schmitendorf, W. E., "Reduced-order H^∞ and LQR Control for Wind-excited Tall Buildings," *Engrg. Struct.*, 20(3), 222-236 (1998).
- Lu, K. C., Loh, C. H., Yang, J. N. and Lin, P. Y., "Decentralized Sliding Mode Control of A Building using MR Dampers," *Smart Mater. and Struct.*, 17(5), (2008).
- Dyke, S. J., Spencer, B. F., Sain, M. K., and Carlson J. D., "Experimental Verification of Semi-active Structural Control Strategies using Acceleration Feedback," *Proc. of the Third Intl. Conf. on Motion and Vibration Control*, 101, 291-296 (2000).

Shaking Table Tests on Model Pile in Liquefiable Ground

Tzou-Shin Ueng¹, Chia-Han Chen², Cheng-Hsing Chen³ and Chang-Liang Lin⁴

翁作新¹、陳家漢²、陳正興³、林昌良⁴

Abstract

For the study of the soil-structure interaction in liquefiable ground under one- and two-dimensional shakings, shaking table tests on a model pile in the large biaxial laminar shear box filled with clean sand were conducted at the National Center for Research on Earthquake Engineering, Taiwan. The model pile made of aluminum alloy was used in the shaking table tests. The pile tip was fixed at the bottom of the shear box to simulate the condition of a pile foundation embedded in a firm stratum. The pile head was mounted with various numbers of steel disks. The input shakings included sinusoidal and recorded earthquake accelerations. Strain gauges and accelerometers were placed on the pile surface to obtain the bending strains and accelerations of the pile under shaking. The responses of the model pile and the soil-pile interactions under shakings for liquefied and non-liquefied soil conditions were evaluated according to the measured data. The behavior of the pile foundation was affected by the relation among the dynamic characteristics of the pile and the surrounding soil, and the mass on the pile head.

Keywords: liquefiable ground, model pile, shaking table test, soil-pile interaction

Introduction

Pile foundations have suffered extensive damage in saturated soils in many large earthquakes such as 1964 Niigata Earthquake, 1989 Loma Prieta Earthquake, 1995 Kobe Earthquake and 1999 Chi-Chi Earthquake. Previous studies on soil-pile interactions were conducted in order to understand the mechanism of the dynamic loading on the piles (soil-pile interaction) and their responses under earthquake loading. Lateral loading tests in the field or in the laboratory and shaking table tests on model piles within soil specimens, under either 1 g or centrifugal condition, have been used to investigate the pile behaviors and soil-pile interaction in saturated soil (e.g. Ashford et al., 2006, Dobry & Abdoun, 2001, Tokimatsu et al., 2005). The results of these studies, including bending moments along the piles, pore water pressure variation around the piles and failure mechanisms, can provide information on performance criteria for aseismic design of structures with pile foundations.

However, there are still uncertainties concerning the soil-pile interaction, including (1) the influence of the superstructure; (2) the effect of the dynamic characteristics and their correlations of the pile and the free-field soil; and (3) variations of responses of the surrounding soil and soil-pile system, especially during soil liquefaction. In addition, most studies on soil-pile interaction are tested and analyzed as one dimensional problem. In this study, a large biaxial laminar shear box developed at the National Center for Research on Earthquake Engineering (NCREE) as the soil container and an instrumented aluminum model pile was installed inside the shear box filled with saturated sand. Besides lateral loading tests on the model pile, the biaxial shear box with the model pile in a saturated sand specimen was placed on the shaking table at NCREE and tested under one- and multi-directional sinusoidal and recorded earthquake shakings. The responses of the model pile and soil-structure interaction under various testing conditions were studied.

¹ Professor Emeritus, Department of Civil Engineering, National Taiwan University.

² Assistant Researcher, National Center for Research on Earthquake Engineering, chiaham@ncree.narl.org.tw

³ Professor, Department of Civil Engineering, National Taiwan University.

⁴ Graduate Students, Department of Civil Engineering, National Taiwan University.

Model Piles and Sand Specimen

The model pile was made of an aluminum alloy pipe, 1600 mm in length, with an outer diameter of 101.6 mm, a wall thickness of 3 mm and a flexural rigidity, $EI = 77.62 \text{ kN}\cdot\text{m}^2$. Resistance-type strain gauges were placed on the pile surface to measure bending strains of the model pile. At each depth, two pairs of strain gauges were mounted on opposite sides of the pile in X- and Y-directions. There are 10 different depths with 15 cm in spacing along the pile axis. Vertical acceleration arrays along the pile were also set up on the model pile in X- and Y-directions for acceleration measurements. The pile was fixed at the bottom of the shear box to simulate the condition of a pile foundation embedded in rock or within a firm soil stratum. Up to 6 steel disks were fixed to the top of the aluminum pile to simulate various conditions of the superstructure. Each steel disk weighs about 37.10 kg.

Clean fine silica sand ($G_s = 2.65$, $D_{50} = 0.30 \text{ mm}$) from Vietnam was used in this study for the sand specimen inside the laminar shear box. The maximum and minimum void ratios are 0.882 and 0.609, respectively, according to ASTM D4253 Method 1B (wet method) and ASTM D4254 Method A. The sand specimen was prepared using the wet sedimentation method after placement of the model pile and instruments in the shear box. The sand was rained down into the shear box filled with water to a pre-calculated depth. The size of the sand specimen is $1.880 \text{ m} \times 1.880 \text{ m}$ in plane and about 1.40 m in height before shaking tests. Details of biaxial laminar shear box and the sand specimen preparation were described in Ueng et al. (2006).

Shaking Table Test

Shaking table tests were first conducted on each model pile without sand specimen to evaluate the dynamic characteristics of the model pile itself. Sinusoidal and white noise accelerations with amplitudes from 0.03 to 0.075 g were applied in X- and Y-directions. The model pile within the saturated sand specimen was then tested under one- and multi-directional sinusoidal (1~24 Hz) and recorded earthquake accelerations with amplitudes ranging from 0.03 to 0.25 g. White noise accelerations were also applied in both X- and Y-directions to investigate the behaviors of the model pile and the sand specimen with amplitude of 0.03 g. Figure 1 shows a shaking table test of the aluminum model pile with 6 steel disks on its top in the sand specimen.

Pile top displacements, strains and accelerations at different depths on the pile, and pore water pressures and accelerations in the sand specimen (near field and far field) were measured during each shaking, as shown in Fig. 2. Besides, the frame movements at different depths of the laminar shear box were also recorded to evaluate the responses and liquefaction of

the sand specimen using displacement transducers and accelerometers. Pore water pressures inside the sand specimen were measured continuously until sometime after the end of shaking to observe the dissipation of the water pressures. The height of the sand surface after each test was obtained for the settlement and density of the sand specimen. Soil samples were taken using short thin-walled cylinders at different depths and locations after completion of the shaking tests to obtain the densities of the sand specimen.



Fig. 1 The instrumented model pile with 6 steel disks on its top in saturated sand specimen on the shaking table

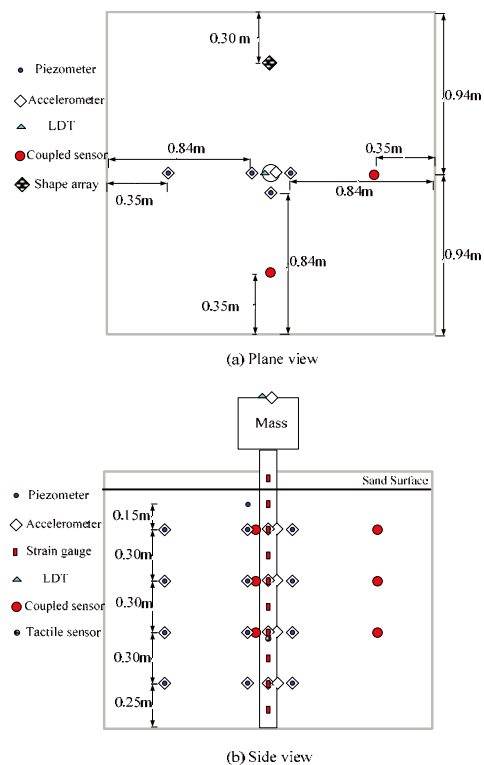


Fig. 2 Instrumentation on the pile and within the sand specimen

Test Results

Dynamic characteristics of the model pile

Shaking table tests on the model pile without sand

specimen were conducted to evaluate the dynamic characteristics of the model pile itself. We consider the behavior of model pile on the shaking table as a single-degree viscously damped system. The amplification curve was obtained from the Fourier spectral ratio of the measured acceleration of the pile top to that of the input motion. Table 1 lists the predominant frequencies of the model pile according to the test data. The average damping ratio of the model piles is about 1.4 % according to observations of the free vibration of the piles after the end of the input motions.

Table 1. Predominant frequencies of the model pile

Mass on pile top	Aluminum pile	
	Freq., Hz	
No mass	21.40	
1 steel disk	5.55	
3 steel disks	3.11	
6 steel disks	2.07	

Dynamic characteristics of soil and soil-pile system under small amplitude of shakings

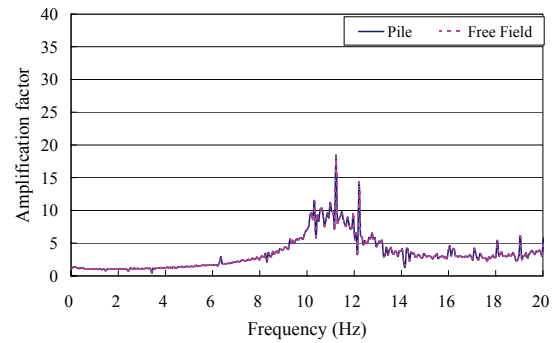
In order to investigate the effect of superstructure on soil-pile interaction prior to soil liquefaction, the dynamic characteristics of the soil stratum and soil-pile system were evaluated by white noise shaking with small amplitude. Table 2 lists the predominant frequencies of the soil and the soil-pile system for the model pile in soil of various relative densities. It can be seen that the density of sand specimen would increase after each shaking.

Table 2. Predominant frequencies of soil and soil-pile system for the aluminum pile in the soil specimen of different relative densities

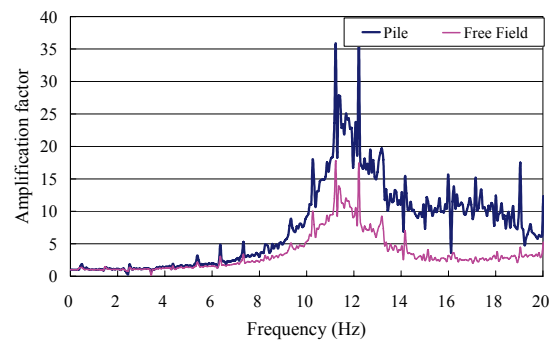
Mass on pile top	Soil	Soil-Pile	Dr %
	Freq., Hz	Freq., Hz	
No mass	11.5	11.5	27.3
1 steel disk	11.5	11.5	38.1
1 steel disk	11.6	11.6	42.8
3 steel disks	12.0	8.70	42.9
3 steel disks	12.7	9.28	50.4
6 steel disks	13.7	4.87	70.2

In addition, for the model pile without mass and with one steel disk of mass, the predominant frequencies of both soil and the soil-pile system are almost the same and these frequencies increase with the relative density of the soil specimen. For the pile with 3 or 6 steel disks, the predominant frequency of soil-pile system is significantly lower than that of the soil specimen. Comparing the predominant frequencies of the model pile without and within soil specimen (Table 1 and Table 2, respectively), one can find that, except for the case without mass on the pile top, the predominant frequencies of the model pile in the soil specimen were higher than those without soil due to the constraint of the soil on the pile. For small inertia force from the superstructure (e.g. no mass or 1 steel disk of mass on the pile top), the pile responses were dominated by the kinematic force from the soil motion, but for large inertia force (e.g. 6 steel disks of mass on the pile top), the response of pile was mainly

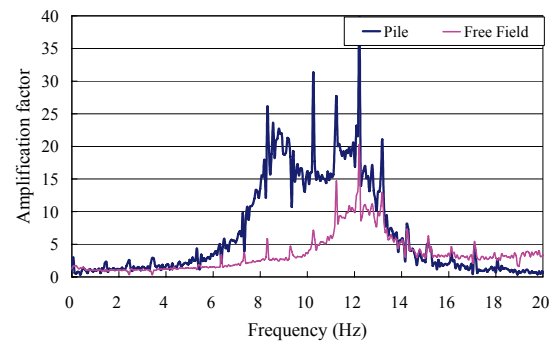
governed by the inertia force from the superstructure. Therefore, these observations suggest that the mass and inertia force induced by the superstructure play an important role on the soil-pile interaction.



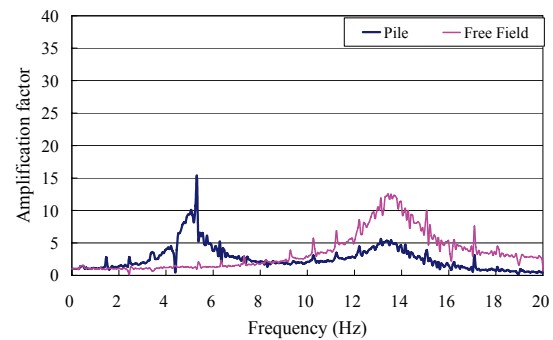
(a) No mass on the pile top (Dr = 27.3 %)



(b) 1 steel disk on the pile top (Dr = 38.1 %)



(c) 3 steel disks on the pile top (Dr = 42.9 %)



(d) 6 steel disks on the pile top (Dr = 70.2 %)

Fig. 3 Amplification factor vs. frequency for free-field soil and the model pile with various mass on its top

Figure 3 shows the amplification curves of free-field soil and the model pile, with and without mass on the pile top, in sand specimen of various relative densities under white noise shakings with amplitude of 0.03 g. It can be seen that, for the model pile without mass, the amplification curves of both soil and the pile are almost the same. As the mass on the pile top increases, there is a tendency to have distinct peaks at two different frequencies for the amplification curve of the model pile. One is the predominant frequency of the soil-pile system and the other is the predominant frequency of the soil specimen. In the case of model pile with 6 steel disks of mass (Figure 3(d)), the inertia effect of the pile and the added mass appears more pronounced than the kinematic effect of the soil movement on the pile behavior under shaking. More tests and analyses are needed to further evaluate the relative importance of the kinematic and inertia effects on the soil-pile interaction and the pile performance during earthquakes.

Response of model pile in liquefiable soil

According to the measurements of mini-piezometers in the sand specimen and accelerometers on the inner frames (Ueng et al. 2010), the sand specimen was fully liquefied under this one-dimensional sinusoidal shaking with frequency of 4 Hz and amplitude of 0.15 g. The amplification curve of the aluminum pile top with 6 steel disks during the post-liquefaction period is shown in Figure 4. The predominant frequency of the model pile within liquefied soil is identified at around 2 Hz. Comparing this result with the predominant frequency of the model pile without soil specimen (Table 1), one can find that the predominant frequency of the model pile within liquefied soil was almost the same as that of model pile without soil specimen. This inferred that the stiffness of the soil almost vanished when soil liquefaction occurred. Further analysis of the soil reaction on the model pile is needed to verify the inference.

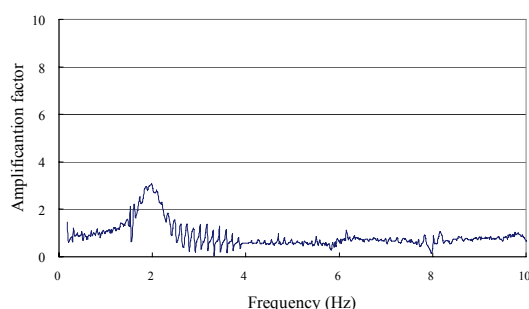


Fig. 4 Amplification factor vs. frequency for model pile with 6 steel disks after initial liquefaction ($D_r = 68.6\%$).

Conclusions

Shaking table tests were conducted on an aluminum model pile in the biaxial laminar shear box with and without saturated sand specimen. The displacements, strains and accelerations at different depths of the model pile were measured. Analyses of the dynamic behavior of the model pile and the pile-soil system during shaking tests were conducted based on the test results. It is concluded that the behavior of the model pile under shaking was affected by the soil specimen density, the dynamic characteristics of the pile and the surrounding soil, and the mass of the superstructure. Dynamic pile behavior was controlled by kinematic effect from ground motion and inertia effect from the superstructure. For a small inertia, the pile responses were dominated by the kinematic force, but for a large inertia, the responses of pile were mainly governed by the inertial force according to the amplification factor. In addition, the stiffness of the soil almost vanished when soil liquefaction occurred. Further tests and analyses of the test data will be performed to obtain more information on the soil-pile interaction, such as the relationship among soil reaction on the pile, pore water pressure generation, and pile displacements and their coupling.

References

- Ashford, S.A., Juirnarongrit T., Sugano T., and Hamada M. (2006). "Soil-pile response to blast-induced lateral spreading. I: field test," *J. Geotech. and Geoenviron. Eng.*, 132(2), 152-162.
- Dobry, R.D. and Abdoun T. (2001). "Recent Studies on Seismic Centrifuge Modeling of Liquefaction and its Effect on Deep Foundations," State-of-the-Art Report (SOAP3), *Proc. 4th International Conference on Recent Advances in Geotechnical Earthquake Engineering and Soil Dynamics*, San Diego, CA, March 26-31, Vol. 2.
- Tokimatsu, K., Suzuki, H., and Sato, M. (2005) "Effect of Inertial and Kinematic Interaction on Seismic Behavior of Pile with Embedded Foundations," *Soil Dynamics and Earthquake Engineering*, 25, 753-762.
- Ueng, T.S., Wang, M.H., Chen, M.H., Chen, C.H. and Peng, L.H. (2006). "A large biaxial shear box for shaking table tests on saturated sand," *Geotechnical Testing Journal*, ASTM, Vol.29 (1): 1-8.
- Ueng, T.S., Wu, C.W., Cheng, H.W. and Chen, C.H. (2010), "Settlements of saturated clean sand deposits in shaking table tests," *Soil Dynamics and Earthquake Engineering*, 30(1-2), 50-60.

Development of Damage Evaluation Techniques for Structural Foundation (II)

Yung-Yen Ko¹ Wei-Kuang Chang² Chia-Han Chen³

柯永彥¹、張為光²、陳家漢³

Abstract

This study aimed to validate and improve the damage evaluation techniques for structural foundation based on vibration measurement proposed last year, including the data processing and the damage quantification. A series of shaking table tests on a pier specimen with exposed foundation using the large shear box were conducted at NCREE. During these tests, ambient vibration measurements were performed on the specimen in various foundation exposure conditions prior and posterior to the excitation to investigate the influences of foundation exposure and the earthquake motion on the vibration characteristics of the pier-soil system and to verify the damage quantification methods. Moreover, field vibration measurements were made at the Shuangyuan Bridge and at the Wanda Bridge in Taiwan to examine the effects of foundation retrofit and foundation exposure on the vibration behavior of bridge superstructures.

Keywords: vibration measurement, damage evaluation, foundation exposure

Introduction

In Taiwan, several major highway bridge failures have occurred in recent years, and most of them were related to the exposure of the pier foundation due to scouring, reducing the bearing capacity of foundation. These disasters can be prevented if the damage or insufficient capacity of the foundation can be detected in advance, and the repair and retrofit works, or restraint of use can be timely executed. However, the pier foundation exposure can not be observed visually if the water table is higher than the foundation level. Although it is possible to inspect the exposure of foundation using instruments installed on it, these instruments might be destroyed in the flood condition.

The structural vibration response of a soil-structure system shows the characteristics of the system itself, and reflects the boundary conditions as well. Hence, the measurement of structural vibration might help to detect the possible damage of the structural foundation. The measurement is easy to perform, data processing methods are well developed, and many vulnerability indices have been widely used. Since the disaster mitigation of bridges has been an important issue, the focus of this study is on the foundation of bridges.

Applications of Vibration Measurement on Structural Damage Evaluation

Vibration characteristics of a structure, such as its natural frequency, damping, and modal shape, are related to its mass, stiffness, and structural integrity. If the structure is damaged, the natural frequency will be lowered due to the stiffness decrease, the damping will be increased because of the growth of cracks, and the modal shape will be changed due to the stiffness redistribution. Consequently, if the variations of the structural vibration characteristics are experimentally examined, the structural damage can be detected, quantified and located. Vibration measurement tests often used for structural characterization include:

1. Ambient Vibration Measurement: The ambient vibration is randomly generated by natural forces and civilian activities in the environment and has wide frequency content. If the input ambient vibration and the excited structural response are measured simultaneously, the transfer function can be deduced for system identification. If the input motion is unavailable, it is possible to characterize the structure merely by its excited response by assuming the ambient vibration as the white noise.

¹ Associate Researcher, National Center for Research on Earthquake Engineering, yyko@ncree.narl.org.tw

² Post-Doctoral Researcher, Department of Civil Engineering, National Taiwan University, d90521008@ntu.edu.tw

³ Assistant Researcher, National Center for Research on Earthquake Engineering, chiaham@ncree.narl.org.tw

2. **Forced Vibration Test:** The artificial vibration sources such as moving vehicles, harmonic vibrator, and hammer are utilized to excite the structure to vibrate, helping to recognize the characteristics of structural vibrations under a larger strain level or for a specific vibration source.

Methods for the data processing and the damage quantification in this study are described as follows:

1. **Average Spectrum Analysis:** When the long-term field vibration measurement is made, the vibration characteristics at different moments show a certain variance since the environment and the vibration source are not constant. To eliminate the dispersion, Samizo *et al.* (2007) used a concept that sections with a fixed duration are extracted from the overall record, and each section is partially overlapped with the next. The Fourier spectrum is calculated in each section, and the structural natural frequency is identified accordingly. All the natural frequencies are then averaged to obtain a representative one. Based on this idea, an averaged spectral curve is deduced, as shown in Fig. 1. Thus, the influence of abnormal events can be diluted, and the structural characteristics are better described.

2. **Simplified 2-DOF Pier Model:** One of the most common seismic failure modes of the bridge pier is the flexural failure at the lower end of the column, where the moment induced by the earthquake loads is usually the largest. If an intact pier is simplified to a single-degree-of-freedom (SDOF) system, as shown in Fig. 2(a), then a damaged pier can be modeled as a 2-DOF system, in which the lower end of the column and the base is connected by an rotation spring, as shown in Fig. 2(b). Thus, the integrity at the lower end of the column can be represented by the stiffness (k_R) of the equivalent rotation spring. A dimensionless rotation impedance ratio $R=k_R/(kh^2)$ is defined here. When the pier is intact, $R \rightarrow \infty$, when it is damaged, R decreases, and when it is about to collapse, $R \rightarrow 0$. Considering that the pier model is excited by a lateral ground motion, the following relationship can be deduced:

$$\frac{\omega_{damaged}}{\omega_{intact}} = \sqrt{\frac{R}{1+R}} \quad (1)$$

where ω_{intact} is the natural frequency of the intact pier, and $\omega_{damaged}$ is the natural frequency of the damaged pier. The R -value can be estimated by Eq(1) for the evaluation of damage level. The rotation spring at the base in the 2-DOF pier model can also be used to simulate the foundation rocking stiffness, which influences the vibration response of the pier top much more than other foundation stiffness components. Thus, the reduction of the rocking stiffness of pier foundation, which could be due to the degradation of supporting soil or the exposure of foundations, can also be represented by the decrease of the R -value.

3. **Nakamura's Vulnerability Index:** Nakamura (1997) proposed the vulnerability index for the railway viaduct based on microtremors, and this idea is introduced here for the damage evaluation of piers. Fig. 3 shows the pier under the excitation of the ground motion. The superstructure experiences an acceleration α_d , then the moment at the lower end of each column generated by the inertia force applied on the deck can be quasi-statically expressed as $M=m\alpha_d h$. Considering the possible flexural failure at the lower column end, the vulnerability is related to the maximum strain at the column section:

$$\begin{aligned} \varepsilon &= \frac{M}{EI} \cdot \frac{b}{2} = \frac{m\alpha_d h}{EI} \cdot \frac{b}{2} = m\alpha_d \cdot \frac{h^3}{3EI} \cdot \frac{3b}{2h^2} = \frac{m\alpha_d}{k} \cdot \frac{3b}{2h^2} \\ &= \frac{3}{8\pi^2} \cdot \left(\frac{b}{h^2} \cdot \frac{A}{f_n^2} \right) \cdot \alpha_g = \frac{3}{8\pi^2} \cdot K_{pier} \cdot \alpha_g \end{aligned} \quad (2)$$

where $k=3EI/L^3$ is the lateral stiffness of the pier, f_n is the natural frequency in Hz of the pier, α_g is the ground surface acceleration, and A is the pier amplification factor at the frequency f_n . Then K_{pier} is defined as the vulnerability index for the pier, which reveals the potential or the status of the flexural failure at the lower column end. K_{pier} -value is increased as the damage state gets more severe. It can also be used to estimate the degradation of supporting soil and the foundation exposure since these phenomena lower the rocking stiffness of pier.

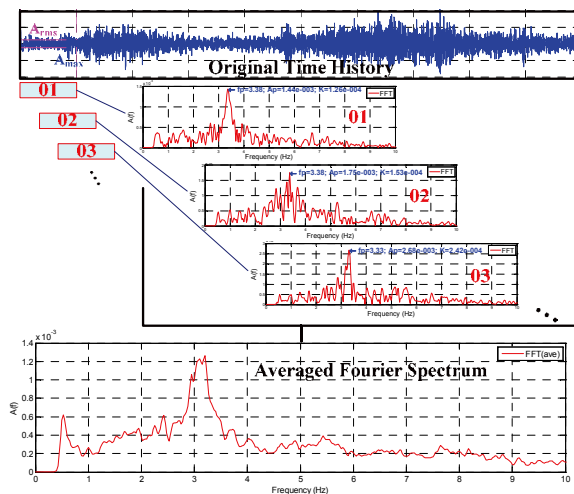


Fig. 1 Procedures of average spectrum analysis.

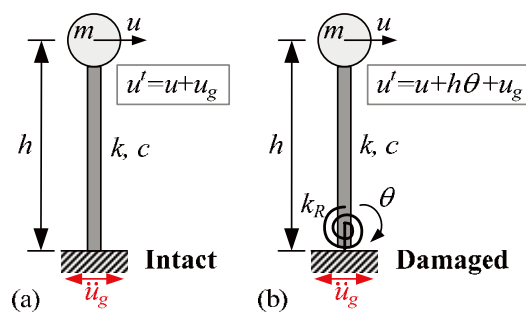


Fig. 2 Simplified pier model: (a) intact; (b) damaged.

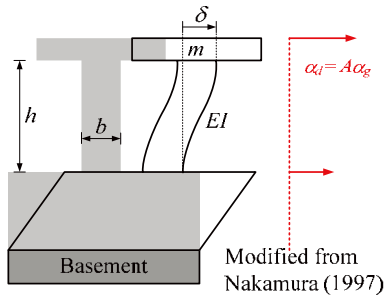


Fig. 3 Viaduct frame excited by ground motion

Ambient Vibration Measurement on Pier Specimens with Foundation Exposure

A series of shaking table tests on pier specimens with various levels of foundation exposure using the large laminar shear box device were performed at NCREE to study the seismic behavior of the scoured bridges. As in Fig. 4, the specimen was composed of a cylindrical steel block representing the mass of the superstructure, a steel pipe as the column, a steel plate as the pile cap, and an aluminum pipe as the pile. The lower end of the pile was fixed at the bottom of the shear box, and dry sand was poured into the box and compacted by layers until the soil surface was firmly in contact with the bottom of pile cap. Four conditions of the foundation were specified: (1) the original one (SBF-O), (2) the soil surface and the bottom of the pile cap had no contact (SBF-NC), (3) the depth of pile exposure was 3 times of the pile diameter (SBF-S3D), and (4) the depth of pile exposure was 6 times of the pile diameter (SBF-S6D). First, the specimen was excited using actual earthquake records in the original condition. Then the soil below the pile cap was partially removed to meet the SBF-NC condition, and the specimen was excited again. After the excitation, the soil surface was lowered to meet the next foundation exposure condition. Thus, the shaking table tests were executed sequentially by stages.

During these tests, ambient vibration measurements were made in each foundation condition prior and posterior to the excitation. The influences of the foundation exposure as well as the earthquake motion on the vibration characteristics of the pier-soil model were investigated. Vibrosensors were attached on the cylindrical steel block and on the top of the shaking table, and vibrations were synchronously recorded for 10 mins. For better characterization of the pier-soil system, the average transfer function of the vibration at the steel block to that at the top of the shaking table was deduced by the average spectrum analysis scheme. The natural frequency of the specimen in each case was identified accordingly, and the dimensionless rotation impedance, R , and the vulnerability index, K_{pier} , were calculated, as shown in Fig. 5.

For the SBF-O condition, the natural frequency of the specimen is 2.98 Hz before excitation, and is 2.00 Hz after excitation, which is a 33% decrease. In the

SBF-NC condition, the natural frequencies are 1.98 Hz and 1.97 Hz before and after the excitation. Since dry sand, which is easy to be disturbed by shaking, was used in these tests, it is presumed that the soil stiffness was significantly decreased and the pile cap and the soil surface were nearly lost contact after the excitation in the SBF-O stage so that no obvious effect due to either the removal of soil or the excitation was observed in this stage. The natural frequencies are 1.60 Hz and 1.53 Hz before and after the excitation in the SBF-S3D stage, while in the SBF-S6D stage the natural frequencies are 1.33 Hz and 1.18 Hz before and after the excitation. It can be noted that the exposure of the pile had considerably reduced the system stiffness and thus lowered the natural frequency, yet the excitation had less influence on the natural frequency, which might be due to the presumption above that the soil stiffness had been decreased at the first stage. Besides, the dimensionless rotation impedance R and the vulnerability index K_{pier} both exhibit the effects of the exposure of pile and the degradation of supporting soil, in which R reflects the soil degradation better, while K_{pier} shows the foundation exposure more effectively.

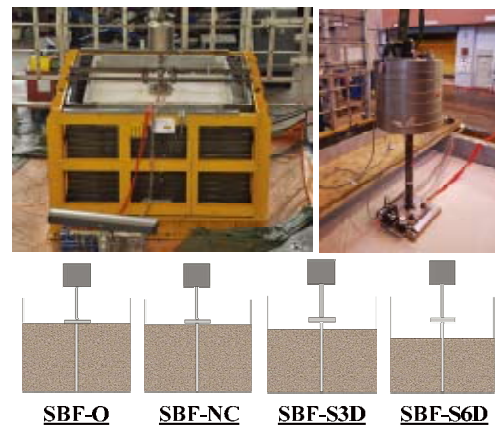


Fig. 4 Pier specimen and test configurations.

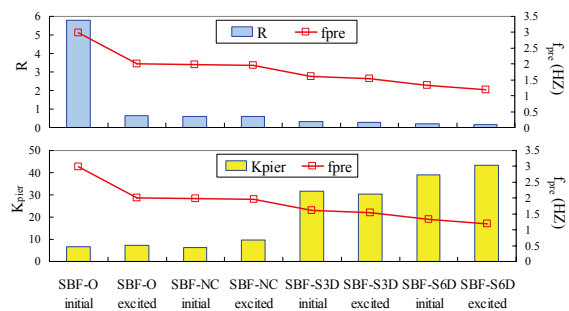


Fig. 5 Natural frequency and damage quantification of the pier specimen in each case.

Field Vibration Measurement of Bridge

During August 7~9, 2009, Typhoon Morakot brought record-high rainfalls to the southern part of Taiwan and induced serious floods, debris flows, and landslides, causing numerous damaged or even

demolished bridges. Among these damaged bridges, the Shuangyuan Bridge of Prov. Hwy No. 17, crossing the Kaoping River and connecting Kaohsiung County and Pingtung County, had not suffered serious scour problem yet part of the bridge was destroyed in this event. For the better understanding of the actual vibration characteristics of bridges, ambient vibration measurements were made at the existing sections of the Shuangyuan Bridge before the temporary bridge was finished. The targets for measurement were Unit P22-P25, which had been retrofitted by enlarging the size of the pile cap and adding piles in the longitudinal direction, and the non-retrofitted Unit P31-P34.

As shown in Fig. 6, vibrosensors were deployed on the deck at all the pier positions, and the ambient vibrations in the horizontal longitudinal (HL) direction and in the horizontal transverse (HT) direction at each pier were synchronously recorded. In data processing, a reference point was chosen, and the cross power spectra of the vibrations of all the measurement points were deduced with respect to the reference point using the averaging scheme. The fundamental frequency of the structure was identified, and the modal shape was obtained according to the amplitude and the phase angle of the cross power spectra.

Fig. 8 shows the modal shapes of Unit P22-P25, including: (a) the HT response of each pier which causes the combined translation and rotation of the deck on HL-HT plane, with a fundamental frequency of 2.07 Hz; (b) the in-phase HL response of each pier, with a fundamental frequency of 2.10 Hz; (c) the HT response of each pier which causes the in-plane bending of the deck, with a fundamental frequency of 3.67 Hz. Concerning Unit P31-P34, the fundamental frequencies corresponding to similar modes as described above are: (a)1.97Hz; (b)1.63Hz; (c)3.63Hz. The retrofit of the foundation was made by adding piles longitudinally, increasing the stiffness in the HL direction, which is reflected by the significantly rise of the fundamental frequency of mode-(b). Regarding mode-(a) and mode-(c), which are mainly composed of the HT response of the pier, the change of the fundamental frequency is relatively small. Especially mode-(c), the fundamental frequency is almost invariant. It can be concluded that the ambient vibration of the superstructure of bridges exhibits the stiffness of the foundation effectively and can be used for the damage evaluation of the foundation.

Vibration measurements were also made at the Wanda Bridge of Prov. Hwy No. 88, which is located upstream of the Shuangyuan Bridge. The targets for measurement were the pier P6, which is located in the flood plain, and the pier P18, which is in the main channel. For P18, the measurements were made during and after the flood season. Vibrosensors were installed on the deck beside the expansion joint at the pier position. The vibrations induced by normal traffic flow in both HL and HT directions were recorded for 10 mins. Using the averaging scheme, the average

Fourier spectrum of the HT vibrations in each case was obtained, as shown in Fig. 8. The main peaks are located at the frequency around 3~3.5 Hz for all the cases yet no significant difference of the predominant frequency is observed. It is presumed that these peaks are related to the local vibration mode of the deck induced by the passing of vehicles and are not able to exhibit well the condition of the foundation. There are also apparent peaks of the spectral curves located around 1.5~2 Hz for all the cases, in which the predominant frequency of P6 is 2.05 Hz, while that of P18 during the flood season is 1.56 Hz, obviously lower than P6. P18 might have suffered scour, causing the foundation to be exposed. The predominant frequency of P18 after the flood season is increased to 1.68Hz, indicating the sediment might have filled the scour hole partially, yet the stiffness of P18 in this case is still lower than P6.



Fig. 6 Layout of measurement at Shuangyuan Bridge.

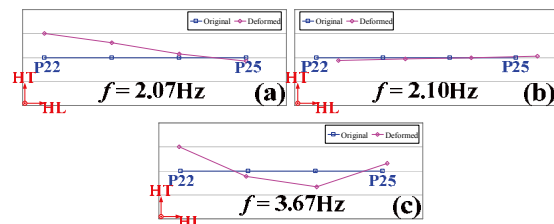


Fig. 7 Modal shapes of Unit P22-P25 of Shuangyuan Bridge.

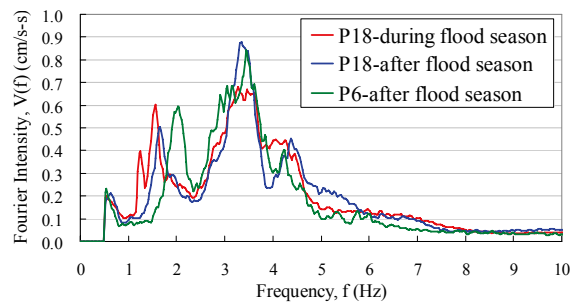


Fig. 8 Average Fourier spectra of HT vibrations of Wanda Bridge.

References

- Samizo M, Watanabe S, Fuchiwaki A and Sugiyama T. (2007), "Evaluation of the structural integrity of bridge pier foundations using microtremors in flood conditions", Quarterly Report of the Railway Technical Research Institute, 48(3), pp. 153-157.
- Nakamura Y. (1997), "Seismic vulnerability indices for ground and structures using microtremor", Proceedings of World Congress on Railway Research, Florence, Italy.

Lateral Loading-Unloading Behavior of an Aluminum Model Pile in Saturated Sand

Jiunn-Shyang Chiou¹, Wei-Lun Tai², Chia-Han Chen³ and Cheng-Hsing Chen⁴

邱俊翔¹、戴偉倫²、陳家漢³、陳正興⁴

Abstract

Pushover tests of an aluminum model pile in saturated loose sand were conducted at the National Center for Research on Earthquake Engineering (NCREE) of Taiwan. The test data were analyzed to investigate the lateral loading-unloading response of the pile. The pushover curves of the pile show a significant loop of hysteresis. The p-y curves obtained also exhibit remarkable hysteretic response. The backbone curves of the p-y curves can be expressed by the secant subgrade reaction modulus which is a function of depth and lateral displacement. The hysteresis locus of the p-y curves can be simulated by the backbone curves with the unloading-reloading model of Masing type to give consistent pushover curves to the measured.

Keywords: Sand, model pile tests, hysteretic response, p-y curves.

Introduction

Piles are commonly used as the foundation of structures to resist both vertical loads and lateral loads transmitted from the structure. For a pile-supported structure subjected to lateral soil pressure, wind forces or earthquake loading, its foundation design is usually governed by the lateral capacity of piles and therefore the lateral performance of piles is an important design concern.

The lateral loads in nature are often repetitive. There are two major features on the lateral behavior of piles for repetitive loading.

First, the lateral resistance of piles may be reduced. For piles in clay, many researchers found a remarkable reduction on the lateral stiffness and strength of piles due to the number of loading cycles. For piles in cohesionless soil, the loss of pile resistance is not as dramatic as that for piles in clay. The behavior of a pile in sand under cyclic loads is governed by the characteristics of the load. The loss of the lateral stiffness and strength of the pile for one-way loading is much more significant than for two-way loading.

The other important feature is the loading-history-dependent unloading-reloading response. The enclosed loop of hysteresis provides a mechanism of energy dissipation to reduce the pile response to dynamic loading. The magnitude of residual displacement is an important index in performance based design to check the structural functionality. Therefore, completely tracing out the locus of loading-unloading-reloading is necessary.

For better understanding of the hysteretic behavior of a laterally loaded pile, this study conducted pushover tests of a model pile-soil system at the National Center for Research on Earthquake Engineering (NCREE) of Taiwan. The pushover curves of the test pile and the corresponding pile responses are investigated in this paper. The hysteretic p-y curves are deduced and their backbone curves and loop patterns are analyzed. The applicability of a simple restoring force model of Masing type for the hysteretic p-y locus is further examined through numerical simulations of the pushover tests.

¹ Associate Researcher, National Center for Research on Earthquake Engineering, jschiou@ncree.org.tw

² Master, Department of Civil Engineering, National Taiwan University

³ Assistant Researcher, National Center for Research on Earthquake Engineering, chiaham@ncree.org.tw

⁴ Professor, Department of Civil Engineering, National Taiwan University, chchen2@ntu.edu.tw

Pushover Tests of A Model Pile-Soil System

The model pile-soil system consisted of a model pile embedded in a sand layer, as shown in Fig. 1. The model pile was an aluminum pipe of outer diameter 101.6 mm, thickness 3 mm and length 1.6 m. Vietnam sand was used. The 1.35 m-thick sand layer was prepared by the wet sedimentation method to be fully saturated in a rigid box with an inner dimension of 2.64m×2.64m×1.52m. The relative density of the soil layer was about 25.6%, which can be categorized as loose sand. The tip of the pile was bolted on the bottom of the box. A fixture was welded onto the top of the pile for mounting the actuators on the pile. The layout of sensors is shown in Fig. 2. Strain gauges were attached onto the pile at elevations of 1.45, 1.30, 1.15, 1.00, 0.85, 0.70, 0.55, 0.40, 0.25 and 0.01 m from the bottom, each with four gauges orthogonally on the four sides of the pile. Piezometers were buried in the soil to measure the variation of water pressure during loading. Four successive tests were conducted. The actuators were displacement-controlled to push the pile. The x and y displacements of the fixture and the applied lateral loads were respectively measured by the LVDTs and the load cells embedded in the actuators. The test sequence is listed in Table 1. Tests C1-1 and C1-2 refer to Y-dir loading with target displacements of 5 mm and 10 mm, respectively. Tests C2-1 and C2-2 refer to X-dir loading with target displacements of 5 mm and 10 mm, respectively. Each test was loaded at a slow rate of about 4 mm/min with one displacement cycle containing positive and negative directions of movement.

Table 1 Test cases

Case	Loading dir.	Target disp. (mm)	Case	Loading dir.	Target disp. (mm)
C1-1	Y	5	C2-1	X	5
C1-2	Y	10	C2-2	X	10

For estimating the flexural rigidity of the pile, flexural tests in two loading directions Y & X were conducted before the sand was poured in the test box. The pile was loaded as a cantilever beam. When the pile was pushed, the strains on the both sides of the pile parallel to the loading direction at the depths z, at which the strain gauges were located, were measured and then the corresponding curvatures were calculated. By means of collecting the curvatures and the corresponding bending moments, the relationship between the moment and the curvature can be established. The slope of the hysteretic loop gives an estimate of effective flexural rigidity of the pile. The average flexural rigidity of 76.634 kNm² is adopted in the subsequent pile response analysis.



Fig. 1. Model pile pushover test

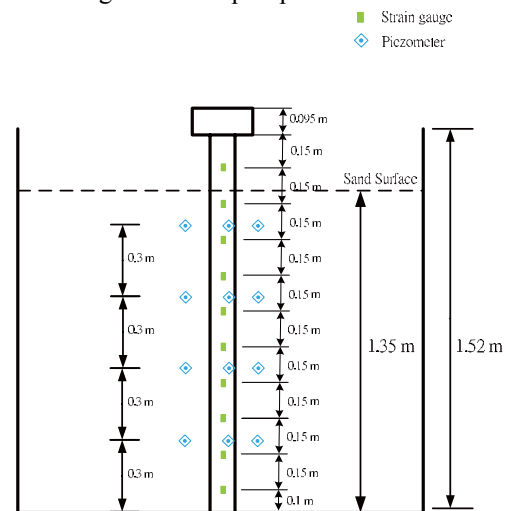


Fig. 2. Layout of instruments

Test Results

Every test case has a complete displacement cycle containing four main loading phases: (I) positive-way loading, (II) unloading to zero, (III) reverse-way loading, and (IV) unloading to zero. For instance, Fig. 3 shows the displacement and loading time histories of C1-1. It can be seen that the loading cycles do not match the displacement cycles due to hysteresis. Fig. 4 shows the load-deflection curves of all the tests which link the displacement to the corresponding load at every time instant. The load-deflection curves in X- and Y- directions are similar. Each test has a significant loop of hysteresis. Both C1 and C2 tests have damping ratio ξ of about 32-34% and the secant slope of the loop K_{sec} value slightly decreases as the u_{max} of the loop increases.

The bending strains along the pile during the loading were measured by the strain gauges. They were transformed to curvatures and the corresponding moments were obtained by multiplying the curvatures with the flexural rigidity of the pile. Figure 5 displays the moment distributions deduced from the strain gauge measurements of C1-1. The trend of the moment distributions varies with the loading phases. In Phase I, the moments at all the measured depths are

positive and they increase as the lateral load increases. The depth of the maximum moment is located at about 0.65 m below the soil surface. In Phase II, the moments above the depth of the maximum moment decrease significantly, but the moments below the depth of the maximum moment decrease slightly. In $t=119.2$ s when the pile-head load decreases to zero, the pile still has residual moments due to the irrecoverable deformation of the soil. In Phase III, the positive moments in the pile gradually turn negative due to the reverse load applied. The depth of the maximum moment is located at the depths 0.55-0.65 m. The higher reverse load gives the deeper position of the maximum moment. In Phase IV, similar to Phase II, the moments in the upper part of the pile decrease significantly while the moments near the pile tip change less. The pile also has residual moments when the pile-head load is reduced to zero.

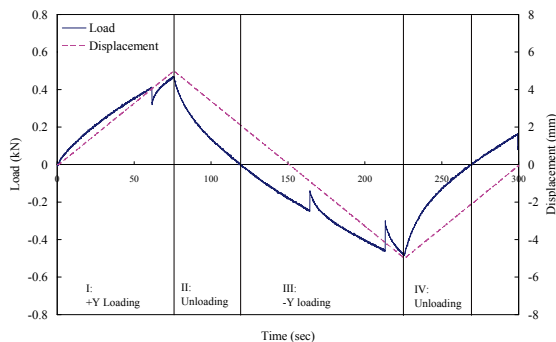


Fig. 3. Loading histories of C1-1

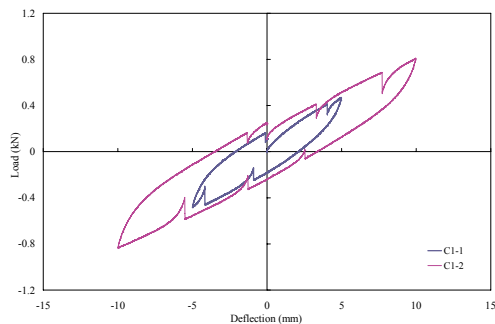


Fig. 4. Load-deflection curves of C1

Pile Responses and Experimental P-Y Curves

According to the beam theory, the pile responses can be further deduced using the measured moment data. The pile displacement can be directly obtained by integrating twice the curvature function, while the shear and the soil reaction distribution are computed by differentiating the moment curve once and twice, respectively. For convenience of differentiation operation, a continuous function is often used to fit the data. Thus, this study adopts a polynomial of fourth order for curve fitting.

Collecting p and y distributions gives the $p-y$

curves for each test. Figures. 6 (a) and (b) show the $p-y$ curves for C1-1 and C1-2 tests, respectively. The trends of the $p-y$ curves of these tests are similar. The $p-y$ curves show significant hysteretic loops and their stiffnesses increase with increasing depth.

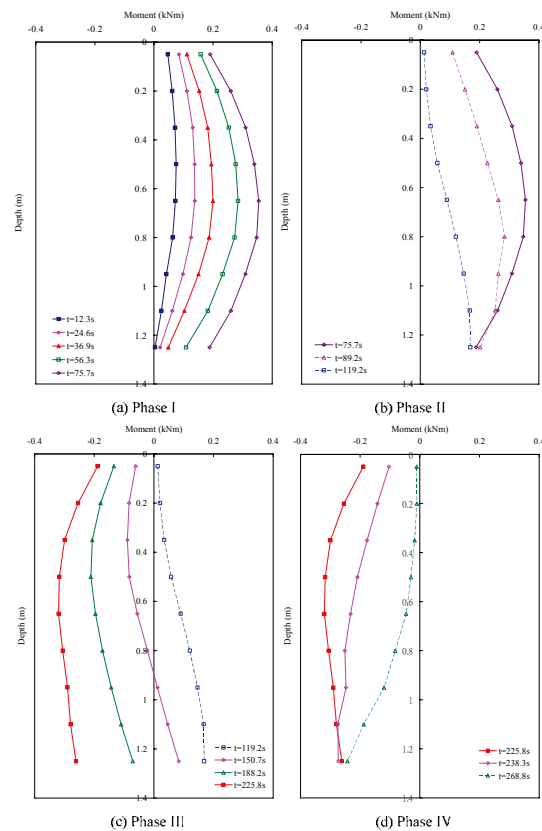


Fig. 5. Moment deduced from strain gauges of C1-1

Characteristics Of P-Y Curves

Two elements are required to describe the complete locus of a $p-y$ curve: (1) a backbone curve and (2) a restoring force model. The backbone curve refers to an envelope of the loop of the $p-y$ curve. For example, the backbone curves of the experimental $p-y$ curves for C1 are shown in Fig. 7. The pattern of the backbone curves is further analyzed. The variation trends of secant subgrade reaction modulus with respect to depth and to displacement are examined. With a common reference of comparison, a reference displacement y_r is set to be $0.01D$, say 1 mm. For each depth, the secant subgrade reaction modulus at y_r can be computed and a relationship of E_{s_r} versus depth can be constructed as shown in Fig. 8. It can be seen that the relationships of E_{s_r} versus depth of C1 and C2 tests are similar and seem to be linear. However, for C2 tests, within a depth of about 0.2 m, the values of subgrade reaction modulus are larger and slightly deviate from the trend of linearity. As a whole, the slope of the subgrade reaction modulus which varies with depth is about $1733-1833 \text{ kN/m}^3$ and is denoted as the subgrade reaction coefficient n_h of cohesionless soils.

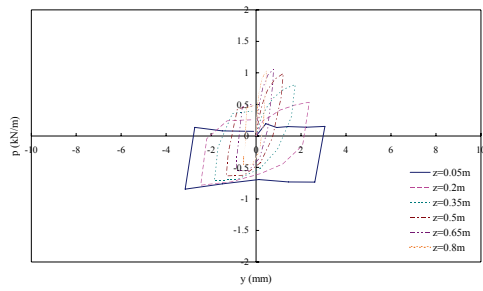


Fig. 6 (a). P-y curves of C1-1

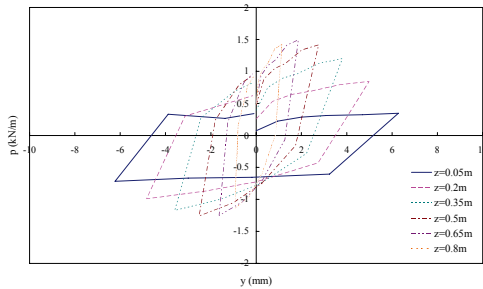


Fig. 6 (b). P-y curves of C1-2

On the other hand, the secant subgrade reaction modulus decreases with increasing lateral displacement. To describe this decay, the relationships of E_s/E_{s_r} versus y/y_r are constructed. Figure 7 represents that of C1. In the figures, it can be seen that the ratio of E_s/E_{s_r} decreases with the ratio of y/y_r of an order of about -0.5.

The hysteretic loops of the p-y curves form because of the plasticity of the soil. To trace the locus of the p-y loop, a simple restoring force model of Masing type is examined. This model magnifies the backbone curve by a factor of two to describe the branch of the hysteretic loop. To demonstrate the applicability of this model, nonlinear pushover simulations for C1 and C2 tests are performed using SAP 2000. Fig. 10 shows the overall load-deflection curves of C1 tests. The fits are fairly good.

Conclusions

Even for a small lateral displacement of the pile, the soil exhibit high nonlinearity and significant hysteresis on the load-deflection curves. The reference secant modulus of the p-y backbone curves E_{s_r} at the reference displacement $y_r = 1\text{mm}$ in this paper is an approximately linear function of depth. And, the secant subgrade reaction modulus ratio E_s/E_{s_r} may decay with increasing lateral displacement ratio y/y_r with an order of about -0.5. The restoring force model of Masing type can be applied to model the hysteretic loop of the p-y curve for properly tracing the nonlinear loading-unloading-reloading response of the pile.

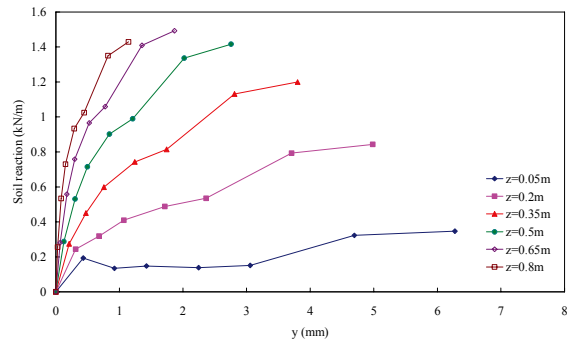


Fig. 7. Backbone curves of the p-y curves of C1

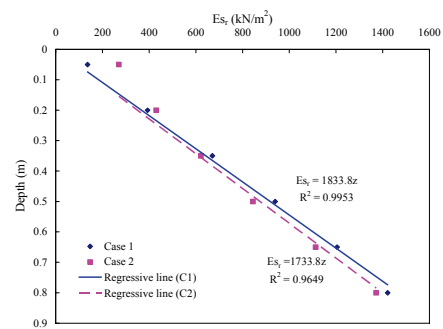


Fig. 8. Reference subgrade reaction modulus versus depth for C1 and C2

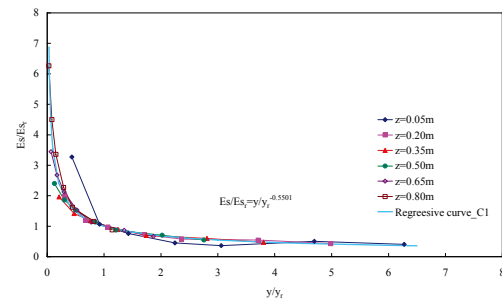


Fig. 9. Modulus ratio versus displacement for C1

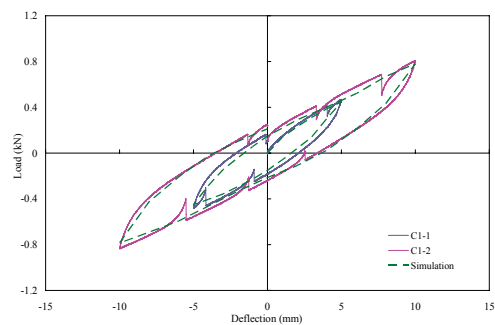


Fig. 10. Simulation of pushover tests for C1

Earthquake Source Parameters and Micro-tremor Site Characteristics Study-Geochemical Monitoring

Vivek Walia¹, Shih-Jung Lin², Tsanyao Frank Yang³ and Kuo-Liang Wen⁴

瓦里亞¹、林世榮²、楊燦堯³、溫國樑⁴

Abstract

The present study is proposed to investigate geochemical variations of soil-gas composition in the vicinity of the geological fault zones and to determine the influence of such formations on the enhanced concentrations of different gases in soil to monitor the tectonic activity in the region. To carry out the present investigations, variations in temporal soil-gases compositions were measured at continuous earthquake monitoring stations established along different faults. Before selecting a monitoring site, the occurrence of deeper gas emanation was investigated by the soil-gas surveys and followed by continuous monitoring of some selected sites with respect to tectonic activity to check the sensitivity of the sites. From the results of long term geochemical monitoring at the established monitoring stations we can divide the studied area in two different tectonic zones. We proposed tectonic based model for earthquake forecasting in Taiwan and tested it for some big earthquakes occurred in recent past. Based on the anomalous signatures from particular monitoring stations we are in a state to identify the area for impending earthquakes of magnitude ≥ 5 and we have tested it for some earthquakes which rocked the country in last six months. Most of earthquakes having magnitude ≥ 5 with local intensity ≥ 2 at the monitoring stations, epicentral distance < 100 kms with focal depth < 40 kms have shown precursory signals and fitted very well according to the proposed model for the region.

Keywords: Soil-gas, Fault, Earthquake, Tectonic, Radon, CO₂

Introduction

Earthquakes account for more loss of life and property than any other natural phenomena. The research on seismogeochemical models is aimed at defining relations between seismic parameters, such as earthquake magnitude and epicentral distance, and geochemical anomalies occurring in subsurface gases. Such relations can be classified both theoretically and empirically (Walia et al., 2005; Etiope et al., 1997).

Changes in subsurface gases concentration have been observed to precede earthquake occurrence and therefore has potential to monitor the tectonic activities in the region (Walia et al, 2009a; Walia et al., 2005; Fu et al., 2005; Yang et al., 2006). There

are a number of variables other than seismic events that influence radon emanation from earth's surface at a given location. The most important factor is influence of meteorological parameters. Influence of meteorological parameters on radon emanation was reported from time to time by various authors (Walia et al., 2005; Etiope et al., 1997).

The island of Taiwan is a product of the arc-continent collision between Philippine Sea plate and Eurasian plate which makes it a region of high seismicity. In the southern area of island, the Eurasian plate is subducting under the Philippine Sea plate while in the northern area of the island, the Philippine Sea plate bounded by the Ryukyu trench is subducting beneath the Eurasian plate. Behind the

¹ Associate Research Fellow, National Center for Research on Earthquake Engineering, walia@ncree.org.tw

² Assistant Research Fellow, National Center for Research on Earthquake Engineering, sjlin@ncree.org.tw

³ Professor, Department of Geosciences National Taiwan University, tyyang@ntu.edu.tw

⁴ Deputy Director, National Center for Research on Earthquake Engineering, [wengk1@ncree.org.tw](mailto:wenk1@ncree.org.tw)

Ryukyu trench, the spreading Okinawa trough has developed. The northern part of Taiwan Island is located at the western extrapolation of the Okinawa trough. The present work is focused on Hsincheng fault in Hsinchu area and Hsinhua fault in Tainan for earthquake monitoring using soil gas method. It is well established that distribution of soil gas compositional variations can be employed as the precursors for earthquakes (Walia et al., 2005; Yang et al., 2006) and for mapping of fault zones (Walia et al., 2009a; Fu et al., 2005).

Presently our work is focused on temporal geochemical variations of soil-gas composition at established geochemical observatories along the above said faults in Hsinchu, Tainan and Ilan areas of Taiwan, respectively and to determine the influence of enhanced concentrations of soil gases to monitor the tectonic activity in the region. Based on the data generated at monitoring station and collaboration with other monitoring station run by NTU, we proposed a tectonic setting based model and we tested the model during some big earthquakes happened during observation period of year 2010.

Methodology

To carry out the present investigation, temporal soil-gases compositions variations were measured regularly at continuous earthquake monitoring stations using RTM2100 (SARAD) for radon and thoron measurement (for details see previous reports).

Results from monitoring stations

Investigations during the observation period have shown potential precursory signals for some major earthquakes in the region. Both the above said faults are located on/near National Science Industrial Park (NSIP), the industrial hub of Taiwan, and can be a cause of concern for urban life making it necessary to check the activity to these faults. During the observation we have found that in some cases a number of earthquakes occur in short span of time i.e within 1-5 days. These earthquakes can be considered as aftershocks/foreshocks of big earthquakes or different earthquakes. In the present study we have considered these as one seismic event.

Hsincheng Monitoring Station

Results from the observation period Jan., 2006 until Dec., 2009 have been published in previous reports. The temporal data for soil-gas variation and its correlation with different seismic events observed during year 2010 has been plotted in Fig. 1. In the observation period potential precursory signals were recorded for some major earthquakes that occurred in the region.

Hsinhua Monitoring Station

A continuous monitoring station was established at selected point at end of October, 2006 using radon detectors RTM 2100 along with carbon-di-oxide detector. In the observation period potential precursory signals were recorded for some earthquakes that occurred in the region.

Results from the observation period Jan., 2006 until Dec., 2009 have been published in previous reports. The temporal data for soil-gas variation and its correlation with different seismic events observed during year 2010 has been plotted in Fig. 2. This monitoring station has shown better confidence level (see previous reports) than monitoring station along the Hsincheng fault, hence seems to be a better station. It has been found that during period of observation we recorded more number of seismic events as well as number of precursory anomalies at Hsinhua as compare to Hsincheng fault which may indicate the this region may be seismically more active.

Jiaosi Monitoring Station

In addition to above said monitoring stations, we established continuous monitoring station at Jiaosi, Ilan area at a selected point using radon detectors RTM 2100 along with carbon-di-oxide detector. The temporal data for soil-gas variation and its correlation with different seismic events observed during year 2010 has been plotted in Fig 3.

Hualien Area

In addition to continuous monitoring at established monitoring stations, during this phase of the project we did some field surveys along the Yuli fault in Hualien area using the soil-gas sampling procedure (reported in previous reports). Samples were collected and analyzed for ^{222}Rn , ^4He (Fig. 4). During the surveys about 39 samples were along the 5 profiles and analyzed for radon and helium concentrations (Fig. 4). Results shows show large spatial variation in gas concentrations along the tectonic features present in that area. Spatial distribution of radon and helium values helps us to identify the location of Yuli fault (Fig. 4).

Discussions

Long term geochemical monitoring for the earthquake studies at the established earthquake monitoring stations along Hsincheng and the Hsinhua faults within the Hsinchu and Tainan areas, respectively, has been done continuously. These two areas lie in the north and south part of Taiwan, respectively. Results have shown that Hsinhua and Hsincheng faults have different tectonic settings. It has been found that variations in soil gas at

Hsincheng fault are disturbed by the stress variation due to tectonic activities along Okinawa Trough and Rkukyu Trough which are located in north and central eastern part of Taiwan, respectively, in addition to local earthquakes within periphery of about 50kms from the monitoring station. Whereas in the case of Hsinhua fault, soil-gas variations are observed to be due to tectonic activities along the Luzon Arc and other tectonic activities in southern part of Taiwan. So, we have noticed that Hsinhua monitoring station shows precursory signals for earthquakes occurring south or south eastern part of Taiwan, whereas, for Hsincheng faults, most of soil-gas variation precursory signals are recorded for the earthquakes that occurred north or north-eastern part of Taiwan. These findings enabled us to propose a model dividing Taiwan into various tectonic zones and these findings were reported in last year report (Walia et. al, 2009b). Data is obtained from the monitoring stations run by NCREE and NTU in collaboration and fit well in the proposed model. Based on the anomalous signatures from particular monitoring stations we are in a state to identify the area for impending earthquakes of magnitude ≥ 5 and we have tested it for some earthquakes which rocked the country during last year. Earthquakes having magnitude ≥ 5 with local intensity ≥ 2 at the monitoring stations, epicentral distance < 100 kms with focal depth < 40 kms have shown precursory signals and fitted very well according to the proposed model. One good example for this of the earthquake occurred on March 4th, 2010 in Southern Taiwan with magnitude of 6.4 (M_L), depth 22.6 kms. Our monitoring stations in south and south eastern of Taiwan, which had the local intensity ≥ 2 for this earthquake, have shown precursory signals (Fig. 5). Moreover if we draw periphery epicentral distance circles having radius ≤ 60 kms for these monitoring stations, we can observe that the above said earthquake occurred in the intersection of these circles (Fig. 5). Whereas monitoring station present in north and north eastern Taiwan did not show precursory signals for the above said earthquake. We also try to filter out the noise in our data from different meteorological parameters and an attempt was made using the Empirical Mode Decomposition (EMD) technique (Fig. 6).

References

- Etiopie G., Calcara, M., Quattrocchi, F. (1997). "Seismogeochemical algorithms for earthquake prediction: an overview". *Annali Di Geofisica*, 40(6), 1483-1492.
- Fu, C.C., Yang, T.F., Walia, V., Chen, C.H. (2005). "Reconnaissance of soil gas composition over the buried fault and fracture zone in southern Taiwan". *Geochemical Journal*, 39,427-439.
- Walia, V., Yang, T.F., Lin, S.J., Hong, WL., Fu, C.C., Wen, K-L.,Chen, C-H. (2009a). "Geochemical

variation of soil-gas composition for fault and earthquake precursory studies along Hsincheng fault in NW Taiwan". *Appl. Radiat. Isotopes*, 67, 1855- 1863.

- Walia, V., Yang, T.F., Lin, S.J., Hong, W.L., Fu, C.C., Wen, K.L.,Chen, C.H. (2009b). "Continuous temporal soil.gas composition variations for earthquake precursory studies along Hsincheng and Hsinhua faults in Taiwan". *Radiat. Meas.*, 44, 934.939.
- Walia, V., Virk, H.S., Yang, T. F., Mahajan, S., Walia, M. and Bajwa, B.S. (2005). "Earthquake prediction studies using radon as a precursor in N.W Himalayas, India: a case study". *TAO*, 16(4), 775.804.
- Yang, T.F., Chou, C.Y., Chen, C.H, Chyi, L.L., Jiang, J.H. (2003). "Exhalation of radon and its carrier gases in SW Taiwan". *Radiat. Meas.* 36, 425.429.
- Yang, T.F., Fu, C.C., Walia, V., Chen, C.H., Chyi, L.L., Liu, T.K., Song, S.R., Lee, M., Lin, C.W., Lin, C.C., (2006). Seismo.geochemical variations in SW Taiwan: multi.parameter automatic gas monitoring results, *Pure Appl. Geophys.*, 163, 693.709.

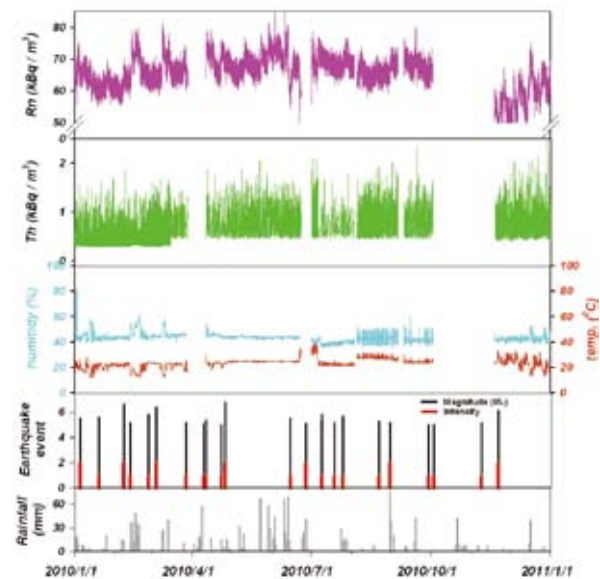


Fig.1. Variations of radon, thoron, carbon dioxide and rainfall at Hsinchu monitoring station and its correlation with earthquakes during 2010.

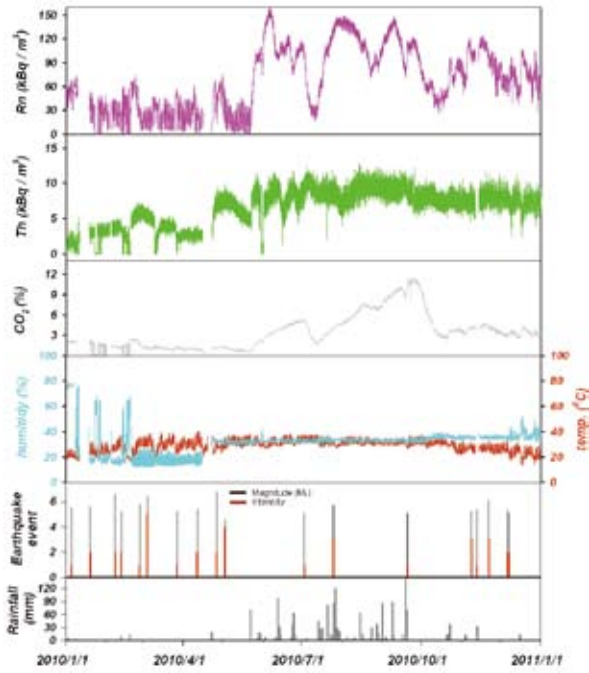


Fig.2. Variations of radon, thoron, carbon dioxide and rainfall at Hsinhua monitoring station and its correlation with earthquakes year 2010.

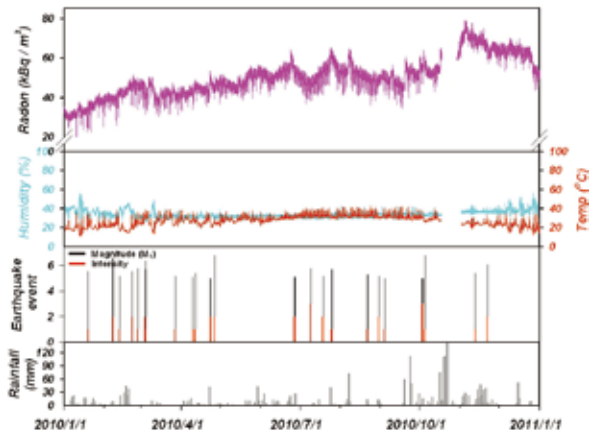


Fig.3. Variations of radon, thoron, carbon dioxide and rainfall at the Jiaosi, Ilan area and its correlation with earthquakes year 2010.

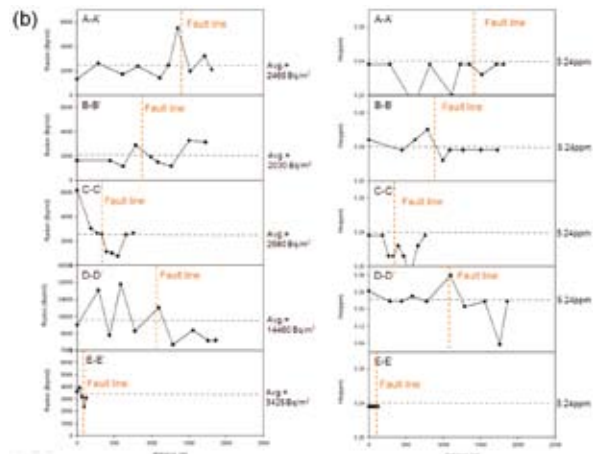
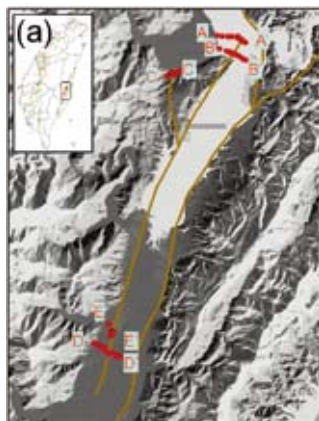


Fig.4. (a) Distribution of soil-gas survey in Yuli fault (in Hualien area) (red dot represent the sampling points) (b) radon and helium concentration along profiles at the Yuli fault, Hualien area.

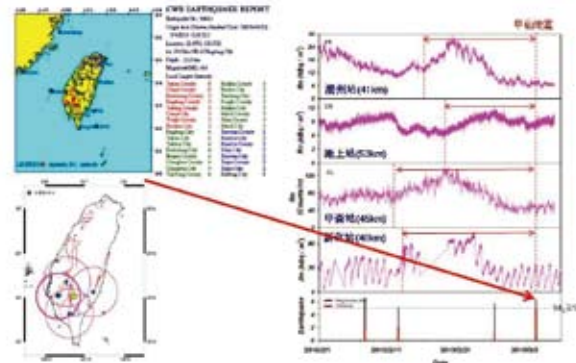


Fig.5. Precursory signals for March 4, 2010 earthquake at different monitoring stations in south and south eastern of Taiwan.

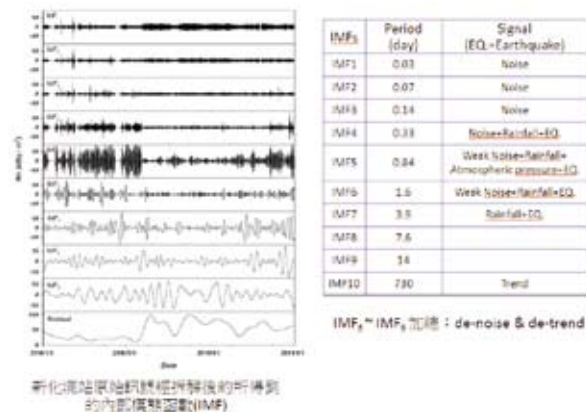


Fig.6. Empirical Mode Decomposition (EMD) technique used to filter out different meteorological parameters noise from the data.

Characteristics of Near-Surface S-wave Velocity

Chun-Hsiang Kuo¹, Kuo-Liang Wen², Hung-Hao Hsieh³, and Che-Min Lin¹

郭俊翔¹、溫國樑²、謝宏灝³、林哲民¹

Abstract

Near surface S-wave velocity is a major factor in seismic wave amplification. The so-called Vs30, for example, is a critical simplified parameter in engineering to illustrate seismic site effect. This study was based on the Engineering Geological Database for TSMIP (EGDT), which is being undertaken by the National Center for Research on Earthquake Engineering (NCREE) and the Central Weather Bureau (CWB) in Taiwan since 2000. EGDT contains 469 surveyed stations so far, the number is about 69% (469/682) of the free-field TSMIP network. We therefore used the database to evaluate empirical S-wave velocity (Vs) equations for different regions by relating Vs to depth and N-value, and the site categories of drilled strong motion stations were classified according to the Vs30 criterion of Building Seismic Safety Council (BSSC). In addition, researchers and engineers in related fields can search their stations of interest and apply for the data on the website: <http://egdt.ncree.org.tw/>.

Keywords: EGDT, Vs30, TSMIP, S-wave velocity, site classification.

Introduction

Site effect is a very important issue in both earthquake engineering and seismology. Diversified characteristics of near surface layers cause various effects at sites. The so-called Vs30, the average shear wave velocity of the top 30 meter layers, is a well-known parameter used in defining site effects. Vs30 is recommended as a significant parameter in the recent building code (BSSC 2001), and was used by the Next Generation Attenuation (NGA) of ground motions project on strong ground motion prediction studies (Chiou et al. 2008). It should be noted that many strong motion recordings in Taiwan were also included in the NGA database by the coordinators, i.e. the Pacific Earthquake Engineering Research Center (PEER) in partnership with the United States Geological Survey and the Southern California Earthquake Center.

In order to use more effectively and precisely the collected strong motion recordings on earthquake

engineering, NCREE and CWB are launching a free-field strong motion drilling project to construct the EGDT since 2000. A total of 469 free-field strong motion stations have been surveyed so far (Hsieh et al. 2011).

The 439 of the 469 surveyed stations included wave velocity profiles, while most of the profiles (386 stations) reached the depth of 30 m, so that site classification was done according to the Vs30 criterion of the National Earthquake Hazard Reduction Program (NEHRP) Provision. In the process, Vs30 were estimated by a reliable extrapolation for the profiles that did not reach 30 meters. Otherwise, considering that no local Vs empirical equation for different districts of Taiwan, we also analyzed the relations between Vs, N value, and depth to evaluate empirical Vs equations in different regions of Taiwan.

¹ Associate Research Fellow, National Center for Research on Earthquake Engineering, chkuo@ncree.narl.org.tw; cmlin@ncree.narl.org.tw

² Professor, Dep. of Earth Science, National Central University and Division Manager, National Center for Research on Earthquake Engineering, wenkl@ncree.narl.org.tw

³ Assistant Research Fellow, National Center for Research on Earthquake Engineering, hhhsieh@ncree.narl.org.tw

Evaluation of Empirical Vs Equations in Different Regions of Taiwan

Empirical equations of S-wave velocity had been evaluated in many studies because of its efficiency and economy. Kuo et al. (2011) quoted thirteen representative results and then evaluated the empirical Vs equations for the Taipei Basin and the Ilan County, Taiwan. This study followed the procedure proposed by Kuo et al. (2011) to evaluate empirical Vs equations in other regions of Taiwan. The station codes of TSMIP were given according to the abbreviations of seven regions of Taiwan, which are TAP, TCU, CHY, KAU, TTN, HWA, and ILA, respectively. Kuo et al. (2011) had evaluated the equations for TAP (Taipei Basin) and ILA (Ilan County). The present study evaluated the equations for other five regions using the gathered data of EGDT, and the results were shown in Fig. 1 along with the published results in TAP and ILA (Kuo et al. 2011). It should be noted that the empirical equations in Fig. 1 used the data until 2009. However, the equations can be applied to the strata in the top 50 m as well as for N smaller than 50 because of the nature of data collected.

The simplified description of the evaluation procedures proposed by Kuo et al. (2011) is discussed as follows: The regression model (linear or power-law relationship) is decided by the data itself, i.e. depend on the maximum correlation coefficient between Vs and N or depth. Afterward, the multivariable analysis, which can increase the correlation coefficient between regression equation and the data, was implemented to evaluate the regression equations unless the data could not pass either of the following two examinations. 1. *Rule of thumb test*: statisticians usually suggested correlation coefficient between any two independent variables should be smaller than 0.7. 2. *Stepwise selection*: This is a combination of backward and forward approaches and thus the set criteria are the probability of F had to be statistically lower than 0.05 for entry and higher than 0.1 for removal. The suggested examinations can help avoid a potentially coupling between N and depth since we did not execute overburden corrections. Soil types (sand and clay & silt) and geological epoch were also considered in the regression process only if they could increase correlation coefficient of the evaluated empirical Vs equations.

In the case of developing equations in HWA and TCU, although they passed the rule of thumb test, they failed in stepwise selection, thus we could not implement multivariable analysis for the data in the two regions due to multicollinearity. There are only a few data sets in HWA and TTN (fewer than 200), so the soil types were not considered as it might be unreasonable in statistics. The evaluated empirical Vs equations were plotted in Fig. 1 together with those adopted by the revised Building Code of Taiwan

recently (Ministry of the Interior Order 2011; Japan Road Association 2002). The empirical Vs equations in Fig. 1 are displayed as a function of N with a fixed depth of 20 m. The S-wave velocity in TTN and HWA are obviously larger than in other regions. This phenomenon reflects the real geological background of Taiwan.

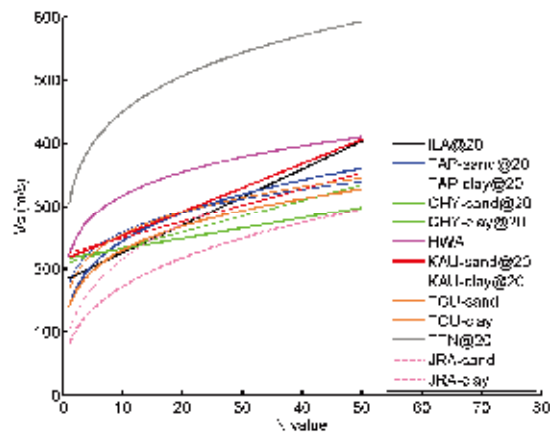


Fig. 1 Empirical Vs equations in seven different regions of Taiwan with the two others suggested by Japan Road Association (JRA) (2002). The marker “@20” indicates the curve is the case at the depth of 20 m. The thick curves are sand soil or all soils, whereas the thin curves are clay & silt soils, but represented only as clay in the legend.

The Suitable Extrapolation of Vs30 for Taiwan

A total of 53 of the 439 drilled boreholes did not reach 30 m in the EGDT. It is a common problem when calculating properly the Vs30 for not only the sites in Taiwan, but also for those in other countries. The earlier article of Kuo et al. (2011) discussed this problem and then compared three frequently used techniques, i.e. least square of single station (LSS), statistical extrapolation (STS), and bottom constant velocity (BCV). They indicated that BCV is the most accurate method for stations in TAP and ILA regions.

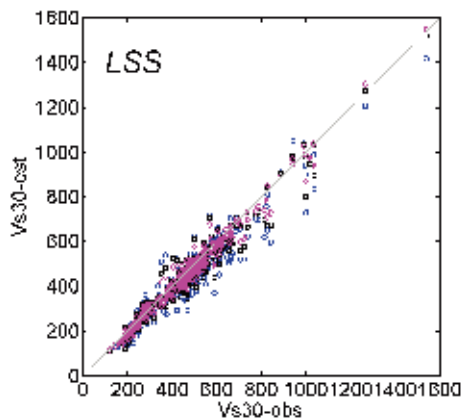
Based on the established procedures of Kuo et al. (2011), the accuracy of the three techniques were further compared using the datasets (until 2009) that extends to at least 30 m. A total of 367 boreholes were used in the examination by defining an error percentage (Err%) expressed as:

$$Err\% = \frac{\sum |V_{rel} - V_{est}|}{n} \times 100\% \quad (1)$$

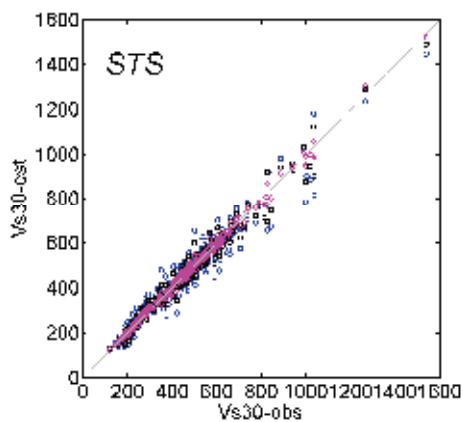
Where V_{rel} is the measured S wave velocity, V_{est} is the estimated S-wave velocity by extrapolations, and n is the number of data. The error percentages were

shown in Table 1, indicating obviously that BCV is the most accurate and stable extrapolation in Taiwan, the same result as Kuo et al. (2011).

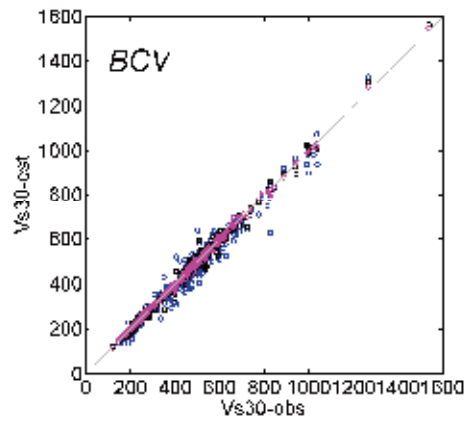
Fig. 2 illustrates the estimated Vs30 (y-axis) by the three extrapolations (Fig. 2(a) ~ (c)) as well as the estimated results by Lee and Tsai (2008) (Fig. 2(d)) versus the observed Vs30 (x-axis) obtained by PS-logging for the 367 boreholes. The assumed depths of 15, 20, and 25 m were represented as open blue circles, open black squares, and open magenta diamonds, respectively. The discrepancies between the estimated and observed Vs30 decrease as assumed depths increase as can be seen in Fig. 2(a) ~ (c). Otherwise, the divergences of BCV are the least. The phenomena indicate that errors are becoming smaller as depth increases; otherwise BCV can get the best Vs30 in Taiwan. Fig. 2(d) denotes that the results of Lee and Tsai (2008) still have large disagreements even if the largest estimated Vs30 had been restricted by a value of about 760 m/s. It should be noted that Lee and Tsai (2008) also used the data of EGDT but only until 2005, as well as other 4885 engineering boreholes in their geo-statistical method.



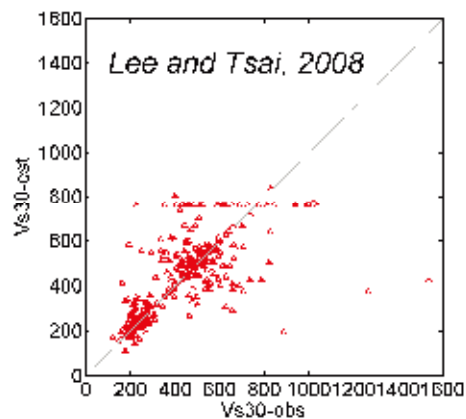
(a) Estimated Vs30 by LSS versus real Vs30.



(b) Estimated Vs30 by STS versus real Vs30.



(c) Estimated Vs30 by BCV versus real Vs30.



(d) Estimated Vs30 by Lee and Tsai (2008) versus real Vs30.

Fig. 2 Estimated Vs30 by different methods (y-axis) versus observed Vs30 measured by a PS-logging system (x-axis).

Table 1 Err% obtained from extrapolations at three assumed depths. The percentages after “±” are the standard deviations.

Assumed depth	Mean Err% of 367 boreholes		
	LSS	STS	BCV
15 m	11.26% ±8.03%	7.37% ±6.61%	6.66% ±5.69%
20 m	8.06% ±6.15%	4.68% ±4.05%	3.12% ±2.85%
25 m	5.69% ±4.41%	2.17% ±1.95%	1.17% ±1.27%

Site Classification of Drilled Free-field TSMIP Stations

Site classifications were achieved for the 439 drilled TSMIP stations according to the Vs30 criteria of NEHRP (BSSC 2001). Vs30 was estimated by the BCV method for those stations did not be drilled up to 30 m. The locations of stations and classifications were illustrated in Fig. 3. There are one of Class A, 29

of Class B, 200 of Class C, 193 of Class D, and 16 of Class E. In Taiwan, most drilled stations belong to Class C and D (89.5%), this might be due to the reason that most of the stations were installed in the metropolitan districts that often are located on sediments or soft rocks; the others account only to 10.5%. Stations of Class D and E are mainly distributed on plains and basins with unconsolidated sediments; stations of Class C are located on northwestern part of Taiwan and around the Central Mountain and the Coast Range; stations of Class B are mostly located on the north of Taiwan and on several mountain areas; the unique Class A in the database only appears at the Coast Range. The significant results of classification provide an important reference material for prevalent studies of NGA.

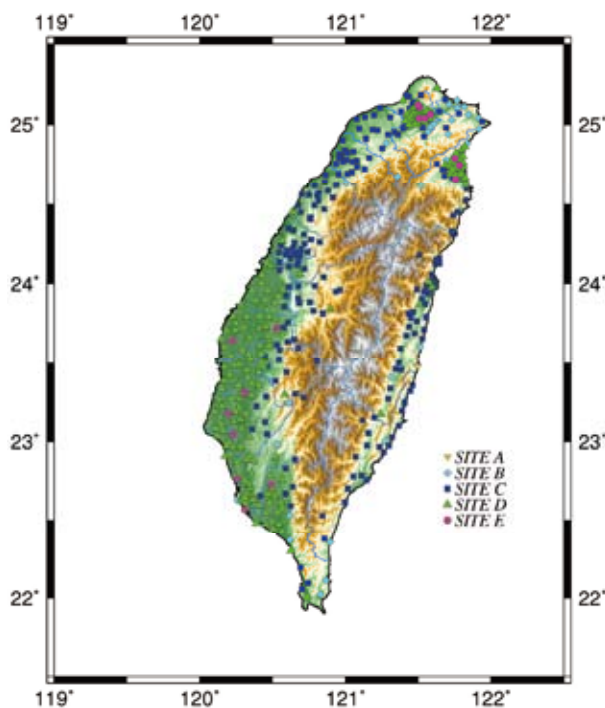


Fig. 3 Distributions and site classifications of 439 drilled free-field TSMIP stations in Taiwan.

Conclusions

This study aimed to analyze characteristics of near-surface S-wave velocity in Taiwan by means of evaluating the empirical V_s equations and examining the velocity variations. Empirical V_s equations could offer important information about near-surface velocity profiles for calculations of seismic wave propagation, like SHAKE. Also, V_{s30} provides the significant parameter in estimating the site effect on earthquake engineering and in strong ground motion prediction. Furthermore, the suggested empirical V_s equations (Japan Road Association 2002) when compared with the evaluated ones in the present study (Fig. 1) depict that the JRA's equations seems yielded conservative estimations of V_s in Taiwan excessively.

The local empirical V_s equations are believed to have reflected the real geological situations in different regions of Taiwan. We believe they are more suitable and should be adopted for future seismic design specifications in place of the makeshift JRA's equations. Moreover, site classification (Fig. 3) in the present study was found to be much better than that of Lee and Tsai's (2008). According to the comparison in Fig. 2, the better and more accurate classification might cause a significant improvement in the applications. Data requests are free to date, but are for research purposes only. Interested individuals just need to download, fill, and send back the filled form from the website, and then the administrator will send the requested datasets.

References

- Building Seismic Safety Council, BSSC (2001), "NEHRP Recommended Provisions for Seismic Regulations for New Buildings and Other Structures", Washington, DC.
- Chiou, B., Darragh, R., Gregor, N., and Silva, W. (2008), "NGA Project Strong Motion Database", *Earthquake Spectra*, 24(1), 23-44.
- Hsieh, H.H., Wen, K.L., and Kuo, C.H. (2011), "Engineering Geological Database for TSMIP", *2010 NCREE Research Programs and Accomplishments*, in press.
- Japan Road Association (2002), "Specification for Highway Bridges, Part V: Seismic Design," Tokyo, Japan, 406 pp. (In Japanese)
- Kuo, C.H., Wen, K.L., Hsieh, H.H., Chang, T.M., Lin, C.M., and Chen, C.T. (2011), "Evaluating Empirical Regression Equations for V_s and Estimating V_{s30} in Northeastern Taiwan", *Soil Dynamics and Earthquake Engineering*, 31(3), 431-439.
- Lee, C.T. and Tsai, B.R. (2008), "Mapping V_{s30} in Taiwan", *Terrestrial, Atmospheric and Oceanic Sciences*, 19(6), 671-682.
- Ministry of the Interior Order (2011), "Revision on Partial Provisions of Seismic Design Specifications and Commentary of Buildings", *Executive Yuan Gazette*, 17(15), 106 pp. (In Chinese)
- National Center for Research on Earthquake Engineering (2011), "Engineering Geological Database for TSMIP", <http://egdt.ncree.org.tw/>.

Earthquake Source Parameters and Micro-tremor Site Characteristics (Micro-Earthquake Monitoring)

Che-Min Lin¹, Tao-Ming Chang², Hung-Hao Hsieh³

Kuo-Liang Wen⁴, and Chun-Hsiang Kuo¹

林哲民¹、張道明²、謝宏灝³、溫國樑⁴、郭俊翔¹

Abstract

A micro-earthquake monitoring network for the Science parks of Taiwan was set up to evaluate the activities and source parameters of active faults using dense broadband seismometers. In 2010, we relocated the earthquakes we observed based on the double-difference earthquake location algorithm and solved the focal mechanisms to understand the relations between micro-earthquakes and the faults or other seismogenic structures. Many earthquakes had concentrated on the southeastern side of the Tapingti Fault in Hsinchu, Taiwan. The spatial distribution of earthquake occurrences slightly dipped to southeast. The seismicity in the southeast side of the Shihtan and Shenchoshan Faults in Miaoli is also high. But, the densest and most active seismogenic area is located in the Sanyi-Puli double-seismic zone. The earthquakes in this seismic zone are separated into two groups that are dipped to southeast direction with different dip angle. In the Southern Taiwan Science Park (STSP) area, the high seismicity is along the Chukou, Muchiliao and Liuchia Faults. In the northern region of STSP, the earthquakes concentrated in the eastern side of Tachienshan and Chukou Faults. Furthermore, an unusual earthquake group with high and concentrated seismicity was observed at the northern end of the Chishan Fault. The linear and dipping seismic structure and focal mechanisms suggest the activity of the north Chishan Fault. However, the seismicity is both quiet in the areas near the Meishan and Hsinhua Faults which have dislocated and induced massive and destructive earthquakes in history.

Keywords: Science Parks, earthquake monitoring, active fault, earthquake location, focal mechanism

Introduction

The high-technology industry is one of the major economic resources of Taiwan after its major developments in the past decades. This project is part of a series of studies being guided by the National Center for Research on Earthquake Engineering (NCREE) Taiwan regarding the highly-technological Science Parks in the island, and aimed to determine active parameters of faults, numerical simulations of

ground motions, site effects, earthquake early warnings, etc. This study established a monitoring network for the active faults in the region using dense broadband seismometers. Micro-earthquakes and anomalous seismicity could be observed as well as fault activities and source parameters, which are relevant materials in numerical simulations and analyses of earthquake potential that are being established.

Since 2005, the micro-earthquake monitoring

¹ Associate Research Fellow, National Center for Research on Earthquake Engineering, cmlin@ncree.narl.org.tw, chkuo@ncree.narl.org.tw

² Associate Research Fellow, National Center for Research on Earthquake Engineering, tmchang@ncree.narl.org.tw

³ Assistant Research Fellow, National Center for Research on Earthquake Engineering, hhhsieh@ncree.narl.org.tw

⁴ Professor, Dep. of Earth Science, National Central University and Division Manager, National Center for Research on Earthquake Engineering, wenkl@ncree.narl.org.tw

networks of Hsinchu Science Park (HSP), Southern Taiwan Science Park (STSP) and Central Taiwan Science Park (CTSP) were installed one by one. The monitoring area includes all active faults between Hsinchu and Tainan in the western Taiwan. Micro-earthquake activities in the said area are monitored continuously over a long period of time. In 2010, the earthquakes were traced back based on the double-difference earthquake location algorithm and the focal mechanisms were solved to understand the relationships between micro-earthquake activity and the faults or other seismogenic structures.

Micro-Earthquake Activity

The data processing program on network monitoring was developed in this project. A total of 11,454 earthquakes were located by the established network from 2006/1/22 to 2009/04/30. The distribution of epicenters is shown in Fig. 1. According to the comparison made with the catalog of Taiwan Strong Motion Instrumentation Program (TSMIP), our network could monitor most earthquakes with magnitudes lower than 2.5. Furthermore, our monitoring capability is much better than that of TSMIP for earthquakes with magnitudes lower than 1. The NCREE Micro-Earthquake Monitoring Network, which is powerful enough in monitoring small earthquakes, provides opportunity to observe the actions and characteristics of faults near the Science Parks.

From the investigation, the seismicity at HSP and Hsinchu County is very low. Most micro-earthquakes occurred in the eastern or southeastern side of active faults in the Western Foothills. Most earthquakes concentrated on the southeastern side of the Tapingti Fault in Hsinchu County. The seismicity in the southeast side of the Shihtan and Shenchoshan Faults in Miaoli County is also high. The densest and most active seismogenic area is located at the Sanyi-Puli seismic zone. The seismic zone lies on the north of Sanyi, Chelungpu and Tamaopu-Shuangtung Faults and trends to the southeast direction.

In the STSP region, the epicenters are more dispersed and were observed to be in between the Western Foothills and the coastal area. The earthquakes concentrated in the eastern side of Tachienshan and Chukou Faults in the region's northern part. In the central part of STSP, the high seismicity is located along the Chukou, Muchiliao and Liuchia Faults. Earthquakes occurred in both side of these faults and were distributed uniformly along the fault traces. Furthermore, an unusual earthquake group with high and concentrated seismicity was observed at the north end of the Chishan Fault. And, there is also a group of linear earthquakes which crossed through Chishan, Liukuei and Chaochou Faults and dipped to the southeast direction. However, the seismicity is quiet in both the area near the Meishan and Hsinhua

Faults which have dislocated and induced massive and destructive earthquakes in history.

Based on the background seismicity, if the Chi-Chi earthquake and its aftershocks are ignored, the central Taiwan is an aseismic zone. The result also confirms the said phenomenon. The central part of the network is relatively a quiet area for micro-earthquakes. The aseismic zone may result from the existence of the ancient basement, Peikang High, under the central part of the western coastal plain of Taiwan. The strong crust may have difficulty in producing micro-earthquakes, but the stresses may have been obstructed and are being accumulated in long term thus might induce big earthquakes at the long fault observed in the surface.

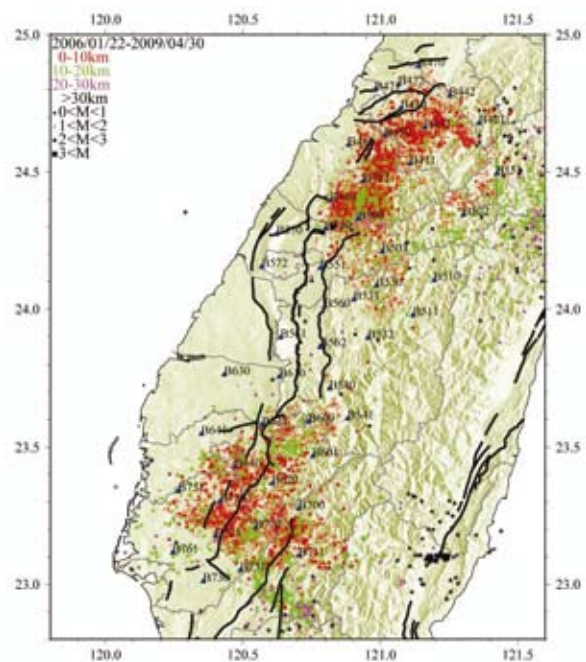


Fig. 1 Epicenters located by the network of this study

Double-Difference earthquake location

The Double-Difference (DD) technique is a useful tool to relocate earthquake groups and emphasize the underlying seismogenic structures. This technique takes advantage of the fact that if the hypocentral separation between two earthquakes is small compared to the event-station distance and the scale length of velocity heterogeneity, then the ray paths between the source region and a common station are similar along almost the entire ray path (Waldhauser and Ellsworth, 2000). In this case, the difference in travel time of two events observed at one station can be attributed to the spatial offset between the events with high accuracy. The DD equations were based on differencing Geiger's equation in locating earthquakes. The residual between observed and calculated travel-time difference between two events at a common station are related to adjustments in the relative position of the hypocenters and origin times

through the partial derivatives of the travel times for each event with respect to the unknown. In this study, the program, Hypo DD, was used to relocate the micro-earthquakes observed and to understand the relation between epicenters and active faults.

In the catalog of the established Micro-Earthquake Monitoring Network, 5,527 earthquakes were relocated by the DD technique. Fig. 2 and Fig. 3 are, respectively, the DD locations of epicenters in HSP and STSP regions. After performing relocation of earthquakes using DD technique, the epicenters of some major earthquake groups concentrated or exhibited more linear distribution. The accurate depths of earthquakes provided the spatial information about the shape of seismogenic faults and structures.

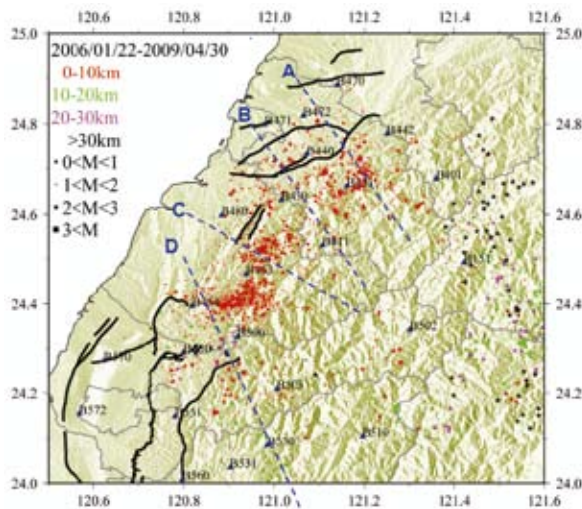


Fig. 2 Double-difference locations in HSP region

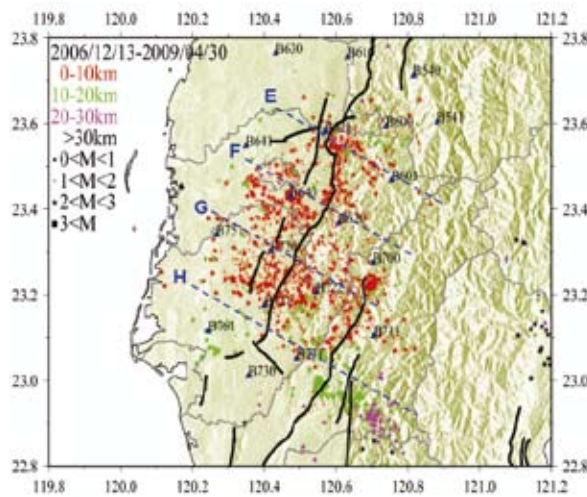


Fig. 3 Double-difference locations in STSP region

Four cross-sections of the relocated epicenters in HSP region were plotted and are shown in Fig. 4. Sections A and B crossed perpendicularly to the Hsinchu and Hsincheng Faults. In the two sections, the depths of earthquakes were less than 10 km. The earthquakes are mostly distributed in the southeastern side of the Tapingti Fault and were slightly dipped to southeast direction. Section C of the earthquake group

refers to the southeast part of Shihtan Fault. This group exhibited dense and concentrated epicenters without linear structures. The said phenomenon may have resulted from the fault fracture zone in the area. Section D is parallel to the Sanyi-Puli seismic zone. The recorded earthquakes are densely distributed with depth from 10 km to near-surface near Taian and Dahu in Miaoli County. The observed earthquakes were separated into two groups that are both dipped to southeast direction but with different dip angle. The deeper group extends down the depth of 30 km near the northern end of Tamaopu-Shuangtung Fault with dip angle of 45°. The shallower group has a dip angle of 20° and extends down the depth of 25 km under the Puli basin. The Sanyi-Puli double seismic zone was seen as a transfer zone between two thrust structures.

Figure 5 shows cross-sections E to H of the relocated epicenters in the STSP region. Section E crosses the earthquakes concentrated on the east side of the Tachienshan and Chukou Fault traces. Although the seismicity is highly related to the fault trace, the epicenters did not exhibit any linear distribution caused by the fault plane. Sections F, G and H show numerous and uniform seismicity. In section G, there was a horizontal earthquake group at the depth of about 3 km near the Muchiliao, Liuchia and the south part of Chukou Faults. The earthquake group at the northern end of the Chishan Fault exhibited a dipping plane with a high dip angle. The extension of the earthquakes was not deep, but can be observed to be highly concentrated on the linear structure. The position of seismogenic structure suggested the activity of the north Chishan Fault. In the southeast part of section H, the seismic zone mentioned that crossed the Chishan, Liukuei and Chaochou Faults shows a long, dipping and linear seismogenic structure. But, the relation between this linear structure and the faults is still hard to define. Furthermore, this linear structure is perpendicular to the dip of the fault plane of the M_L 6.4 earthquake occurred on March 4, 2010. The phenomenon reflected the seismic complexity of the area.

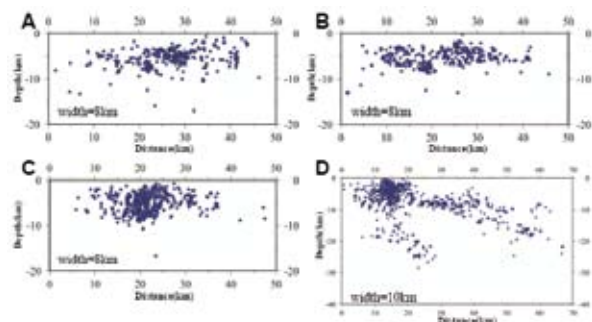


Fig. 4 Cross sections A to D in HSP region

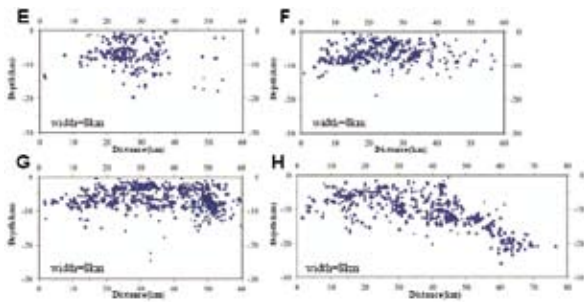


Fig. 5 Cross sections E to H in STSP region

Focal Mechanism

The focal mechanism is the double couple fault plane solution based on the observed first motion polarities for an earthquake. The mechanism is most often estimated using P-wave first-motion polarities recorded at local seismic stations. Each observed P arrival is mapped to the orientation at which the ray left the focal sphere, and nodal planes are fit to the set of observations. The inverted fault and nodal planes define the P axis (maximum principal stress), T axis (minimum principal stress) and B axis. Therefore, the fault type and the parameters (strike, dip and rank) of fault plane can be defined based on the focal mechanism of source model.

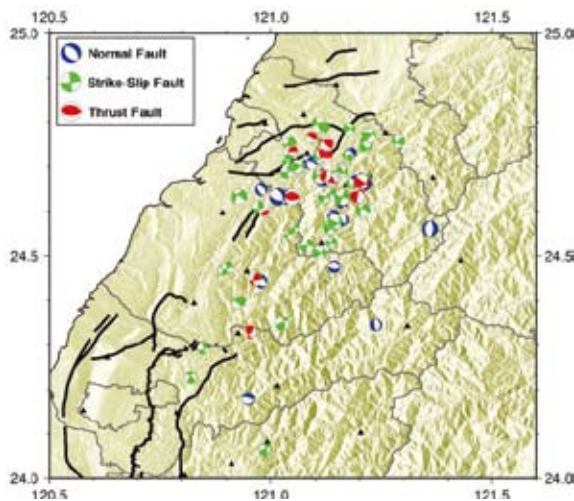


Fig. 6 Focal mechanisms located in HSP region

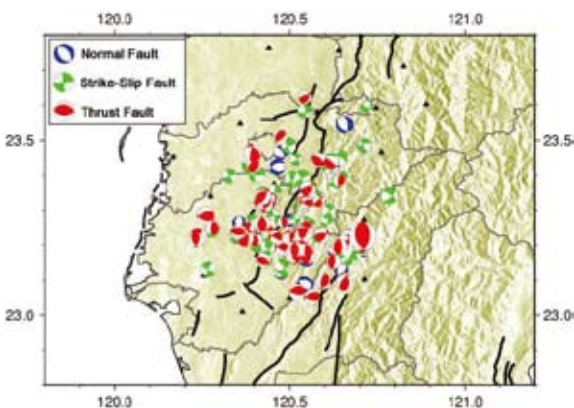


Fig. 7 Focal mechanisms located in STSP region

The program, HASH, developed by USGS (Hardebeck and Shearer, 2002; 2003) was utilized in determining the focal mechanisms of earthquakes observed. A total of 412 focal mechanisms were inverted and classified. Fig. 6 and Fig. 7 show, respectively, the focal mechanisms in HSP and STSP region. The focal mechanisms in HSP region were mostly located concentrated on the southeastern side of the Hsincheng and Tapingti Faults. Most of the sources belonged to the strike-slip fault mechanism, especially in Hsinchu County. Normal fault mechanism was the second most type of the sources observed, but this type was distributed over a broader area. The number of thrust faults is the least. In the STSP region, most of the sources belonged to the thrust and strike-slip faults. Normal fault sources were rare. Furthermore, majority of earthquake mechanisms that neighbored the fault trace on the northern end of Chishan Fault were thrust and strike-slip types. The strikes of these fault planes were NE-SW direction and are similar with the Chishan Fault. These earthquakes were induced by the northern part of the Chishan Fault according to the linear distribution and focal mechanisms.

Conclusions

Earthquake location using Double-difference technique and focal mechanism inversion have been studied based on the seismic data observed by the established NCREE Micro-Earthquake Monitoring Networks for Science Parks in Taiwan. The results are found to be helpful in analyzing the relationship between earthquakes and faults or seismogenic structures and in understanding the activities and source parameters of active faults in the region. When the earthquake monitoring was stopped at the end of 2010, a large volume of data has been recorded and is further being studied. These ongoing studies are hoped to provide more relevant information in the field of seismology and earthquake engineering.

References

Hardebeck, J. L. and Shearer, P. M. (2002), "A new method for determining first motion focal mechanisms", *Bull. Seism. Soc. Am.*, 92, pp2264-2276.

Hardebeck, J. L. and Shearer, P. M. (2003), "Using S/P amplitude ratios to constrain the focal mechanisms of small earthquakes", *Bull. Seism. Soc. Am.*, 93, pp2434-2444.

Waldhauser, F., and Ellsworth W. L. (2000), "A double-difference earthquake location Algorithm: method and application to the northern Hayward fault, California", *Bull. Seism. Soc. Am.*, 90, pp1353-1368.

Assessment of Damage and Serviceability of Water Systems Following Earthquakes

Gee-Yu Liu¹ and Hsiang-Yuan Hung²

劉季宇¹、洪祥瑗²

Abstract

A technology used for the assessment of water transmission and distribution systems following earthquakes has been preliminarily developed in a previous research work. To further enhance the developed technology, efforts that account pipe damages caused by earthquake-induced ground failure were made this year, and renewed probability models of pipe breaks and leaks and improved algorithm for simulating the locations of pipe damages have been proposed in this study. Also, the damage and serviceability of water mainlines in Yi-lan, Taiwan under an M7.1 earthquake scenario has been assessed in detail.

Keywords: water systems, serviceability, seismic scenario simulation

Background

In the past decade, scenario simulation has played a more and more important role in urban earthquake hazard mitigation and emergency operation. Various implementations have been proven of great help before and after an earthquake occurrence. Both public and private sectors can be enhanced in terms of their seismic preparedness and response if proper simulation is implemented effectively. Regarding water utilities, system-wide retrofit, emergency planning and exercise can be conducted based on seismic risk assessment to reduce the likely damage and losses prior to the occurrence of a devastating earthquake. Post-earthquake personnel and material dispatching, emergency water supply for hospitals and fire fighting, temporary water supply for affected people, strategies for restoration and recovery, etc. can all benefit from the result of a scenario-based analysis. If combined with the technology of early seismic loss estimation (ESLE), the information on estimated losses and emergency response demands can be generated and be provided immediately after an earthquake event. Such undertaking would be helpful to any decision-making body of water utilities or other agencies during emergency situation.

In order to realize the feasibility of the proposed technology, several pivotal technologies have to be well utilized and be integrated to become a technology

for post-earthquake damage and serviceability assessment of water pipe networks. As depicted in Fig.1, these technologies may comprise of earthquake source model and seismic hazard analysis (estimation of ground shaking and failure), empirical formulae for pipe repair rates, damage and malfunction model for equipment in water facilities, hydraulic modeling of water network system in terms of pressurized pipe flow analysis, hydraulic models of various pipe damages, and, finally, the skill of spatial analysis through GIS (geographic information system) tool.

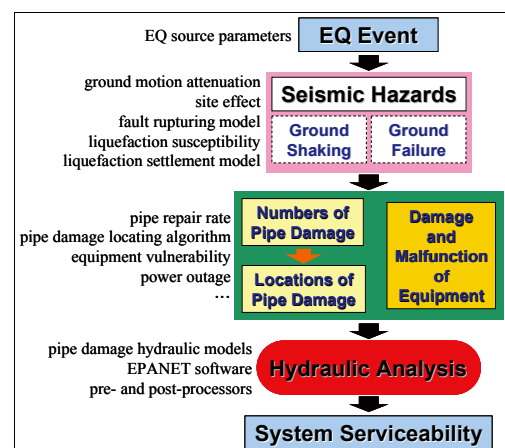


Fig. 1 Flowchart for the serviceability assessment of water systems following earthquakes

¹ Associate Research Fellow, National Center for Research on Earthquake Engineering, karl@ncree.narl.org.tw

² Assistant Research Fellow, National Center for Research on Earthquake Engineering, hyhung@ncree.narl.org.tw

NCREE has been working on such research topics during the past few years (Liu *et al.*, 2009). Recently, several improvements have been made in developing such methodology. The damaging effect to pipeline networks by earthquake-induced permanent ground displacement, either due to soil liquefaction or fault rupturing, has been successfully taken into account. This was done through an effort to develop a PESH (potential earth science hazards) modulus based on the seismic hazard analysis model of the software called TELES (Taiwan Earthquake Loss Estimation System). In addition, a new algorithm for simulating the locations of pipe damage has been developed. Finally, probability models for deciding the properties of a pipe damage point (pipe break or any type of pipe leaks) have been proposed, too. These models are essential in performing the post-earthquake damage and serviceability assessment of water pipe networks by the Monte Carlo method.

Simulation of Pipe Damage Points

During the seismic scenario simulation, the PESH modulus was used first to estimate the distribution of ground shaking and failure in terms of the peak ground acceleration (PGA) and the permanent ground displacement (PGD). The information of PGD was further used to calculate the distribution of strains at ground surface. The values of $Strain_{liq}$ (due to liquefaction), P_{liq} (probability that liquefaction will occur), and $Strain_{fault}$ (due to fault rupturing) can be attained at any site of the study area. Accordingly, the empirical formulae for pipe repair rates developed by Yeh *et al.* (2006) can be employed to calculate the combined pipe repair rate wherever a pipe is, which can be expressed as

$$RR = RR_{PGA}(\cdot) + RR_{Strain}(\cdot) \quad (1)$$

where the repair rate caused by ground failure is chosen as the larger value of $RR_{Strain}(Strain_{fault})$ and $RR_{Strain}(Strain_{liq}) \cdot P_{liq}$.

Conventionally, a stationary Poisson process is widely used to simulate the location/s of damage along a pipe. In this study, an approach based on the expected number of damages of pipes was otherwise proposed. From Fig. 2, let the length of a typical pipe segment be L . Assume there are a total of N pipes in the water pipe network under study. Let all pipes be broken down into segments of constant length L from their beginning nodes (the length of the last segment of each pipe may not equal to L), and be denoted as (i, j) , where i refers to pipe i ($i=1, \dots, N$) and j refers to its j -th segment. The expected number of pipe damage of any pipe segment (i, j) can be decided according to its length and the seismic hazard in reference to its location. Denote the number as e_{ij} . Starting from the origin of the number line, if all the expected numbers of pipe damage $e_{11}, e_{12}, \dots, e_{21}, e_{22}, \dots, e_{N,N}$ (where J_N refers to the last segment of pipe N) can be sequentially accumulated as $(e_{11}), (e_{11}+e_{12}),$

$(e_{11}+e_{12}+e_{13}), \dots, (e_{11}+e_{12}+\dots+e_{N,N})$ and be denoted on the number line, then the interval $[0, E_R]$, where E_R equals to the summation of all the expected numbers of pipe damage, will consist of N sub-intervals of lengths $e_{11}, e_{12}, \dots, e_{21}, e_{22}, \dots, e_{N,N}$. This also means that there exists a mapping between any real-number within $[0, E_R]$ and a specific pipe segment.

To simulate a location of damage along the pipe, first, an arbitrary number between 0 and E_R can be generated using a random number generator that follows uniform distribution. It can refer to one single segment, says e_{nm} , along the axis. Finally, the midpoint of the m -th segment of the n -th pipe is designated as a pipe damage location. The same process can be repeated E_R times to determine all pipe damage locations.

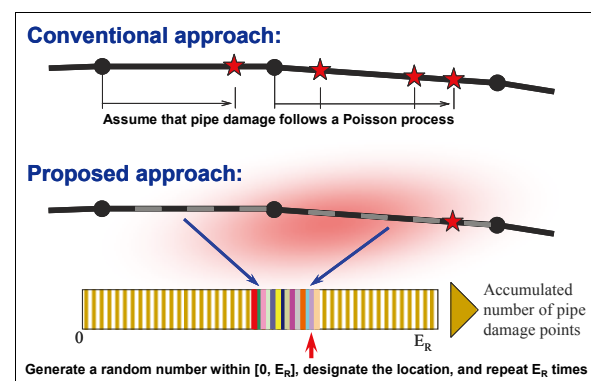


Fig. 2 Comparison between the conventional and the proposed approaches for simulating the locations of pipe damage in a pipe network

Probability Models of Pipe Damage

Various kinds of pipe materials have been adopted in the waterworks of Taiwan. Similar to other countries, the most common pipes are CIP (cast iron pipes), DIP (ductile iron pipes), MJP (mechanical joint pipes), and PVC (polyvinylchloride pipes). Among these, DIP and PVC are most widely used. On the other hand, JCCP (jointed concrete cylinder pipes) and HDPE (high-density polyethylene pipes) are occasionally used; SP (welded steel pipes) and PCCP (pre-stressed concrete cylinder pipes) are very popular in large diameter mainlines, while riveted steel pipes are never used. Since some of the joint details and installation practices of water pipes in Taiwan are different from those of other countries, the characteristics of their damage due to the effects of earthquake load are supposed to be different, too.

Earthquake-induced pipe damages can be roughly classified into two categories: (1) pipe leaks and (2) pipe breaks. In a study by Shi *et al.* (2006), a model that specifies the probability of occurrence of a leak or a break for each of the five popular water pipe materials in the United States has been proposed. Based on this study, another probability model

suitable for water pipes in Taiwan, as summarized in Table 1, has been proposed by the authors. The listed parameters are either slightly modified from the ones suggested by Shi *et al.* (2006) or decided according to past earthquake experiences and expert judgments. In addition, Shi *et al.* (2006) examined water pipe damage data and, accordingly, classified pipe leaks into five different types, namely: annular disengagement (L1), round crack (L2), longitudinal crack (L3), local loss of pipe wall (L4), and local tear of pipe wall at welded slip joint (L5). They further proposed a model that specifies the probability of occurrence of each type of pipe leaks for various pipe materials in the United States. Following this, another probability model, as summarized in Table 2, has been proposed in this study for the case in Taiwan.

Table 1 The proposed probability model of pipe leak and break for various pipe materials

	Leaks	Breaks
CIP	0.8	0.2
DIP	0.8	0.2
JCCP	0.8	0.2
SP*	0.4	0.2
MJP	0.8	0.2
PVCP	0.8	0.2
HDPEP*	0.2	0
PCCP*	0.2	0

*: Assume these pipe materials are very ductile and with many repairs caused merely by deformation and thus without any significant effect on their ability to convey water.

Table 2 The proposed probability model of different pipe leaks for various pipe materials

	L1	L2	L3	L4	L5
CIP	0.3	0.5	0.1	0.1	-
DIP	0.8	-	0.1	0.1	-
JCCP	1.0	-	-	-	-
SP	-	0.3	0.3	-	0.4
MJP	0.5	0.5	-	-	-
PVCP	0.5	0.5	-	-	-
HDPEP	-	-	-	-	1.0
PCCP	-	-	-	-	1.0

Case Study

The water system in Yi-lan County, Taiwan was chosen as a subject for seismic assessment. The entire water system is operated by the Eighth Branch of Taiwan Water Corporation. It covers 10 townships, or 814 km² in total. There are 11 pump stations and 18 distribution reservoirs. The total length of its pipelines is 126,520 km. The system considered in this study is actually a simplified system (*i.e.* all pipes with diameter less than 100mm are neglected). The corresponding hydraulic model was consisted of 358 nodes and 439 pipes; among the 358 nodes, 85 were specified with a demand. These nodes were supposed to be responsible for the water supply to customers.

Therefore, after hydraulic analysis was completed, the simulation of the resultant water supply of these nodes was divided according to township to see the distribution of the remaining capacity of water supply. The serviceability of the water mainline system was expressed in terms of SI (serviceability index), which is defined as the remaining capacity divided by the original capacity of the intact system.

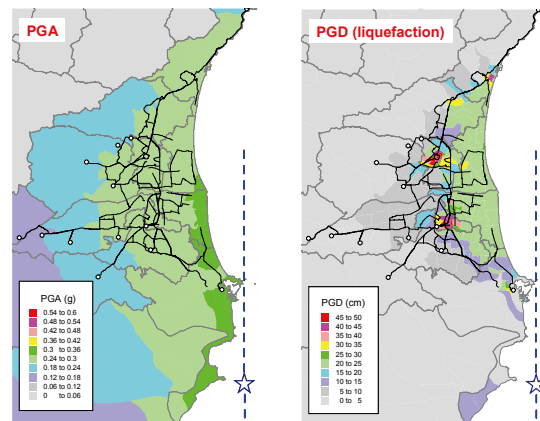


Fig. 3 Simulated ground shaking and failure in Yi-lan County induced by an offshore earthquake scenario with a magnitude of 7.1 and focal depth of 20km (line source model with N-S direction depicted as the dashed line)

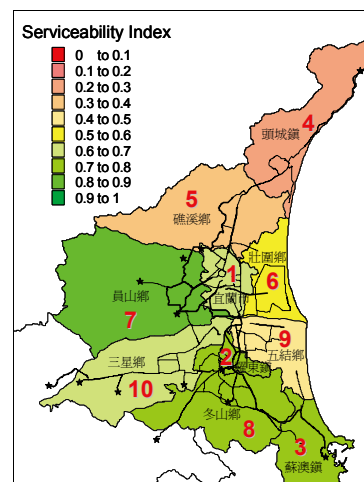


Fig. 4 Simulated distribution of serviceability index for the water network system in Yi-lan area under the M7.1 earthquake scenario

From Fig. 3, the occurrence of an M7.1 offshore scenario earthquake near Yi-lan area was considered. The location of epicenter was at (121.88° E, 24.48° N) and the focal depth was 20km. A line earthquake source model, depicted as the dashed line in Fig. 3, was employed. Using the PESH modulus developed in this study, the earthquake-induced ground shaking and ground deformation (soil liquefaction only) in terms of PGA in unit g and PGD in cm, respectively, can be simulated as depicted in Fig. 4. This seismic hazard information can be used to simulate the damage of the

pipe network in Yi-lan area in terms of exact locations of all pipe damage points and their properties (a break, or a leak together with its type, and hydraulic parameters for modeling the leakage).

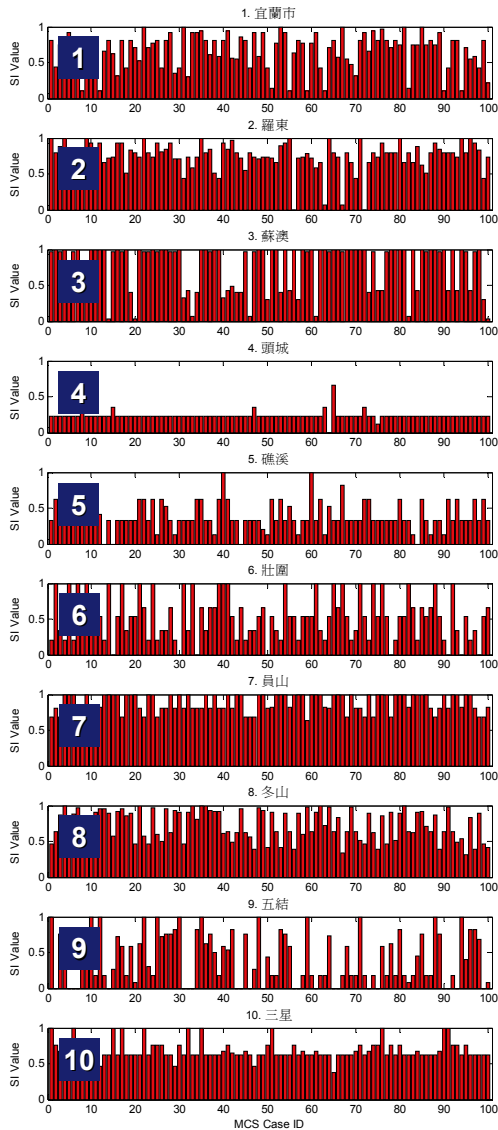


Fig. 5 The 100 simulated SI values, obtained during the Monte Carlo method, for each township in the Yi-lan water network system under the M7.1 earthquake scenario

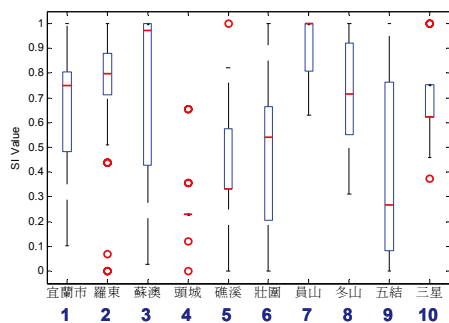


Fig. 6 The boxplot of the 100 simulated SI values depicted in Fig. 5

With the approach of Monte Carlo method, the simulated distribution of serviceability index for the water network system in Yi-lan area under the M7.1 earthquake scenario was obtained as illustrated in Fig. 5. It represents an average of 100 simulations of which the damages in pipes were decided in a random process that follows probabilistic models proposed in this study. It was found that the worst reduction in water supply happened in Toucheng (Area 4), where the SI was reduced to 0.2380. The second worst reduction happened in Jiaoxi (Area 5) and Wujie (Area 9), where the SIs reduced to 0.3897 and 0.4189, respectively. The SI of each township from the 100 simulations were depicted in Fig. 5, and the degree of dispersion and skewness of the simulation results can be easily observed from the corresponding boxplot depicted in Fig. 6.

Conclusion

An enhance technology for assessing water network systems following an earthquake has been developed in this study. The damaging effect of earthquake to pipes by not only ground shaking but also ground failure has been fully considered. A new algorithm for simulating the locations of pipe damage has been developed, and probability models for deciding the properties of a pipe damage point (pipe break or any type of pipe leak) have been proposed, too. The damage and serviceability of water mainlines in Yi-lan County, Taiwan under an M7.1 earthquake scenario has been assessed in detail.

Acknowledgement

This research work was funded by Water Resource Agency, MOEA, Taiwan, under Grant No. MOEA-WRA-0990095, and was carried out using the water network data of the Eighth Branch (Yi-lan County), Taiwan Water Corporation, for hydraulic analysis. Both are gratefully acknowledged.

References

Liu, G.-Y. and Hung, H.-Y., (2009) "Hydraulic Performance Analysis of Water Systems under Major Earthquakes," Proc. 6th Taiwan-US-Japan Workshop on Water System Seismic Practices, Taipei, Taiwan.

Rossman, L. A. (2000). EPANET 2 User's Manual, EPA, Cincinnati, OH.

Shi, P., O'Rourke, T. D. and Wang, Y. (2006). "Simulation of Earthquake Water Supply Performance", Proc. 8th U.S. Nat. Confer. Earthquake Eng., Paper No. 1295, San Francisco, CA.

Yeh, C. H., Shih, B.-J., Chang, C.-H., Chen, W.-Y. Walter, Liu, G.-Y. and Hung, H.-Y., (2006). "Seismic Damage Assessment of Potable Water Pipelines," Proc. 4-th Int. Confer. Earthquake Eng., Taipei, Taiwan.

Engineering Geological Database for TSMIP

Kuo-Liang Wen, Hung-Hao Hsieh and Chun-Hsiang Kuo

Abstract

More than 680 seismic stations all over Taiwan have been established by the Central Weather Bureau (CWB) to record ground motion data. In order to obtain the geological conditions and soil profiles at these strong motion stations, a site investigation project was developed by the National Center for Research on Earthquake Engineering (NCREE) and CWB in 2000. The site investigation mainly consists of three parts: (1) the basic description of a site, (2) the on-site boring, and (3) the Suspension P-S Logger technique, which was used to determine the P-wave and S-wave velocities of the strata at various depths. The Suspension P-S Logger technique, using a single down-hole probe with one source and two receivers, allows continuous measurements of wave velocities with high resolution. There were 21 seismic stations investigated in 2010. With reference to Kyoshin Net in Japan and ROSRINE in the USA, a preliminary engineering geological database for 448 seismic stations investigated from 2000 to 2009 has been constructed on the Engineering Geological Database for TSMIP (EGDT) website for researchers' convenient access to their needed data.

Keywords: Geological database, wave velocity, seismic station, P-S Logger, suspension P-S velocity logging system, TSMIP, EGDT

Introduction

Taiwan is located at the Circum-Pacific seismic belt - the most active seismic region in the world. Preventing severe losses of lives and properties caused by large devastating earthquakes is a major concern for the people in this region. The Taiwan Strong Motion Instrumentation Program (TSMIP) was initiated by CWB in 1991 to monitor ground motions at over 680 free-field stations around Taiwan. Once a major earthquake happens, all the records of ground motions from TSMIP provide useful information for the operation on hazard mitigation. The ground responses monitored by seismographs reveal the characteristics of ground motions in different geological conditions, and these can be used to improve the design spectrum and the current building codes.

More than 1,000 seismic stations have been installed in Japan to monitor ground responses during an earthquake. Researchers can download the data on ground responses via a website called, "Kyoshin Net". Basic information of a station site, physical properties of soils, and wave velocity of the strata measured by the down-hole velocity logging technique are also available on the site. After 1994 Northridge earthquake, a project called, "Resolution of Site

Response Issues from the Northridge Earthquake", ROSRINE, was conducted to study the site responses in the USA. To download the geological information and the wave velocity profile of a specified station, related information can be accessed in the ROSRINE website.

The distribution of seismic stations in Taiwan is the densest in the world, although the amount of seismic stations installed by CWB is less than that in Japan and in the USA. However, the application of earthquake data is being restricted by having an incomplete geological database. Therefore, in 2000, NCREE and CWB collaborated to perform site investigations in obtaining basic soil properties and wave velocity of the underlying strata. There were 21 seismic stations investigated in 2010 and are shown in Fig. 1. The code of the stations is listed in Table 1. There were 469 seismic stations investigated during the period of 2000 to 2010 and are shown in Fig. 2. With reference to Kyoshin Net in Japan and to ROSRINE in the USA, a preliminary engineering geological database for the 448 seismic stations investigated during years 2000 to 2009 has been constructed on EGDT website for convenient access of related information. This project was named, "Engineering Geological Database for TSMIP (EGDT)" and its website address is at

<http://egdt.ncree.org.tw> (as shown in Fig. 3).

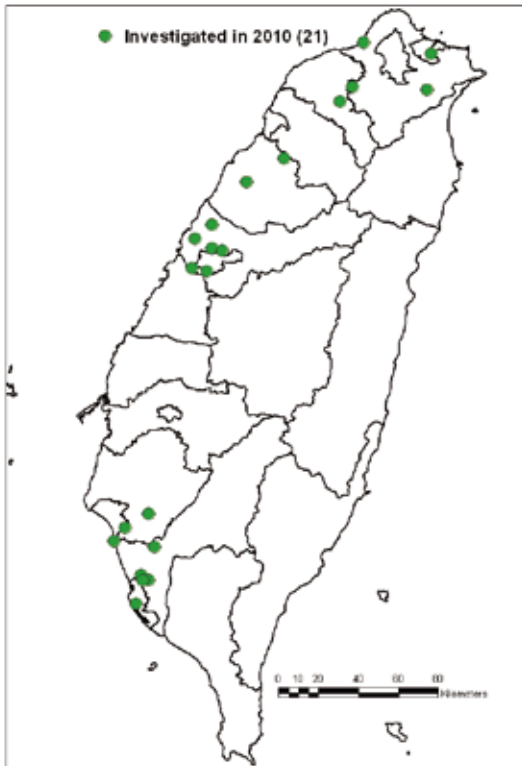


Fig. 1 The 21 seismic stations investigated in 2010.

Thus, a complete geological database is essential in earthquake engineering for the evaluation of seismic site effect.

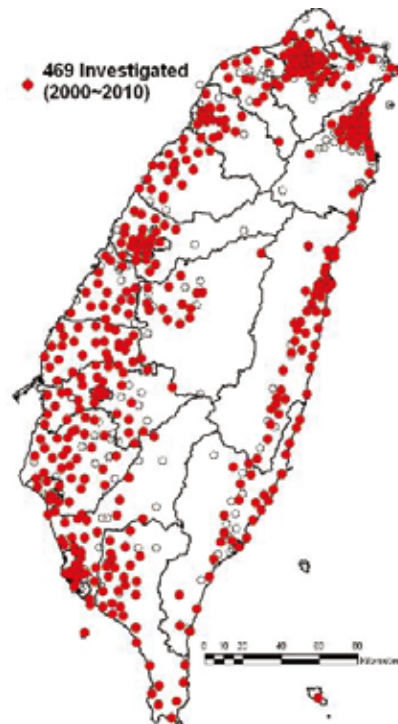


Fig. 2 The 469 seismic stations investigated during years 2000 to 2010.

Table 1. The code of seismic stations investigated in 2010.

Sta. Code	Sta. Code	Sta. Code
CHY063	KAU066	TCU059
CHY070	TAP047	TCU060
KAU012	TAP050	TCU061
KAU059	TAP063	TCU066
KAU062	TAP085	TCU127
KAU063	TCU011	TCU134
KAU065	TCU032	TCU135

Local site conditions play an important role in determining ground responses during an earthquake. Different site conditions could induce amplification or de-amplification at different period ranges in the response spectra. This phenomenon is called, the “site effect”. Besides, in a seismic hazard analysis, the motion at a site’s bed rock is predicted by the attenuation low from the earthquake source. According to the 2000 Uniform Building Code (UBC), 1997 National Earthquake Hazards Reduction Program (NEHRP) provisions in the USA, and the revised Earthquake-resistant Code in Taiwan, the ground motion at free field is evaluated by the product of response at bed rock and the coefficient of site effect. The coefficient of site effect is related to the magnitude of earthquake and the local site conditions.



Fig. 3 Engineering Geological Database for TSMIP (EGDT) website

Suspension P-S Logging Technique

The Suspension P-S Logging Technique developed by the OYO Corporation in Japan was used in this project to measure the primary wave velocity (V_p) and the shear wave velocity (V_s) of the strata. The source and the receiver of this measuring system were integrated into a single probe within a short distance. Therefore, the wave velocities of the strata can be measured continuously and precisely.

A borehole was first drilled at the chosen site and then filled with water. If the surrounding soil on a

borehole is not stable and is easily eroded, the borehole may be lined with a plastic tube. The probe was then put into the borehole at a specified depth. A primary wave or a shear wave may be generated by the source in the probe. The primary wave was propagated through the surrounding soil in the direction perpendicular to the borehole axis (horizontal direction). Also, the shear wave was propagated through the soil along the vertical direction. Each receiver consists of a hydrophone and a geophone in receiving the primary wave and the shear wave, respectively. A normal pulse and a reverse pulse were then triggered by the source in order to check the received signals. The time histories of those received signals should then be in the same shape but with 180° phase difference, since the two shear waves were propagated through the same soil media.

Typical measured signals of the primary waves and the shear waves from the logging computer are shown in Fig. 4, where H1 and /H1 represent the signals received by the upper receiver in normal and reverse directions, H2 and /H2 represent the signals received by the lower receiver in normal and reverse directions, V1 and /V2 represent the signals received by the upper and lower receivers, respectively. From the time histories of H1 and H2, the first arrival time for the upper receiver and the lower receiver was picked as t_{s1} and t_{s2} . Since the distance between the two receivers is 1 m, the shear wave velocity can be determined by the following equation:

$$v_s \text{ (m/sec)} = \frac{1}{t_{s1} - t_{s2}} \quad (1)$$

Similarly, the primary wave velocity is:

$$v_p \text{ (m/sec)} = \frac{1}{t_{p1} - t_{p2}} \quad (2)$$

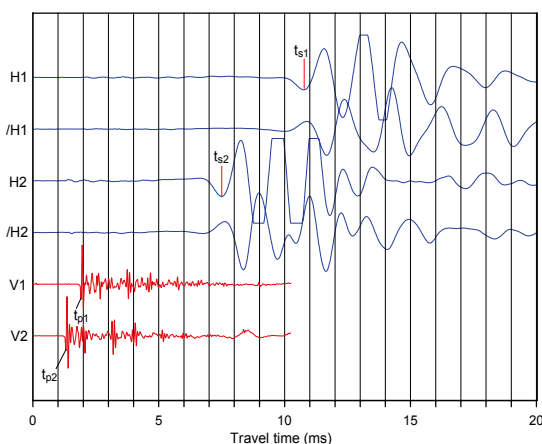


Fig. 4. Typical measurements from the Suspension P-S Logging System.

Engineering Geological Database

There are three major items in Taiwan's Engineering Geological Database. The first item is the general information of the station site that includes latitude and longitude of the station, ground water level, geographical or topographical conditions, and surrounding structures. The second item refers to the physical properties of soils. The SPT-N value, water content, unit weight, soil classification, and grain size distribution were obtained by on-site boring, sampling, and laboratory testing. After the borehole was drilled, the Suspension P-S Logging Technique was utilized to measure the wave velocity of the strata at every 0.5m. The wave velocity of the strata is an important index for site classification, thus was selected as the third item in the database. If the geological condition of the station site is classified as a rock outcrop, only the general environmental investigation was performed to collect the basic information of the station.

This project has been conducted for eleven years. At present, site investigations at 469 station sites were completed with the following distribution: 37 stations in 2000, 65 stations in 2001, 49 stations in 2002, 54 stations in 2003, 40 stations in 2004, 26 stations in 2005, 50 stations in 2006, 49 stations in 2007, 31 stations in 2008, 47 stations in 2009 and 21 stations in 2010. These stations are located on alluvial deposits, gravels, or even rock sites. The results were summarized on EGDT website. For example, as shown in Fig. 5, the general information for station TTN023 (the photo of the seismograph, the plan section and the cross-section of the surrounding environment), the soil profile, the SPT-N value, the shear wave velocity, and the primary wave velocity of the strata are all available on the website.

Most studies on site effect of earthquake ground motion are based on soil properties of the upper 30-m layer. In the 1997 UBC and 1997 NEHRP provisions in the USA, the average of the shear wave velocities for the top 30-m layer of soils was used as an index for the site classification. In the site classification of TSMIP stations, the site conditions were classified as Class B (rock), Class C (soft rock or very dense soil), Class D (stiff soil), and Class E (soft soil) according to the geological age, rock type, and the average SPT-N values of the upper 30-m layer of the strata.

With detailed subsurface soil profile and quantitative soil properties (SPT-N values and wave velocities) on a station site, the site effect of ground motions can be analyzed easily for a certain class of site conditions. Engineers may evaluate appropriate peak ground acceleration for the earthquake-resistant design of structures. According to the Classification Code of average shear wave velocities on the top 30-m soil layer (see Table 2), the 19 seismic stations investigated in 2010 can then be classified. The classification is shown in Table 3. All the investigated stations were classified by averaging shear wave

velocities on the top 30-m soil layer and are shown in Fig. 6.

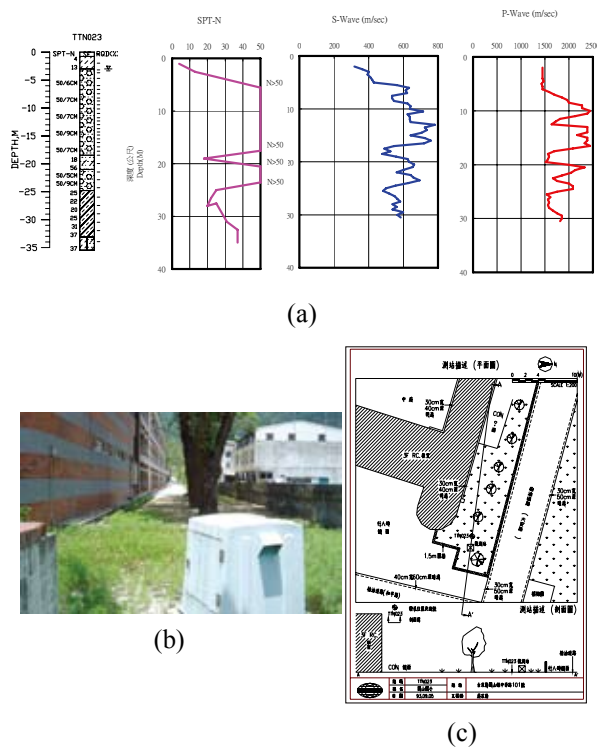


Fig. 5 The information for station TTN023 in the database shown at EGDT website.

- (a) Soil profile, SPT-N value, and wave velocity profile.
- (b) Photo of the seismic station in the field.
- (c) Description of the plan section and the cross-section in the field.

Table 2 Classification Code of shear wave velocity for the top 30-m soil layer (1997 UBC and NEHRP provisions).

Classification	The average of the shear wave velocity for the top 30m (V_{30})
A	$V_{30} \geq 1500$ m/sec
B	$760 \text{ m/sec} \leq V_{30} < 1500$ m/sec
C	$360 \text{ m/sec} \leq V_{30} < 760$ m/sec
D	$180 \text{ m/sec} \leq V_{30} < 360$ m/sec
E	$V_{30} < 180$ m/sec

Table 3 Classification of 19 seismic stations investigated in 2010.

Sta. Code	Classification	Sta. Code	Classification
CHY063	D	TAP085	B
CHY070	D	TCU011	B
KAU012	C	TCU032	C
KAU059	D	TCU059	D
KAU062	D	TCU060	C
KAU063	D	TCU061	C
KAU065	D	TCU066	C

KAU066	D	TCU127	B
TAP047	C	TCU135	C
TAP050	D		

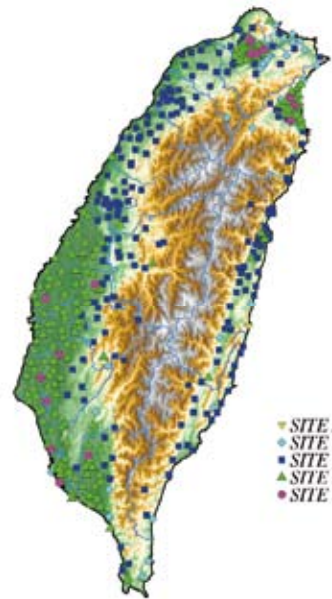


Fig. 6 All the investigated stations were classified by averaging shear wave velocities on the top 30-m soil layer

Conclusions

Site investigations at 469 TSMIP stations were completed by NCREE in cooperation with Taiwan's CWB. By sampling the soils in the borehole and using the Suspension P-S Logger Technique, specific geological and geotechnical data were obtained that include soil profile, physical properties of soils, and wave velocities of the strata. All the results of investigations were organized systematically in the database and made available in a preliminary web site. This project will be performed continuously in the following years. Combining with GIS techniques, the engineering geological database for TSMIP will provide more convenient information through web services. If an engineering project site is close to the strong-motion station, engineers may retrieve the geological and geotechnical properties of soils from the database to evaluate the site's ground response. Thus, this database is helpful for the seismic site effect analysis and earthquake-resistant design.

References

Chun-Hsiang Kuo, Kuo-Liang Wen, Hung-Hao Hsieh, Tao-Ming Chang, Che-Min Lin, Chun-Te Chen (2011). "Evaluating empirical regression equations for V_s and estimating V_{s30} in northeastern Taiwan", *Soil Dynamics and Earthquake Engineering*. 31, 431-439.

An Image-based Measurement Method for Plane Strain and Crack Observations

Yuan-Sen Yang¹, Chang-Wei Huang², Chiun-lin Wu³

楊元森¹、黃仲偉²、吳俊霖³

Abstract

A simple image-based method for measuring plane strain fields on the surface of specimens in earthquake engineering experiments was developed. This method integrated camera calibration, stereo triangulation, image metric rectification and image template matching techniques to develop a method that was cost-effective, easy to apply and provided a satisfactory level of measurement accuracy. A zero-strain test conducted using this method showed that the measurement accuracy achieved was 0.04 pixels. That is, the relative displacement accuracy achieved was 0.005 mm and the strain accuracy was 0.001. This level of accuracy was achieved using eight-mega-pixel digital cameras to measure a 17cm-by-28cm measurement region. Cracks that were 0.012 mm wide were identified in the concrete by examining the displacement fields calculated through the application of this image-based method in an RC-wall experiment. Further descriptions of this method can be found in [1].

Keywords: image-based measurement, strain measurement, concrete crack measurement

Introduction

The measurement of strain field plays an important role in earthquake engineering experiments. Locations with high strains may be at high risk of failure. Strain fields observation is also useful for investigation of hysteresis behaviors of structural components, which is very critical in earthquake engineering. Strain gauges are commonly used in conventional strain measurement and work by measuring the longitudinal strain on the surface of the small area that the gauge is attached to. However, when the region of interest is large, it becomes increasingly impractical to paste thousands of strain gauges over such a large area. Distributing the needed wires to the gauges results in increased set up time and obstructs viewing of the structure's surface. There are also added safety concerns when needing to deploy strain gauges to dangerous or unreachable regions.

Image analysis is an alternative way of measuring strain fields. By taking high-definition photos, the surfaces of the specimens can be recorded in an image format. Any shape and surface changes of the

specimens during the experiment can be recorded and analyzed. Due to improvements in digital technology, digital cameras that are currently available on the consumer electronics market are almost powerful enough to carry out image-based strain field measurements in earthquake engineering experiments. Also, as developments in digital technology are and continue to be rapid, image-based strain-field measurement techniques are likely to become a cost-effective method of choice for conducting experiments and structural health monitoring. Many researchers have already adopted image analysis techniques for material tests [2], strain-field measurement in concrete slab tests [3], large and dynamic displacement measurements in shake table tests [4], large strain measurements in laminated rubber bearing tests [5], particle trajectory measurement in fluid flow [6], and many other applications.

This work developed a simple measurement method which is suitable for earthquake engineering experiments. This method has the following

¹Assistant Professor, National Taipei University of Technology, ysyang@ntut.edu.tw

²Assistant Professor, Chung-Yuan University

³Associate Research Fellow, National Center for Research on Earthquake Engineering

characteristics:

- (1) This method does not require cameras to be placed perfectly parallel to the measurement region. Perspective effects are mathematically removed in this method. Earthquake engineering experiments typically have many devices around to simulate earthquake loads and to measure responses. Space for cameras may be limited. This method is adaptable with other experimental devices.
- (2) This method employs camera calibration so that optical distortion of images is mathematically removed. The camera calibration photos shall be taken before the experiment.
- (3) This method allows that partial visual range is covered by unavoidable obstacles between the measurement region and one of the cameras as shown in Fig. 1.

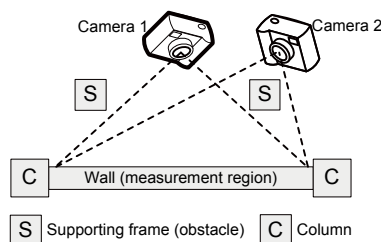


Fig. 1 Dual-camera setup for experiments with obstacles (a top view)

- (4) The strain accuracy of this method is insensitive to stereo triangulation error. Stereo triangulation error is likely to be induced by slight movement of cameras through hours of experimental time.
- (5) The specimen photos shall be taken in the pre-experimental stage to obtain the initial base line. The same specimen and cameras shall be used through the experiment.

This work used digital cameras that are relatively inexpensive and mass produced in a simple method to estimate the strain fields within concrete surfaces and then applied this method to a precast post-tensioned reinforced concrete (RC) wall experiment. The experiment is described by Chen [6] and Rahman and Sritharan [7]. A software program called ImPro Strain was developed based on a 2D-displacement analysis tool called ImPro [4] during this work to carry out image-based strain measurements. This paper presents the formulations and procedures used in an image-based strain-field measurement method, image analysis techniques, and their application in a zero-strain test and an RC-wall experiment.

Procedure of the Measurement Method

This image-based method assumes that the measurement region is a plane and remains a plane throughout the entire experiment. The proposed method is applicable to the measurement of surface

strain fields on walls, rectangular beams and columns, floors and ceilings. There are nine steps in the proposed measurement method: (1) paint on measurement region, (2) setup cameras, (3) take calibration photos, (4) take experimental photos, (5) run camera calibration analysis, (6) position control points, (7) run image metric rectification, (8) calculate displacement fields, and (9) calculate strain fields. Steps (1) to (3) are done in the laboratory before an experiment; step (4) during the experiment. Steps (5) to (9) are done after the experiment. More complete descriptions can be found in [1].

Measurement Accuracy

A zero-strain test was conducted to estimate the accuracy of the proposed image-based measurement method. The zero-strain test measured the strain fields of a rigid planar board. The strain fields of the speckled rigid board were measured. As the measurement region is of a rigid board (whose strain is known to be zero), the measured strains indicate the accuracy of the image-based measurement method.

The zero-strain test results show that refinement of the measurement grid is one of the factors affecting the strain measurement accuracy. The actual strain over the measurement region is zero. The strain measurement accuracy is better in a coarser grid than in a more refined grid. This result is analogous to a large strain gauge having better accuracy than a smaller strain gauge. A conventional strain gauge averages the strain over the area that it is attached to. The measured strain of a small gauge is relatively sensitive to microstructure variance and defects of the measured material. For image-based measurement, the displacement of a cell is calculated through pixel-based operations. The displacement of a small cell is sensitive to the noise of pixel light intensity because of its relatively small denominator. In addition, a small cell may contain insufficient distinctive intensity pattern for image analysis. Its strains are further amplified due to small denominators. Different refinements of measurement grids were investigated in the zero-strain tests. These grids were 31x51, 36x58, 42x67, 50x81, 63x101, and 84x135 cells. The cell sizes of the above measurement grids were 40 pixels, 35 pixels, 30 pixels, 25 pixels, 20 pixels, and 15 pixels, respectively. The equivalent pixel accuracy was calculated. The maximum measured strain error using the 84x135 grid was found to be about +/-0.008, and decreased down to +/-0.001 as larger cell sizes were used in the measurement grid. The maximal error in the 84x135 grid was much higher than that in the 63x101 grid, possibly because the cell size in the 84x135 grid (15 pixels) was so small that a few cells did not contain enough unique speckle features to produce accurate template matching results. Thus, using a coarser measurement grid provides better accuracy, however the measurement grid refinement must remain high

enough to produce acceptable detail in the calculated strain fields.

Sub-pixel precision is achieved by hierarchy image matching. Fig. 2 demonstrates how sub-pixel precision is achieved. Level 1 ((a) and (b)) reaches 1-pixel precision, while after image resizing in Level 2 ((c) and (d)), 1/3-pixel precision is achieved.

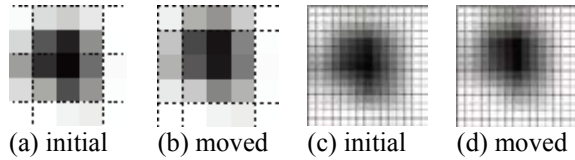


Fig. 2 Example of hierarchy image matching

Accuracy is never superior in image-based strain measurement systems when compared to measurements taken with conventional strain gauges. The strain gauge accuracy is commonly 10-4 to 10-6 and thus much better than 0.001 to 0.008 mentioned above. When using a 31x51 grid, the majority of cells achieved 0.02 pixels of equivalent pixel accuracy (see the standard deviation lines); about 99% of cells were better than 0.03 pixels (see the 99.5 and 0.5 percentile lines). Even the worst cell among the 1,581 (31x51) cells achieved an equivalent pixel accuracy of 0.04 pixels. For measurement tasks that require better accuracy, industrial cameras and sophisticated image correction should be seriously considered.

Application on an RC-Wall Test

The proposed image-based strain measurement method was applied to a large-scale RC-wall experiment [7]. The blue frame in the photo was a supporting frame that prevented the wall from out-of-plane movement. Each measured region is 30 cm by 20 cm. Further description of the measurement can be found in [1].

Tensile and compressive strains that were smaller than +/-0.0005 were measured in this RC-wall experiment. The average measured strain ϵ^{YY} was -0.0005. The results of zero-strain tests presented in section 3.6 indicated that when the cell size was 25 pixels, the maximal measured strain error may be larger than 0.002. This error is a much larger value than the average measured strain however, the majority of measured strain values ϵ^{YY} were within -0.0008 and -0.0001. Small cracks (if any) were likely to be closed and the strain ϵ^{YY} was roughly uniformly distributed, therefore large strain values measured here can be seen as measurement noise.

Small horizontal cracks appeared at the early stage of the test, and were observed using the proposed method in the RC-wall experiment. The measured results do not represent the strain values of material if there were cracks present. The measured strain values along these areas were about +0.001, which is larger than the limiting tensile strain of concrete. When

cracks appeared, the distance between the cells across the crack increased. This lead to large measured strain values around the crack. Unlike many crack detection methods, this method needs initial images of the specimen prior to any deformation to compare with the later deformed images. Many crack detection methods detect cracks by finding lines of darkness in images without the need of initial images because cracks can be seen directly in the current status. In these methods, a crack needs to be wide enough so that the darkness can be identified. In this method, a crack can be found before it appears darker. It is found through examining the displacement and strain fields, which the initial images are required.

Small horizontal cracks appeared at the early stage of the test, and were observed using the proposed method in the RC-wall experiment. A crack induces discontinuity of displacement field, and causes large calculated strains. For brittle materials like concrete, a continuous line of large values in a measured strain field may imply that there exists an opening crack, and does not represent any strain. Figure 2 shows a measured strain ϵ^{YY} and its displacement along Y in this test, showing that very small crack openings can be observed and measured.

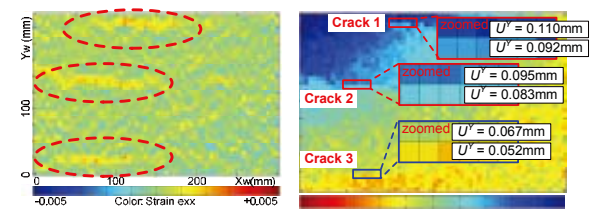


Fig. 2 A measured ϵ^{YY} (left) and disp. Y (right)

Some surface concrete at both corners broke off from the original plane or fell apart in the later stage of the experiment. Out-of-plane displacement of the concrete surface increases the strain measurement error in this method. The image of out-of-plane area in the rectified image was distorted. The out-of-plane displacement or loss of material from the surface leads to poor image template matching, and results in erroneous displacement values. They can be detected through examination of the similarity factor field results as shown in Figure 3. A high similarity factor (close to one) of a cell means that a sub-image can be found that is a good match with the deformed image. A low similarity factor may be due to many reasons including a crack passing through the cell, very large strains, out-of-plane displacement, or loss of material from the surface.

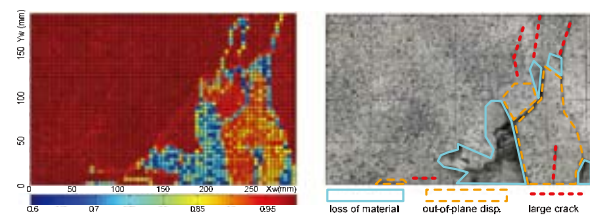


Fig. 3 A similarity field and rectified image

In the above test, deformation of well constructed concrete wall induced relatively continuous displacements with a few cracks. However, for structures with rough surfaces and aggregates, like eroded concrete piers, deformation pattern is much different. The deformation majorly induces cracks among aggregates rather than continuous strains. These cracks may be identified by examining the displacement and strain fields calculated by this method if the measurement grid is fine enough. However, if the cracks are densely distributed that distances among them are smaller than the size of measurement cells, cracks are not able to be identified by this method. If so, a finer measurement grid with smaller cells can be tried so that cracks may be observed more clearly. In this case, it is suggested that cameras should be zoomed-in when mounting cameras, so that the cells in the fine measurement grid contain clear and sufficient image patterns, and template matching can be successfully conducted.

Conclusions

A simple method integrating camera calibration, stereo triangulation, image metric rectification, and image template matching techniques are integrated in this work to measure concrete surface strain fields in a reinforced concrete (RC) wall experiment. Surface strain fields were estimated by analyzing pairs of images taken by commodity digital cameras, which are commonly affordable by most of the earthquake engineering laboratories. Camera calibration was carried out to correct geometrical and optical distortions. Stereo triangulation technique was employed to position measurement regions in the 3D space. Image metric rectification was adopted to generate un-distorted images of initial and deformed measurement regions. Image template matching technique was employed to estimate in-plane displacement fields of the measurement regions. Strain fields were calculated according to the measured displacement fields.

The measurement is applicable for static and pseudo-dynamic experiments that experimental photos can be taken clearly by digital cameras. For dynamic experiments such as shake table tests, high-speed cameras are needed so that specimen photos can be taken clearly. For practical applications on real-time structural health monitoring, further studies on camera movements and vibrations, temperature effects, image noises filtering (induced by rain, dusts, shadows, etc.), hardware fault tolerance, data communication and power supply are required.

The measurement accuracy of the proposed method was carefully estimated by conducting a zero strain test. Relative displacement measurement accuracy can be within ± 0.04 pixels, resulting in a strain measurement accuracy of 0.001 while a 31-by-51 measurement grid with cell size of 40 pixels was used. In addition to the strain fields, surface

cracks can be detected by examining the measured displacement and strain fields. Small concrete cracks with 0.02mm width can be found by examining the measurement results. Compared with commercial products, this method is cost effective and easy to use, and provides satisfactory accuracy for strain measurement and crack examination for earthquake engineering experiments. For those experiments which are dangerous for people to approach, this method is a safe way to monitor deformation, strain fields, and surface cracks. Further descriptions of this method can be found in [1].

References

- Yang, Y. S., Huang, C. W., & Wu, C. L. (2011). "A simple image-based strain measurement method for measuring the strain fields in an RC-wall experiment," *Earthquake Engineering & Structural Dynamics*. Accepted.
- Tung, S. H., Shih, M. H., Kuo, J. C. (2010). "Application of digital image correlation for anisotropic plastic deformation during tension testing," *Optics and Lasers in Engineering*, **48**(5), pp. 636-641
- Capéran P. "Displacement and strain field photogrammetric measurements of a reinforced concrete slab submitted to an earthquakes loading," *Proceedings of the OPTIMESS2007 Workshop*, Leuven, Belgium, May 28-30, 2007.
- Wu, C.L, Kuo, W. W., Yang, Y. S., Hwang S. J., Elwood, K. J., Loh, C. H., Moehle, J. P. (2009). "Collapse of a nonductile concrete frame: Shaking table tests," *Earthquake Engineering & Structural Dynamics*, **38**(2), pp. 205-224.
- Lewangamage, C. S., Abe, M., Fujino, Y., Yoshida, J. (2004). "Strain field measurements of rubber by image analysis and design criteria for laminated rubber bearings (LRB)," *Earthquake Engineering & Structural Dynamics* **33**(4), pp. 445-464.
- Capart, H., Young, D. L., Zech, Y. (2002). "Voronoi imaging methods for the measurement of granular flows," *Experiments in Fluids* **32**(1), pp. 121-135.
- Chen, P. C. (2008). "International collaborative test on post-tensioned RC shear wall," *NCREE Newsletter*, **3**(1), pp. 6.
- Rahman, M. A., Sritharan, S. (2006). "An evaluation of force-based design vs. direct displacement-based design of jointed precast post-tensioned wall systems," *Earthquake Engineering & Engineering Vibration*, **5**(2), pp. 285-296

Numerical Simulation Studies of Buried Pipes

Ren-Zuo Wang¹, Bing-Chang Lin², Steve (C.H.) Huang³,

Xin-Han You⁴, You-Hao Wang⁵

王仁佐¹、林炳昌²、黃昭勳³、尤信翰⁴、王佑豪⁵

Abstract

In this project, numerical simulation of buried pipes, and analysis and evaluation of their seismic performance using the American Lifelines Alliance (ALA) method have been studied. Through this research, predicted large deformation of the buried pipes in thrust fault zone has been examined. The vibration analysis of the pipes under seismic loading was computed. This study can be divided into two parts. The first part involves the numerical analysis based on ABAQUS software to analyze the large deformation of buried pipes. In this, numerical simulation of the pipe-soil interaction was done. ASCE (1984) nonlinear spring model was adopted also. Numerical simulation results of buried pipes were compared with the results of experiments discussed in the NEESR-SG Report (circa 2008). Numerical and test results show very close values. The second part focuses on the ALA method that considers the internal temperature and pressure of the pipe, the vertical live load, and the static load on buried pipes. The total strain of the pipe from these forces shall not exceed their allowable strain.

Keywords: buried pipeline analysis, American Lifelines Alliance (ALA), ABAQUS, pipe-soil interaction

Introduction

When an earthquake occurs, underground pipeline systems suffer seismic damage and failure. In order to assess buried water pipe, oil pipe and natural gas pipe damages due to seismic forces, recent advances in the numerical analysis of buried pipes and their design methods were explored and studied. The findings were compared with other test results and numerical results to prove the feasibility and applicability of the chosen analysis and design methods. For the analysis of large deformation of buried pipes, researchers have proposed a number of theoretical analyses and numerical simulations. For example, they have recommended using shell elements and soil springs along the pipeline to simulate the large deformation of buried pipes as shown in Fig. 1. In this numerical model, the local buckling at cross-sections of the pipes can be simulated. The soil spring model was derived from ASCE (1984) model, which is a reasonable

model to calculate soil deformation.

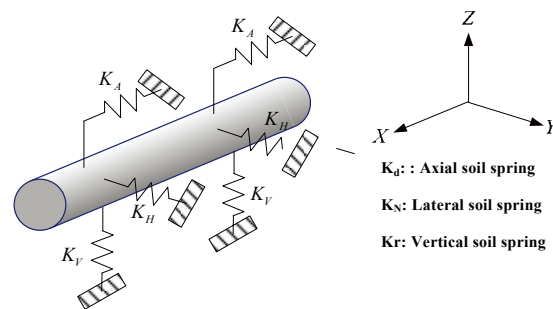


Fig. 1 Stiffness of soil spring along buried pipes

Numerical Simulation of Pipe-Soil Interaction

The pipe-soil interaction effect in buried pipe is due to the friction force on interacting surfaces of the soil and the pipe. In this study, the soil spring model

¹ Associate Researcher, National Center for Research on Earthquake Engineering, rzwang@ncree.narl.org.tw

² Professor, Department of Civil Engineering, Chung Yuan Christian University, binchan@cycu.edu.tw

³ Associate, Department of Civil Engineering, National Taipei University of Technology, steve@ntut.edu.tw

⁴ Graduate Student, Department of Civil Engineering, Chung Yuan Christian University.

⁵ Graduate Student, Department of Civil Engineering, National Taipei University of Technology

was used to compute the deformation of the soil. These soil springs were connected to the nodes of the pipe elements. The established model can be adopted to analyze the large deformation of buried pipes along the fault rupture zone. In this project, the ASCE (1984) soil spring models adopted are three-directional spring models that include the axial direction, the lateral direction, and the vertical direction springs as shown in Fig. 2. These ASCE spring models are consist of forces and displacements relationship per unit length.

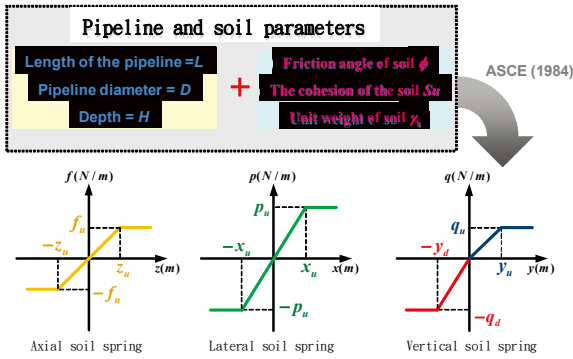


Fig.2 ASCE (1984) soil spring models

The accuracy of the ASCE (1984) soil spring model is significant, thus this study compared the experimental and numerical results (vertical soil spring) on the uplift force and the displacement of buried pipes as shown in Fig. 3.

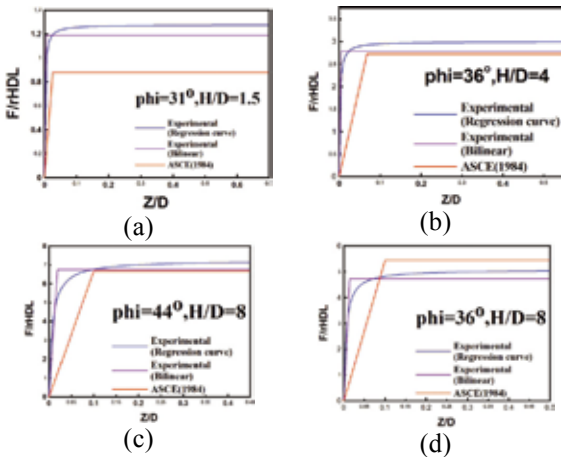


Fig. 3 Comparison of experiment and numerical results (vertical soil spring) on uplift force and displacement

Test results on the lateral pressure of the soil in NEESR Report were compared with numerical results. In this case, The ASCE (1984) soil spring model was adopted. From Fig. 3, it can be learned that the lateral soil pressure in NEESR Report is higher than the numerical result.

American Lifelines Alliance (ALA) Method

In this study, in order to understand the computations involve in the ALA method, a flowchart was studied as shown in Fig. 4. This ALA flowchart considered four items (i.e., earthquake wave effect, intrinsic pressure and temperature, surface live load, and vertical earth load) in a buried pipeline system.

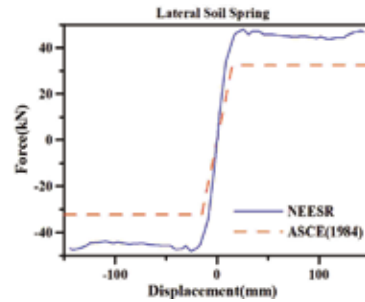


Fig. 3 Comparison of test and numerical simulation results (lateral soil spring) of buried pipes

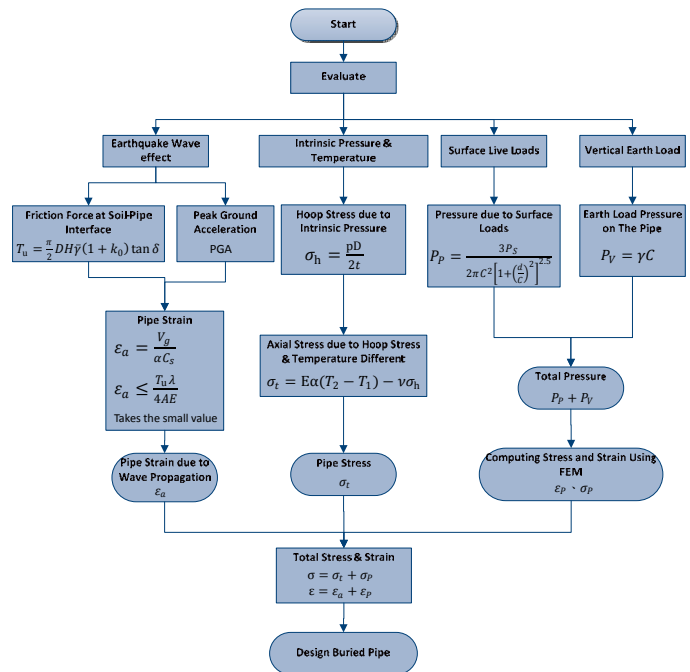


Fig. 4 Flowchart of ALA method

Earthquake Wave Effect

The earthquake wave effect is a dynamic response of buried pipes. In this study, earthquake wave effect was computed as shown in Fig. 4. T_u is the friction force per unit length at soil-pipe interface and V_g is the peak ground velocity (PGV). The PGV value can be computed using peak ground acceleration (PGA). ϵ_a is the axial strain of the

buried pipes. This strain is induced by wave propagation. C_s is the apparent propagation velocity for seismic waves. In Fig. 4, the λ refers to the apparent wavelength of the seismic waves at ground surface (1.0 km). The values A and E are the pipe's cross-sectional area and modulus of elasticity, respectively.

Intrinsic Pressure and Temperature

The intrinsic pressure and temperature of buried pipes are static loads. They can be computed using laws on mechanics of materials. In Fig. 4, σ_h is the hoop stress due to the pipe's internal pressure, and σ_t is the longitudinal stress due to the difference in temperature associated with σ_h .

Surface Live Loads

In ALA method, a car or a train is considered to provide surface live load. P_p is the pipe pressure when is the pipe is subjected to a concentrated surface load, P_s . In Fig. 4, C is the depth of cover of the pipe and d is the offset distance from the center line of the pipe to the position of surface load.

Vertical Earth Load

In ALA method, vertical earth load is a static load. In Fig. 4, P_v is the pipe pressure when the pipe is subjected to a vertical earth load, C is the depth of cover, and γ is the unit weight of fill. Since earthquake wave effect is a dynamic load and if ALA method is adopted in Taiwan, the PGA must be modified because site effects in different countries vary.

Numerical Examples

In this research, two examples have been studied. The first example considered using pipe elements and soil spring elements. For the second example, the shell element was adopted to model buried pipes. In order to simulate effectively the deformation behavior of buried pipes due to fault rupture effect, the software ABAQUS was adopted. The examples are discussed in the succeeding sections.

Comparison Between Numerical Simulation and Strike-Slip Fault Test in Cornell University (CU), USA

In this first example, the test results in Cornell University utilized the ABAQUS software to simulate large deformation of buried pipes under strike-slip fault dislocation. Figure 6 shows the numerical model of buried pipes. Simple support was

used for the boundary condition of the pipes. The deformation of the soil was computed using soil spring model. In order to model moving fault, the displacement control was adopted. Along the fault line, as shown in Fig 6., the azimuth angle was $\alpha = 65^\circ$ and the corresponding translation was measured at 1.22m.

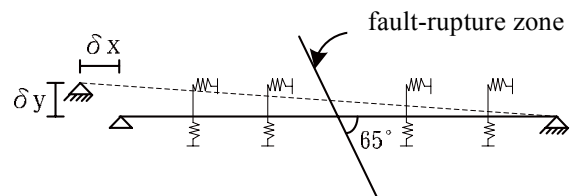


Fig. 6 Numerical simulation model for buried pipes using pipe elements and soil spring elements

The use of ASCE soil spring model and ABAQUS pipe elements helped in determining the large deformation response of buried pipes as evident by the conducted tests in Cornell University, USA. The ABAQUS/Standard analysis and a static analysis were utilized. The deformation response of buried pipes and soil spring are shown in Fig. 7.

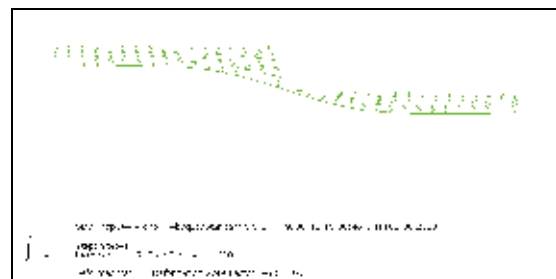


Fig.7 The deformation response of buried pipes and soil spring for ABAQUS analysis.

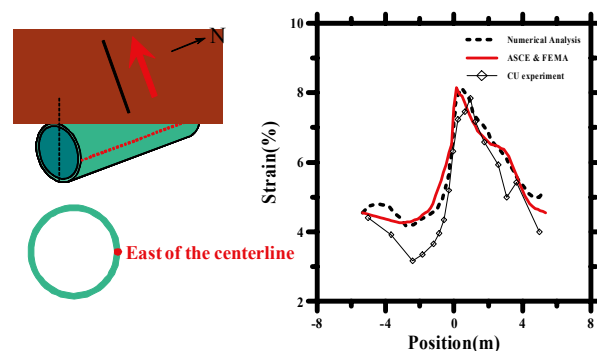


Fig. 8 Numerical and test results at the centerline axial strain of buried pipes (east direction)

The results of the centerline axial strains of buried pipes were compared with ABAQUS result (ASCE & FEMA), numerical analysis (CU FEM result)

and test results at CU (see Fig. 8).

Numerical Simulation of Modeling Pipe as Shell Elements

The second example involves numerical simulation of modeling buried pipes as shell elements (Takada *et al.*, 1998). In this case, shell elements were used to model the deformation of pipe. Similarly, ASCE soil spring model was used for the deformation of soil. The use of shell elements can compute the local buckling of the buried pipe, but need more time during the process. The numerical simulation model is shown in Fig. 9. The angle of the reverse fault was 45° and the fault displacement was measured at 0.5m. In order to model the soil spring was easy. Its fixed ends were placed with a big outer tube. It then has a higher stiffness to avoid the deformation of the big outer tube (see Fig. 9). According to previous study (Takada *et al.*, 1998), the shell elements must be made of small size mesh at reverse fault zone. The inner tube was adopted to model buried pipes from the left of each node to 0.5m. Figure 10 shows five conditions, *i.e.* initial condition, the deformation of buried pipes at 0.1m, 0.2m, 0.3m, and 0.4m fault displacement.

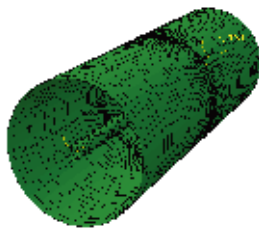


Fig. 9 Numerical model of buried pipes in ABAQUS analysis

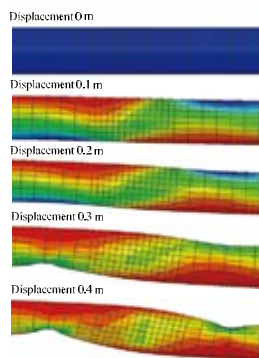
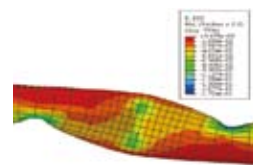


Fig. 10 The deformation of buried pipes using shell elements at five conditions

Takada *et al.* (1988) has performed similar numerical analysis. The local deformation of buried pipe was compared between ABAQUS result and Takada *et al.*, (1998) numerical result at 0.5m reverse fault displacement shown in Figs. 11(a) and (b). The said figures elucidate that the position and the shape of local buckling for buried pipes are very close. This shows that the numerical analysis using shell elements can determine the deformed status of buried pipes under buckling phenomenon.



(a) ABAQUS result



(b) Takada *et al.*, (1998) numerical result

Fig. 11. Comparison between ABAQUS result and Takada *et al.*, (1998) numerical result at 0.5m reverse fault displacement.

Conclusion

In this project, numerical simulation of buried pipes has been conducted. In Figs. 8 and 11, the numerical results found are very close to that of the tests and previous works by Takada *et al.*, (1998). It has been proven that the ASCE soil spring model and nonlinear FEM method can be adopted to compute the large deformation of buried pipes in a thrust fault zone. In addition, the American Lifelines Alliance (ALA) method has been explored and has been found to be useful in computing the nonlinear dynamic responses under seismic loading of buried pipes.

References

- ALA (American Lifelines Alliance) (2001). Seismic Fragility Formulations for Water Systems, <http://www.Americanlifelinesalliance.org>.
- CU, RPI and Science Discovery Center, (2007). "NEESR-SG, Annual Report."
- Takada, S., Liang, J.-W. and Li, T. (1998) "Shell-Mode Response of Buried Pipelines to Large Fault Movements," *Journal of Structural Engineering*, Vol. 44A, pp. 1637-1646.

Design of Experiment and Numerical Analyses of Impacts on Concrete

Ren-Zuo Wang¹, Keh-Chyuan Tsai², Bin-Chang Lin³ and Fan-Jun Xie⁴

王仁佐¹、蔡克銓²、林炳昌³、謝汎鈞⁴

Abstract

This project aimed to develop a system that elucidates the impacts of collision on concrete. The system will be used to measure five significant items, which are: (1) the velocity of blocks before collision, (2) the position of blocks, (3) the velocity of block during collision, (4) the image data for velocities, positions, strains and displacements of blocks, and (5) To ensure the feasibility of the design of experiment for the system, test experiments have been carried out. The proposed system can be divided into two parts. The first part is a simple pendulum device. This device is composed of cantilever steel frames and cables. The second part is a quick-release system, which is made of a quick-release device, a cable, and steel frames. The measurement devices include speedometers, laser measurement system, infrared gun (to measure distance), accelerometer, and high-speed camera. From the comparison of the analytical solution and the conducted experiments, results are found to be in good agreement.

Keywords: system of impact, design of experiment, impact test

Introduction

From previous strong earthquakes, buildings and bridges were severely damaged. As observed, earthquake effects and impact of collision among structural components caused the collapse of those structures. In this, to understand the collision state of the overall impact between the structural members in the collapse of structures, a system that determines and studies the effects of impact of the collision of various structural members has been established in this research project. The impact of system likes an experimental platform. Until now, the collision experiments in Taiwan or in other countries are still on small scales or in numerical simulations since full-scale collision experiments (FSCE) require enough test sites, equipments, and the capacity of the test center to do the collision's numerical simulation. Fortunately, the National Center for Research on Earthquake Engineering (NCREE), Taiwan has provided the sufficient conditions to establish the FSCE. The use of a cantilever structure system fixed

onto the reaction wall was adopted. The advantage of the established impact system with the reaction wall was that various collision components can be removed at different phases of the collision. The impact system allows changing the speed of the colliding blocks. Moreover, the high-speed camera was easy to use in measuring the contact state of the colliding blocks.

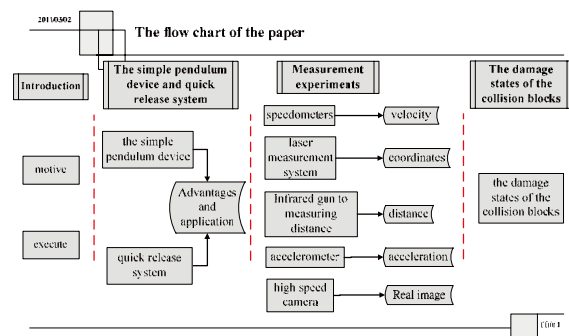


Fig. 1 Flow chart of the study

¹ Associate Researcher, National Center for Research on Earthquake Engineering, rzwang@ncree.narl.org.tw

² Professor, Department of Civil Engineering, National Taiwan University

³ Professor, Department of Civil Engineering, Chung Yuan Christian University

⁴ Graduate Student, Department of Civil Engineering, Chung Yuan Christian University.

Simple Pendulum Device and Quick Release System

In this project, the flow chart of the study is adopted as shown in Fig. 1. The simple pendulum device (see Fig. 2) has the following advantages: (1) an equilibrium state during the contact-impact state where there are no block accelerations but there are the relative accelerations of the two colliding blocks, and (2) a simple structural configuration since the simple pendulum is a cantilever type of structure. It has not any cover body at contact position. Also, the boundary condition in the simple pendulum system of the passive collision block is a hinge condition, thus the collision blocks can have a free motion. The quick release system was included in two parts. The first was in a steel frame perpendicular to the ground. The second part was through a quick release mechanism.

To ensure that surfaces of the passive and active blocks are in direct contact as required, the active block's motion must be kept traveling along a linear direction.

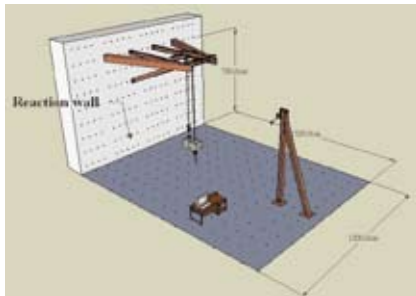


Fig. 2 3D schematic diagram of the simple pendulum device



(a) Actual simple pendulum device



(b) Quick release system

Fig. 3 Established impact system

The impact test procedures are summarized below. First, the active block was set up on its designed position (see Fig. 3). Wait until the passive block and active block are in equilibrium state (see Fig. 4). A cable was then connected for the quick release mechanism. Finally, the cable was subjected to external force by researcher (refer to Fig. 4).



Fig. 4 Equilibrium state and designed position of two blocks

Measuring Devices

In this research, various measuring devices were utilized, namely: (1) speedometers, (2) laser measurement system, (3) infrared gun (to measure distance), (4) accelerometer, and (5) high-speed camera. These devices and system can measure the position of motion, velocity, acceleration and displacement of the collision blocks.

(1) Speedometers

The speedometers (see Fig. 5) were used to measure the velocity of blocks before collision. The speedometers have two light sensors. Their distance was fixed. If the active block passes through the two light sensors, they send a voltage signal to the acquisition system that consequently shows the voltage-time curve as shown in Fig. 6. The time difference can be computed in Fig. 6. The formula was used to determine the velocity of blocks before collision.

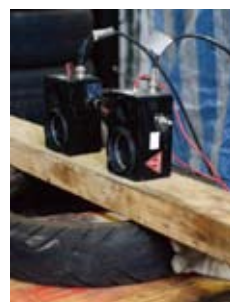


Fig. 5 Speedometers

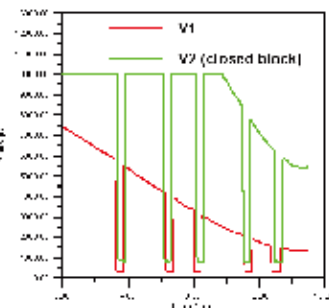


Fig. 6 Voltage versus time output

((2) Laser measurement system

The laser measurement system (see Fig. 7) was used to record the position of the motion of blocks at each period of time required. This system can not only accurately record each displacement or position of the blocks, but also can calculate their velocity.

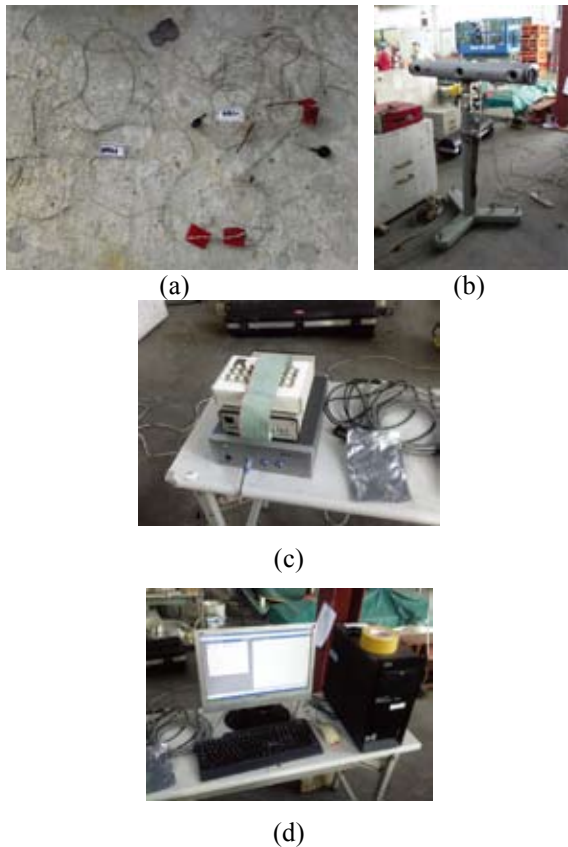


Fig. 7 Image data acquisition and control systems: (a) induction line, (b) camera, (c) image data acquisition, and (d) control system.

(3) Infrared gun

The infrared gun was used to measure distance (see Fig. 8) and was adopted to measure the sizes of the simple pendulum device and the position of blocks. The dead load from the simple pendulum device may cause deflection of the steel frame that in turn may influence the accuracy of the experiment. At each test, infrared gun was used to measure positions of the measuring point or reference point, but in some instances, researchers might unconsciously shake the test blocks, which may cause errors on the designed and measured heights. Table 1 shows the percentage error found between the designed and measured points.



Fig. 8 Infrared gun used to measure distance

(4) Accelerometer

Since the time of collision is rapid, the higher frequency acceleration gauge and data acquisition systems (see Fig. 9) were adopted. Results of impact tests are shown in Fig. 10.

Table 1. Percentage error on the designed and measured height

Position	Design (cm)	Measure (cm)	Error (cm)	Percentage (%)
Center	762.5	761.4	1.1	0.14%
Right	737.5	737.9	-0.4	-0.05%
Left	737.5	735.3	2.2	0.30%



Fig. 9 The higher frequency acceleration gauge and data acquisition systems

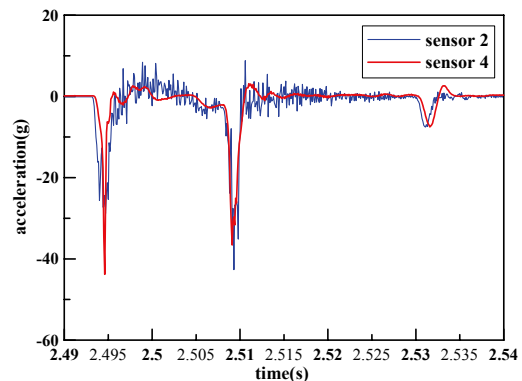


Fig. 10 Acceleration versus time

(5) High-speed camera

The high-speed camera was adopted to study the images of the colliding blocks. According to the recorded image data, the position, displacement, strain and velocity of the collision blocks can be computed. In this study, the software Vic-2D was used to analyze the recorded data. The Vic-2D software is based on a digital image correlation (DIC) method. The set projection speed of the high-speed camera was 3,000 fps. This projection speed can measure the change of the speed of blocks during collision.

From the recorded image data of colliding blocks, three states of collision were established, i.e. before collision, during collision, and after collision as detailed in Table 2. Using high-speed camera, one can clearly observe the position field, displacement field, strain field and velocity field of the two collision blocks by Vic-2D as shown in Tables 3(a) to 3(d). The two collision blocks have a small angle

during collision as shown in Fig.11.

Table 2. Positions of the collision blocks

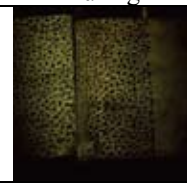
Before	During	After
		

Table 3(a) Position field

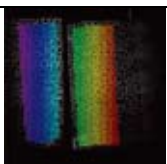
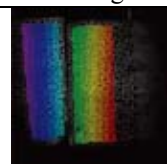
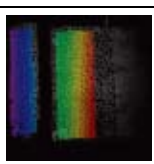
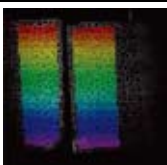
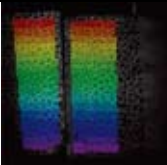
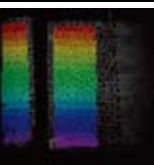
	Before	During	After
x			
y			

Table 3(b) Displacement field

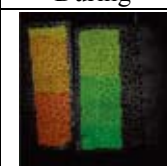
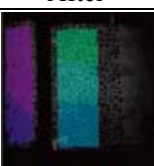
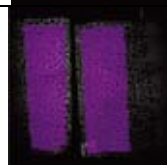
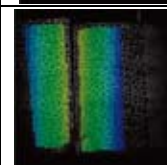
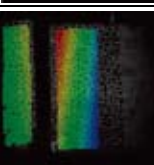
	Before	During	After
U			
V			

Table 3(c) Strain field

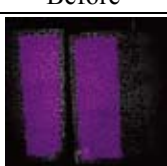
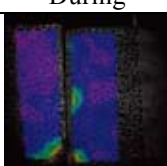
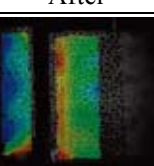
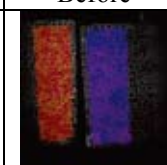
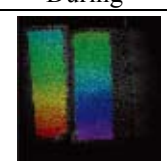
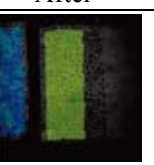
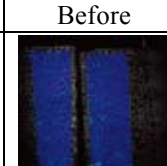
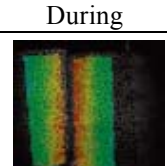
	Before	During	After
U			

Table 3(d) Velocity field

	Before	During	After
U			
V			

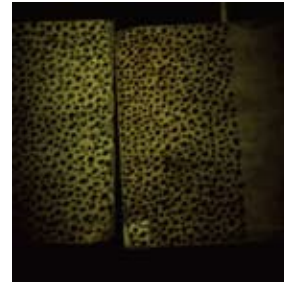


Fig.11. Small angle between two blocks in collision moment

Damage States of the Collision Blocks

The size of a collision block is 45cm×45cm×45cm. Figure 12 shows the damage states of the collision blocks.

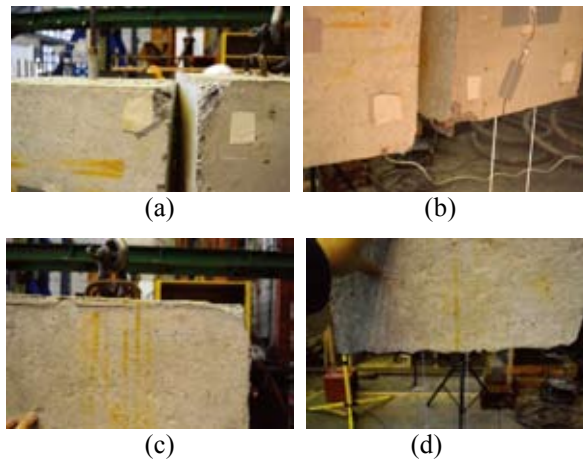


Fig. 12 The damage states of the collision blocks

Conclusion

In this project, an impact system has been developed. Using high-speed camera and Vic-2D software, the velocity of block before collision was 3.6566m/s. The analytical solution result was 3.66 m/s. The error is very small. Moreover, according to the results, the accuracy of the established impact system is satisfactory. Next year, the quick release system will be modified, which seeks to reduce the collision angle between two blocks during collision.

Numerical Simulation on the Effect of Bond Slip in Reinforced Concrete Structures

Ren-Zuo Wang¹, Chung-Yu Wang², Jen-Hui Liu³

王仁佐¹、王仲宇²、劉人慧³

Abstract

To compute the deformation of reinforced concrete (RC) structures, the vector form intrinsic finite element (VFIFE) method of analysis was adopted in this study. The effect of bond slip in the interface of the concrete and the reinforcing steel was considered. The RC structure was modeled using three types of element in the VFIFE method. At first, the two-dimensional (2D) solid element was used to model the deformation of the concrete. In addition, an equivalent uniaxial strain model by Darwin and Pecknold (year) can effectively simulate the nonlinear monotonic loading behavior of the concrete material. For the second type, the truss elements were adopted to model the deformation of the reinforcing steel using elastic-plastic material model. And last, to model the effect of bond-slip on the interface of concrete and reinforcing steel, the bond-link element was used between the node of a 2D solid element and a truss element. Comparison of results from the test on RC structural element (simply-supported beam) under monotonic loadings and the numerical results using the VFIFE method are presented to demonstrate both the capability and the accuracy of VFIFE method in modeling the response of RC structures.

Keywords : vector form intrinsic finite element, RC structure, bond-slip

Introduction

The effect of bond-slip in RC structure is important because, if RC structure is subjected to external loadings, the interface of the reinforcing steel and the concrete will crack and undergo seismic loading mechanism. Due to the developed cracked interface in RC structural members, the capacity of RC structure is consequently reduced. Recently, two numerical models were introduced. These numerical models include: (1) the continuous model, and (2) the discontinuous model. Most of the numerical models in RC structures used the former model. However, the continuous model fails to simulate the true nonlinear deformation and the failure status of RC structures, although the computational time in the analysis with the continuous model is much less than the latter.

In this project, a motion analysis method called vector form intrinsic finite element (VFIFE) method was adopted. In 2010, the National Center for

Research on Earthquake Engineering (NCREE), Taiwan has used this method to simulate large deformation of RC structure using continuous model. This year, the discontinuous model of RC structure was focused. In order to model the effect of bond-slip, 2D solid elements, truss elements and bond-link elements were adopted to simulate the responses of concrete, reinforcing steel and the bond-slip in RC structure, respectively.

Fundamentals of the VFIFE Method

The basic assumptions made in the VFIFE method are summarized as follows:

- 1) In a path element, the deformation of the structural element is small. The internal nodal force is small deformation and large displacement.
- 2) In a path element, the geometrical change of the internal nodal force can be neglected.

¹ Associate Researcher, National Center for Research on Earthquake Engineering, rzwang@ncree.narl.org.tw

² Professor, Department of Civil Engineering, National Central University, cywang@ncu.edu.tw

³ Graduate Student, Department of Civil Engineering, National Central University.

In the spatial point, basic assumptions in the VFIFE method are summarized as follows:

- 1) The deformation of the structural element is adopted to be approximately uniform.
- 2) The displacement interpolation functions of element are adopted.
- 3) The element mesh is continuum.

For the analysis of RC structure, the key VFIFE steps are:

- 1) In a path element, the deformation coordinates are adopted to describe the pure deformation of the structural element. In addition, the fictitious reversed rotation can remove the displacement of rigid body motion in structural member.
- 2) From step 1, the nodes of displacements in 2D solid element were decided since the bond-link element is connected to node of 2D solid element and truss element. Thus, the relative displacement (slip displacement) of bound slip element is calculated. According to bond stress-slip relationship, the bound stress can be computed.
- 3) From step 1, the pure strains of 2D solid element and truss element can be computed. Computing pure strains and using constitutive model of concrete and reinforcing steel, the stress and internal force of 2D solid element and truss element can be calculated.
- 4) By superposition of all internal forces and external forces of elements in mass points, based on equation of motion the displacement of mass points can be computed.
- 5) Steps 1 to 4 are repeated to achieve desired results.

The flowchart of processes in VFIFE is shown in Fig. 1.

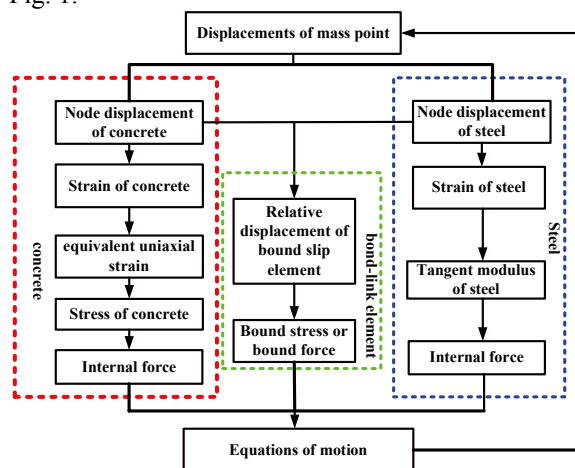


Fig. 1 Flowchart of processes in VFIFE method.

Constitutive Models of Concrete and Reinforcing Steel

Concrete has a non-orthotropic material behavior. The constitutive model of concrete was adopted from Darwin & Pecknold's model (DP model). The advantage of this model is the reduction of

two-dimensional model of concrete to an equivalent uniaxial strain model. In this project, the material frame between VFIFE and FEM is different. The DP model was constructed in the deformation coordinates. In addition, the principal stress direction was made equal to the principal strain direction. Based on this assumption, the material property, i.e. shear modulus G , remained constant in different coordinate systems. The constitutive model for non-orthotropic material can be written as follows:

$$\Delta\sigma = \frac{1}{1-\nu^2} \begin{bmatrix} E_1 B_{11} & E_1 B_{12} & E_1 B_{13} \\ E_2 B_{21} & E_2 B_{22} & E_1 B_{23} \\ E_3 B_{31} & E_3 B_{32} & E_1 B_{33} \end{bmatrix} \begin{Bmatrix} d\varepsilon_1 \\ d\varepsilon_2 \\ d\gamma_{12} \end{Bmatrix} \quad (1)$$

By rearranging equation (1), it can be rewritten as of the index formulation. The equivalent uniaxial strain can be expressed as follows:

$$d\varepsilon_{iu} = B_{i1}d\varepsilon_1 + B_{i2}d\varepsilon_2 \quad (i=1,2) \quad (2)$$

Equation (2) can be expressed in a matrix form as follows:

$$\begin{Bmatrix} d\sigma_1 \\ d\sigma_2 \\ d\tau_{12} \end{Bmatrix} = \begin{bmatrix} E_1 & 0 & 0 \\ 0 & E_2 & 0 \\ 0 & 0 & G \end{bmatrix} \begin{Bmatrix} d\varepsilon_{1u} \\ d\varepsilon_{2u} \\ d\gamma_{12} \end{Bmatrix} \quad (3)$$

where, E_1 , E_2 and ν are the tangent modulus at principal axes 1 and 2 and the Poisson's ratio, respectively, while G is the shear modulus. Since the reinforcing steel in RC structures can only carry tensile and compressive forces, the truss element was adopted in this study.

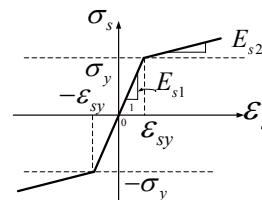


Fig. 2 Stress-strain relationship of the reinforcing steel

If the reinforcing steel is subjected to tensile stress (see Fig. 2), the tangent modulus of the reinforcing steel is

$$\text{when } \varepsilon_s \leq \varepsilon_{sy}, \quad E_s = E_{s1} = E_{s0} \quad (4)$$

$$\text{when } \varepsilon_s > \varepsilon_{sy}, \quad E_s = E_{s2} = 0.01E_{s0} \quad (5)$$

where E_{s0} is the initial modulus of the reinforcing steel, ε_{sy} is the yield strain of the reinforcing steel, $\varepsilon_{sy} = \sigma_y / E_{s0}$

If the reinforcing steel is subjected to compressive stress (see Fig. 2), the tangent modulus of the reinforcing steel is

$$\text{when } \varepsilon_s \geq -\varepsilon_{sy}, \quad E_s = E_{s1} = E_{s0} \quad (7)$$

$$\text{when } \varepsilon_s < -\varepsilon_{sy}, \quad E_s = E_{s2} = 0.01E_{s0} \quad (8)$$

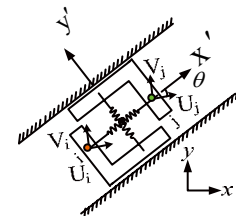


Fig. 3 Bond-link element in VFIFE

Bond-Link Element

Two types of elements have been proposed to simulate the effect of bond-slip in the finite element analysis of RC structures. The first type of element is the “bond-link” element by Ngo and Scordelis (1967). The second type of element is the “Goodman interface” element. In this study, the bond-link element (see Fig 3.), which consists two orthogonal springs connecting the nodes of concrete and reinforcing steel, was adopted in this study.

Using two orthogonal springs, one spring represents the relationship of the slip relative displacement to the bond force. The other one represents the relationship between the vertical relative displacement and the force. The relative deformations of the bond-link element can be computed as follows:

$$[\Delta\omega'] = \begin{bmatrix} \Delta U' \\ \Delta V' \end{bmatrix} = \begin{bmatrix} -C & -S & C & S \\ S & -C & -S & C \end{bmatrix} \begin{bmatrix} U_i \\ V_i \\ U_j \\ V_j \end{bmatrix} \quad (9)$$

where, $\cos\theta$ and $\sin\theta$ are represented as the C and S, respectively, in Eq. (9). The angle θ is the angle between the local coordinates ox' and the global coordinates ox . In Equation (9), index i and index j are the node numbers of concrete and reinforcing steel. The relative deformations versus spring forces can be written as:

$$[N'] = \begin{bmatrix} N'_x \\ N'_y \end{bmatrix} = \begin{bmatrix} k_h & 0 \\ 0 & k_v \end{bmatrix} \begin{bmatrix} \Delta U' \\ \Delta V' \end{bmatrix} = [D][\Delta\omega'] \quad (10)$$

where, k_h and k_v are the stiffness of the springs at x' and y' directions, respectively. These stiffnesses (k_h and k_v) relate to the diameter and the spacing of reinforcing steel, and the material properties of concrete and reinforcing steel. The spring forces of the bond-link element in the global system can be expressed as

$$[F] = [B]^T [N'] \quad (11)$$

In which,

$$[F] = [X_i \ Y_i \ X_j \ Y_j]^T \quad (12)$$

Substituting Eq. (10) to (11), the spring forces can be derived from

$$[F] = [K][\delta] \quad (13)$$

where,

$$[K] = \begin{bmatrix} -C & S \\ -S & -C \\ C & -S \\ S & C \end{bmatrix} \begin{bmatrix} k_h & 0 \\ 0 & k_v \end{bmatrix} \begin{bmatrix} -C & -S & C & S \\ S & -C & -S & C \end{bmatrix} \quad (14)$$

Equation (14) is the global stiffness matrix of the bond-link element. All spring forces are exerted on mass points in VFIFE method.

Effect Of Bound Slip in RC Structure

The effect of bound slip is due to the damaged interface between concrete and reinforcing steel. If the ultimate tensile strain (ϵ_{cr}) of concrete at tension zone in RC member is reached, then the crack of the concrete at tension zone appears. At the position of the crack, the tensile stress of the concrete is zero. But, the tensile stress of the reinforcing steel at the tension zone is added (see Fig. 4). This means that after cracking, the failure behavior of RC beam is like as if it is pulling off a rubber band. The concrete and reinforcing steel have interaction forces at their interfaces. If the distance x of RC beam increases, the tensile stress in concrete also increases.

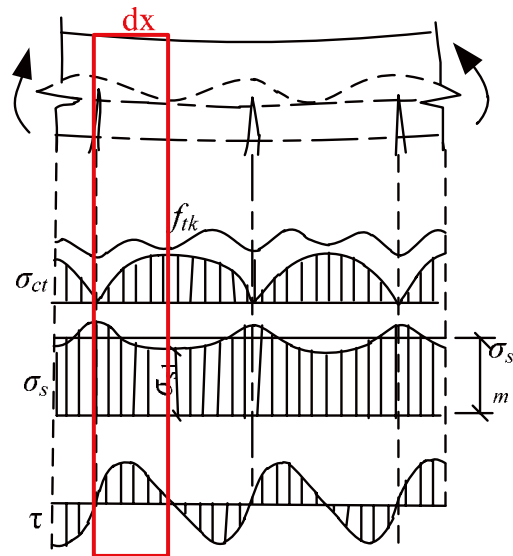


Fig. 4 Average stress of reinforcing steel and concrete

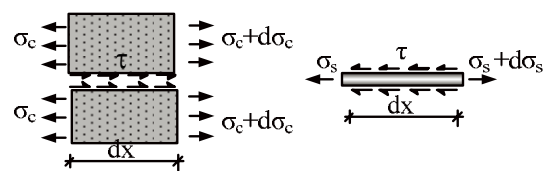


Fig. 5 Free-body diagram of concrete and reinforcing steel

According to force balance and compatibility in RC element (see Fig. 5), the relationship of the slip displacement to shear force on slip surface can be derived. Thus, the shear stress on slip surface and normal stress on the cross section of reinforcing steel can be found using the following equation:

$$\tau = \frac{4}{d} \cdot \frac{d\sigma_s}{dx} \quad (15)$$

where, d is the diameter of reinforcing steel, and x is a variable location. The force balance in a small RC section can then be satisfied. Equilibrium equation can be written as follows:

$$A_s \cdot d\sigma_s + A_c \cdot d\sigma_c = 0 \quad (16)$$

where, μ is the area ratio A_s / A_c of the reinforcing

steel and concrete and E_s/E_c is the modulus ratio α_E of the reinforcing steel and concrete. Substituting the area ratio and the modulus ratio into Eq. (16), the strains of concrete and reinforcing steel can be found from

$$\varepsilon_c = -\alpha_E \cdot \mu \cdot \varepsilon_s \quad (17)$$

where, ε_s is the strain of the reinforcing steel and ε_c is the strain of concrete. The formulation of strain versus slip displacement relationship can be computed using capability condition as

$$s = s_1 + \int (\varepsilon_s(x) - \varepsilon_c(x)) dx \quad (18)$$

where s_1 is the relative slip displacement at the position of loading. Substituting Eq. (17) into (18) and performing a differential calculation for Eq. (18), the following expression can be established:

$$\frac{ds}{dx} = -(1 + \alpha_E \cdot \mu) \cdot E_s \quad (19)$$

Multiplying the modulus E_s on both sides of Eq. (19), the stress relationship between reinforcing steel and slip displacement can be expressed as

$$\sigma_s = -\frac{E_s}{1 + \alpha_E \cdot \mu} \cdot \frac{ds}{dx} \quad (20)$$

Substituting Eq. (20) into (15), the shear stress on slip surface and the normal stress on the cross-section of reinforcing steel can be computed from the equation

$$\frac{d^2s}{dx^2} = \frac{4 [1 + \alpha_E \cdot \mu]}{d E_s} \tau \quad (21)$$

According to Eq. (21) and the experiment, many researchers have proposed an analytical formulation of the slip displacement versus the shear stress on slip surface. In this study, three formulations were introduced as follows:

1) The Nilson formulation for the effect of bound slip is based on RC test data under reversed cyclic loading (Bresler and Bertero, year)

$$\tau = 10^3 s - 58.5 \times 10^6 s^2 + 8.53 \times 10^9 s^3 \quad (22)$$

where τ (kgf/cm²) is the shear stress on slip surface.

2) Houde and Mirza (year) have proposed a formulation based on 62 pull-out tests of RC members as follows:

$$\tau = (5.3 \times 10^2 s - 25.7 \times 10^6 s^2 + 5.98 \times 10^9 s^3 - 0.558 \times 10^{12} s^4) \sqrt{\frac{f'_c}{415}} \quad (23)$$

In which, f'_c (kgf/cm²) is the compressive strength of concrete.

3) CEB-FIP Model Code 1990 has introduced a formulation of the shear stress on slip surface and the slip displacement as follows:

$$\tau = \phi(s) \cdot \Psi(x) \quad (24)$$

where

$$\psi(x) = \begin{cases} 1.35 \left[1 - \left(1.25 \frac{x}{l_a} - 1 \right)^2 \right] & (x \leq 0.8l_a) \\ 1.35 \sqrt{1 - \left(5 \frac{x}{l_a} - 4 \right)^2} & (x > 0.8l_a) \end{cases} \quad (25)$$

Numerical Example

In this project, a simply-supported RC beam was tested and studied to demonstrate the capability condition and the accuracy of the VFIFE method in performing a nonlinear dynamic analysis of RC structures. The results of the numerical simulations by VFIFE method and the conducted experiment (Burns & Siess, year) were compared and are shown in Fig. 8.

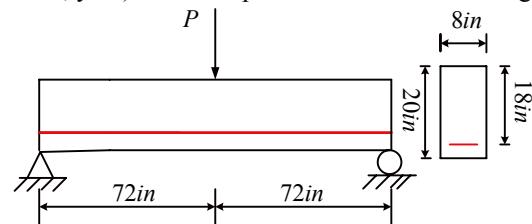


Fig. 7 Test on simply-supported RC beam

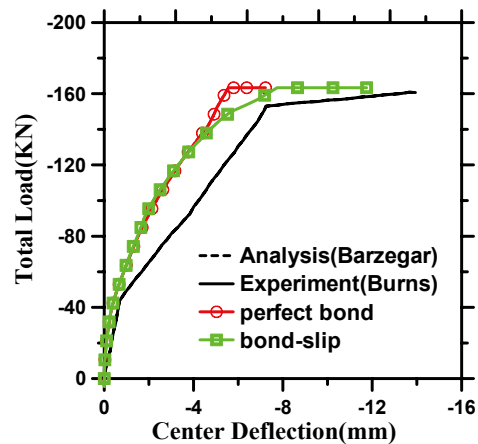


Fig. 8 Center deflection versus load of the simply-supported RC beam

Conclusion

In this project, the effect of bound slip has been considered using VFIFE method. In addition, the bond-link element and the relationship of slip displacement versus the shear stress on slip surface were adopted in determining the deformation of RC structure. Results of the test conducted on an RC structural element (simply-supported beam) and the numerical results of VFIFE method were compared and studied. Based from the comparison, the VFIFE method was found to be accurate and efficient.

A Neural Network-Based Approach for On-site Earthquake Early Warning System

Chu-Chieh Jay Lin¹, and Ze-Ping Shen²

林主潔¹、沈哲平²

Abstract

The on-site earthquake early warning system is under development for the area near the earthquake epicenter to provide information such as earthquake magnitude, the arrival time and the intensity of the strong shaking for free field as well as the structural response, etc. The real-time strong motion signals recorded from Taiwan Strong Motion Instrumentation Program (TSMIP) were used to train neural networks and the characteristics of the sensed earthquake accelerograms were learned. The neural networks provide a seismic profile of the arrival ground motion instantaneously after the shaking is felt at the sensors by analyzing the three components of the earthquake signals. Each data sample, consist of the first 1~10 second envelope of the complete earthquake accelerogram, was used as the input of the neural networks. The output of the neural networks provides estimates of the structural response and the time for emergency action. The neural network based algorithm is trained with 50149 accelerograms from 2505 earthquakes recorded in Taiwan. By producing informative warnings, the neural network based methodology has shown its potential to increase significantly the application of earthquake early warning system (EWS) on hazard mitigation.

Keywords: on-site earthquake early warning system, neural network, structural response

Introduction

Large-scale earthquake, as one of the catastrophic natural disasters, often caused tremendous damages to human beings. These damages include loss of human lives, public and private properties, huge adverse economic impacts and it is irreversible and painful. The magnitude 7.3 Chi-Chi earthquake in 1999 has collapsed more than 11 thousand house and claimed more than 2340 of human lives. The 2004 magnitude 9.1 earthquake at North Sumatra triggered the tsunami and made huge damage. In 2006, the people in central Java Indonesia suffered heavy damage and casualties from the magnitude 6.2 earthquake at Yogyakarta. In 2008, the magnitude 8.0 earthquake at Sichuan, China killed nearly 70000 people and 18000 still missing. More recently, the 2010 Haiti, Chile, and New Zealand earthquakes remind people need to pay attention to the potential earthquake hazards.

Taiwan has suffered from the threatening of moderate earthquakes for a long time since Taiwan is

located between Euro-Asian and Philippines tectonic plates on the Pacific Earthquake Rim. Furthermore, the hillside areas account for 73% of Taiwan due to steep terrain of the island. Plus the high population density (639 people/km²), in order to provide more living space and a better quality of life, mostly high-rise building structures were built at urban area. Usually people lived in the high-rise buildings will feel greater degree of shaking during the earthquake because of buildings' relatively low natural frequency. Therefore, the environment for the residents living at higher stories is endangered and their safety is threatened.

In Taiwan, a so-called regional Earthquake Early Warning System (Hsiao, 2006) is developed by Central Weather Bureau (CWB). With the strong motion sensor network, the epicenter of an occurring earthquake can be located and the magnitude can also be determined within 18 seconds. When the area is far from the epicenter, say 100 kilometer, we will have at

¹ Associate Researcher, National Center for Research on Earthquake Engineering, jaylin@ncree.narl.org.tw

² Assistant Researcher, National Center for Research on Earthquake Engineering, zpshen@ncree.narl.org.tw

most 15 seconds reaction time before the strong S-wave arrives if the sensor at the observation station was able to pick up the earthquake signal (P-wave) right away.

However, there is a “blind zone” (area within the 50 km of radius from the epicenter) for the regional EEWS needs to be eliminated, the on-site EEWS is for the improvement to provide more robust protection. This study is the continuation of the previous study (Tsai, K.C. et al, 2009; Lin and Shen 2010), to predict structural response including the maximum floor acceleration (MFA) and its arrival time on the roof by the first couple seconds of the P-wave using neural networks, so the residents in the building can be prepared prior to the strong vibration of the earthquake, to preserve the security of the people and property integrity within the building.

On-Site Earthquake Early Warning System

The on-site earthquake early warning system (EEWS) was developed for seismic hazard mitigation. The important information such as the magnitude of the earthquake, the seismic intensity as well as the peak ground acceleration (PGA) of the shaking, the arrival time of strong shaking (S-wave), the dominant frequency of the earthquake and the estimation of structural response can be provided. The development of the on-site EEWS is divided into 2 stages. Earlier in the 1st stage, the methodology of estimating the basic characters and time-related information of the earthquake were studied. Recently, the prediction of the structural response using neural network is developed in the 2nd stage. In the 1st stage, the body wave method and neural network methods were used to model the nonlinearities caused by the interaction of different types of earthquake ground motion and the variations in the geological media of the propagation path, and the learning techniques for the analysis of the earthquake seismic signal were also develop (Lin and Shen 2010). In the 2nd stage, two different approaches (general and tailored) are used to satisfy the different demands for the rapid estimation of structural responses. Both modules can rapidly estimate the structural response either using sensed P-wave directly or the output from the first stage. The general module is proposed to provide a low-cost, general-application and rapid estimation of the structural responses using only the common data of the structure (height, structure type, floor, location ... etc). Meanwhile, the customized module is able to provide a more accurate and detailed structural response estimation as a scenario-based response predictor.

Although the accuracy of the on-site EEWS may be less than the regional EEWS due to less earthquake information obtained. The more time provided for response, especially for the area near the epicenter,

increases the importance of the on-site EEWS. Both the regional EEWS and the on-site EEWS should be integrated to make a more robust EEWS and provide protection to people combining auto-control technology for different purpose. After any major earthquake, the warning message from EEWS integrated with automated shut-down device with gas line as well as other equipment will hopefully reduce the occurrence of post-earthquake fire, lower the earthquake casualties and economic losses caused by secondary disaster.

Numerical Building Model Analysis

This study use the recorded earthquake free field time histories collected from 1992-2006. Each earthquake record was marked P-wave and S-wave by automatically P-wave trigger program and verified manually. Then these earthquake accelerograms were consolidated into the earthquake free-field accelerogram database. Among the 59 observed buildings within the Taiwan Strong Motion Instrumentation Program (TSMIP) by CWB, the Tai-Power building is chosen since its significant features. There are totally 73 earthquake records from Tai-Power building. There are 26 time histories recorded from each sensor installed for each earthquake record. It is the tallest building when it is constructed. There are totally 26 tri-axial strong motion sensors installed in the building. Since the data recorded is not enough for training a neural network, the time history structural analysis software PISA-3D is used to build a numerical model for Tai-Power building. The 73 recorded earthquake time histories from Tai-Power building were used to modify and calibrate the numerical model of Tai-Power building. Then the chosen earthquake records from the earthquake free-field accelerogram database were used as input to run the PISA-3D and the response time histories were obtained to form the earthquake response accelerogram database. The structural response is assumed to be linear (elastic) behavior.

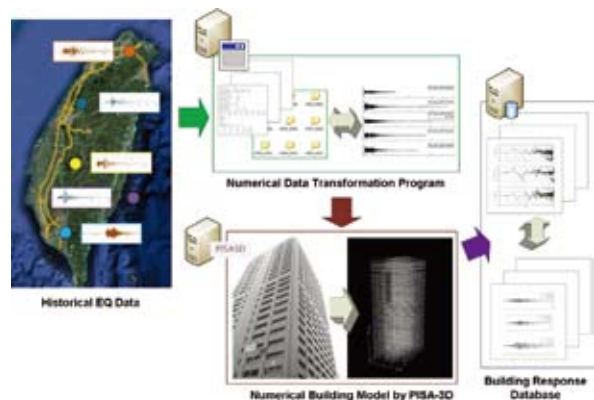


Figure 1 Flowchart of numerical building model analysis using PISA3D

To increase the records of structural response for the neural network training, all the earthquake records in the earthquake free-field accelerogram database were considered. The records with PGA range from 5-500 gal were chosen to run the PISA-3D for structural response. There are totally 10,097 records were used for further analysis (Chang, K.C. et al., 2010). Figure 1 shows the flowchart of numerical building model analysis using PISA3D. All the results from PISA-3D were collected into the building response database for further research.

Neural Networks

The neural networks are known as the biologically inspired soft computing tools that possess the massively parallel structures. Their learning capabilities allow the development of the neural networks based methods for certain mathematically intractable problems. Since seismic waves inside the earth passes through the media all over the floor, in the face through the different media will produce the refraction and reflection effect, starting from the source to the surface in the process, the high degree of complexity of linear and nonlinear behavior is a great challenge for the traditional mathematical model. Therefore, the neural networks have been applied to the ground motion generation, prediction and other difficult tasks since 1997. Previous researches showed that the neural networks make it possible to provide more accurate, reliable and immediate earthquake information for society by combining the EEWs and applying it to the planning of hazard mitigation.

This paper presents a neural networks based methodology for predicting the structural response before PGA arrival using initial part of P-waveform measured on-site. The information can be used as warning alarm for earthquake hazard mitigation. The neural networks program developed by Lin using FORTRAN was used in this study. A combination of the quick-prop algorithm and the local adaptive learning rate algorithm were applied to the multiple layer feed-forward back-propagation neural networks to speed up the learning of the networks. The supercomputer is also used to train the neural networks (Lin, 1999). The validity and applicability of the method have been verified using the CWB observation data sets of earthquakes occurred in Taiwan.

The architecture of neural networks used in this study is set to be different. Two neural networks, NN_{T0-3} and NN_{T0-10} , were used for on-site EEWs with the Fast Fourier Transform (FFT) of the initial 3 seconds and 10 seconds sensed earthquake waveform as input respectively. Each of the neural networks was used to analyze the relationship between the initial three or ten seconds of the sensed earthquake accelerogram and structural response of the Tai-Power building for that specific earthquake.

Case Study

In this study, the numerical model of Tai-Power building is built using PISA-3D. There are 73 earthquake records between 1994 and 2006 recorded from the sensors installed on the Tai-Power building were used to modify and calibrate the numerical model for structural response. The simulated responses for the roof of the Tai-Power building were within 10% of error. Then the 10097 earthquake records from the database of CWB were chosen as input to run the time history analysis using PISA-3D. The structural response of these 10097 earthquake records were then integrated into building response database.

The neural networks were used to learn (analyze) the relationship between free field ground motion and the structural response on the roof of the Tai-Power building. The 10097 earthquake records were divided into training group and testing group randomly. 8082 earthquake records (80% of the total) were used to train the neural networks while 2015 earthquake records (20% of the total) were used to test and validate the trained neural networks. The Fast Fourier Transform (FFT) of the digitized signal from the first 3 seconds of the earthquake time history after p-wave were used as input to the model NN_{T0-3} while the FFT from first 10 seconds of the earthquake time history were used as input to the model NN_{T0-10} . The structural responses for the roof of the Tai-Power building from the building response database were used as output for the neural networks. The comparisons of the real and estimated structural response are shown in figures 2-5.

The comparison of the real and estimated seismic intensity for NN_{T0-3} and NN_{T0-10} were shown in figure 2. The results of NN estimated MFA versus the real MFA from 2015 novel testing cases is plotted in the figure 2. The green area means that the intensity of the NN estimated MFA is the same as the intensity of the real MFA. The red area means that the intensity of the NN estimated MFA is one grade less than the intensity of the real MFA. The purple area means that the intensity of the NN estimated MFA is one grade larger than the intensity of the real MFA.

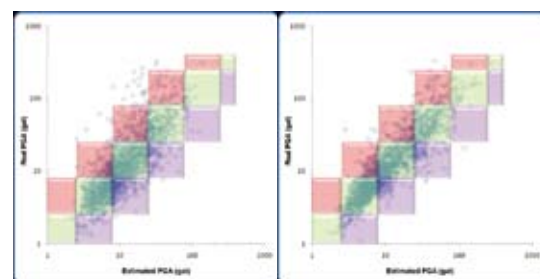


Figure 2 Comparison of the real and estimated seismic intensity (NN_{T0-3} , NN_{T0-10})

Both the results from NN_{T0-3} and NN_{T0-10} are acceptable and the regression analysis R^2 is 0.638 for NN_{T0-3} and 0.787 for NN_{T0-10} . Which shows more

input information the neural network model, more accuracy result can be obtained from the neural networks. Which means NN_{T0-10} is doing better than NN_{T0-3} . If the acceptable range for the intensity prediction is set to be ± 1 grade, the accuracy for NN_{T0-3} will be 91.5% (1844/2015) and 93.7% (1888/2015) for NN_{T0-10} .

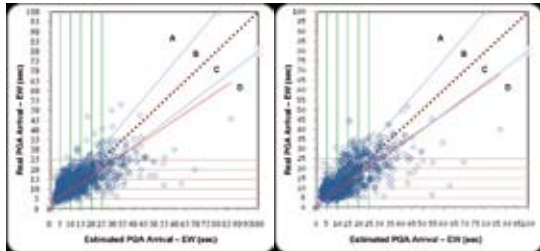


Figure 3 Comparison of the real and estimated arrival time for MFA-EW (NN_{T0-3} , NN_{T0-10})

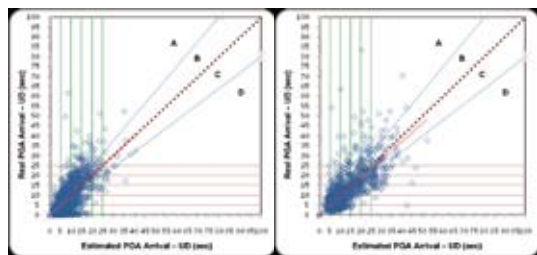


Figure 4 Comparison of the real and estimated arrival time for MFA-UD (NN_{T0-3} , NN_{T0-10})

The comparison of the real and estimated arrival time for MFA measured on the roof in two directions (horizontal and vertical) from both NN models (NN_{T0-3} and NN_{T0-10}) were shown in figures 3-4. The results have shown convergence and the regression analysis R^2 is 0.67 for NN_{T0-3} and 0.70 for NN_{T0-10} in East-West direction. As for North-South direction, the regression analysis R^2 is 0.644 for NN_{T0-3} and 0.662 for NN_{T0-10} . As for Up-Down (vertical) direction (figures 7 and 8), the regression analysis R^2 is 0.676 for NN_{T0-3} and 0.7 for NN_{T0-10} . These results show that the performance of NN_{T0-10} is better than NN_{T0-3} . The conclusion can be made that more input information (longer earthquake time history) to the neural network; more accuracy of the prediction can be increased.

In figures 3-4, the blue lines indicated the relative error of plus or minus 20% of the real values. The B area means the estimation is slightly small than the real value within 20% of error. The C area means the estimation is slightly larger than the real value within 20% of error. If the allowable error range is set to be plus or minus 20% of the real values (B and C areas indicated in figures), then the average accuracy for NN_{T0-3} is 28.3% and 31.6% for NN_{T0-10} . However, in the sense of early warning, the A area should be considered acceptable since the estimation is less than the real value, i.e. the warning is still effective to the people. Therefore, the allowable error range can be set to be A, B, and C areas indicated in figures, the

average accuracy for NN_{T0-3} is 60.2% and 66.9% for NN_{T0-10} .

Conclusion

When a severe earthquake occurs, preparedness and proper response are crucial since most dangers can be prevented beforehand. In this paper, the authors presented the further development of the on-site EEWs using neural networks. The structure response can be estimated in term of intensity and the arrival of the MFA. The methodology is described and its result shows great potential. The time issue is the key countermeasure during a large earthquake, thus using the estimation from NN_{T0-3} for announcement and keeping updates every seconds is suggested. Furthermore, the challenge of using only 1 second of observed earthquake accelerogram to predict the structural response is under development. The accuracy and reliability of earthquake intensity and arrival time are of the utmost importance and are of immense benefit in the mitigation of earthquake hazards. The verification of the reliability of the communication lines as well as the system is needed to ensure reliable operation of the on-site EEWs in the future. In such, the on-site EEWs is able to consequently bring huge benefits on the earthquake hazard mitigation.

References

- Chang, K.C., P.Y. Lin, C-C.J. Lin, T.K. Lin, Y.B. Lin, J.L. Lin, Y.T. Weng, T.M. Chang, S.K. Huang, Z.P. Shen, and Y.C. Lin, 2010, *Database for Fast Estimated Response of Structure*, NCREE-10-007, National Center for Research on Earthquake Engineering.
- Hsiao, N.G., 2006, *The Application of Real-Time Strong-Motion Observations on the Earthquake Early Warning in Taiwan*, PhD Thesis, Graduate Institute of Geophysics, National Central University
- Lin, C-C.J., 1999, "A Neural Network Based Methodology for Generating Spectrum Compatible Earthquake Accelerograms" *Ph.D. thesis, Dept. of Civil Engrg., UIUC, Urbana, IL*
- Lin, C-C.J., and Z.P. Shen, 2010, "Application of Neural Networks on Recent Development of the Earthquake Early Warning System for Taiwan", *Proceeding, the 9th US National and 10th Canadian Conference on Earthquake Engineering*, (2010EQConf), Toronto, Canada.
- Tsai, K.C., P. Y. Lin, C-C.J. Lin, T. K. Lin, Y. B. Lin, J. L. Lin, Y. T. Weng, T. M. Chang, Z. P. Shen, and C. S. Chung, 2009, *Preliminary Study of Added-Value Information and Analysis for Earthquake Early Warning System*, NCREE-09-013, National Center for Research on Earthquake Engineering.

Application of Seismic Hazard Mitigation on 3D-GIS/3D-VR Platform

Chin-Hsun Yeh¹, Chu-Chieh Jay Lin² and Chih-Hsin Chen³

葉錦勳¹、林主潔²、陳志欣³

Abstract

Taiwan has suffered from the threatening of moderate earthquakes for a long time since Taiwan is located between Euro-Asian and Philippine tectonic plates on the Pacific Earthquake Rim. Large-scale earthquake, as one of the catastrophic natural disasters, often caused tremendous damages to human beings. These damages include loss of human lives, public and private properties, and huge adverse economic impacts. The M7.3 Chi-Chi earthquake in 1999 has collapsed more than 11,000 houses and claimed about 2,340 human lives. After a major earthquake, generally, the emergency response can not be efficiently operated immediately due to the lack of information on the damaged area. Obtaining high-resolution spatial images and terrain data directly after a disaster has occurred is just as important for emergency response and rescue operations. This study illustrates the development of a near real-time, high-resolution, global earth observation on a three-dimensional (3D) platform for disaster monitoring and assessment in Taiwan. The 3D data has encompassed FORMOSAT II space borne images of the whole Taiwan and airborne images in local areas following OGC standard for data exchange and integration. The high-performance 3D visualization and grid technologies were used as core cyber-infrastructure to implement an on-time, semi-automated image processing procedures and 3D display, and analyzes capability through the use of NASA World Wind 3D sub-platform for leveraging high-resolution Landsat imagery. Further, the 3D GIS Taiwan platform can link to end-users the disaster prevention database, analyzed model and assessment methods, real-time observation data and images, and human collaborative and communication systems for comprehensive integration of relevant information in supporting immediate decision making. The 3D-GIS/3D-VR platform was combined with the Taiwan Earthquake Loss Estimation System (TELES) for application on seismic hazard mitigation. The combined use of space remote sensing images and ground 3D photography provides multi-viewpoint information in the devastated area, thus enhances the quality level of emergency response and rescue operations.

Keywords: 3D-GIS, 3D-VR, TELES, Seismic Hazard Mitigation

Introduction

Earth observation interacts with space, remote sensing, communication and information technologies, and plays an increasingly significant role in earth-related scientific studies, resource management, homeland security, topographic mapping, and development of a healthy, sustainable environment and community. Contemporary geospatial technology

provides an in-depth and broad collection of recent progress in earth observation. Today, spatial information technologies play increasingly important roles in emergency management. Large numbers of applications enhance the level of emergency management and the capability of the prevention and disposal of cases for sudden natural disasters, such as earthquake, hurricanes, forest fire, landslides and mudslides. Increasing demands are being made on use

¹ Researcher, National Center for Research on Earthquake Engineering, chyeh@ncree.narl.org.tw

² Associate Researcher, National Center for Research on Earthquake Engineering, jaylin@ncree.narl.org.tw

³ Assistant Researcher, National Center for Research on Earthquake Engineering, chhschen@ncree.narl.org.tw

of spatial information in emergence system.

Taiwan is densely populated and situated in a highly seasonal subtropical region with dominance of typhoon-generated hydrology. Not only flood and induced inundation, and landslide occurring frequently during typhoon season, but also occasional earthquakes, which subsequently cause severe damages to properties and losses of human life. Therefore, it is very crucial to monitor in a longer period our living environment through earth observation. One way is to adopt satellite remote sensing images and aerial images together with associated terrain data to build the spatial multidimensional geographic information system environment, especially using the high-resolution image data. The most challenging fact we face is the access to and usage of reliable, accurate and most updated spatial information for disaster management as it is an important concept in disaster response for a timely update and accurate spatial information that illustrates the current situation in a comprehensive response to an emergency event. Sharing information among involved organizations in order to facilitate coordinated disaster response operations is another challenge in disaster management.

Based on the need of disaster management in Taiwan, this study has developed a near real-time, high-resolution, global earth observation 3D platform for disaster monitoring and assessment. The platform has encompassed Formosat-2 space borne images in whole Taiwan areas and airborne image in local areas following OGC standard for data exchange and integration. The high-performance 3D visualization, grid technologies and conceptual cloud service are the core technologies used to implement the near-real time image processing, with display and analyses capabilities through the use of NASA World Wind 3D system for leveraging high-resolution Land Sat imagery. Moreover, this study has covered multi-scale earth observation methodologies, including large scale remote sensing observation viewed from space and *in situ* small scale but higher resolution 3D photography observation viewed from ground surface. The features of the 3D GIS Taiwan platform will be explored through the demonstration on typhoon, inundation, and earthquake-related events. This study also elucidates that the 3D GIS Taiwan platforms can be linked further with the existing monitoring sensor network, human communication system, end-user's database, and models and assessment results to support decision makers as they study the situation in a certain disaster on how to respond immediately and appropriately.

Development of 3D-GIS Taiwan Platforms

The development of a near real-time, high-resolution, global earth observation 3D platform for applications to disaster monitoring and assessment

in Taiwan, in short the “3D-GIS Taiwan” platform, has been developed through the synergy of National Applied Research Laboratories (NARL) on its environmental and disaster reduction capability. Six institutes under NARL have been involved in the project. Three layers of the integrated platform can be classified, *i.e.*, image resource, display platforms, and application layers. The 3D-GIS Taiwan platform is an innovation and technology based on interdisciplinary platform that established a complete vertically integrated value chain linking the multi-institution capability, practical application and international cooperation functions. Through the validation function processing, it can turn into a service platform to provide decision support to government on environment monitoring and disaster assessment.

The 3D-GIS Taiwan platform can be divided into two sub-platforms: one is the 3D-VR sub-platform and another is the Web 3D-GIS sub-platform. The former is tasked to display directly and locally high-resolution remote sensing image using stereo projector, 3D LCD, and Tile Display Wall (TDW) facilities without network connected with remote data; while the latter is a networked system connecting remote data. With the readiness of these two display platforms, NCREE was able to enhance decision support performance of disaster prevention and accuracy of environmental monitoring through the platforms.

Moreover, for a quick response to natural disasters, the near real-time remote sensing observation and image processing are very crucial to be used in determining the real scenario of the disaster rescue and response operations. It is significant that immediately after a natural event such as earthquakes, sufficient image data must be obtained prior to judgment and emergency response decision making. In this, it is of utmost importance to integrate the image processing and display platform sequence in speeding up the image processing time and the display of 3D terrain data in the 3D-GIS platform.

Development of 3D-VR Platform

The 3D-VR platform has been developed based on OpenGL language, with features of volume rendering and discrete level-of detail. The satellite images with 2M resolution covering the whole Taiwan area have a total data size of 33Gb. Digital terrain models (DTM) with 5m resolution covers an area of 36,000 km² in which grid/mesh size created is 40,388 x 75,526 and has approximately 6 billion of triangles. The challenge encountered for the 4K VR projection system was the handling of the large size of data. The high-performance streaming system conceptually comprises of a 2 x 2 TDW in each projector, where 8-CPU Cluster is required for a 4K projector display. The 4K solution is expected to provide the highest resolution for display of 3D environmental features.

The image sources in the above description for 3D-VR display are viewed from air, like satellite and aircraft. Image taken from air can cover large area of earth and land areas with certain level of image resolution. For example, the Formosat-2 image has a 2-meter resolution. But it still could not cover the details of *in situ* scenario from human's viewpoint. Usually, during the disaster, rescuers find it difficult to reach the affected individuals in the area. When the devastated area becomes stable, it is only by then possible to take *in situ* 3D photos and have these photos analyzed to establish a high-resolution panoramic scene. This provides a different scale of human's viewpoint from *in situ* perspective compared with those of viewpoint from the atmosphere. Different scales of image can be combined and used that can provide comprehensive angles and multi-scale viewpoints.

Development of Web 3D-GIS Platform

The Web 3D-GIS platform has been developed based on NASA World Wind system, typically used for leveraging high-resolution Landsat imagery and applications to environmental monitoring and disaster mitigation. World Wind is an open source 3D interactive world viewer created by NASA's Learning Technologies project and was released in mid-2004. It is now being continuously developed by NASA's staff and open source community developers. World Wind allows any user to zoom from outer space into any place on Earth. World Wind uses satellite imagery and elevation data to allow users experience earth terrain in visually rich 3D imaging, just as if they are really there. Navigation is automated with single click of a mouse as well as the ability to type in any location that will automatically zoom into it. World Wind was designed to run on recent computer hardware with 3D acceleration.

The web 3D-GIS platform was developed through the modification of World Wind system and which encompasses FORMOSAT II space borne and airborne images incorporated with data warehouse/fusion and high-performance visualization technologies, as it attempts to implement a near real-time and semi-automation image processing procedures, links with end-users' disaster prevention database, and analyzes model and assessment methods for decision support to disaster assessment and scenario identification. Moreover, the objectives can be extended to the illustration of the structure data pipeline, associated grid technologies, and cloud service for the integration and sharing of distributed image resources. For example, through the pipeline it can be linked with other processed images of remote sensing research institutes in Taiwan, and can possibly be connected with other international remote sensing image database, such as Sentinel Asia. The transmission of data in the pipeline was designed following the OGC standard. The web 3D-GIS

platform can accommodate the integration of satellite and airborne images, as well as the *in situ* panoramic scene and 3D photos.

Application of the Seismic Hazard Mitigation

As for the application to earthquake-related events, the 3D-GIS Platform has imported data from the TELES (Taiwan Earthquake Loss Estimation System). TELES provides assessment and evaluation of damages induced by earthquakes. As Fig. 1 shows, the data representing the earthquake strength can be filled with color and be overlaid on both satellite and aerial images via the Web Map Service (WMS) and the Web Feature Service (WFS) provided by the 3D-GIS Platform. Therefore, a more realistic comprehension of the damages based on integrating numeric data and images can be achieved.

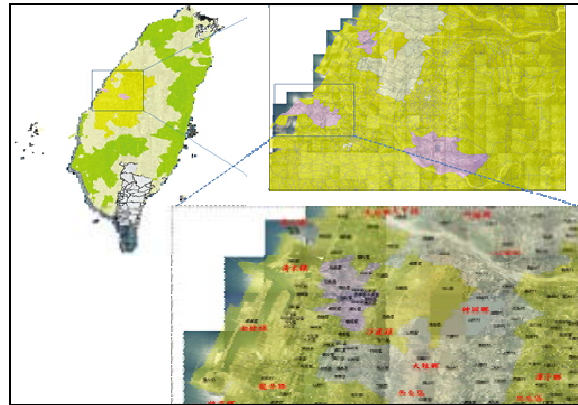


Fig. 1 3D-GIS platform applied with TELES

The near real-time high-resolution digital maps, such as aerial images and FORMOSAT II satellite images, can be obtained through the established platform. The loss distribution of the damaged buildings with regional (local) information can be understood, as shown in Fig. 2.



Fig. 2 The loss distribution of the damaged buildings

With the provided information of the 3D-GIS Platform, the concerned government agencies or individuals can obtain information through different types of thematic maps from early seismic loss assessment. Figure 3 shows the peak ground acceleration maps with satellite image.



Fig. 3 Map of peak ground acceleration

Through the application of 3D display platform, with a digital elevation map, users can observe the condition of the terrain. And, the system could be combined with the historical traces of active faults, the sources of the earthquakes, and other related information, as shown in Fig. 4.

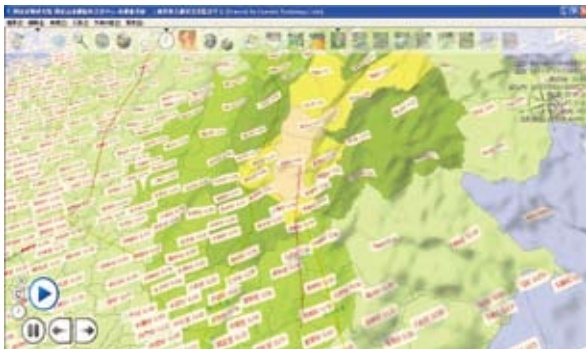


Fig. 4 Thematic map of 3D peak ground acceleration

In addition to the post-seismic applications, the system can also be used on disaster prevention and rescue drills through disaster preparedness and awareness trainings. Figure 5 shows the distribution of the historical active faults. The disaster relief and contingency operations procedures can be better arranged with the understanding of spatial situation.



Fig. 5 Map of historical active faults

Furthermore, the distribution of damaged buildings in 921 Chi-Chi earthquake and the details of each building damages were archived and can be displayed on the 3D-GIS platform, as shown in Fig. 6 and 7. The original information, such as investigation form, reconnaissance report and photos, can be retrieved and used for educational purpose as well as a reference for future structural analysis.



Fig. 6 Distribution of damaged buildings in 921 Chi-Chi earthquake

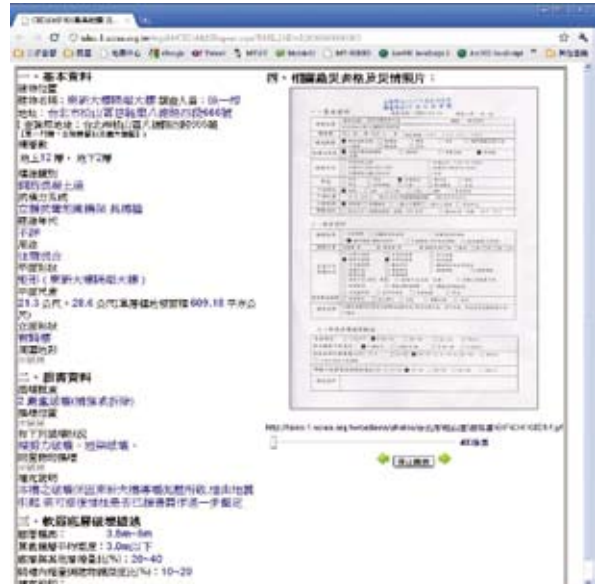


Fig. 7 Building damage investigation form for 921 Chi-Chi earthquake

Conclusions

The ability to respond quickly after an earthquake disaster is very important. The more complete analysis of the disaster can be provided, the better the relief operation will be carried. The high-resolution environmental observation 3D platform for disaster assessment project was initiated by the synergy of NARL's core competence on environmental monitoring and disaster reduction techniques, which include high-resolution satellite image processing, 3D visualization, grid computing and cloud service, and disaster mitigation technology along with the vision for implementing the advanced cyber-infrastructure for GEO science (is this another

project or it refers to geological science). For a quick response to an earthquake event, the near real-time remote sensing observation and image processing was developed to get insight into the disaster scenario. The combined use of space remote sensing images and ground 3D photography provides multi-scale viewpoint scenario information in the affected area that enhances the quality level of disaster-related decision making of concerned agencies and/or individuals. The application of 3D-VR / 3D-GIS platform on seismic hazard mitigation has been studied. The 3D geographic information coupled with the statistics of the building damage, casualties, and estimated intensity of ground vibrations information are provided to aid in emergency operation. More information such as transportation system, road network, pipeline etc. will be added to this platform in the future to enhance its efficiency for relief operations.

References

- Tsai, W.F., T.L. Chung, C. Chang, F.P. Lin, J.Y. Chang, P.Y. Li, C.Y. Sun, B.C. Chen, G.S. Chang, N.Y. Chen, D.S. Shih, Y.C. Wang, W.R. Su, T.M. Huang, C-C. J. Lin, and M.C. Chen, "Development of High-resolution Environmental Observation 3D Platform for Disaster Assessment", *Proceeding, International Conference in Commemoration of the 10th Anniversary of the 1999 Chi-Chi Earthquake, Taiwan*, September 2009.
- Lin, C.-C. J., W. C. Chen, and C. H. Yeh, "Application of Taiwan Earthquake Loss Estimation System (TELES) on Seismic Disaster Simulation Website ", *Proceeding, International Symposium on Social Management System, (ISMS 2007)*, YiChang, China, March 2007.
- Yeh, C. H., C. H. Loh and K. C. Tsai, 2006, "Overview of Taiwan Earthquake Loss Estimation System", *Natural Hazards*, 37, pp. 23-37.

Research Programs and Accomplishments



National Center for Research on Earthquake Engineering

200, Sec. 3, Xinhai Rd., Taipei 106, Taiwan, R.O.C.
TEL : +886-2-6630-0888 FAX : +886-2-6630-0858
<http://www.ncree.org.tw>

ISBN : 978-986-85281-7-8



9 789868 528178